Beam-induced current studies of CdTe/Cds solar cells.

Edwards, Paul Roger

How to cite:

Edwards, Paul Roger (1999) *Beam-induced current studies of CdTe/Cds solar cells.*, Durham theses, Durham University. Available at Durham E-Theses Online: http://etheses.dur.ac.uk/1109/

Beam-Induced Current Studies of CdTe/CdS Solar Cells

by

Paul Roger Edwards, B.Sc., A.R.C.S.

A thesis presented in candidature for the degree of
Doctor of Philosophy in the University of Durham

Department of Physics
December 1998

Abstract

This work concerns the application of scanning beam experiments and luminescence techniques to the study of thin-film CdTe/CdS solar cells. Particular emphasis has been placed on characterising the effect of the post-deposition annealing of these devices with cadmium chloride.

Electron and optical beam-induced current measurements (EBIC and OBIC) have been used to probe variations in the carrier collection efficiency of the solar cells. Although the spatial resolution of OBIC is limited, removal of the glass substrate has allowed EBIC to be carried out in the illumination geometry. These measurements have shown that one effect of the $CdCl_2$ treatment is the passivation of the CdTe grain boundaries.

EBIC measurements as a function of the electron beam current have shown a dependence of the contrast on the carrier injection density. A model has been proposed to explain this in terms of the onset of high injection conditions, and the effect has been exploited to yield information about spatial variations in the equilibrium carrier density in the device. This has shown that the regions near the grain boundaries are more *p*-type than the grain interiors, and that the presence of the sulphide layer increases the overall majority carrier concentration in the CdTe. Measuring EBIC as a function of the beam energy has demonstrated the presence of a buried homojunction, and has shown the chloride treatment to increase the spatial extent of minority carrier collection in the absorber layer.

Photoluminescence measurements on chemically bevelled cells have been used to probe the concentration of impurities as a function of depth, and this has been complemented by the use of spatially resolved cathodoluminescence imaging. These results support the EBIC data, with higher concentrations of shallow levels observed near to the grain boundaries, and also show that the presence of sulphur increases the concentration of optically active centres.

Declaration

I declare that, unless otherwise stated, all the work presented in this thesis was carried out by the candidate. I also declare that none of this work has previously been submitted for any degree and that it is not being submitted for any other degree.

K. Durose

Dr. K. Durose
Supervisor

P. R. Edwards

P. R. Edwards
Candidate

Acknowledgements

I would like to thank all those who have assisted me during the course of my PhD. Thanks are due in particular to Dr. Ken Durose, for his patient and encouraging supervision of my project. His enthusiasm for cadmium telluride is as contagious as it is disturbing.

I am grateful to Dr. Andy Brinkman and Dr. Douglas Halliday for their willingness to share with me some of their considerable expertise in solar cells and luminescence measurements. I am grateful too to Dr. Simon Galloway, both for his invaluable help during the first months of my PhD at Durham, and latterly at Oxford Instruments. Thanks are also due to Norman Thompson and David Pattinson for their expert and friendly technical support.

Many thanks also to Dr. Dieter Bonnet and Dr. Hilmar Richter at ANTEC GmbH, without whose involvement this work would not have been possible. I am also very grateful for the help afforded to by members of other universities in the use of their facilities. In particular I would like to thank Dr. Peter Wilshaw at Oxford University for the use of the OBIC equipment, and Dr. I. M. Dharmadasa and Malcolm Ives at Sheffield Hallam University for the GDOES measurements.

Finally, I would like to acknowledge the contribution of past and present members of the II-VI Semiconductors and Ceramics research group, each of whom has helped to make the lab a friendly and rewarding place in which to spend the last three years: Nick Aitken, Saleh Al-Amri, Josep Carles-Alabert, Mike Cousins, Aislinn Crozier, Tooraj Hashemi, Matt Hogan, John Mullins, Mehmet Parlak, Mark Potter, Dirk Rose and Thomas Schmidt.

This work was funded by the Engineering and Physical Sciences Research Council.

Contents

Chapter 6: Front-wall EBIC imaging 88

Chapter 7: Variation of EBIC with beam voltage 122

Chapter 9: Conclusions 169

Appendix: List of publications and awards 175

List of symbols

A	diode quality factor	dimensionless
C	EBIC contrast	dimensionless
c	speed of light in vacuum	ms^{-1}
D_n, D_p	carrier diffusion coefficients	cm^2s^{-1}
E_A	energy of acceptor impurity	eV
E_b	electron beam energy	keV
E_C	energy of bottom of conduction band	eV
E_D	energy of donor impurity	eV
E_F	Fermi level energy	eV
E_g	bandgap energy	eV
E_V	energy of top of valance band	eV
E_X	exciton energy	eV
$\boldsymbol{E}$	electric field	Vm^{-1}
I_b	electron beam current	A
I_D	EBIC at a crystal defect	A
I_{EBIC}	electron beam-induced current	A
I_p	EBIC in perfect crystal	A
G	EBIC gain	dimensionless
g	generation rate	$cm^{-3}s^{-1}$
h	Planck's constant	Js
$\boldsymbol{J}$	current density	Acm^{-2}
J_0	reverse saturation current density	Acm^{-2}
J_{sc}	short-circuit current density	Acm^{-2}
J_L	photogenerated current density	Acm^{-2}
k	Boltzmann's constant	JK^{-1}
L_n, L_p	carrier diffusion lengths	cm
N_A	acceptor concentration	cm^{-3}
N_D	donor concentration	cm^{-3}
n	electron density	cm^{-3}

p	hole density	cm^{-3}
n_0, p_0	equilibrium carrier densities	cm^{-3}
Δn, Δp	excess carrier densities	cm^{-3}
q	electron charge	C
R	recombination rate	$cm^{-3}s^{-1}$
R_G	Grün range	cm
T	absolute temperature	K
U	net recombination rate	$cm^{-3}s^{-1}$
W_d	depletion layer width	cm
V_{bi}	built-in voltage	V
V_{oc}	open-circuit voltage	V
x	radial co-ordinate	cm
x	molar fraction	dimensionless
z	depth co-ordinate	cm
Z	atomic number	dimensionless
α	optical absorption coefficient	cm^{-1}
Γ	photon flux	$cm^{-2}s^{-1}$
η	solar cell efficiency	%
ε_s	dielectric constant	Fm^{-1}
λ	wavelength	nm
μ_n, μ_p	carrier mobilities	$cm^2V^{-1}s^{-1}$
τ_n, τ_p	carrier lifetimes	s

List of abbreviations

AM	air mass
BE	backscattered electron
CBD	chemical bath deposition
CSS	close-space sublimation
CL	cathodoluminescence
CVD	chemical vapour deposition
DAP	donor acceptor pair
EBIC	electron beam-induced current
EDX	energy dispersive X-ray analysis
GDOES	glow discharge optical emission spectroscopy
ITO	indium tin oxide
LBIC	light beam-induced current
MOCVD	metal-organic chemical vapour deposition
OBIC	optical beam-induced current
PL	photoluminescence
PV	photovoltaic(s)
PVD	physical vapour deposition
REBIC	remote EBIC
SE	secondary electron
SEM	scanning electron microscope, ~/scopy
SIMS	secondary ion mass spectrometry
SLS	scanning light spot
SOM	scanning optical microscope
TCO	transparent conducting oxide

Chapter 1: Introduction to photovoltaic solar cells

1.1 INTRODUCTION: THE NEED FOR SOLAR CELLS

The rapid depletion of the earth's fossil fuel reserves and concern over the effect of carbon dioxide emissions on the environment have led to new energy sources being sought to supply the world's ever-increasing energy demand. Of the various renewable alternatives, photovoltaic (PV) solar cells offer one of the most versatile solutions, since they allow solar radiation to be converted directly to electricity. This chapter aims to outline the physical principles behind these devices and to review the currently established and emerging technologies.

1.2 PHOTOVOLTAIC EFFECT

The photovoltaic effect was first observed in 1839 by Becquerel [1], who detected a voltage between two electrodes in an electrolyte solution under sunlight. The subsequent discovery of a similar effect in selenium [2] led to the development of the first solid-state photovoltaic cells, used for many years in photographic exposure meters [3]. Whilst these devices exhibited conversion efficiencies of less than 1%, the same junction phenomena are today exploited in modern devices.

The photovoltaic effect in semiconductors is the result of two processes taking place concurrently. The first is the interaction of incident photons with the crystal lattice to produce pairs of charge carriers. Electrical current is then generated via the second process, whereby the electrons and holes are accelerated in different directions due to the presence of an electric field. These processes are explained in greater depth in the following sections.

1.2.1 Photo-generation of charge carriers

When photons with an energy of at least that of the bandgap are incident on a semiconductor, they have a probability of interacting with the lattice, resulting in the promotion of a valence band electron to the conduction band. This results in the photon flux Γ varying exponentially with distance z through the material:

$$\Gamma(\lambda,z)=\Gamma_0(\lambda)e^{-\alpha(\lambda)z} \tag{1.1}$$

where the absorption coefficient α is a function of the wavelength λ.

This process results in excess carriers being injected, and the mass action law

$$np=n_i p_i \tag{1. 2}$$

which relates the carrier concentrations n and p at thermal equilibrium to the intrinsic concentrations, no longer applies. Unless collected by an electric field, these excess carriers will then recombine to give a steady state.

If the energy of the incident photon is greater than the semiconductor bandgap E_g, the electron excited from the valence band will have an energy above that of the conduction band minimum. This excess energy is usually subsequently lost via phonon interactions. However, if the initial photon energy is greater than $2E_g$, then the newly excited conduction band electron may produce another carrier pair by the process of impact ionisation. This effect has been found to cause a measurable improvement in the performance of some crystalline Si and SiGe solar cells [4].

1.2.2 Carrier collection

Carrier collection in solar cells is achieved by creating a built-in electric field. Such a field arises when a semiconductor is placed in intimate contact with a metal (a Schottky barrier), or another semiconductor. In the latter case, the semiconductors may be either differently doped examples of the same material (a *homojunction*) or different compounds (a *heterojunction*). All three of these systems are used in solar cells.

Schottky barrier Figure 1.1a shows a band diagram before the formation of a Schottky contact between an n-type semiconductor of bandgap E_g and electron affinity χ_s and a metal with a work function φ_m. When these two materials are placed in intimate contact (Figure 1.1b), the difference in carrier concentrations on either side of the interface causes a flow of majority carriers (in this case electrons) from the semiconductor to the metal. This creates a region of positive space charge in the semiconductor, and a much narrower region of negative space charge in the metal.

The net diffusion will reach zero when conditions for thermal equilibrium are met, with coinciding Fermi levels and continuous vacuum level. This is shown in Figure 1.1b.

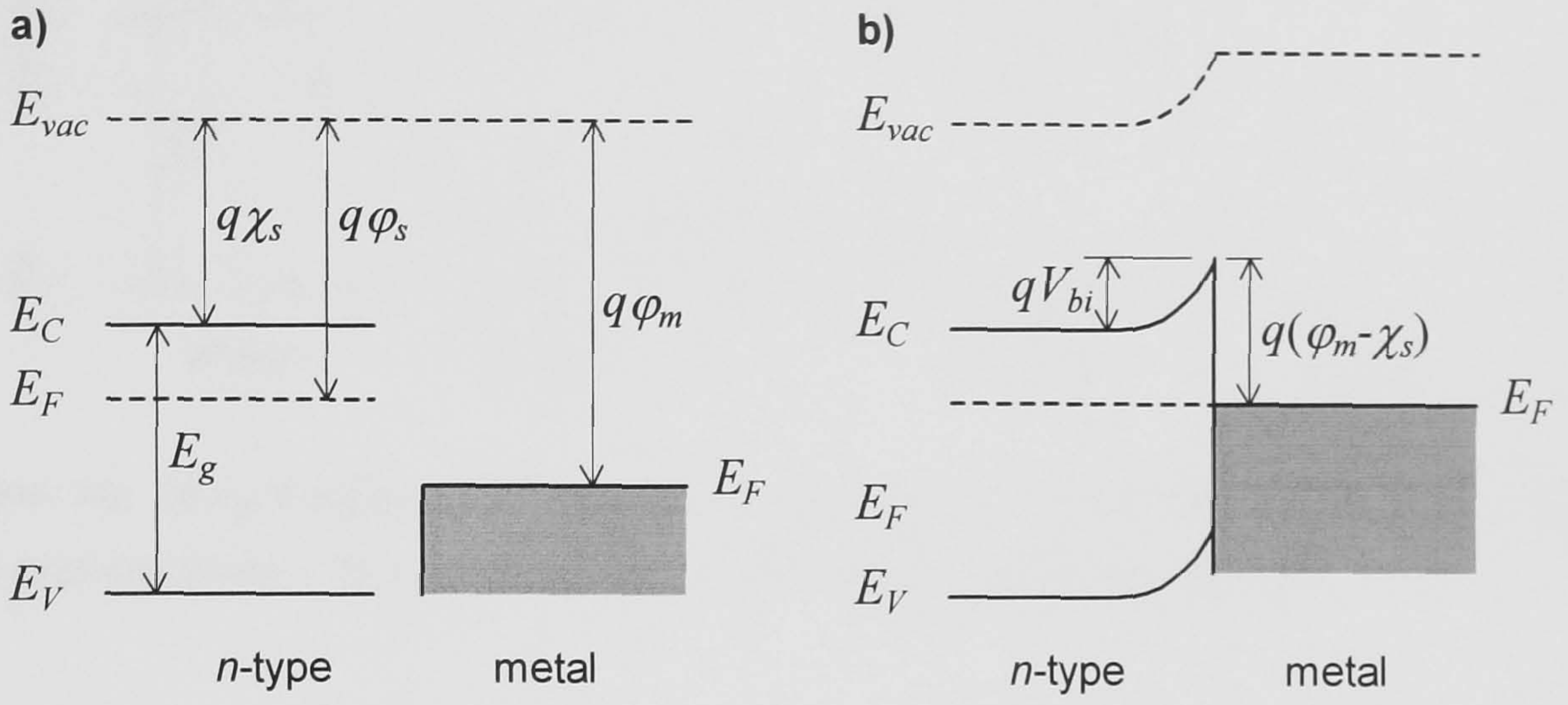

Figure 1.1 Band diagrams showing the formation of a Schottky barrier. **a)** Isolated semiconductor and metal. **b)** Semiconductor and metal in contact and in thermal equilibrium.

The region of space-charge is referred to as the depletion region, and results in a built-in electric field. This is manifested by the bending of the conduction and valence bands of the semiconductor. The total built-in voltage, V_{bi}, is determined by the difference in the two work functions.

Figure 1.1b also shows the barrier to the flow of majority carriers which is characteristic of metal-semiconductor contacts. The height of this Schottky barrier determines whether the contact exhibits ohmic or rectifying characteristics, and has important implications for the back contact of CdTe solar cells (see Section 2.3.5).

Homojunction Similar band bending arises from forming a junction between *n* and *p*-type regions of the same semiconductor. This is shown in Figure 1.2.

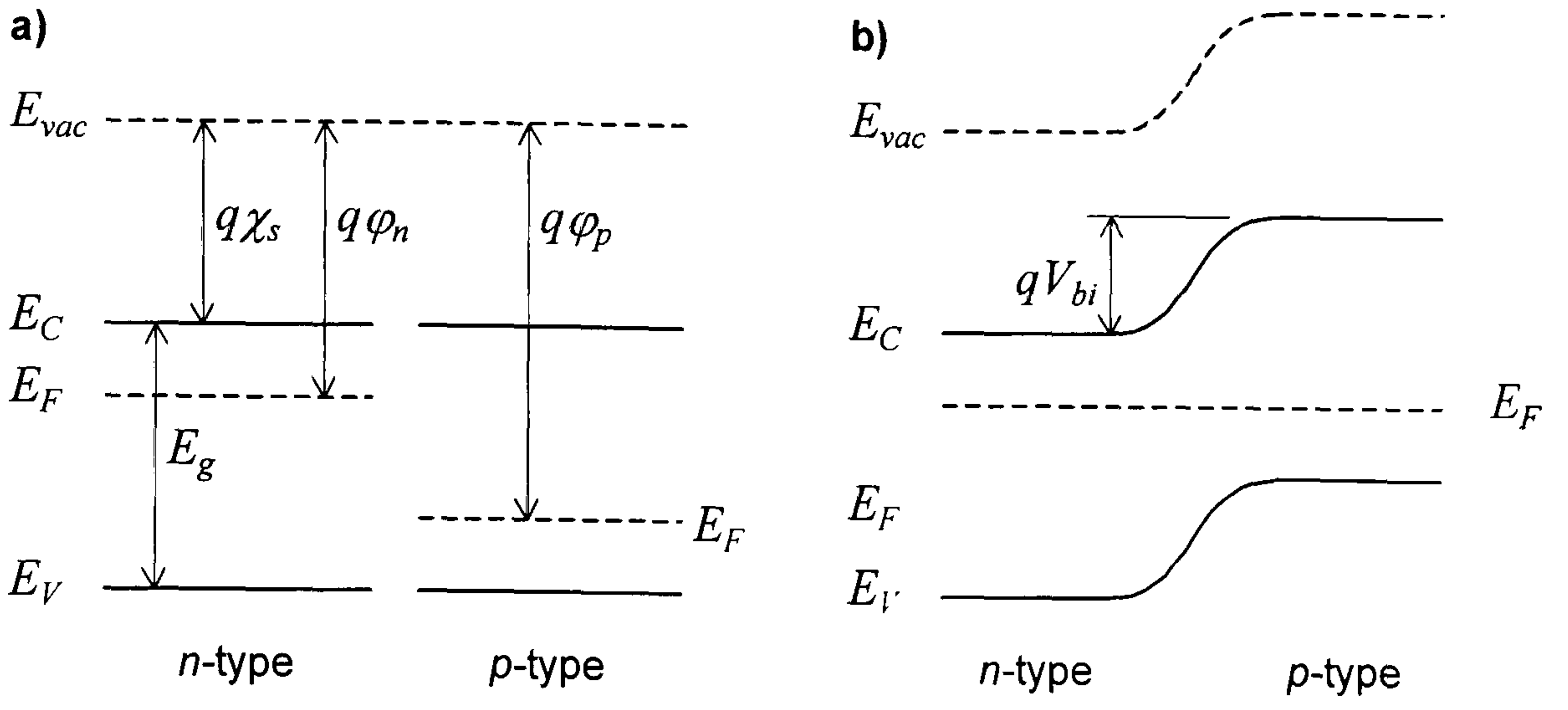

Figure 1.2 Band diagrams showing the formation of a homojunction. **a)** Isolated *n* and *p*-type semiconductors. **b)** *n* and *p*-type in contact and in thermal equilibrium.

The homojunction has the advantage that the energy bands of the two halves are aligned. This avoids the formation of barriers or spikes, as seen in some Schottky contacts and heterojunctions (see below). However, a disadvantage in the use of homojunctions in solar cells is that the side of the junction on which the light falls must be very thin to prevent the absorption of a significant part of the incident light. This means that the collecting junction itself must be close to the device surface, where surface recombination can result in current loss. Despite this potential drawback, the currently most widely used solar cell, the crystalline silicon device, uses this type of junction.

Heterojunction The problem of surface recombination can be reduced by using a wider bandgap semiconductor at the front of the cell (the *window* layer), and a narrower bandgap material beyond this (the *absorber* layer). Since the wide gap layer will be transparent to most wavelengths of light, it can be made thicker than would be tolerated for a homojunction.

The different bandgaps and electron affinities of the window and absorber layers make the band diagrams less straightforward to determine than in the homojunction case. However, the Anderson model, shown in Figure 1.3, is generally used as a first approximation.

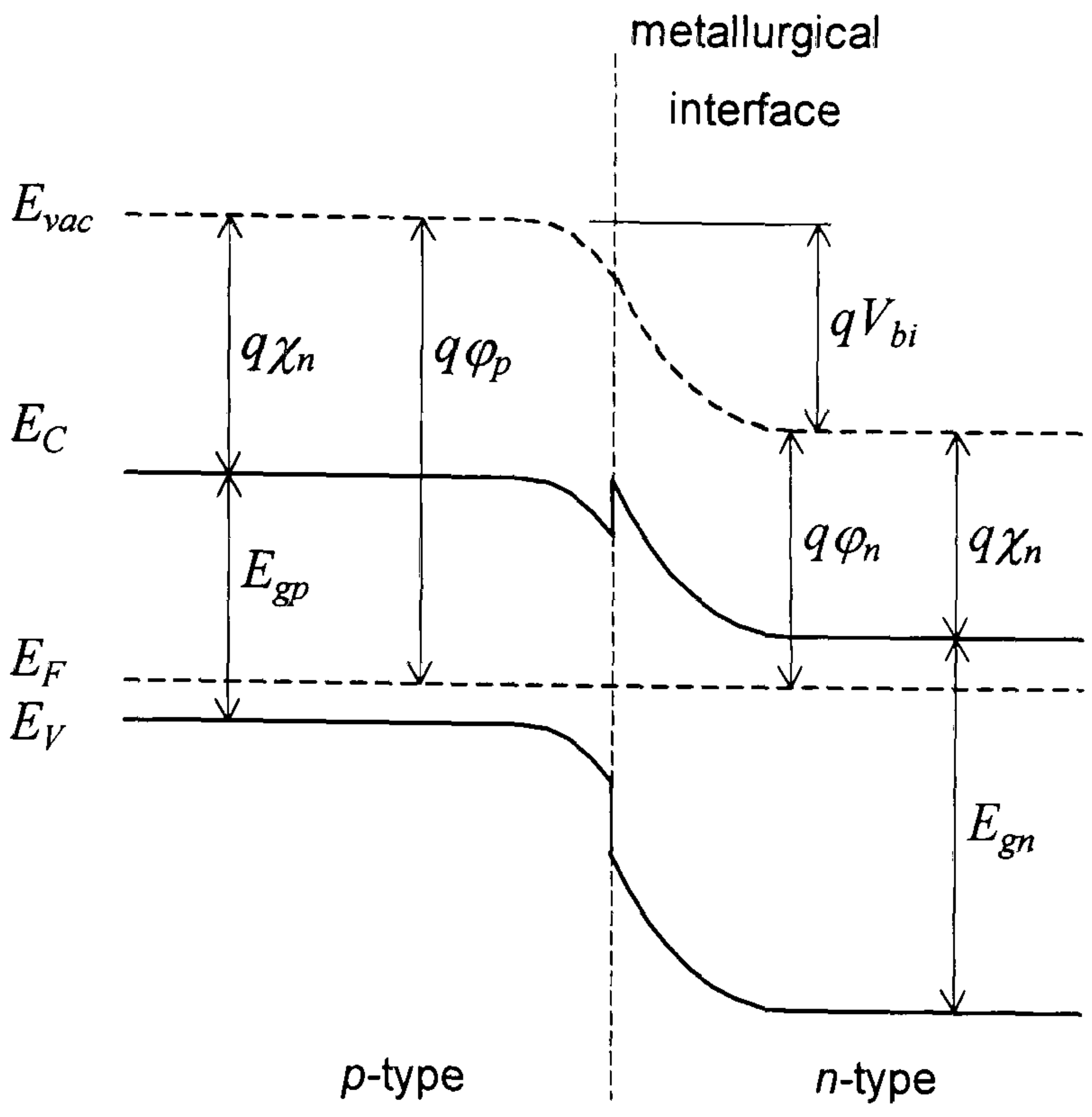

Figure 1.3 Band diagrams showing the formation of a heterojunction. The two layers are in contact and in thermal equilibrium.

Depending on the bandgap, electron affinity and doping concentrations of the two semiconductors, a spike may appear in either the conduction band (as shown) or the valence band. Such spikes will act as barriers to the flow of electrons and holes respectively.

In reality, the above model is an oversimplified representation of a real device. Interface states in the middle of the junction may also contribute to a potential barrier, and the presence of oxides and other contaminants at the interface may result in a thin insulating layer between the window and absorber. Both of these effects can lead to non-ideality in the current-voltage characteristics of the solar cell, which are described in the next section.

1.3 FUNDAMENTAL SOLAR CELL CONCEPTS

1.3.1 Air mass

If direct comparisons are to be made between different solar cells, it is necessary to define standard testing conditions. This testing standard varies depending on the illumination conditions for which the device has been designed.

To a zeroth approximation, the sun can be considered to radiate as a black body at a temperature of 5780K [5]. However, the average spectrum and intensity of sunlight vary with both the latitude and altitude of the observer, due to the change in the path length of the sun's rays through the earth's atmosphere. The *air mass* (*AM*) value describes the spectrum of light after it has passed through a given multiple of the earth's atmosphere's thickness. At sea level, therefore, it is defined as the secant of the angle of the sun to the zenith (see Figure 1.4).

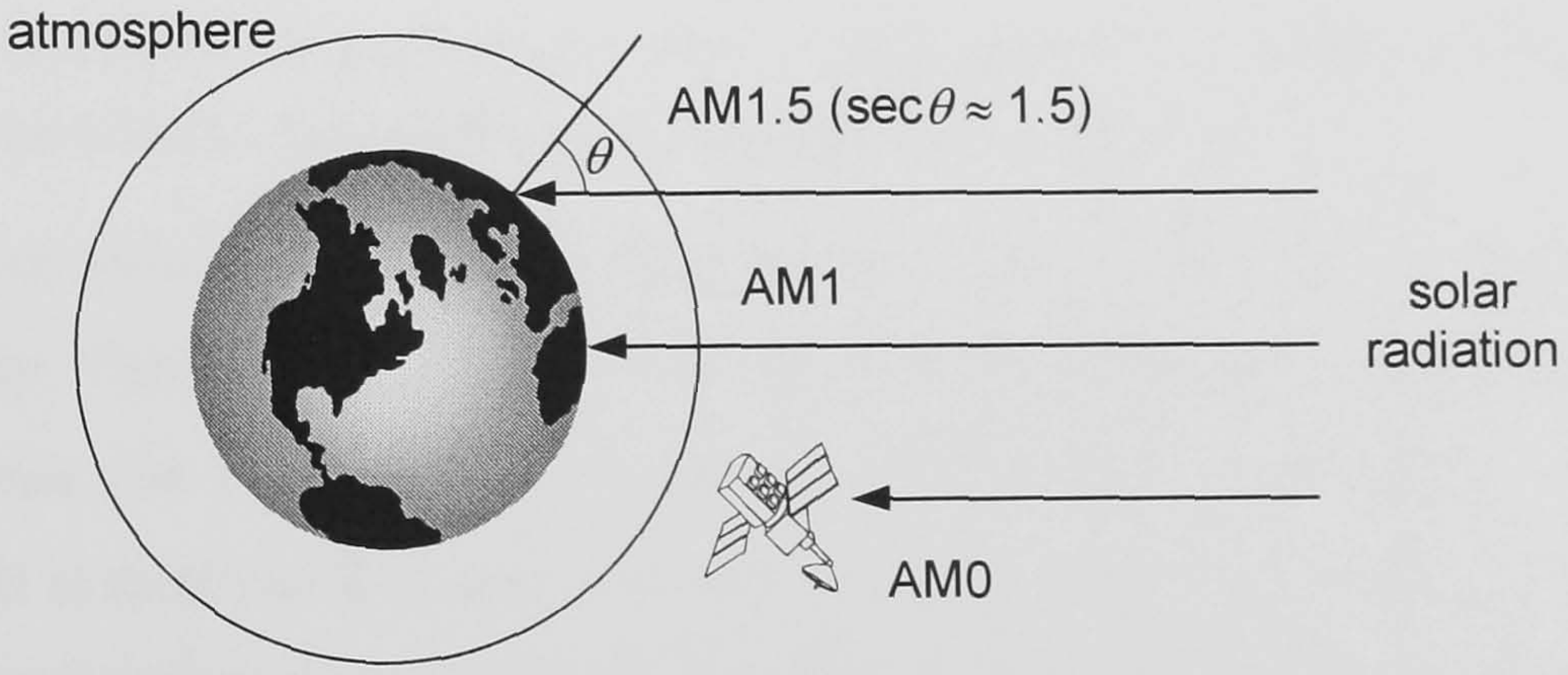

Figure 1.4 Definition of the air mass nomenclature for describing different observed solar spectra.

Thus AM0 describes the spectrum in space, and AM1 that at the equator. The most commonly used standard for solar cells is AM1.5, which corresponds approximately to the light seen at temperate latitudes. The AM1.5 spectrum is shown in Figure 1.5.

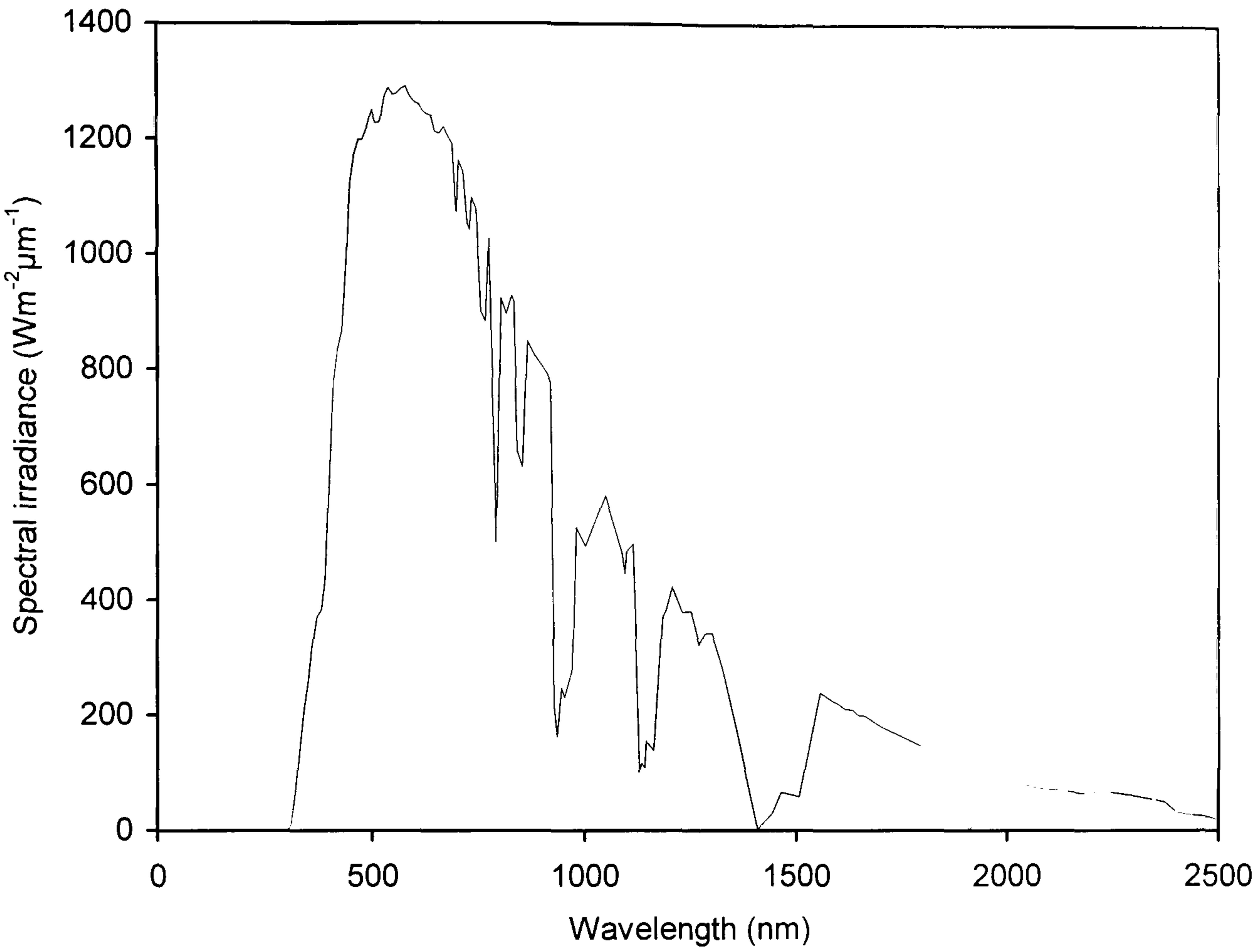

Figure 1.5 Spectrum corresponding to AM1.5 sunlight, as used in standard solar cell testing conditions (from NASA data quoted by Fahrenbruch and Bube [3]).

The air mass value describes only the spectrum of the light; it does not define the intensity. This is especially relevant when considering solar concentrators, which can condense the sunlight by a factor of 1000 without significantly altering the spectrum. It is therefore necessary when defining illumination conditions to state also the power per unit area; the standard generally used is $100mWcm^{-2}$ for AM1.5, and $150mWcm^{-2}$ for AM1. The $100mWcm^{-2}$ AM1.5 standard, with a cell temperature of 25°C, has been used for all current-voltage measurements in this work.

1.3.2 Current-voltage characteristics

In the dark, the relationship between the current density (*J*) flowing through a solar cell's *p-n* junction and the voltage (*V*) across it is ideally given by Shockley's equation for a diode:

$$J = J_0\left\{\exp\left(\frac{qV}{nkT}\right) - 1\right\} \tag{1. 3}$$

where J_0 is the *reverse saturation current density*, a function of the material properties, and n is an *ideality factor* which takes account of recombination in the diode. For most diodes, this is a value between 1 and 2, depending on whether the characteristics are dominated by the ideal diffusion current or the recombination current, respectively [6]. However, for devices in which there is a non-uniform spatial distribution of recombination centres across the depletion region, the junction asymmetry can result in values of $n > 2$ [3].

Under illumination, another term must be added to equation 1 to take into account the photocurrent, J_L, that is generated, giving:

$$J = J_0\left\{\exp\left(\frac{qV}{nkT}\right)-1\right\}-J_L \qquad (1.4)$$

This characteristic, shown in Figure 1.6, allows power to be extracted from the device at forward bias.

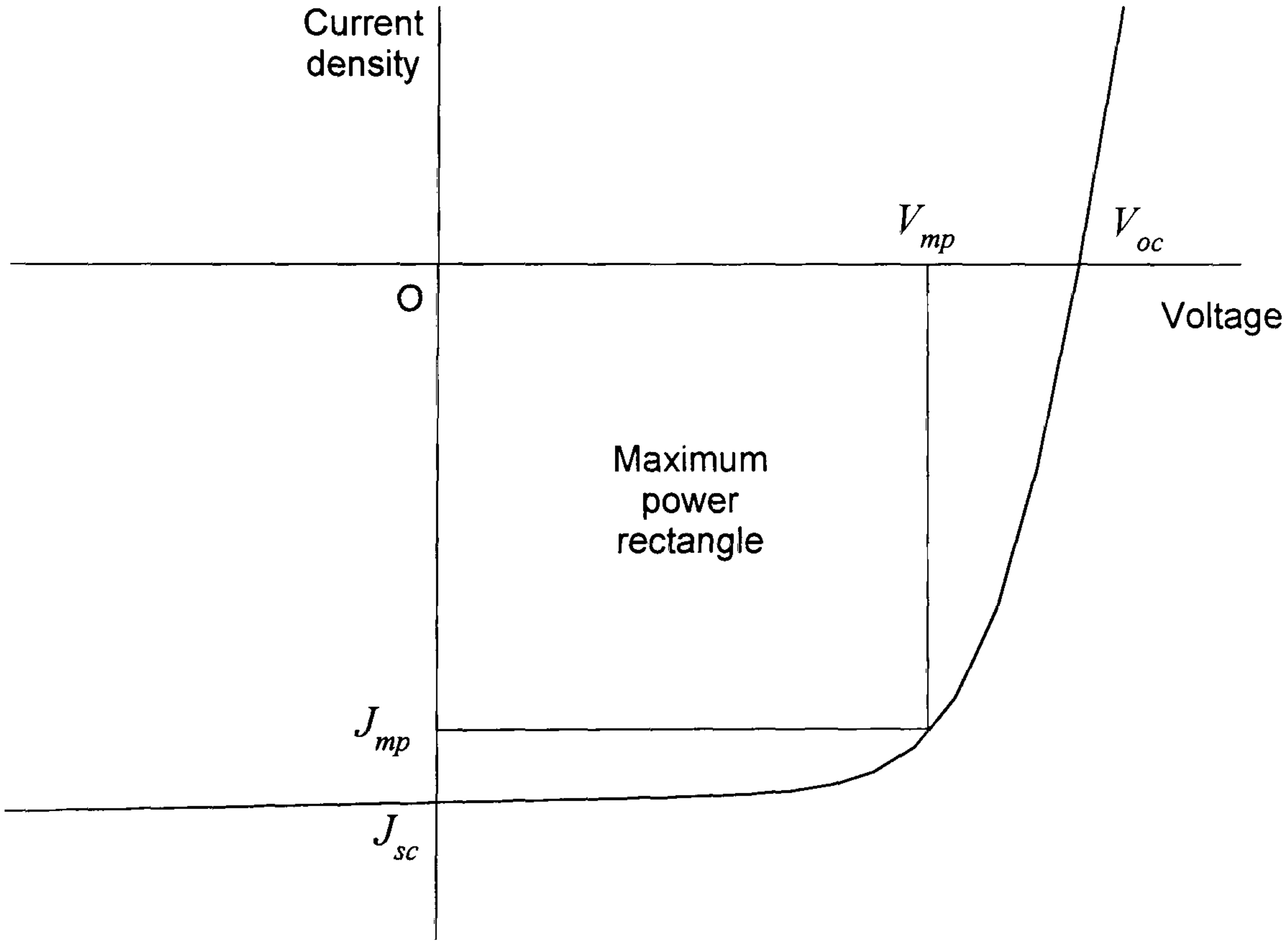

Figure 1.6: Typical solar cell *J-V* curve, showing the point at forward bias where the device yields most power

In real devices, the single diode description of the solar cell is a gross over-simplification, and other parameters must be taken into consideration, such as:

- Series resistance, arising from both the finite bulk resistivities of the semiconductors and from the sheet resistances of any thin layers in the device
- Shunt, or parallel, resistance, due to *pinholes* in the window layer. This is a particular problem with thin-film cells, where discontinuities in this layer allow short-circuits to occur between the absorber and the front contact.
- The possible non-ohmic behaviour of the contacts made between the semiconductors and the external load circuit.

Studying the deviations from ideality of the *J-V* curves can yield valuable information about the device junction. This is described further in Section 3.2.1.

1.3.3 Solar cell parameters

Comparison of the electrical characteristics of different solar cells is commonly carried out by considering various parameters extracted from the *J-V* curves. Four such parameters are: efficiency; short-circuit current; open-circuit voltage; and fill factor. These terms are defined below:

Efficiency The most important parameter of a solar cell in terms of its ultimate function is clearly the photovoltaic conversion *efficiency*, η. This is defined as the ratio of the output power (electricity) to input power (light). The output power per unit area of the solar cell can be found from the *J-V* curve by evaluating the area of the rectangle formed between the operating point and the two axes. This operating point will depend on the load impedance, and so a point is found at which the cell provides maximum power. This maximum power point, denoted as (V_{mp}, J_{mp}), is shown with the *J-V* curve in Figure 1.6. The ratio of the area of this maximum power rectangle to the illumination intensity therefore gives the cell's efficiency.
i.e. under standard AM1.5 testing conditions:

$$\eta = \frac{J_{mp} \times V_{mp}}{100\mathrm{mWcm}^{-2}} \qquad (1.5)$$

Short circuit current The current density measured with zero voltage applied is known as the *short-circuit current density*, J_{sc}. This value is affected primarily by series resistance losses in the device.

Open circuit voltage The *open-circuit voltage* is the applied voltage at which no current flows through the device. This quantity is left unaffected by series resistance losses in the cell, but is sensitive to shunt losses.

Fill factor Another device parameter determined from the J-V characteristics is the *fill factor*. This is a measure of how "square" the forward bias diode characteristics are, and is defined as the ratio of the area of the maximum power rectangle to the product of the short-circuit current and the open-circuit voltage:

$$FF = \frac{J_{mp} \times V_{mp}}{J_{sc} \times V_{oc}} \tag{1.6}$$

Typical fill factors for solar cells range from 60 to 80 percent [3].

1.3.4 Quantum efficiency

The *quantum efficiency*, in contrast to the power conversion efficiency described above, is defined as the number of electron-hole pairs generated per incident photon. As measured, this value is strictly referred to as the *external* quantum efficiency. If corrections are made to allow for reflection losses at the front of the cell, the quantity is then known as the *internal* quantum efficiency.

The quantum efficiency of a solar cell is strongly dependent on the energy of the individual photon. This is due to both the wavelength dependence of the optical absorption coefficients in semiconductors and also the depth dependence of the carrier collection probability. The quantum efficiency is therefore measured as a function of wavelength under monochromated light; this is referred to as the spectral response of the cell.

The maximum quantum efficiency generally seen in solar cells is 100%. However, due to the impact ionisation process mentioned in Section 1.2.1, quantum efficiencies of greater than unity have been reported for photon energies above $2E_g$ for some materials [4].

1.4 SOLAR CELL SEMICONDUCTORS

In this section, the major semiconductor PV technologies are reviewed, and the advantages and disadvantages of each system are discussed.

1.4.1 Crystalline cells

The development of bulk crystal growth techniques for the microelectronics industry has led to the availability of large semiconductor wafers with low defect densities and well-controlled doping concentrations. These materials are used to produce highly efficient photovoltaic devices, but are not currently considered viable for large-scale terrestrial power conversion. This is due to both their high financial cost (*i.e.* ECU/W_p) and the long energy payback time.

Crystalline silicon Donors are diffused into *p*-type doped single crystal silicon wafers, which are produced by either the Czochralski or float zone growth methods. The resulting shallow homojunction has exhibited efficiencies of up 24.0%[†].

Multicrystalline silicon A less expensive version of the silicon solar cell can be made using lower-grade silicon. This is produced by casting in ingots of up to 500kg in mass, resulting in a multicrystalline structure with grain sizes on the scale of 1-10mm. This material is naturally *p*-type due to the presence of aluminium donor impurities. Solar cells are then fabricated from this material using similar technologies to those used for the crystalline silicon, resulting in a maximum recorded efficiency of 18.6±0.6%.

III-V compounds The highest efficiency solar cells yet produced have been from III-V compound semiconductors. GaAs wafers are widely available, if expensive, and lattice-matched ternary III-V materials can be epitaxially grown on these substrates. The resulting junctions are relatively free of dislocations, and several such systems have been exploited for photovoltaic applications. GaAs homojunctions have been recorded with efficiencies of up to 25.1±0.8%, whilst even higher

---

[†] All efficiencies given in this section are quoted from reference [7].

performances have been measured for the multijunction GaInP/GaAs device (30.3%). However, the high cost of these cells has restricted their use mainly to space applications.

1.4.2 Thin film cells

Although the bulk cells described above have been used in an increasing number of applications over the past few decades, power generation on the scale needed to compete with conventional energy sources requires considerably cheaper devices. For this reason, several low-cost thin-film devices are currently under investigation.

Amorphous silicon Silicon in the amorphous state exhibits electrical and optical properties very different from those of the crystalline form. In particular, the hydrogenated material (a-Si:H) effectively behaves as a direct bandgap semiconductor, with an optical bandgap of ~1.7eV [8]. The resulting higher optical absorption coefficient means that films as thin as ~0.5μm absorb most of the incident sunlight. This allows devices to be deposited on glass substrates, using considerably less active material and thus saving on cost. This technology has been marketed for a number of years and now accounts for around one third of all solar module sales [8].

Microcrystalline silicon Silicon thin films can also be deposited on various substrates in a polycrystalline form [9]. Because of the low optical absorption of silicon, such films are generally thicker than other thin-film devices (up to 100μm) and also make use of optical confinement to absorb more light. 16% efficiency has been achieved with such a structure, and the material is also being investigated for use in a heterojunction device with a-Si:H.

Cadmium telluride Heterojunctions based on CdTe have been considered for use in solar cells since the early 1960's, and both bulk [10] and thin-film devices on a glass substrate have been investigated. The near-optimum bandgap and high optical absorption of CdTe make it an attractive material for the low-cost devices of the future, with efficiencies of up to 16% obtained to date. This solar cell will be discussed in greater depth in Chapter 2.

Chalcopyrites The other main contender for large-scale terrestrial applications is the family of I-III-VI chalcopyrite cells. The most promising of these devices are heterojunctions comprising of an absorber of the type $Cu(In,Ga)(S,Se)_2$ with a CdS window layer. Efficiencies exceeding 16% have been reported for several such materials [11]. Although further from production than CdTe cells, these devices have the significant political and environmental advantage of lower toxicity [12].

1.5 AIMS AND SCOPE OF THIS WORK

This work is concerned exclusively with the polycrystalline thin-film CdTe/CdS solar cell. Optical and electron beam techniques are used in order to examine some of the many outstanding materials problems associated with this type of cell. These include:

a) The effect of grain boundaries on device performance.

b) The mechanism behind the widely used efficiency-enhancing treatment using cadmium chloride.

c) The extent and effect of intermixing at the CdTe/CdS junction.

These issues, together with details of the cadmium telluride solar cell, are described further in the following chapter.

REFERENCES FOR CHAPTER 1

[1] E. Becquerel (1839) *On electric effects under the influence of solar radiation*, Comptes Rendus Hebdomdaires des Seances de l'Acedemie des Sciences **9** pp.561

[2] W.G. Adams and R.E. Day (1877) *The action of light on selenium*, Proceedings of the Royal Society of London, Series A **25** pp.113

[3] A.L. Fahrenbruch and R.H. Bube, *Fundamentals of solar cells*, (Academic Press, New York, 1983)

[4] A. De Vos and B. Desoete (1998) *On the ideal performance of solar cells with larger-than-unity quantum efficiency*, Solar Energy Materials and Solar Cells **51** (3-4) pp.413-424

[5] *Handbook of Chemistry and Physics*, 78th Edition, Ed. D.R. Lide (CRC Press, Boca Raton, 1997)

[6] S.M. Sze, *Semiconductor Devices, Physics and Technology*, (Wiley, New York, 1985)

[7] M.A. Green, K. Emery, K. Bücher, D.L. King and S. Igari (1998) *Solar cell efficiency tables (version 11)*, Progress in Photovoltaics **6** (1) pp.35-42

[8] H.J. Möller, *Semiconductors for Solar Cells*, (Artech House, Boston, 1993)

[9] A. Catalano (1994) *Polycrystalline thin-film technologies: status and prospects*, Proceedings of First World Conference on Photovoltaic Energy Conversion, Hawaii. pp.52

[10] K.W. Mitchell, *Evaluation of the CdS/CdTe heterojunction solar cell*, (Garland, New York, 1979)

[11] W.H. Bloss, F. Pfisterer, M. Schubert and T. Walter (1995) *Thin-film solar cells*, Progress in Photovoltaics: Research and Applications **3** (1) pp.3-24

[12] D.L. Morgan, C.J. Shines, S.P. Jeter, M.E. Blazka, M.R. Elwell, R.E. Wilson, S.M. Ward, H.C. Price and P.D. Moskowitz (1997) *Comparative pulmonary absorption, distribution, and toxicity of copper gallium diselenide, copper indium diselenide, and cadmium telluride in Sprague-Dawley rats*, Toxicology and Applied Pharmacology **147** pp.399-410

Chapter 2: Introduction to the CdTe/CdS solar cell

2.1 INTRODUCTION

Thin-film cadmium telluride/cadmium sulphide solar cells are currently considered to be the most promising candidate for large-scale terrestrial power conversion. However, there are still several materials issues that remain unresolved. This chapter is intended to provide an introduction to these devices and their outstanding problems, in order to place in context the materials analysis work presented later.

2.2 HISTORICAL OVERVIEW

The potential of cadmium telluride for use as a solar cell semiconductor has long been recognised, due to its bandgap energy being almost ideally suited to the solar spectrum. Early attempts to exploit this in the 1960s focussed on CdTe homojunctions. However, the short minority carrier lifetimes and high optical absorption meant that the collecting junction had to be very close to the surface. This led to excessive loss of carriers via surface recombination, limiting the efficiencies of such devices at the time to around 6% [1]. Whilst some research on these solar cells has continued (with an efficiency of 11% achieved by 1982 [2]), a heterojunction solution was sought to avoid the surface effects.

The first heterojunctions to be made with CdTe were constructed from a thin film of the *n*-type material and a layer of *p*-type copper telluride ($Cu_{2-x}Te$), producing the first efficient CdTe-based thin-film device [3]. However, these devices showed similar stability problems to those encountered with the analogous $Cd_{2-x}S$/CdS solar cell, which was the result of the diffusion of copper from the *p* layer.

The lack of suitable materials with which to form heterojunctions on *n*-type CdTe, and the stability problems of the $Cd_{2-x}S$/CdS device, have stimulated investigations into *p*-CdTe/*n*-CdS junctions since the early 1970s. Adirovich *et al.* [4] first deposited the films on TCO-coated glass; this is now used almost universally for CdTe/CdS cells, and is referred to as the *superstrate configuration.* In 1972, Bonnet and Rabenhorst [5] reported efficiencies of 5-6%, in what was intended as an intermediate step in the development of a graded bandgap CdS_xTe_{1-x} solar cell. Since then, however, it has been shown that the presence of an alloy layer between the CdS and CdTe has a deleterious effect on the quantum efficiency of the device at short wavelengths. This fact, coupled with the difficulty of preparing continuously graded compositions using materials with such a large miscibility gap (see Section 8.1.1) has led to a decline in interest in this system in favour of the simpler CdTe/CdS junction. Nevertheless, it is widely accepted that a small amount of S and Te interdiffusion at the interface is beneficial in reducing dislocations caused by the lattice mismatch, and is, moreover, inevitable to some degree.

Since these pioneering studies, continuing work on CdTe/CdS heterojunction devices has led to a wide range of deposition methods being developed. This apparent insensitivity to the deposition technique has proved to be a major advantage when transferring the technology to large-scale production lines. However, each of the methods which have yielded efficiencies in excess of 10% (reviewed in Section 2.4.1) has in common the introduction of both chlorine and oxygen impurities during either the deposition or treatment stages.

2.3 DEVICE LAYERS

Figure 2.1 shows the basic construction of a typical cadmium telluride/ cadmium sulphide thin film solar cell.

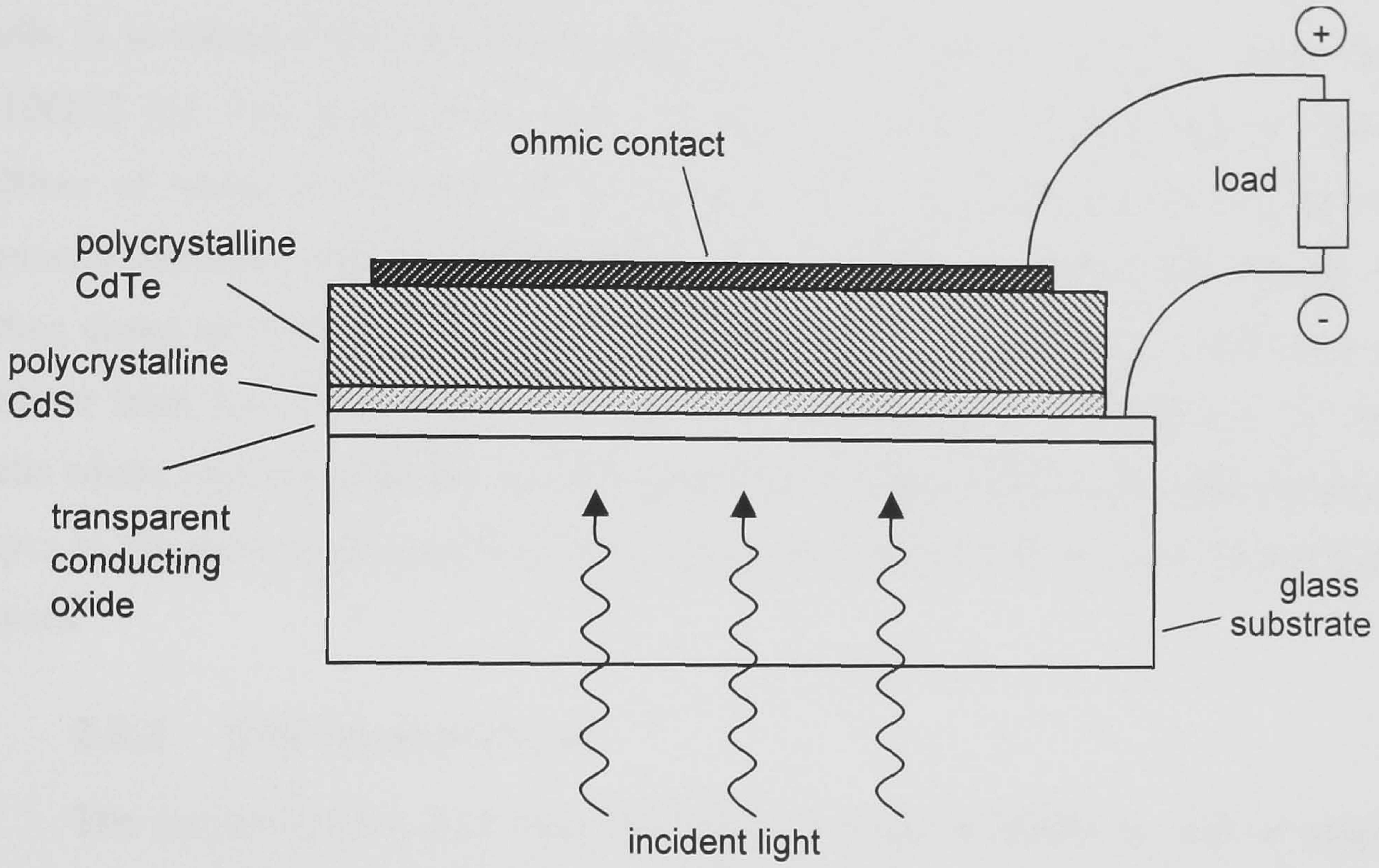

Figure 2.1 Composition of the thin-film CdTe/CdS solar cell. Note that the layer dimensions are not shown to scale.

The functions of each of the different layers are described in the following sections.

2.3.1 Substrate

The solar cell is produced on a substrate of glass, because it is transparent, strong and cheap. Typically around 2-4mm in thickness, this acts as a substrate for deposition, protects the active layers from the environment and provides mechanical strength. Since the active layers of the device are those on top of the glass substrate, this construction is referred to as the *superstrate* configuration.

Common types used are soda-lime glass, which is inexpensive, and borosilicate glass. The latter has a higher softening temperature, and is often used for the higher temperature deposition methods. Corning #7059 barium borosilicate glass is particularly widely used, as its low alkali (0.3%) content lessens the diffusion of acceptor atoms into the CdS layer. The outer face of the pane often has an anti-reflective coating, such as magnesium fluoride, to enhance its optical transmission.

2.3.2 Front contact

A layer of transparent conducting oxide (TCO) is used as the front contact to the device. It is needed to reduce the series resistance of the device, which would otherwise arise from the sheet resistance of the thin CdS layer. For high efficiency cells, it is required that the sheet resistance of the front contact is no more than ~10Ω/□ [6]. The most widely used material is tin oxide (SnO_2), approximately 100nm of which is deposited onto the glass either by sputtering or atmospheric pressure chemical vapour deposition. This material has an improved conductivity when doped with indium to produce indium tin oxide (ITO). However, diffusion of indium from the ITO has been implicated in reducing device performance in solar cells where high temperatures have been used during manufacture. For this reason, a layer of the more stable undoped SnO_2 is often included between the ITO and CdS layers.

2.3.3 CdS window layer

The polycrystalline CdS layer is *n*-type (as CdS invariably is, due to native donors and sulphur vacancies), and therefore provides one half of the *p*-*n* junction. As a wide band gap material (E_g ~2.42eV at 300K), it is largely transparent down to wavelengths of around 515nm, and so acts as the window layer. Below that wavelength, some of the light will still pass through to the CdTe, due the thinness of the CdS (~ 100nm).

CdS material deposited by low temperature techniques is often treated with cadmium chloride before deposition of the CdTe absorber layer. This process is described further in Section 2.4.2. However, this treatment has been found to be less influential for layers deposited by such methods as close-space sublimation, spray pyrolysis and screen printing, where temperatures in excess of 500°C are used during deposition.

2.3.4 CdTe absorber layer

The CdTe layer is, like the CdS, polycrystalline, but is *p*-type doped. Its energy gap (1.45eV) is ideally suited to the solar spectrum, and it has a high absorption coefficient for energies above this value. Because it is less highly doped than the

CdS, the depletion region is mostly within the CdTe layer. This is therefore the active region of the solar cell, where most of both the carrier generation and collection occur. The thickness of this layer is typically 1-30µm, with grain sizes strongly dependent on the deposition technology used.

2.3.5 Back contact

The role of the back contact is to provide an electrical connection to the CdTe without adding excessively to the series resistance to the device. Fahrenbruch [7] has estimated that the specific contact resistivity R_c of the back contact should be kept to a maximum of 0.3Ωcm², where

$$R_c = \left.\frac{\mathrm{d}V}{\mathrm{d}J}\right|_{V=0} \tag{2.1}$$

However, *p*-type CdTe is a notoriously difficult material on which to produce an ohmic contact, due to its high work function [8]. This can be seen in Figure 2.2, which shows a simple model of the band structure of a metal contact on *p*-type CdTe at thermal equilibrium.

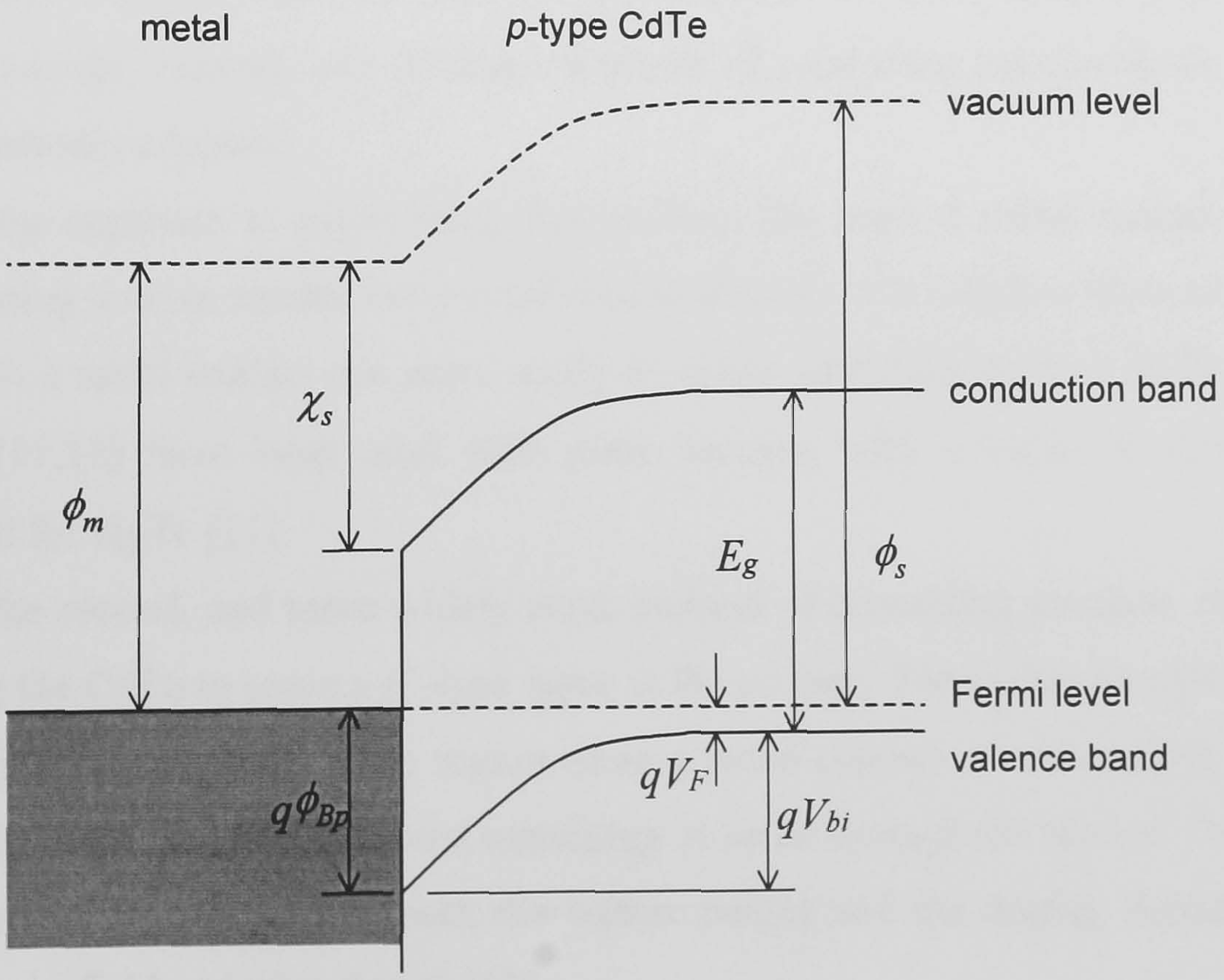

Figure 2.2 Band diagram for an ideal metal/*p*-CdTe contact.

During normal device operation (*i.e.* at forward bias under illumination), majority carriers will be moving from the CdTe to the metal. These holes will encounter a barrier, as shown on the diagram, over which they must pass via a thermionic emission process. The height, V_{bi}, of the barrier will be equal to the difference of the two work functions:

$$V_{bi} = \phi_s - \phi_m \tag{2. 2}$$

The work function of a semiconductor depends on its doping concentration, but for highly *p*-type semiconductor its limiting value will be given by:

$$\phi_m \approx \chi_s + E_g \tag{2. 3}$$

where χ_s is the electron affinity of the semiconductor.

For there to be no potential barrier to the majority carriers leaving the CdTe, the Mott-Gurney condition must therefore be met:

$$\phi_m \geq E_g + \chi_s \tag{2. 4}$$

or, for *p*-CdTe

$$\phi_m \geq 1.45\text{eV} + 4.28\text{eV} \text{ [9]}$$

$$\geq 5.73\text{eV}$$

The absence of any commonly available metals with a high enough work function means that a simple Schottky junction will therefore not be sufficient to produce an ohmic contact. Instead, two different methods of producing pseudo-ohmic contacts are commonly adopted.

One approach to overcoming this problem has been to make contact with the CdTe using a more conductive *p*-type semiconductor, with a higher electron affinity, to which a metal contact can more easily be made. Materials such as ZnTe [10] and HgTe [11,12] have been used with some success, with a value of R_c=0.1Ωcm^2 reported for HgTe [11].

The second, and more widely used, method of contacting involves chemically treating the CdTe to leave a p^+-type layer at the surface. The higher acceptor density results in a narrower depletion region when a metal contact is subsequently applied. This allows the thermally assisted tunnelling of holes through the barrier. The contact resistance is then related to both the barrier height and the doping density by the thermionic-field emission theory [13].

Various chemical etchants may be used to provide the p^+ layer. One approach is the reduction of telluride ions to leave a tellurium rich (and hence more p-type) layer at the surface. For example, this can achieved using alcoholic solutions of bromine [14] via the reaction:

$$\mathrm{Br_2 + Te^{2-} \rightarrow 2Br^- + Te^0} \tag{2.5}$$

The use of this etch followed by the evaporation of gold is widely used for making contacts for research purposes, despite reported resistances of ~20Ωcm^2 [7]. Other etchants commonly used include acidified dichromate [15] and nitric/phosphoric acid solutions [16]. These have both yielded satisfactory contacts even when the gold is replaced by either nickel or a Ni/Au alloy, which have lower work functions but are considerably cheaper.

Another contacting process involves the deposition of a graphite paste, by one of a variety of techniques including painting, screen printing and spraying. The major advantage of this technique, besides that of cost, is that it allows the addition of dopants directly into the contact material before deposition. When the complete structure is then annealed, the impurities diffuse into the CdTe to produce a p^+ layer. Depuyt *et al.* [17] have compared various impurities and found that the lowest resistance contact was formed using Cu ions, which act as acceptors in CdTe.

2.4 DEVICE FABRICATION

2.4.1 Deposition techniques

Physical vapour deposition PVD (otherwise referred to simply as vacuum evaporation) involves the vaporisation in a vacuum of a source of either the compound (CdS or CdTe) or a mixture of the separate elements (Cd + S or Cd + Te). The resulting vapours recombine on the surface of the substrate (which can be heated, but is still much cooler than the source) to deposit the required polycrystalline material. The stoichiometry of the deposited layer is difficult to control accurately, as it depends strongly on the equilibrium vapour pressures of the elements, as well as the stoichiometry of the source material [18].

Close-space sublimation CSS, which has been used to produce the highest efficiency cells so far [19,20], is based on the reversible dissociation of the semiconductors at high temperatures, *i.e.* [21]

$$2CdS(s) \Leftrightarrow 2Cd(g) + S_2(g) \qquad (2.6)$$

$$2CdTe(s) \Leftrightarrow 2\,Cd(g) + Te_2(g) \qquad (2.7)$$

The source is of a large area and is positioned a short distance (0.5-2mm) from the substrate. The substrate is maintained at a high temperature (but below that of the source) such that the elemental vapours will not condense on the substrate. The compound form, however, is deposited due to its lower equilibrium vapour pressure. A major advantage of this technique is the high deposition rate, which is typically 1μm/min.

Chemical vapour deposition CVD can also be used to deposit both semiconductors. It involves chemical reactions between precursor vapours to produce the required species, which condense on the substrate to form the compound. A variation of this method, metal-organic CVD (MOCVD), is widely used for depositing CdTe. This makes use of metallo-organic precursors, such as dimethyl-cadmium as a source for cadmium and diallyl- [22], diisopropyl- [22], or diethyl- [23] telluride for tellurium. Despite the slow deposition rate (~1μm/hr), this technique is suitable for scaling up for commercial production, due both to its low cost and to the high degree of control over stoichiometry and doping which is possible.

Solution growth This is sometimes used for depositing CdS films [24], and involves producing the required ions in a solution by chemical means, which combine and precipitate out onto the substrate if the required equilibrium conditions are met. For example, cadmium ions can be produced by the hydrolysis of $Cd(OH)_2$:

$$Cd(OH)_2 \Leftrightarrow Cd^{2+} + 2(OH)^- \qquad (2.8)$$

and sulphide ions from an alkaline aqueous solution of thiourea:

$$(NH_2)_2CS + OH^- \Rightarrow CH_2N_2 + H_2O + HS^- \qquad (2.9)$$

$$HS^- + OH^- \Rightarrow H_2O + S^{2-} \qquad (2.10)$$

CdS then precipitates onto the substrate when the concentration product of the sulphide and cadmium ions exceeds the solubility product of CdS:

$$Cd^{2+} + S^{2-} \Rightarrow 2CdS \qquad (2.\ 11)$$

However, this method can not be used for CdTe, due to the difficulty of synthesising tellurides [25]. This process is also referred to as electroless or chemical bath deposition (CBD).

Electrodeposition The electrodeposition technique is widely used to deposit CdTe films [24], and in general uses an acidified solution of a cadmium salt and tellurium oxide. A negative potential is applied to the substrate, allowing cathodic deposition to take place via firstly the reduction of tellurium:

$$HTeO_2^{+} + 3H^{+} + 4e^{-} \Rightarrow Te + 2H_2O \qquad (2.\ 12)$$

followed by the reaction of the deposited tellurium with the cations:

$$2Te + Cd^{2+} + 2e^{-} \Rightarrow CdTe \qquad (2.\ 13)$$

The use of $CdCl_2$ in the solution to supply the cadmium ions means that no chloride need be added later during the post-deposition annealing (see Section 2.4.2).

Screen printing Screen printing can also be used to produce both semiconductor layers. High-purity elements are milled into a fine powder, to which typically 10% by weight [26] $CdCl_2$ is added to act as a fluxing agent. Propylene glycol is used as a binding agent to produce a slurry, which is printed onto the substrate through a fine mesh. After drying, the layer is sintered at 600-700°C for around 1 hour. Thicker layers are required than with other techniques in order to avoid the effects of pinholes, and the grain sizes following sintering are also correspondingly larger, with 20-30μm commonly observed [21].

Spray pyrolysis A similar slurry to that used for screen printing can also be sprayed onto a heated substrate, in a technique known as spray pyrolysis. As well as the CdS and CdTe thin films, the ITO layer can also be deposited with this method. This makes the process highly suitable for upgrading to commercial production, and this has already been exploited. However, the use of proprietary techniques means that few experimental details are reported in the literature.

2.4.2 Post-deposition processing

The presence of chloride ions has been found to be essential to create a high efficiency (η~10%) CdTe solar cell [27]. The introduction of these ions is usually achieved using cadmium chloride, which is often applied after completing the layer deposition by either evaporation or coating with an aqueous solution. However, in some deposition methods the chloride ions are introduced during the layer growth, as seen in the previous section. Toušková *et al.* [28], for example, have shown the presence of chloride ions in the electrolyte solution during electrodeposition to be essential in order for the later post-deposition treatment to be effective.

Whether the cadmium chloride is introduced during or after the initial layer deposition, it has in most cases been found necessary to apply some heat treatment to the cell. (This is with the exception of the screen printing and spray pyrolysis techniques, in which the layers have already been subject to high temperatures in the presence of this chloride.) This treatment typically consists of subjecting the cell to a temperature of ~400°C for 20-30 minutes in an oxygen-containing atmosphere, and often results in an improvement in the device efficiency of an order of magnitude.

Many different mechanisms have been implicated in this processing step. The most widely cited effect is the type conversion of the CdTe from *n* to *p*-type. It is known that CdTe is difficult to extrinsically *p*-type dope, due to its tendency to self-compensate. However, by comparing the temperature dependent *J-V* data to simulated curves, Niemegeers *et al.* have shown that the $CdCl_2$ treatment causes an increase in the acceptor density in space-charge region [29]. This causes a narrowing of the depletion layer, so increasing the electric field and therefore decreasing the recombination rate in this region. *J-V* results have also shown a decrease in the resistivity of the CdTe, which is likely to be due to the increase in the doping concentration [30].

The origin of the acceptors remains unclear. Photoluminescence measurements as a function of processing conditions have shown an increase in the density of shallow-level states following chloride treatment, which may be responsible [31]. A possible centre may be a cadmium vacancy complex which is known to form in chlorine-doped CdTe, and acts as an acceptor [32].

A further contribution is likely to be that of isoelectronic doping with oxygen, which also forms a shallow acceptor in II-VI materials [33]. Tyan *et al.* have used junction capacitance and cross-section EBIC measurements to measure the acceptor density and junction position as a direct function of the amount of O_2 present during CSS growth [34]. This showed that the oxygen increases the acceptor density, ensuring the formation of a heterojunction rather than a buried homojunction.

Passivation of the CdTe grain boundaries, and thus reducing recombination losses, is thought to be another effect of the post-deposition processing. Cahen and Noufi [35] have implicated oxygen in this process. Further evidence of such passivation is seen in the high-resolution beam-induced current results of Galloway *et al.* [36].

In films with small CdTe grains, such as those produced by electrodeposition (a few hundred angstroms), grain growth is known to be an important factor in the post-deposition processing. Since band bending at grain boundaries acts as a barrier to the flow of majority carriers, a lower density of such boundaries will decrease the resistivity of the device. Levi *et al.* have observed PVD grown CdTe grains to grow by a factor of 5 following treatment, but saw no measurable growth in CSS deposited films [37]. This latter result has been independently verified by Cousins [38].

A further major effect of $CdCl_2$/heat treatment concerns intermixing at the CdS/CdTe interface. This has been shown to occur following treatment using various techniques, including Auger electron spectroscopy, secondary ion mass spectrometry (SIMS) and optical transmission measurements [39]. SIMS studies by Dhere *et al.* have also shown that chlorine is transported during the processing via the grain boundaries, accumulating at the interface region [40]. The same study showed that there is a greater degree of diffusion of sulphur into CdTe than tellurium into CdS. The resulting anion vacancies in the CdS layer then result in the formation of a one-sided n^+-p junction and improved collection from the CdTe.

X-ray diffraction studies have indicated that the presence of $CdCl_2$ during annealing increases the amount of CdS/CdTe intermixing [41]. This may be explained to some extent by the CdTe-$CdCl_2$ and CdS-$CdCl_2$ phase diagrams, which show eutectic lines at the relatively low temperatures of 508°C and 525°C respectively [42]. This suggests that at 400°C the species at the interface would perhaps be more mobile with $CdCl_2$ present.

In addition to its effect on the optical absorption of the cell layers, it has been reported that interdiffusion causes a reduction in the lattice mismatch at the CdTe/CdS junction [43]. The resultant reduction in the density of misfit dislocations leads to an increase in the carrier collection length, as observed in spectral response measurements [44]. This same reduction in the number of recombination centres is also manifested through a change in the dominant dark current transport mechanism, from interface recombination to depletion region recombination. This information was derived from temperature-dependent *J-V* data for PVD [30] and molecular beam epitaxy [44] cells, but was not observed for CSS devices [29].

It is clear that more than one mechanism contributes to the efficiency-enhancing influence of the chloride/heat treatment on these solar cells. It is also evident that the extent by which each mechanism affects a device depends on the deposition method used.

2.5 CURRENT STATUS

2.5.1 The state of the art

The maximum verified conversion efficiency for a small area CdTe/CdS solar cell is currently 16.0±0.2% [20]. This was fabricated using MOCVD-grown CdS and CSS CdTe, although a CSS cell approaching the same efficiency has also been produced using CBD-deposited CdS [19]. The most efficient modules have also been produced using the CSS technique for the CdTe, in this case also using the same process for the CdS deposition. These were produced by ANTEC, with efficiencies measured at 10.6±0.3% for 10cm×10cm submodules [45]. The current work examines material produced by this company.

2.5.2 Production status

Several companies have already begun the commercial production of CdTe modules, and others are currently in the pre-production stage. The technologies being used widely vary, and include: CSS (ANTEC GmbH, Solar Cells Inc.);

electrodeposition (BP Solar); screen printing (Matsushita); and spray pyrolysis (Photon Energy Inc.).

The production costs for a CdTe solar cell plant with an annual output of 60MW$_p$ have been estimated by BP Solar to be around 0.6 ECU/W$_p$ [46], falling to a predicted 0.28 ECU/W$_p$ for a 500MW$_p$/year plant [47]. Such a cost would be sufficiently low to compete with conventional power generation. The particularly short energy payback time of around 1.6 months (mostly due to the energy used in the glass production) is also highly competitive by comparison with silicon solar cells [47].

2.5.3 Current research issues

In order to further increase the efficiency of CdTe solar cells, research is currently focussed on three main issues:

a) Determining the exact mechanisms behind the effect of the $CdCl_2$ treatment. This should allow greater control over the post-deposition processing, without the necessity of relying on empirical methods.

b) Examining the extent and effect of the sulphide/telluride interdiffusion at the device junction.

c) Development of a cheap, stable and low-resistance back contact.

2.6 SUMMARY

The science and technology of CdTe/CdS thin film solar cells have been reviewed. It has been shown that the optical and electrical properties of CdS and CdTe are well-suited to use in PV, and that the flexibility of the system in terms of the wide range of deposition methods available make the technology highly promising for large-scale production. However, a greater understanding of the materials issues is required in order to further improve device performances. This thesis will address these issues, using the techniques outlined in the following chapter.

REFERENCES FOR CHAPTER 2

[1] K. Zanio *"Cadmium Telluride"* in *Semiconductors and Semimetals*, Vol.13. edited by R. K. Willardson and A. C. Beer, (Academic Press, New York, 1978)

[2] G. Cohen-Solal, D. Lincot and M. Barbé (1982) *High efficiency shallow p^+nn^+ cadmium telluride solar cells*, Proceedings of 4th EC Photovoltaic Solar Energy Conference, Stresa. pp.621-624

[3] B.M. Basol (1990) *Thin film CdTe solar cells - a review*, Proceedings of 21st IEEE Photovoltaic Specialists Conference, Kissimimee. pp.588-594

[4] E.I. Adirovich, Y.M. Yuabov and G.R. Yagudaev (1969) *Photoelectric effects in film diodes with CdS-CdTe heterojunctions*, Fiz. Tekh. Poluprovodnikov **3** (1) pp.81-85

[5] D. Bonnet and H. Rabenhorst (1972) *New results on the development of a thin-film p-CdTe-n-CdS heterojunction solar cell*, Proceedings of 9th IEEE Photovoltaic Specialists Conference, Silver Spring.

[6] R.W. Birkmire and E. Eser (1997) *Polycrystalline thin film solar cells: present status and future potential*, Annual Review of Materials Science **27** pp.625-653

[7] A.L. Fahrenbruch (1987) *Ohmic contacts and doping of CdTe*, Solar Cells **21** pp.399-412

[8] A.W. Brinkman *"Contacts to Cd/Zn/Te/Se compounds"* in *Properties of Narrow Gap Cadmium - based Compounds*, Vol.10, edited by P. Capper, (INSPEC, London, 1994)

[9] R.K. Swank (1967) *Surface properties of II-VI compounds*, Physical Review **153** (3) pp.844-849

[10] P.V. Meyers (1988) *Design of a thin film CdTe solar cell*, Solar Cells **23** pp.59-67

[11] E. Janik and R. Triboulet (1983) *Ohmic contacts to p-type cadmium telluride and cadmium mercury telluride*, Journal of Physics D: Applied Physics **16** pp.2333-2340

[12] B.M. Basol and E.S. Tseng (1986) *Mercury cadmium telluride solar cell with 10.6% efficiency*, Applied Physics Letters **48** (14) pp.946-948

[13] A.Y.C. Yu (1970) *Electron tunneling and contact resistance of metal-silicon contact barriers*, Solid-State Electronics **13** pp.239-247

[14] I.M. Kotina, L.M. Tukhkonen, G.V. Patsekina, A.V. Shchukarev and G.M. Gusinskii (1998) *Study of CdTe etching process in alcoholic solutions of bromine*, Semiconductor Science and Technology **13** pp.890-894

[15] H. Jäger and E. Seipp (1981) *Transition resistances of ohmic contacts to p-type CdTe and their time-dependent variation*, Journal of Electronic Materials **10** (3) pp.605-618

[16] J. Sarlund, M. Ritala, M. Leskelä, E. Siponmaa and R. Zilliacus (1996) *Characterization of etching procedure in preparation of CdTe solar cells*, Solar Energy Materials and Solar Cells **44** pp.177-190

[17] B. Depuydt, M. Burgelman, M. Casteleyn, A. Niemegeers and A. Vervaet (1995) *The effects of diffusion of impurities from graphite back contacts on CdS/CdTe cells*, Proceedings of 13th European Photovoltaic Solar Energy Conference, Nice. Vol.1 pp.593-596

[18] C.R.M. Grosvenor, *Microelectronic Materials*, (Institute of Physics Publishing, Bristol, 1989)

[19] J. Britt and C. Ferekides (1993) *Thin-film CdS/CdTe solar-cell with 15.8% efficiency*, Applied Physics Letters **62** (22) pp.2851-2852

[20] T. Aramoto, S. Kumazawa, H. Higuchi, T. Arita, S. Shibutani, T. Nishio, J. Nakajima, M. Tsuji, A. Hanafusa, T. Hibino, K. Omura, H. Ohyama and M.

Murozono (1997) *16.0% efficient thin-film CdS/CdTe solar cells*, Japanese Journal of Applied Physics Part 1-Regular Papers Short Notes & Review Papers **36** (10) pp.6304-6305

[21] L.C. Chu and S.S. Chu (1995) *Thin film II-VI photovoltaics*, Solid-State Electronics **38** (3) pp.533-549

[22] R. Sudharsanan and A. Rohatgi (1991) *Investigation of metalorganic chemical vapor deposition grown CdTe/CdS solar cells*, Solar Cells **31** pp.143-150

[23] H.G. Bhimnathwala, N.R. Taskar, W.I. Lee, I. Bhat, S.K. Ghandi and J.M. Borrego (1987) *Photovoltaic properties of CdTe layers grown by OMVPE*, Proceedings of 19th IEEE Photovoltaic Specialists Conference, New Orleans. pp.1476-1481

[24] J. Barker, S.P. Binns, D.R. Johnson, R.J. Marshall, S. Oktik, M.E. Ozsan, M.H. Patterson, S.J.R. Ransome, S. Roberts, M. Sadeghi, J. Sherbourne, A.K. Turner and J.M. Woodcock (1992) *Electrodeposited CdTe for thin film solar cells*, International Journal of Solar Energy **12** pp.79-94

[25] K.L. Chopra and S.R. Das, *Thin film solar cells*, (Plenum Press, New York, 1983)

[26] I. Clemminck, A. Vervaet, M. Burgelman and A. Demeyere (1988) *Electrical and microstructural properties of screenprinted CdS layers for CdS-CdTe solar cells*, Proceedings of 20th IEEE Photovoltaic Specialists Conference, Las Vegas. pp.1585-1590

[27] B.M. Basol (1992) *Processing high efficiency CdTe solar cells*, International Journal of Solar Energy **12** pp.25-35

[28] J. Toušková, D. Kindl and J. Toušek (1997) *Preparation and characterization of CdS/CdTe thin film solar cells*, Thin Solid Films **293** pp.272-276

[29] A. Niemegeers, M. Burgelman, H. Richter and D. Bonnet (1997) *A simple model for the effects of the $CdCl_2$ treatment on the performance of CdTe/CdS solar cells*, Proceedings of 14th European Photovoltaic Solar Energy Conference, Barcelona, pp.2079-2082

[30] H. Bayhan and C. Erçelebi (1997) *Electrical characterization of vacuum-deposited n-CdS/p-CdTe heterojunction devices*, Semiconductor Science and Technology **12** pp.600-608

[31] D.-E. Arafah and R. Ahmad-Bitar (1998) *Influence of substrate temperature on the processing of CdTe and CdS thin films*, Semiconductor Science and Technology **13** pp.322-328

[32] S. Seto, A. Tanaka, Y. Masa and M. Kawashima (1992) *Chlorine-related photoluminescence lines in high-resistivity Cl-doped CdTe*, Journal of Crystal Growth **117** pp.271-275

[33] K. Akimoto, H. Okuyama, M. Ikeda and Y. Mori (1992) *Isoelectronic oxygen in II-VI semiconductors*, Applied Physics Letters **60** (1) pp.91-93

[34] Y.S. Tyan, F. Vazan and T.S. Barge (1984) *Effect of oxygen on thin-film CdS/CdTe solar cells*, Proceedings of 17th IEEE Conference Photovoltaic Specialists, pp.840-845

[35] D. Cahen and R. Noufi (1991) *Surface passivation of polycrystalline, chalcogenide based photovoltaic cells*, Solar Cells **30** pp.53-59

[36] S.A. Galloway, A.J. Holland and K. Durose (1996) *A study of CdS/CdTe thin film solar cells using beam injection techniques*, Journal of Crystal Growth **159** pp.925-929

[37] D.H. Levi, H.R. Moutinho, F.S. Hasoon, B.M. Keyes, R.K. Ahrenkiel, M. Al-Jassim, L.L. Kazmerski and R.W. Birkmire (1996) *Micro through nanostructure investigations of polycrystalline CdTe - correlations with*

processing and electronic-structures, Solar Energy Materials and Solar Cells **41** (2) pp.381-393

[38] M.A. Cousins (1998) *A study of the depth dependence of grain size in CdTe/CdS solar cells*, First Year Ph.D. Report, Department of Physics, University of Durham

[39] B.E. McCandless and R.W. Birkmire (1991) *Analysis of post deposition processing for CdTe/CdS thin film solar cells*, Solar Cells **31** pp.527-535

[40] R. Dhere, D. Rose, D. Albin, S. Asher, M. Al-Jassim, H. Cheong, A. Schwartzlander, H. Moutinho, T. Coutts, R. Ribelin and P. Sheldon (1997) *Influence of CdS/CdTe interface properties on the device properties*, Proceedings of 26th IEEE Photovoltaic Specialists Conference, Anaheim. pp.435-438

[41] J.D. Painter, K.D. Rogers and D.W. Lane *"An investigation into the effect of annealing on the microstructure of CdTe/CdS solar cells"* in *Growth and Processing of Electronic Materials*, edited by N. M. Alford, (IOM Communications, London, 1998)

[42] K. Durose, P.R. Edwards and D.P. Halliday (1998) *Materials aspects of CdTe/CdS solar cells*, Journal of Crystal Growth **197** pp.733-742

[43] H.C. Chou, A. Rohatgi, N.M. Jokerst, S. Kamra, S.R. Stock, S.L. Lowrie, R.K. Ahrenkiel and D.H. Levi (1996) *Approach toward high-efficiency CdTe/CdS heterojunction solar-cells*, Materials Chemistry and Physics **43** (2) pp.178-182

[44] S.A. Ringel, A.W. Smith, M.H. MacDougal and A. Rohatgi (1991) *The effects of $CdCl_2$ on the electronic properties of molecular-beam epitaxially grown CdTe/CdS heterojunction solar cells*, Journal of Applied Physics **70** (2) pp.881-889

[45] D. Bonnet, H. Richter and K. Jaeger (1995) *The CTS thin film solar module - closer to production*, Proceedings of 13th European Solar Energy Conference, Nice, pp.1456-1461

[46] J.M. Woodcock, H. Schade, H. Maurus, B. Dimmler, J. Springer and A. Ricaud (1997) *A study of thin film solar cell manufacture towards* $500MW_p$ *per annum*, Proceedings of 14th European Photovoltaic Solar Energy Conference, Barcelona, pp.857-860

[47] W.H. Bloss, F. Pfisterer, M. Schubert and T. Walter (1995) *Thin-film solar cells*, Progress in Photovoltaics: Research and Applications **3** (1) pp.3-24

Chapter 3: Experimental methods and observations on their previous application to solar cells

3.1 INTRODUCTION

The experiments presented in this thesis include not only the standard solar cell characterisation methods (such as *I-V* and spectral response), but also several microscopic and spectroscopic techniques not universally associated with the characterisation of solar cells. The latter include the beam induced current measurements (OBIC and EBIC), luminescence studies (PL and CL), and GDOES.

In this chapter, a description will be given of the methods and experimental apparatus used, although where appropriate a more detailed description will be deferred to the relevant results chapter. For OBIC, EBIC, PL and CL, a brief review of the previous application of these techniques to the study of CdTe/CdS solar cells will be given. In the case of GDOES, this review will be extended to semiconductor applications generally, as the technique has not previously been applied to CdTe. Also included in Section 3.2.1 is a brief description of illustrative temperature dependent *I-V* studies done in this work but which do not belong in any major results chapter.

3.2 CURRENT-VOLTAGE AND SPECTRAL RESPONSE

3.2.1 Currentdvoltage

As described in Section 1.3.2, illuminated current-voltage (*I-V*) measurement is the technique most directly relevant to solar cell operation. However, in addition to their use in determining the basic photovoltaic parameters, *I-V* characteristics and their variation with temperature can also yield information about materials properties of the devices. This is commonly carried out by fitting experimental data to an equivalent circuit model of the cell.

The simplest such equivalent circuit [1] consists of a non-ideal diode, representing the *p-n* junction, coupled with a current source J_L to account for the collection of light-generated carriers under AM1.5 illumination. In addition, a shunt resistance R_{shunt} is included to model current losses due to carrier recombination and the effect of pinholes; and a series resistance R_{series} simulates the finite conductivity of the semiconductor layers and the device contacts. The complete equivalent circuit diagram is shown in Figure 3.1.

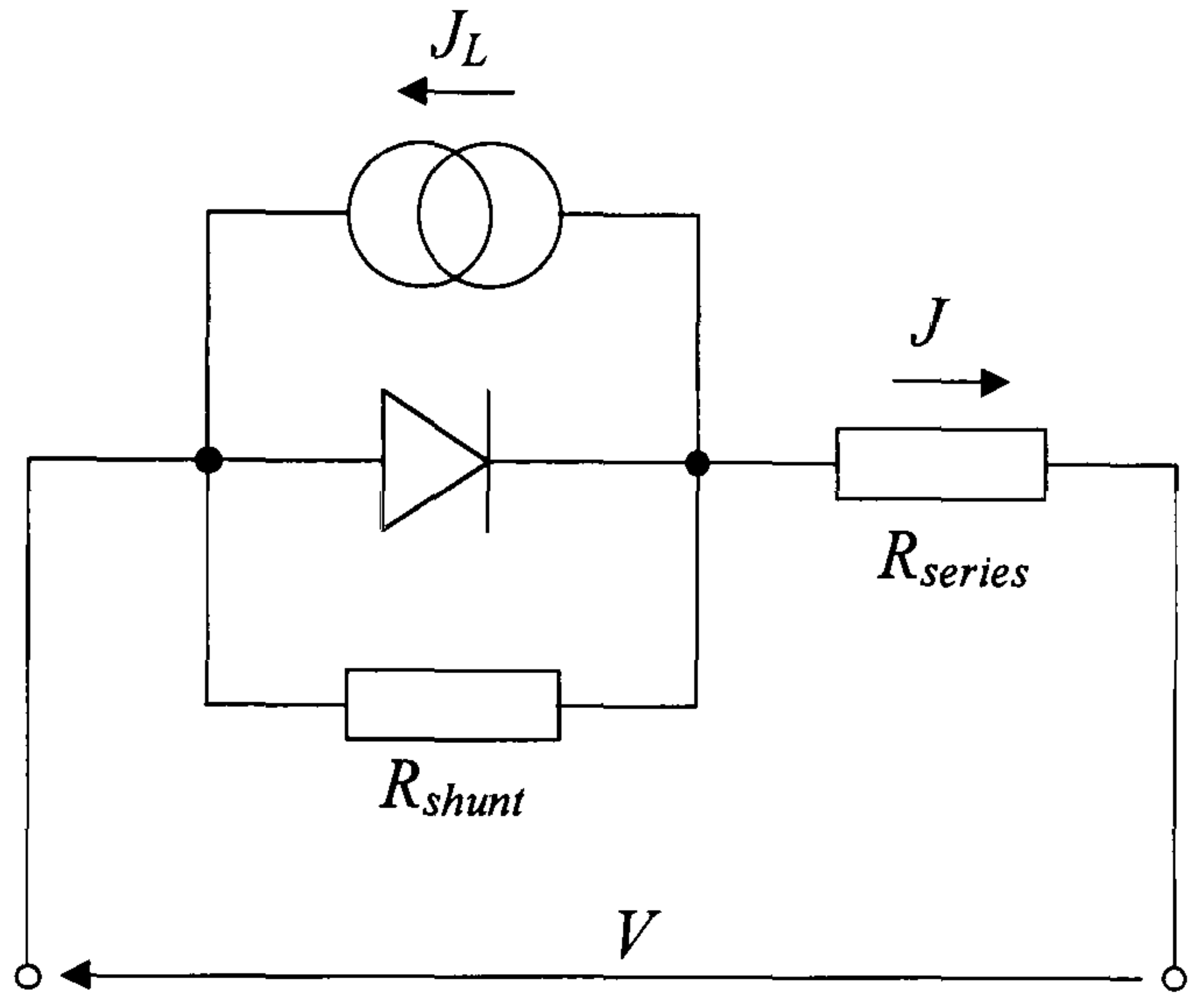

Figure 3.1 Single diode equivalent circuit for solar cell.

Use of the well-known diode equation [2] and a consideration of currents at the nodes then yields the following expression relating the current density J through and the voltage V across the cell:

$$J = J_0\left(e^{\frac{q(V-R_{series}J)}{nkT}} - 1\right) + \frac{V - R_{series}J}{R_{shunt}} - J_L \qquad (3.1)$$

The dark characteristics are similarly modelled, by neglecting the light-generated current term.

Although this expression is suitable for many applications, a more accurate representation of a solar cell's *I-V* characteristics has been found to be the double exponential model. This uses two diodes in parallel, in place of the single component in Figure 3.1, and allows the diffusion current and recombination current in the cell to be considered separately [3-5].

Fitting experimental data to the chosen expression is then carried out in one of two ways:

Analytical methods Although the equation is not analytically soluble in its complete form, analysis of different parts of the *I-V* curve in turn allows considerable simplification of the expression. For example, terms in *V* or *J* can be eliminated by considering the short-circuit and open-circuit cases respectively. Consideration of these and other points on the curve yields a series of equations which are used to calculate each term separately [3,6].

Numerical methods The other widely-used approach is to evaluate a numerical solution to the equation. This is then fitted to the data by adjusting the various parameters in turn using iterative techniques and suitable error criteria [7].

The *I-V* measurements made in this work were carried out using existing apparatus, shown in Figure 3.2.

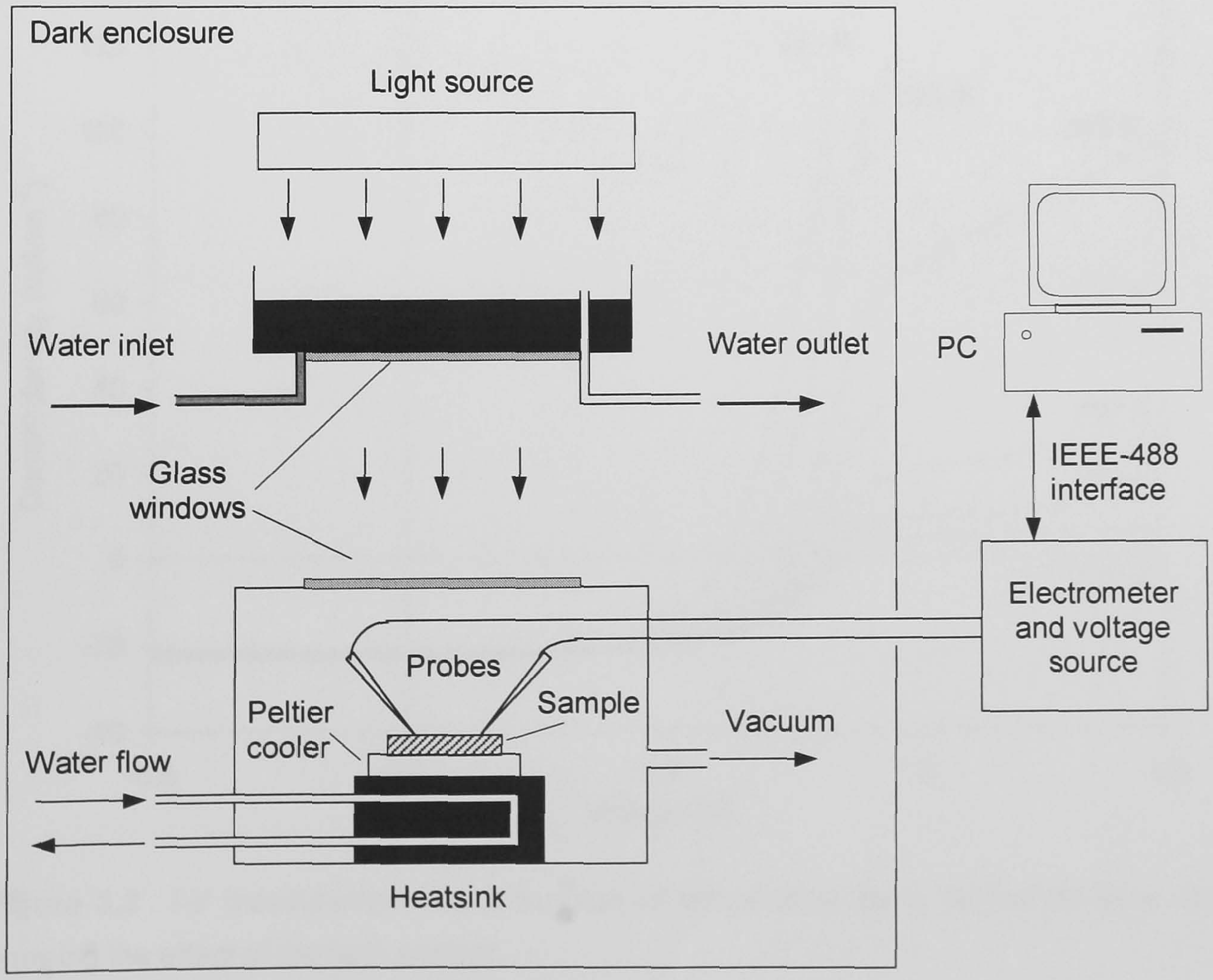

Figure 3.2 Solar simulator used to carry out illuminated *I-V* measurements.

The light source was a 1500W tungsten halogen lamp fitted with a diffuse reflector, with atmospheric absorption simulated by a 2cm deep container of water. The sample was mounted on a Peltier effect heat pump and water-cooled heatsink, to allow control over the temperature. The use of a vacuum chamber prevented the condensation of moisture from the water tray onto the solar cell. Simple two-probe contacting connected the sample to an electrometer, which provided the voltage bias and measured the resultant current. Computer software was written to control the electrometer via an interface bus and to log the measured data.

Some of the device parameters measured using this equipment are shown later in Table 4-I. However, although the *I-V* measurements carried out in this study were mainly to allow correlation to be made between the materials properties and the photovoltaic performance of the cells, they also reveal further interesting aspects of the devices. As an example, Figure 3.3 shows the *I-V* curve of a chloride treated CdTe/CdS solar cell as a function of temperature.

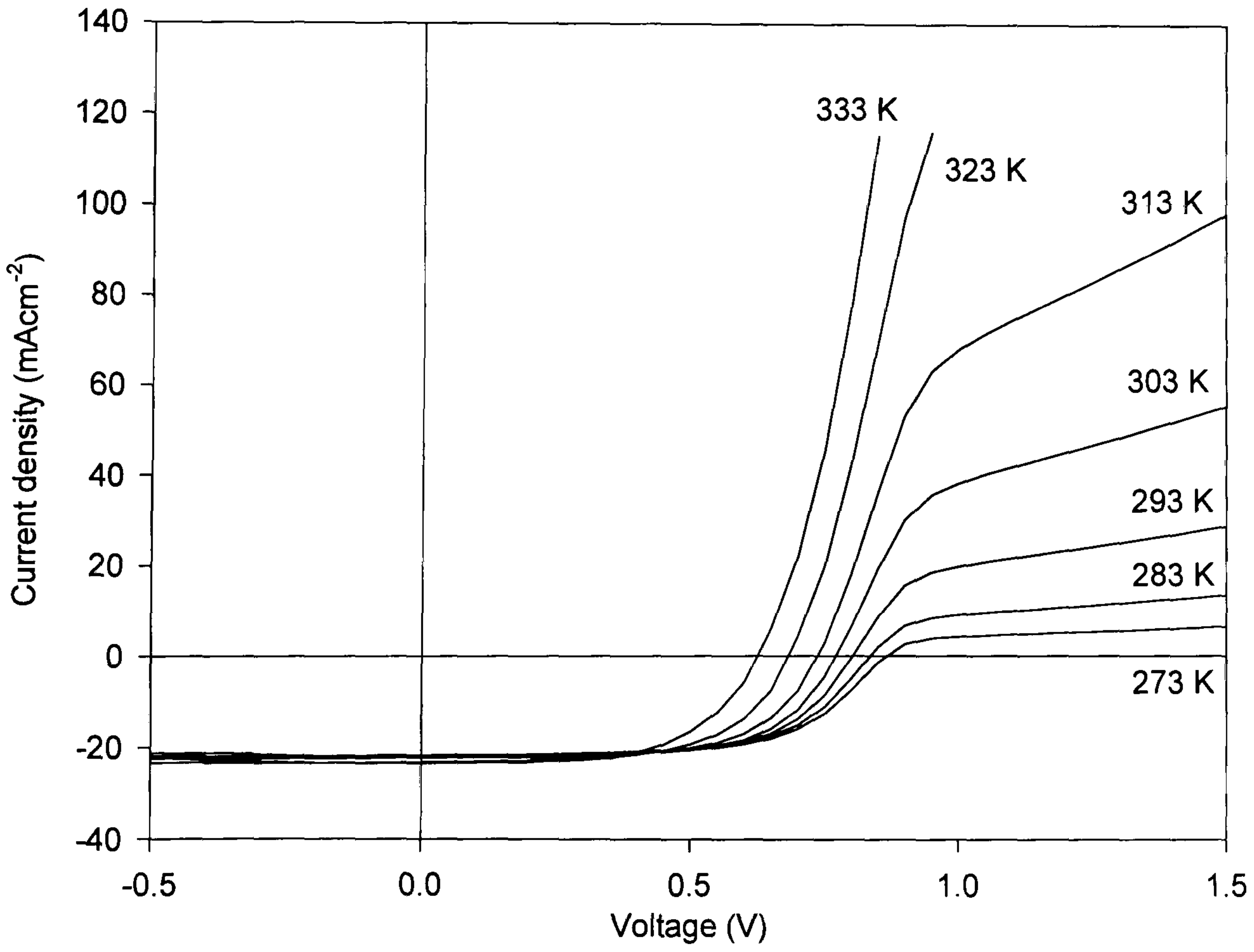

Figure 3.3 *I-V* measurements as a function of temperature for a CdTe/CdS solar cell, showing the effect of the back contact.

As well as showing the detrimental influence on the open-circuit voltage of increasing temperature (as expected from Equation 3.1), a pronounced flattening of the curve is also observed at large forward biases. This so-called “roll-over” effect has also been observed for CdTe/CdS cells by Stollwerk and Sites [8], who have attributed the phenomenon to the rectifying nature of the CdTe back contact. This interpretation suggests that the equivalent circuit in Figure 3.1 should also include a second diode, back-to-back with the first, to represent the contact. Figure 3.4 shows this arrangement.

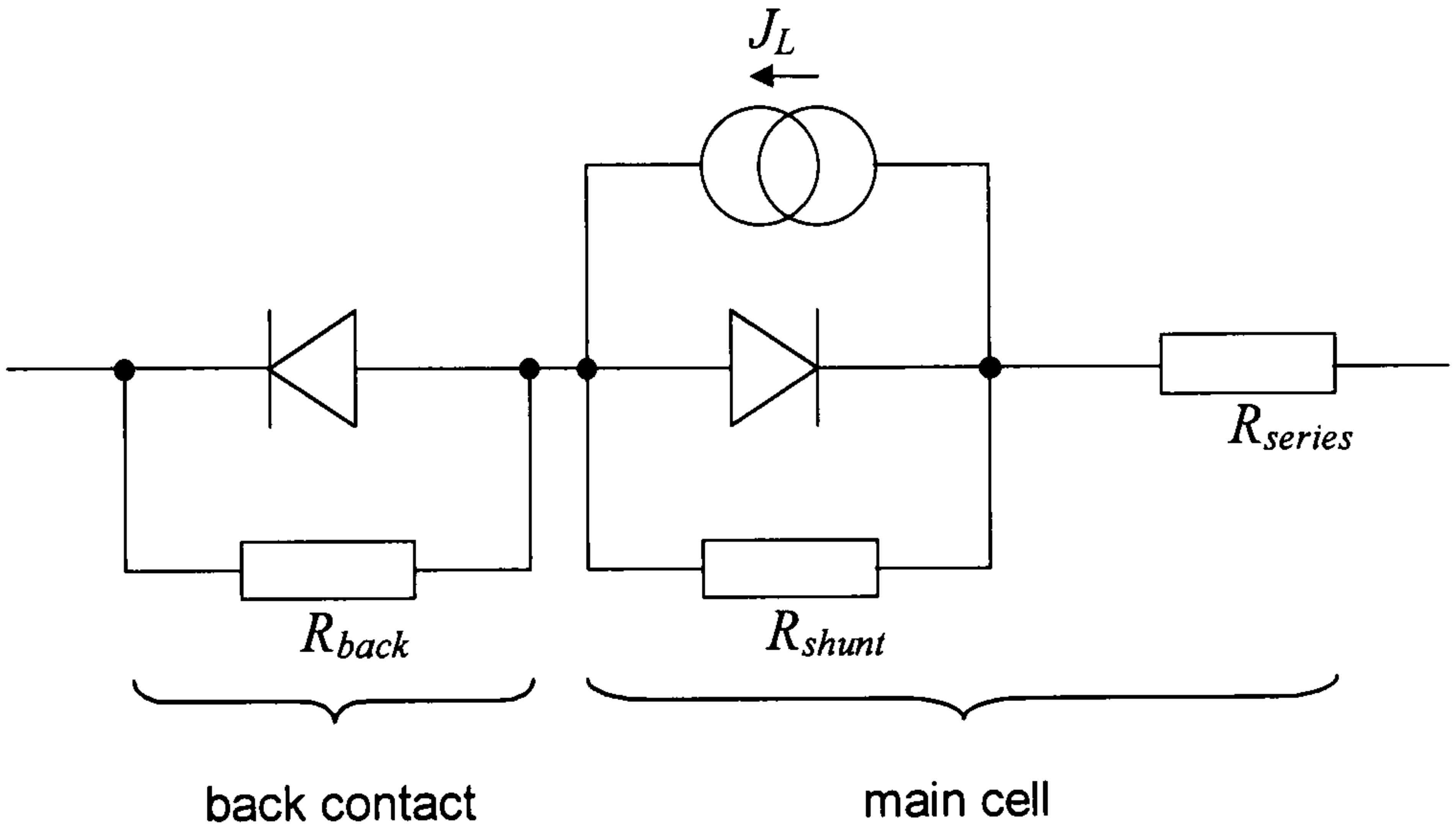

Figure 3.4 Equivalent circuit for a solar cell with a non-ohmic back contact.

Although the shape of the *I-V* curves is consistent with this equivalent circuit, the circuit parameters cannot be extracted without making significant assumptions, and no further *I-V* measurements have been made in this work to examine contact aspects of CdTe/CdS solar cells. However, as the back contact diode can have a significant effect on the photovoltaic properties of a device, its influence on the results of electrical measurements must be considered. In particular, the possible contribution of back contact effects on OBIC and EBIC results will be discussed in later chapters.

3.2.2 Spectral response

Spectral response measurements are used to determine the wavelength dependence of the quantum efficiency of solar cells, as defined in Section 1.3.4. Comparison of this data with simulations of ideal devices allows information to be inferred concerning the origin of losses in the cell, and indicates the nature of the collecting junction involved [9]. This is possible because varying the energy of the incident photons changes their penetration depth, and therefore measuring the current induced as a function of the illumination wavelength allows the position of highest carrier collection to be estimated. In this way it is possible to distinguish between heterojunctions and buried homojunctions from the spectral response data, provided that the absorption spectra of the materials in the device are known.

This technique has been widely used to study the interdiffusion of CdS and CdTe at the device interface [10-13], an effect which causes a decrease in quantum efficiency near to the CdS absorption edge. In this study, the spectral response data is used primarily for comparison with the results of an analogous EBIC experiment, to be presented in Chapter 7.

In order to carry out these measurements, the experimental arrangement shown in Figure 3.5 was constructed.

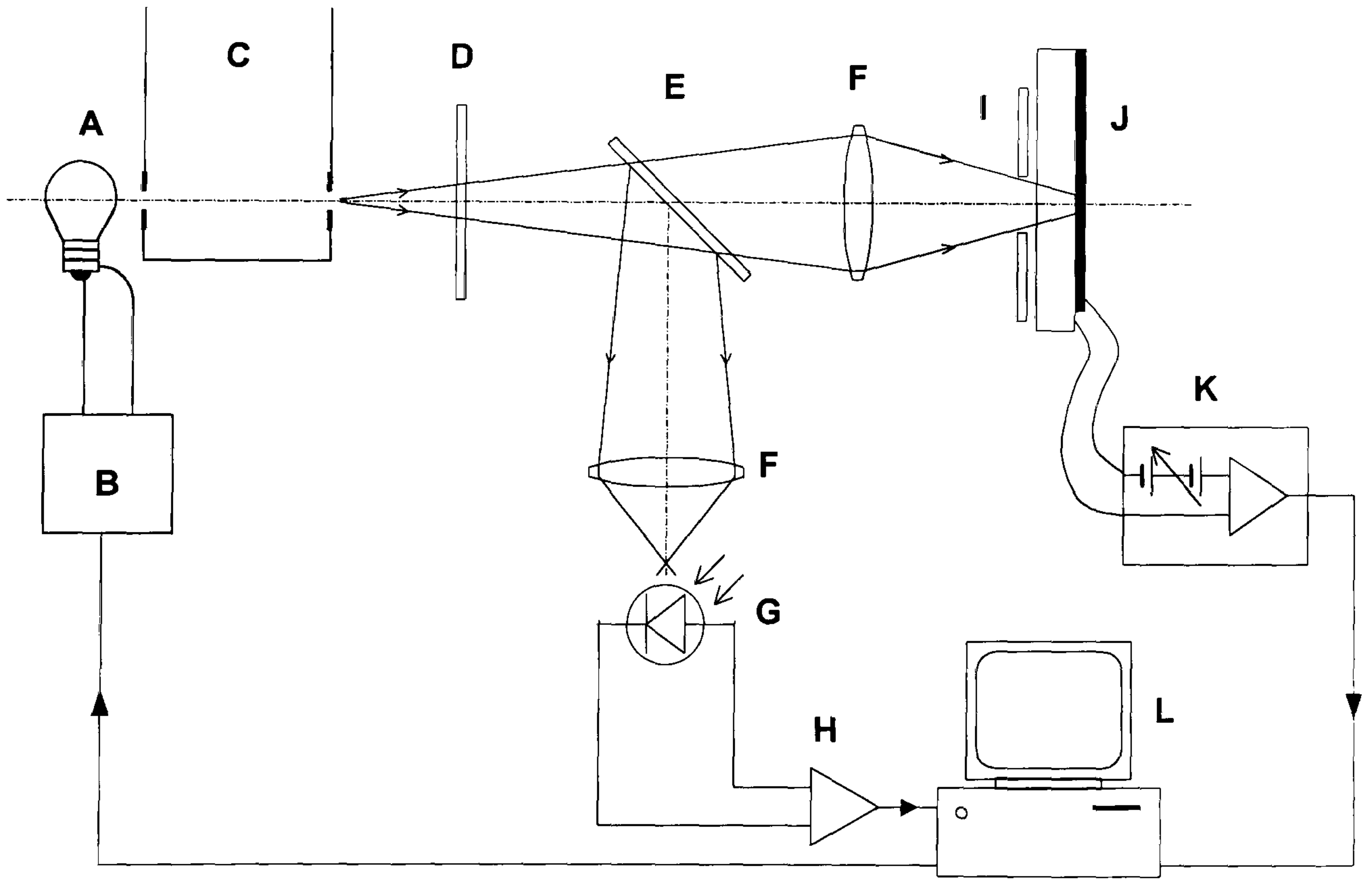

A	Filament lamp	E	Beam splitter	J	Sample
B	Computer-controlled power supply	F	Lens	K	Electrometer
C	Monochromator	G	Photodiode	L	Computer
D	Order sorting filter	H	Current amplifier		
		I	Mask		

Figure 3.5 Experimental arrangement used for spectral response measurements.

A quartz halogen lamp and grating monochromator were used as the light source, with a removable filter used at long wavelengths to remove second order light. The light intensity was monitored using a calibrated photodiode; this was used in a feedback loop to control the intensity of the lamp in order to maintain a constant photon flux at all wavelengths. The current generated by the sample was monitored using an electrometer. The whole experiment was controlled by a computer, including wavelength scanning, data logging and light intensity monitoring.

3.3 OPTICAL BEAM-INDUCED CURRENT (OBIC)

In order to obtain spatially resolved information about the photocurrent in a solar cell, a light beam can be scanned across the sample and the induced current measured at each point to build up a map of photovoltaic performance. This technique has long been used in the PV industry for the quality control of large-scale solar modules [14]. Higher resolution scans have also been used to characterise grain boundary effects in multicrystalline silicon cells, where the grain dimensions are of the order of millimetres [15-17]. Techniques of this resolution are usually referred to as scanning light spot (SLS) or light beam-induced current (LBIC) methods.

Due to the wavelength resolution limit inherent in optical microscopy, micron scale resolution with these techniques requires the optics to be optimised. Such systems have been assembled by several workers [18,19], with resolutions of up to ~0.4μm being reported [19]. At these resolutions, the technique is generally referred to as optical beam-induced current (OBIC). In order to obtain a high resolution, this technique uses a laser beam focused onto the sample using a microscope objective. Scanning of the light spot can be achieved using a system of moving lenses, but more often a confocal geometry is employed and the sample itself is scanned with respect to a stationary beam.

This technique was first applied to thin-film solar cells by Galloway *et al* [20-22], who used it to probe the effects of $CdCl_2$ treatment on CdTe/CdS devices. Their findings showed that the post-deposition treatment acted to homogenise the photovoltaic performance of the cell. In addition, a strong intensity dependence of the photocurrent was observed, which was attributed to the onset of high injection conditions in the device. Such effects were further studied in this work using both

OBIC and its electron beam analogue, EBIC, a technique which is described in Section 3.5.5.

3.4 PHOTOLUMINESCENCE SPECTROSCOPY

3.4.1 Introduction

Photoluminescence (PL), and its electron beam equivalent, cathodoluminescence, offer a way of investigating the various shallow impurity levels present in a semiconductor. In CdTe solar cells, where the introduction of electrically active levels is known to occur but is poorly controlled, this has proved to be a useful technique, even though the quality of the spectra is degraded by the polycrystalline nature of the material.

3.4.2 Principle

When excess carriers are generated in a semiconductor (*e.g.* under optical illumination), the carrier concentrations are no longer in equilibrium. Various recombination mechanisms act to regain equilibrium, all involving the relaxation of an electron from the conduction band back down to the valence band. One such group of processes occurs via the emission of a photon with a wavelength determined by the difference in energy between the two electronic states involved. Some of the different possible transitions are illustrated in Figure 3.6 [43].

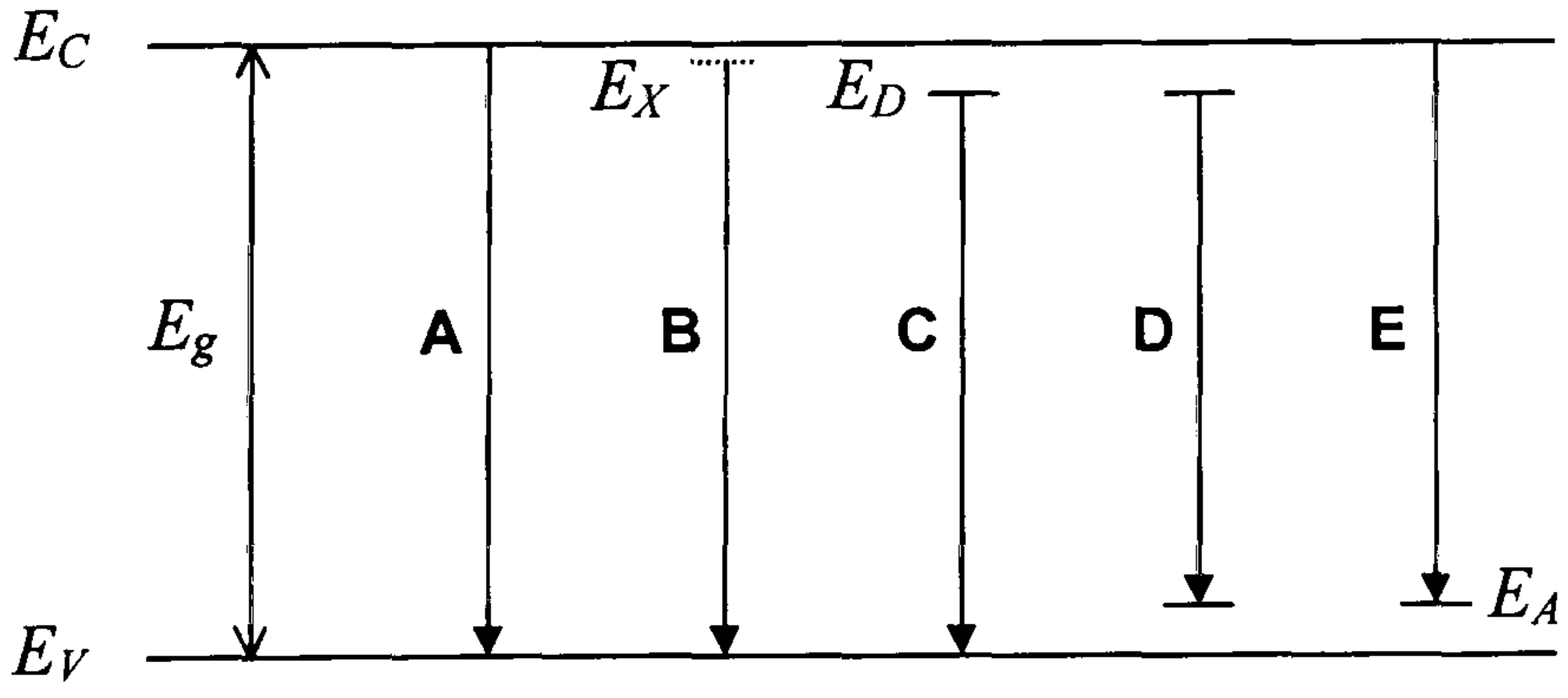

Figure 3.6 Possible radiative transitions: **A** Interband transition; **B** Intrinsic excitonic transition; **C-E** Extrinsic impurity-related transitions.

The transitions labelled A to D in the figure take place between various mid-band states:

A Direct interband transitions between the bottom of the conduction band and the top of the valence band are not commonly observed. If this transition were to occur, the emitted photon would have a high probability of immediately being re-absorbed. Excitonic and impurity-related transitions are also more probable.

B The highest energy transitions generally observed are between an excitonic state and the valence band. Excitons are formed as the result of the Coulombic interaction between an electron in the conduction band and a hole in the valence band. The energy of this state is lower than the bottom of the conduction band by an amount equal to the binding energy of this hydrogen-like system. Transitions between this exciton state and the valence band are known as *intrinsic* transitions, and such peaks are often labelled "X" on luminescence spectra.

At low temperatures, the observed light intensity from such free-exciton transitions is low, due to re-absorption of the emitted photon. However, excitons can also be trapped by impurities, and the energy levels of such states are reduced further by an amount known as the *localisation energy*. The excitons can be bound to either donors or acceptors, and these impurities can be either neutral or ionised. The peaks involving these transitions are labelled "D^0X" and "D^+X" for neutral and ionised donors respectively, and "A^0X" and "A^-X" for acceptors. At low temperatures, *i.e.* when the impurities have not been thermally ionised, neutral impurity-bound exciton transitions will dominate the near-bandgap region of the spectrum.

C-E Transitions involving shallow impurity levels and the bands also occur. Donor-acceptor pair (DAP) luminescence (often labelled "D^0,A^0") results from the interaction of donor and acceptor centres, which are initially both neutral. If the radiative recombination of the donor atom's electron with the acceptor's hole then occurs, the centres will then each become ionised. The resultant Coulombic attraction between the ionised centres will depend inversely on their separation, and this will affect the energy of the emitted photon. Since there is large number of different distances separating all the various impurity atoms in the sample, this results in a broad band typical of DAP luminescence.

3.4.3 Application of PL to CdTe solar cells

PL is rarely applied to CdTe solar cells, presumably on account of the complexities to be encountered in interpreting spectra from polycrystalline samples. The potentials at the grain boundaries may be expected to influence the optical transitions. For a review of luminescence in CdTe, the reader is referred to [23].

Halliday *et al.* have carried out low-temperature PL on CdTe/CdS structures and have observed emission bands corresponding to bound excitons (1.59eV), a free to bound transition (1.55eV) and DAP luminescence (1.45eV) [24]. This latter band is often observed in CdTe luminescence, and is usually attributed to a cadmium vacancy complex. Further studies were carried out on chemically bevelled samples [25,26], where the 1.55eV band was found to be of greater intensity nearer to the device junction. It was speculated that this was due to the presence of isoelectronic oxygen on a tellurium site, resulting in the formation of a shallow acceptor, as suggested by Akimoto *et al.* [27,28]. Similar bevelled samples have been examined in the present work (see Chapter 8).

Studies have also been carried out by Levi *et al.* [29] to evaluate the effect of the back contact on the PL spectra of CdTe/CdS cells excited through the front wall. It was found that tellurium enrichment of the CdTe using the nitric/phosphoric acid etchant, or the deposition of a wide variety of metals, influenced the PL spectra, even though the CdTe was 8μm thick. Although this study is not directly relevant to the work in this thesis, it does serve to illustrate the sensitivity of PL, and also the complexity of the CdTe/CdS solar cell materials system.

Comparison of the photoluminescence technique with the corresponding electron beam technique (cathodoluminescence) will be made in the following section.

3.5 SCANNING ELECTRON MICROSCOPY

3.5.1 Introduction

Conventional optical microscopy is limited in its resolution by the wavelength of the light used, limiting the usefulness of such methods in sub-micron analysis. By contrast, the scanning electron microscope (SEM) is capable of resolving spatial variations on a much smaller scale. A further advantage is that several different modes of operation are available, the physical bases of which are examined in this section.

3.5.2 SEM operation

The scanning electron microscope consists of a focused beam of electrons which is scanned in a raster fashion across a sample. In this way each part of the sample is probed in turn, with some electron beam-induced phenomenon measured at each point; these measurements may then be reassembled to produce an image of the sample. Figure 3.7 shows the essential features of the SEM.

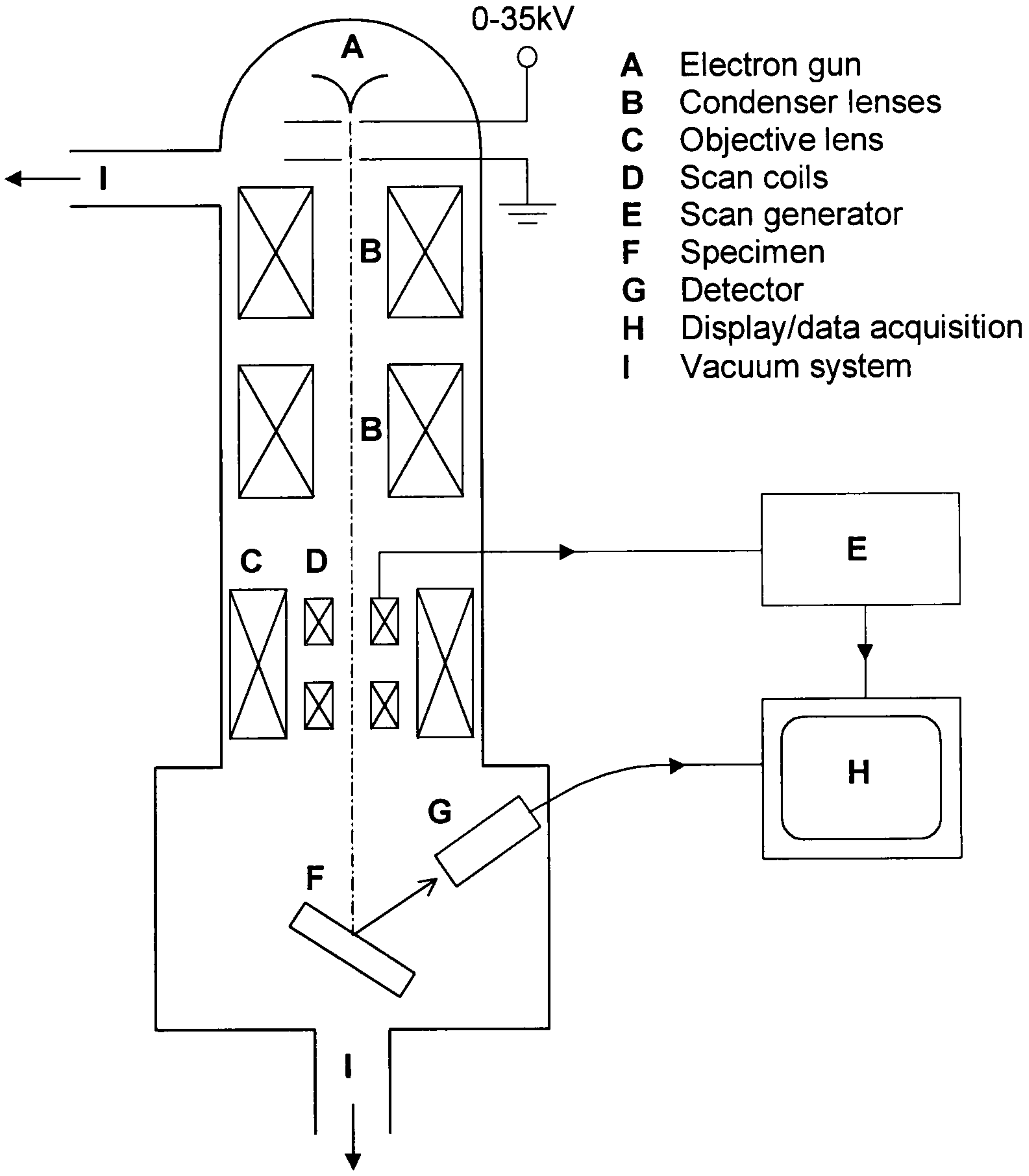

Figure 3.7 Diagram showing the basic arrangement of the scanning electron microscope.

The electron gun contains a tungsten hairpin filament, through which a current is passed to achieve thermionic emission. The emitted electrons are accelerated through a voltage of up to ~35kV, and the resultant beam is finely focussed by a series of magnetic coils to form a spot on the specimen. A scan generator moves this spot across the specimen via two sets of scan coils. One of various types of detector is used to monitor some emission from (or property of) the sample, and the resultant signal is amplified and passed to the display device. Using information from the scan generator, this display system then produces an image or linescan of the specimen.

Different modes of the SEM use different signals to produce the image, as described in the following sections.

3.5.3 Backscattered electron mode

When an electron beam impinges upon a target, high energy beam (or *primary*) electrons are elastically scattered by Coulombic interactions with atomic nuclei in the sample. A significant minority of the primary electrons will be scattered through large enough an angle (after undergoing either a single or successive elastic collisions) that they re-emerge from the incident surface as backscattered electrons. The rate of primary electron backscatter can be measured by the use of a scintillator detector. This detector is shielded from the lower energy secondary electrons (see section 3.5.4) by a wire mesh held at potential of around -100V [30]. Since the cross-section for such scattering events is described by the Rutherford expression, which includes a term in Z^2 (where Z is the atomic number), the rate of backscattered electrons detected carries elemental information. However, the backscattered signal is also dependent on the surface topology of the sample [31], as shown in Figure 3.8.

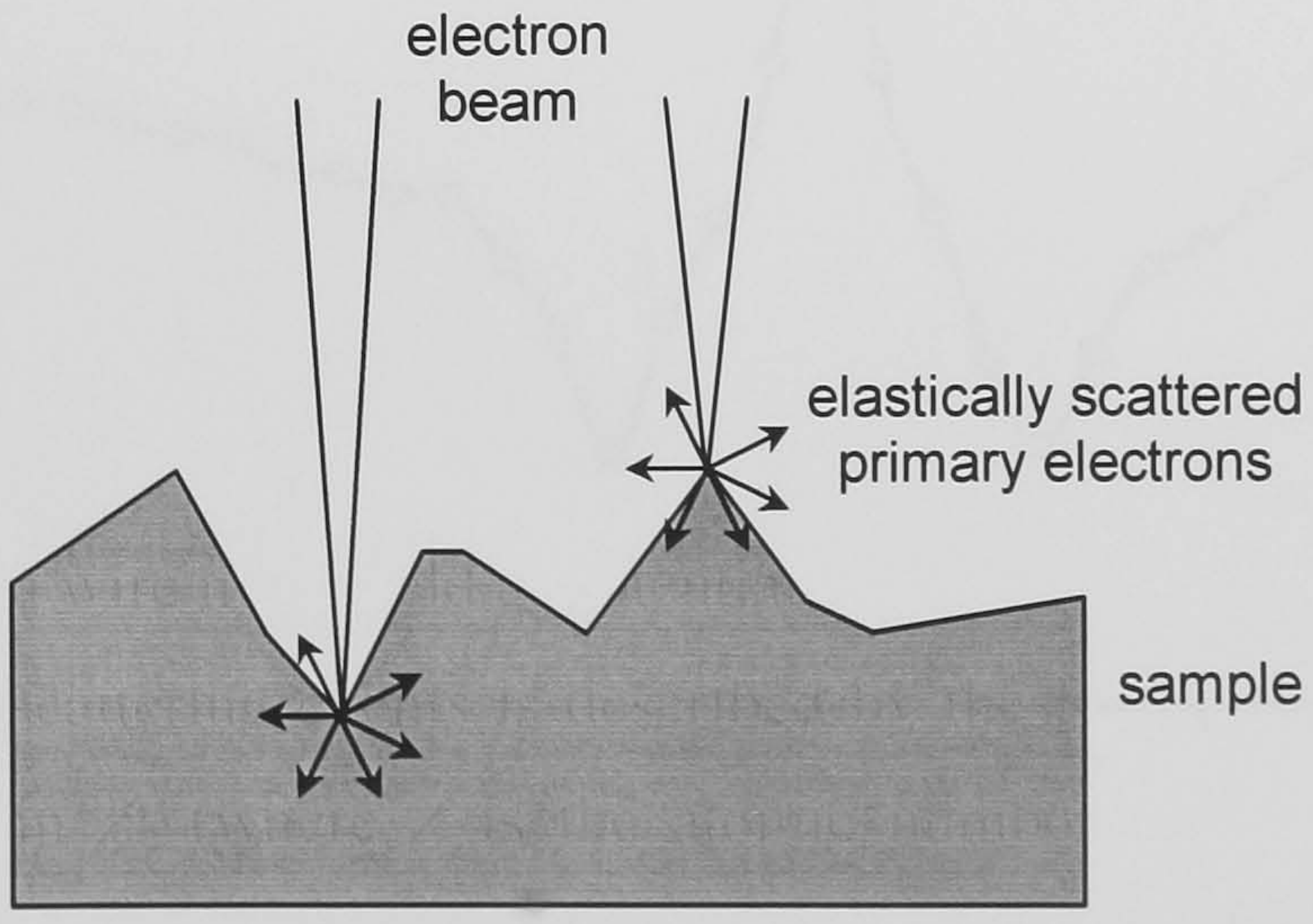

Figure 3.8 The effect of surface topology on the rate of primary electrons backscattered from the sample.

Primary electrons backscattered from within a surface depression have a higher probability of re-entering the sample than those that are backscattered from a protruding feature. Having re-entered the sample, they then have a higher probability of losing their energy via inelastic collisions rather than re-emerge as backscattered electrons.

Although no direct use is made of backscattered electron information in this study, the effect of this phenomenon on other SEM modes must be taken into consideration. Since the backscattered electrons take with them a significant and varying proportion of the electron beam energy, SEM modes such as EBIC and CL that depend on the absorbed beam energy will be affected. A simple analysis of this problem is presented in Figure 3.8, which shows a simulated absorbed current linescan corresponding to a topological surface feature.

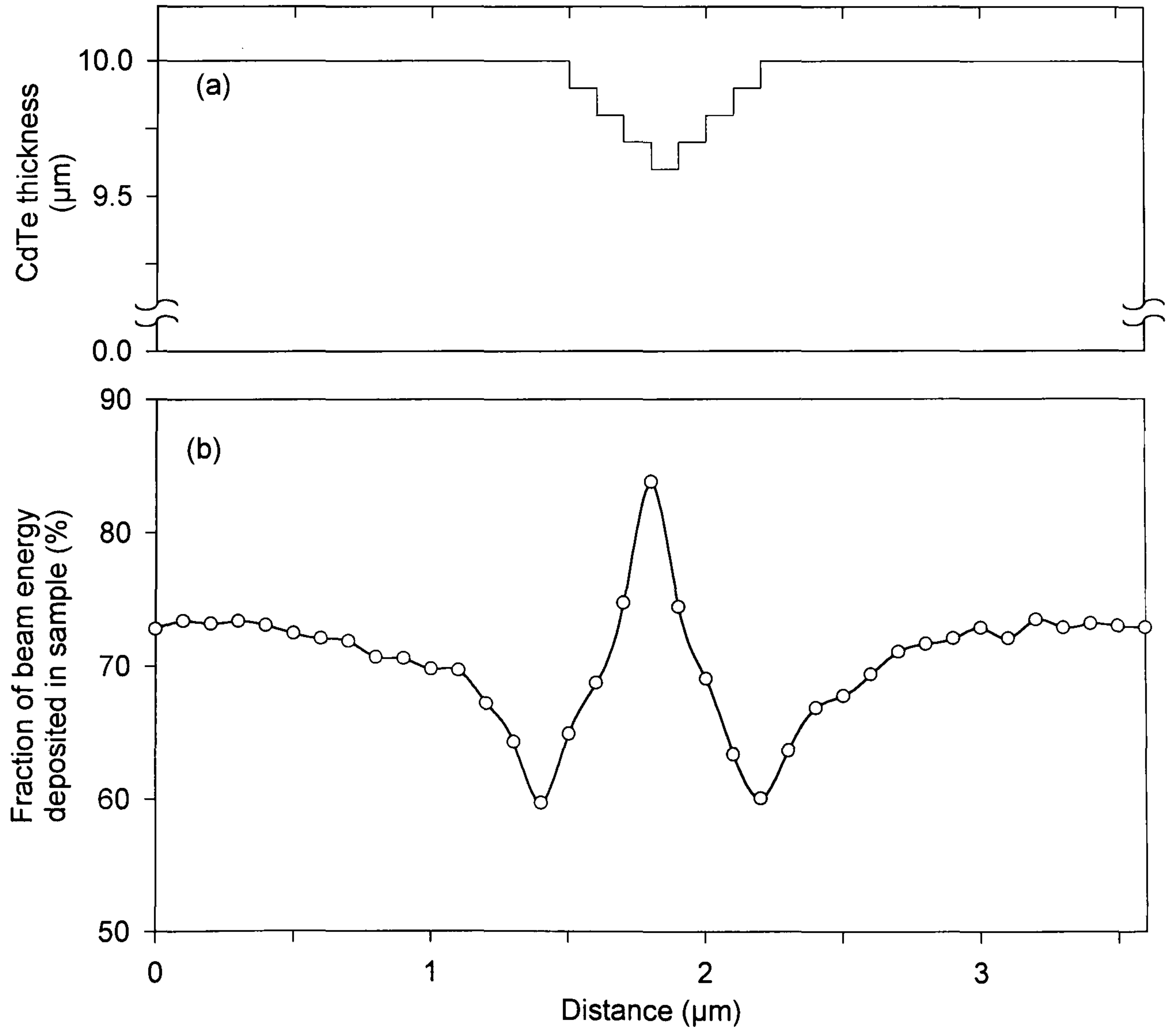

Figure 3.9 Monte Carlo simulation of an absorbed current linescan across a surface feature. The simulation used a 20keV electron beam scanning across a cadmium telluride sample.

This data was simulated using the Monte Carlo software described in Section 3.5.5, and the step-like appearance of the simulated surface feature is due to the finite number of sample layers that the program allows. Despite this limitation, the effect of the topology is clear, with a higher fraction of the beam energy deposited where the surface is concave than where convex. These differences in absorbed energy are attributable to variations in the number of primary electrons backscattered. For this reason it is important that any samples to be examined using an SEM mode that depends on the energy deposition in the sample (*e.g.* CL or EBIC) must be free of topological surface features.

3.5.4 Secondary electron mode

The high-energy incident electrons can also interact with the loosely bound conduction band electrons in the sample. The amount of energy given to these *secondary* electrons as a result of the interactions is small, and so they have a very limited (a few nm) range in the sample. Because of this, only those electrons excited within a short distance of the surface have sufficient energy to leave the sample. This is therefore the mode most commonly used for the analysis of surface topology.

A secondary electron micrograph obtained from the unpolished back surface of a CdTe/CdS solar cell examined in this study is shown in Figure 3.10.

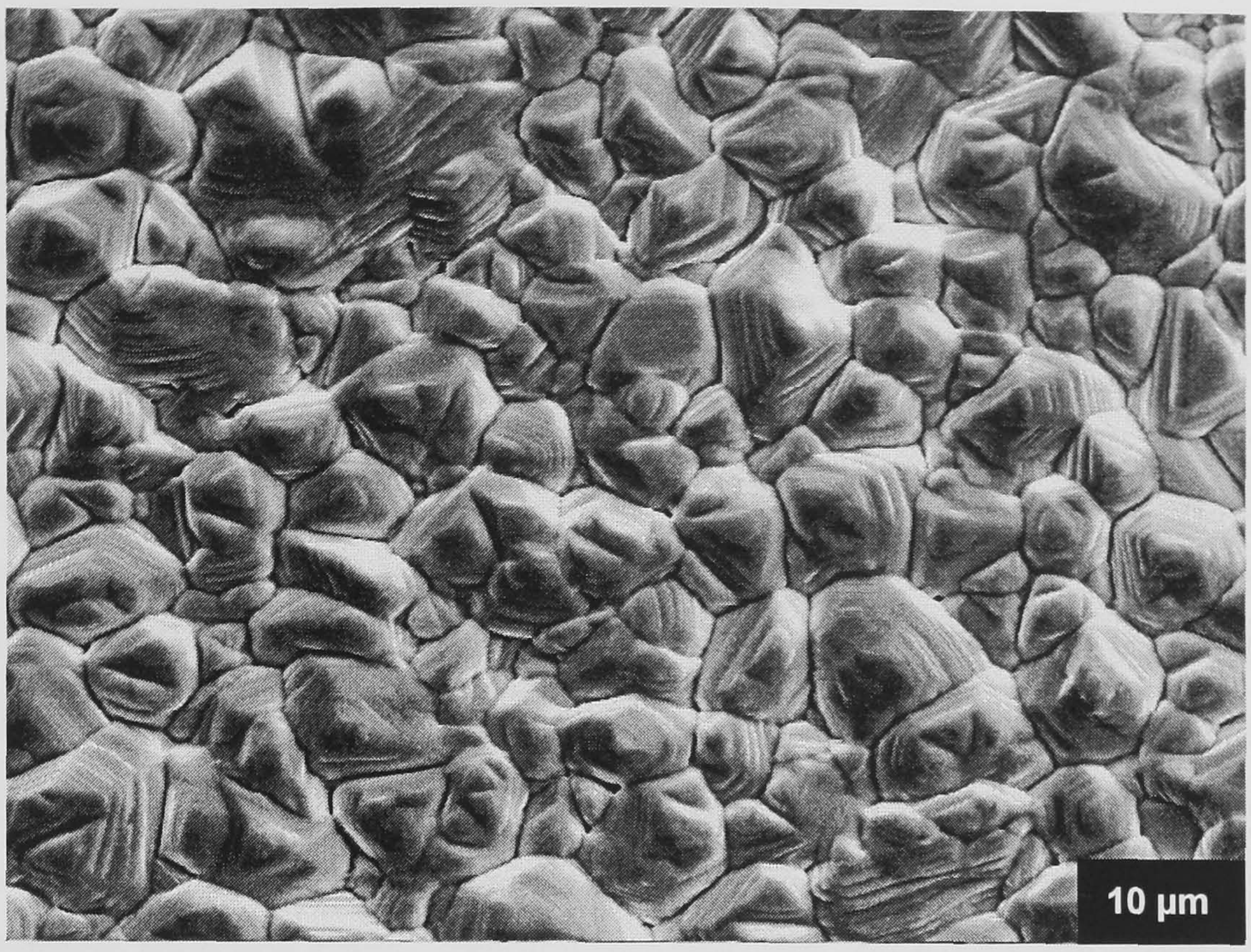

Figure 3.10 Secondary electron micrograph of an untreated polycrystalline CdTe/CdS solar cell.

This clearly shows the polycrystalline nature of the device, with CdTe grains observable on the scale of 10μm. Also visible on the grains are crystal terraces; this is characteristic of films grown by the CSS method, and similar features have been observed elsewhere using atomic force microscopy [32]. This high degree of surface topology will have an effect not only on the electron backscatter rate (as discussed in the previous section) but also on any emitted photons. For these reasons it is vital that a polished surface is first obtained before any back-wall EBIC or CL measurements are carried out.

3.5.5 Electron beam-induced current (EBIC)

The electron beam-induced current (EBIC) technique is similar in principle to OBIC, described in Section 3.3. In this case, however, the optical beam is replaced by a electron beam by placing the sample in the SEM. Electrical connections are made to the cell contacts in the conventional manner, and the measured current is then amplified and used as the input for the SEM display. This section details the physical processes involved in this experiment, and outlines what information this technique can provide about a solar cell.

Carrier generation Unlike OBIC, where electron-hole pairs are excited in a semiconductor via band-to-band optical absorption, the process by which carriers are generated under an electron beam is that of impact ionisation. In this process, a high-energy electron interacts with a valence band electron, which, if sufficient energy is transferred, is excited into the conduction band [30]. These high-energy electrons can either be lattice electrons under the influence of a large electric field (as occurs in avalanche photodiodes) or, as in this case, incident electrons from outside the specimen. The carriers resulting from an incident electron beam are generated in a finite volume of the material, referred to as the carrier generation volume. The basis of the EBIC technique is that, once injected, these electron-hole pairs subsequently behave in the same way as those injected by other means, such as photogeneration.

Application to solar cells The ability to inject a small volume of carriers into a sample allows EBIC to be used to probe spatial variations in the collection probability of a solar cell. This collection probability is a determined by the rates of several processes: recombination, drift and diffusion. Variations on the EBIC method have been used to yield information concerning each of these processes.

a) Recombination The loss of carriers through recombination will clearly lead to a decrease in the current collected by the electric field. This effect is exploited in order to identify crystal defects in semiconductors. Such defects, such as grain boundaries, inclusions and dislocations, are usually associated with enhanced recombination (unless passivated), and therefore exhibit EBIC contrast.

This aspect of EBIC has been widely used in the characterisation of grain boundaries in multicrystalline cast silicon solar cells [33,34]. Several theoretical treatments have also be carried out, and provide methods of extracting the grain boundary recombination velocity from experimental EBIC linescans [35-37]. For thin film devices, however, where the grains are small compared with the minority carrier diffusion length, such treatments are more complicated [38]. McClure *et al.* [39] have modelled the effect of grain boundary recombination in CdTe/CdS solar cells in an attempt to interpret the presence of notches in cross-section EBIC linescans. Planar EBIC on these devices has hitherto only been attempted through the CdTe side of the solar cell, due to the presence of the glass substrate on the front of the device. These results, some of which have been reproduced in Chapter 6, fit the conventional view of grain boundaries as recombination centres by exhibiting dark boundary contrast [20,21].

b) Drift EBIC linescans of solar cell cross-sections (*i.e.* perpendicular to the device layers) are carried out within the depletion region as a method of determining the position of the collecting junction in the device. Since this is the position of maximum electric field, the carriers will be subject to the greatest drift at this point, resulting in a peak in the induced current. Such measurements carried out on CdTe/CdS cells by Galloway *et al.* (also reproduced in Chapter 6), show the presence of a homojunction buried within the CdTe layer.

c) Diffusion In the neutral region of the device, the probability of carrier collection will decrease with distance from the depletion region edge. This is related to a) above, but in this case relates more to the bulk recombination (as described by a characteristic lifetime) rather than the recombination at a particular feature. Ideally this decrease will be exponential with the minority carrier diffusion length L, *i.e.*:

$$I = I_0 \exp\left(\frac{z}{L}\right) \tag{3.2}$$

but this is often an oversimplification as the carrier lifetimes (and hence diffusion lengths) may vary spatially. Nevertheless, the measurement of diffusion lengths using this principle is one of the most widely used applications of EBIC. Such measurements can be carried out in the cross-section geometry [40] or in a planar configuration.

The use of the cross-section method on CdTe/CdS thin-film devices has been reported by Kenny *et al.* [41], who noted the non-exponential nature of the decrease in EBIC with distance from the junction. Numerical modelling of the system was carried out, taking into consideration finite surface recombination and high injection, but it was found that these effects did not fully account for the shape of the observed curve.

If the plan view injection method is used, the depth in the solar cell at which the carriers are injected is varied by changing the accelerating voltage of the electron beam. This has not previously been attempted in the illumination geometry for CdTe/CdS cells due to the presence of the glass substrate, but the technique has been developed for chalcopyrite thin-films by Scheer. This work is further reviewed in Chapter 7, where new results for CdTe/CdS films are also presented.

Limitations of EBIC Although the probe size in EBIC is orders of magnitude smaller than the wavelength-limited spot size in OBIC, this quantity is not the limiting factor in the resolution of EBIC. The smallest volume that can be interrogated by the electron beam in the EBIC mode will be equal to the carrier generation volume. This volume is strongly dependent on the beam voltage, with higher energy electrons producing generation functions with greater depth and lateral spread (see the Monte Carlo simulations of Section 7.3.3). Increasing the beam current will also have a detrimental effect on the resolution, since greater electrostatic repulsion in the beam will result in a less finely focussed spot. Moreover, the greater injection density will have the effect of increasing the lateral diffusion of carriers away from their point of generation, effectively increasing the volume of sample being interrogated. Such high injection effects are routinely ignored, although they have been shown to be an important factor under the beam conditions usually used for EBIC [42].

High injection conditions also influence EBIC experiments because of another related phenomenon, the plasma effect. This occurs when a high density of carriers injected into a semiconductor is sufficient for the carriers to form a plasma, which polarises at the edges and acts to screen the local region from the electric field [43]. The carriers are therefore less likely to be collected by this field, and a decrease in the EBIC signal is observed. This phenomenon was first observed in radiation detectors [44], and was found to occur under an electron beam by Leamy *et al.* [45]. An example of the experimental observation of the effect can be seen in Section 6.3.2, where it is shown to occur in CdTe/CdS solar cells.

3.5.6 Cathodoluminescence

Principle Cathodoluminescence (CL) is based on the same principle as its optical analogue, PL (see Section 3.4). In this case, however, the excess carriers in the material are not photogenerated, but are produced by the impact ionisation mechanism described above. The light emitted due to radiative recombination processes is collected using a parabolic mirror inside the SEM, and is then directed towards a similar spectrometric detection system to that used in PL. Further information on the particular system used for the measurements in this work is given in Chapter 8.

Spectroscopy In most respects, the results obtained from CL spectra are directly comparable to the corresponding PL measurements, and similar information can be derived from them. Section 3.4 gives an overview of the interpretation of luminescence spectra.

Mapping The major advantage of CL over PL is that the small electron beam spot size gives the technique improved spatial resolution. This fact, coupled with the ease with which an electron beam can be scanned, lends the technique to luminescence mapping. This can be carried out using the entire spectrum of emitted light (*panchromatic* imaging), or a narrow band of wavelengths (*monochromatic* imaging). The former technique has the advantage of a large signal, improving the signal-to-noise ratio and allowing faster scan rates; the latter allows the spatial origin of various luminescence bands to be investigated.

Comparison with PL A potential drawback of photoluminescence is that only transitions of a longer wavelength than that of the laser source can be observed. This can be a problem for some of the wider bandgap semiconductors such as CdS (E_g=2.4eV) and ZnS (E_g=3.7eV), for which blue and UV light sources are required respectively. In cathodoluminescence, however, the beam electrons have far higher energies than any transitions related to the bandstructure, allowing all possible luminescence lines to be observed. Furthermore, varying the electron beam energy allows the position of the excitation volume to be moved to different depths in the sample. This can allow some depth-dependent information to be extracted from CL *versus* beam voltage measurements, although the absorption of the emitted luminescence by the semiconductor complicates the interpretation of such results.

Application of CL to solar cells Al-Jassim *et al.* have carried out panchromatic cathodoluminescence imaging [46] and linescans [47] on CdTe/CdS thin film solar cells. They found considerable variation in the CL intensity from grain to grain, which they attributed to different densities of defects. Dark grain boundary contrast was also observed, from which it was concluded that non-radiative mechanisms dominated the recombination in these regions. However, these results were open to some ambiguity due to the amount of surface topology on these unpolished devices.

3.5.7 Summary

Multi-mode scanning electron microscopy allows various high-resolution measurements to be made on a sample, often simultaneously. The main advantage of SEM techniques over their optical analogues is the improvement in spatial resolution. However, a potential drawback is that, whilst a nominally non-destructive technique, the electron beam may introduce defects into the material. This work concentrates largely on the use of the EBIC and CL modes, and these will be discussed in greater depths in the experimental Chapters 6-8.

3.6 GLOW DISCHARGE OPTICAL EMISSION SPECTROSCOPY

3.6.1 Introduction

Optical emission spectroscopy is a method of elemental analysis that is based on transitions between the outer shell electrons of an atom. Since the atomic energy levels depend on the nuclear charge and the atomic quantum numbers, the transition energies are specific to a particular element. The elemental composition of a material can therefore be determined by exciting the atoms and observing the characteristic photon energies emitted. This is the basis of the primitive Bunsen flame tests, and also of a number of more advanced techniques, including atomic emission spectroscopy and the more modern glow discharge optical emission spectroscopy (GDOES) profiling method.

3.6.2 Apparatus

To order to excite the electronic transitions in the material, GDOES makes use of a glow discharge lamp. One of the more commonly used lamps is that developed by Grimm, in which the specimen itself serves as the cathode for the discharge. The plasma occurs within a metal cylinder, which contains a low-pressure argon atmosphere and acts as the anode. Cathodic sputtering occurs at the surface of the sample, into which a successively deeper crater is etched. The plasma excites the valence electrons in the sputtered material, and the resultant light is collected through an optical window and focussed onto the entrance slits of a spectrometer.

In order to simultaneously monitor multiple wavelengths, corresponding to a range of different elements, the spectrometer used is of the type shown in Figure 3.11.

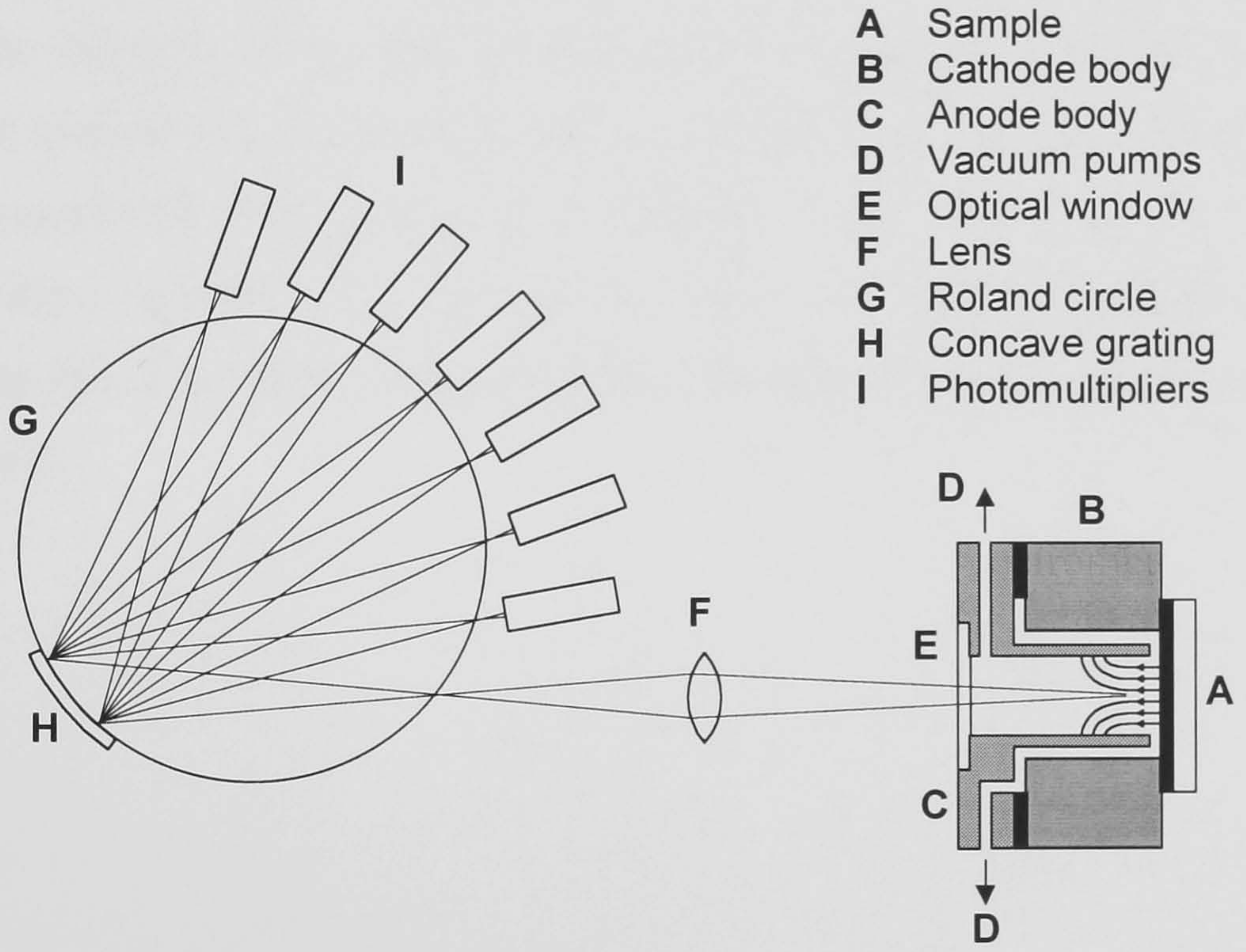

Figure 3.11 Schematic representation of the glow discharge optical emission spectrometer used in this work.

The entrance slits, concave diffraction grating and multiple exit slits are all positioned on the circumference of a Roland circle. The positions of the exit slits are computer controlled, and can be adjusted to select the wavelengths corresponding to the elements of most interest. A photomultiplier is positioned behind each of the slits, and the signal from each is amplified and recorded as a function of time. The intensity of the light measured at the characteristic wavelength of a given element is used as a measure of the relative abundance of that element, and the variation of the intensity with time gives a compositional depth profile of the sample [48].

3.6.3 Application to semiconductors

The fact that the Grimm-type discharge lamp uses the specimen itself as the cathode for the glow discharge requires that the sample be able to sustain a vacuum and also be electrically conducting. The CdTe/CdS solar cell fulfils the first criterion, and, to a certain extent, the second. Whilst more resistive than the metal samples on which the technique is usually applied, work by Dharmadasa *et al.* [49] has shown some semiconducting samples to be capable of conducting sufficient current for the glow discharge to be sustained. However, these preliminary studies were carried out on single crystal devices with highly spatially uniform carrier concentrations. In this study, the relatively low quality polycrystalline material is likely to exhibit significant variation in conductivity between grains, and a uniform sputter rate can not be guaranteed. Furthermore, the different layers may also have different conductivities, especially if (as suspected) there is a doping gradient with depth through the cell. The results of applying the technique to such materials are presented in Chapter 8.

REFERENCES FOR CHAPTER 3

[1] L.L. Kazmerski *"Introduction to Photovoltaics: Physics, Materials, and Technology"* in *Solar Materials Science*, edited by L. E. Murr, (Academic Press Inc., New York, 1980)

[2] S.M. Sze, *Semiconductor Devices, Physics and Technology*, (Wiley, New York, 1985)

[3] A. Hovinen (1994) *Fitting of the solar cell IV-curve to the two diode model*, Physica Scripta **54** pp.175-176

[4] M. Wolf, G.T. Noel and R.J. Stirn (1977) *Investigation of the double exponential in the current-voltage characteristics of silicon solar cells*, IEEE Transactions on Electron Devices **24** (4) pp.419-428

[5] N. Veissid, D. Bonnet and H. Richter (1995) *Experimental investigation of the double exponential model of a solar cell under illuminated conditions: considering the instrumental uncertainties in the current, voltage and temperature values*, Solid-State Electronics **38** (11) pp.1937-1943

[6] Q.X. Jia, K. Ebihara and T. Ikegame (1995) *Analytical solution for solar cell model parameters from illuminated current-voltage characteristics*, Philosophical Magazine B **72** (4) pp.375-382

[7] J.C.H. Phang and D.S.H. Chan (1986) *A review of curve fitting error criteria for solar cell I-V characteristics*, Solar Cells **18** pp.1-12

[8] G. Stollwerk and J.R. Sites (1995) *Analysis of CdTe back-contact barriers*, Proceedings of 13th European Photovoltaic Solar Energy Conference, Nice.

[9] R.H. Bube *"Heterojunctions for Thin Film Solar Cells"* in *Solar Materials Science*, edited by L. E. Murr, (Academic Press Inc., New York, 1980)

[10] G. Stollwerk, *Quantitative separation of photon and back-contact losses in CdTe solar cells: Where have all the photons gone?* (Colorado State University M.Sc. thesis, 1995)

[11] B.E. McCandless and S.S. Hegedus (1991) *Influence of CdS window layers on thin film CdS/CdTe solar cell performance*, Proceedings of 22nd IEEE Photovoltaic Specialists Conference, Las Vegas. pp.967-972

[12] A. Rohatgi, S.A. Ringel, R. Sudharsanan and H.C. Chou (1992) *An improved understanding of efficiency limiting defects in polycrystalline CdTe/CdS solar cells*, AIP Conference Proceedings **268** (1) pp.243-249

[13] D.M. Oman, K.M. Dugan, J.L. Killian, V. Ceekala, C.S. Ferekides and D.L. Morel (1995) *Reduction of recombination current in CdTe/CdS solar cells*, Applied Physics Letters **67** (13) pp.1896-1898

[14] I.L. Eisgruber and J.R. Sites (1996) *Extraction of individual-cell photocurrents and shunt resistances in encapsulated modules using large-scale laser scanning*, Progress in Photovoltaics **4** pp.63-75

[15] J.S. Song and E.S. Yang (1985) *A study of the photovoltaic effect of a semiconductor grain boundary by a scanning laser beam*, Journal of Applied Physics **58** (8) pp.3129-3132

[16] I. Perichaud and S. Martinuzzi (1998) *Prediction of the behaviour of multicrystalline silicon wafer during processing steps by LBIC scan maps at 80 K*, Proceedings of 2nd World Conference on Photovoltaic Solar Energy Conversion, Vienna, pp.1290-1293

[17] D. Borchert, C. Wolffersdorf and W.R. Fahrner (1995) *A simple compact measurement set-up for the optical characterization of solar cells*, Proceedings of 13th European Photovoltaic Solar Energy Conference, Nice.

[18] A.J. Holland, *A scanning optical microscope study of semiconductors* (University of Oxford D.Phil. thesis, 1996)

[19] M. De Vittorio, R. Cingolani, M. Mazzer and D.B. Holt (1997) *Sub-micron characterization tool for fast investigation of defects and morphology of semiconductor materials*, Physics of Low-Dimensional Structures **11/12** pp.63-68

[20] S.A. Galloway, A.J. Holland, P.R. Wilshaw, A.W. Brinkman and K. Durose (1995) *Microscopic characterisation of CdS/CdTe thin film photovoltaic devices using scanning optical and electron beam injection techniques*, Proceedings of 13th European Photovoltaic Solar Energy Conference, Nice. Vol.2 pp.2072-2075

[21] S.A. Galloway, A.J. Holland and K. Durose (1996) *A study of CdS/CdTe thin film solar cells using beam injection techniques*, Journal of Crystal Growth **159** pp.925-929

[22] S.A. Galloway, A.W. Brinkman, K. K. Durose, P.R. Wilshaw and A.J. Holland (1996) *A study of the effects of post-deposition treatments on CdS/CdTe thin film solar cells using high resolution optical beam induced current*, Applied Physics Letters **68** (26) pp.3725-3727

[23] N. Magnea and J.L. Pautrat *"Luminescence of CdTe, CdZnTe and CdSeTe"* in *Properties of Narrow Gap Cadmium-Based Compounds*, Vol.10, edited by P. Capper, (INSPEC, London, 1994)

[24] D.P. Halliday, J.M. Eggleston and K. Durose (1998) *A photoluminescence study of polycrystalline thin-film CdTe/CdS solar cells*, Journal of Crystal Growth **186** pp.543-549

[25] D.P. Halliday, J.M. Eggleston and K. Durose (1998) *A study of the depth-dependence of photoluminescence from thin film CdS/CdTe solar cells using bevel etched samples*, Thin Solid Films **322** pp.314-318

[26] J.M. Eggleston, D.P. Halliday and K. Durose (1996) *Spectroscopic study on the effect of post-growth annealing of CdTe/CdS thin film photovoltaic devices*. Institute of Physics Conference Series **155** pp.441-444

[27] K. Akimoto, H. Okuyama, M. Ikeda and Y. Mori (1992) *Oxygen doping in CdTe, CdS and ZnS*, Journal of Crystal Growth **117** (1-4) pp.420-423

[28] K. Akimoto, H. Okuyama, M. Ikeda and Y. Mori (1992) *Isoelectronic oxygen in II-VI semiconductors*, Applied Physics Letters **60** (1) pp.91-93

[29] D.H. Levi, L.M. Woods, D.S. Albin, T.A. Gessert, D.W. Niles, A. Swartzlander, D.H. Rose, R.K. Ahrenkiel and P. Sheldon (1997) *Back contact effects on junction photoluminescence in CdTe/CdS solar cells*, Proceedings of 26th IEEE Photovoltaic Specialists Conference, Anaheim. pp.351-354

[30] J.I. Goldstein, D.E. Newbury, P. Echlin, D.C. Joy, A.D. Romig, C.E. Lyman, C. Fiori and E. Lifshin, *Scanning Electron Microscopy and X-Ray Microanalysis*, (Plenum Press, New York, 1992)

[31] A.B. Sproul, T. Puzzer and R.B. Bergmann (1998) *"High resolution EBIC imaging of polycrystalline silicon solar cells"*, Proceedings of 2nd World Conf. on Photovoltaic Solar Energy Conversion, Vienna, pp.1355-1358

[32] M. Aguilar, A.I. Oliva, C.-R. R and J.L. Peña (1997) *Observation of macro-terraces in cadmium telluride thin films*, Journal of Materials Science: Materials in Electronics **8** (2) pp.103-107

[33] R. Assumpção (1993) *Quantitative SEM EBIC characterization of defects in semiconductors*, Journal of Physics: Condensed Matter **5** (33A) pp.A403-A404

[34] R. Corkish, A.B. Sproul, T. Puzzer, P.P. Altermatt, G. Heiser and K.L. Luke (1998) *Quantitative analysis of electron-beam-induced-current profiles of grain boundaries in multicrystalline solar cells*, Proceedings of 2nd World Conference on Photovoltaic Solar Energy Conversion, Vienna, pp.1298-1301

[35] C. Donolato (1983) *Theory of beam induced current characterization of grain boundaries in polycrystalline solar cells*, Journal of Applied Physics **13** (3) pp.1314-1322

[36] C. Donolato (1994) *Reciprocity theorem for charge collection by a surface with finite collection velocity - application to grain-boundaries*, Journal of Applied Physics **76** (2) pp.959-966

[37] R.J. Tarento and Y. Marfaing (1992) *Analysis of the recombination velocity and of the electron-beam induced current and cathodoluminescence contrasts at a dislocation*, Journal of Applied Physics **71** (10) pp.4997-5003

[38] R. Sundaresan and D.E. Burk (1984) *Diffusion length and grain-boundary recombination velocity measurements with the scanning electron microscope in a finite polysilicon grain*, Solid-State Electronics **27** (2) pp.177-185

[39] J. McClure, C. Chung and V. Singh (1990) *Grain-boundary effects in the EBIC response of thin-film solar cells*, Solid State Communications **75** (3) pp.171-173

[40] C. Donolato (1982) *On the analysis of diffusion length measurements by SEM*, Solid-State Electronics **25** (11) pp.1077-1081

[41] R.H. Kenny, J.C. McClure and V.P. Singh (1988) *Electron beam induced currents in thin-film CdS-CdTe heterojunction cells*, Proceedings of 8th E.C. Photovoltaic Solar Energy Conference, Florence. Vol.II pp.1097-1101

[42] J.L. Maurice and Y. Marfaing (1991) *Theoretical-study of high injection effects in EBIC measurements of grain-boundary recombination velocity in silicon*, Journal De Physique IV **1** (C6) pp.77-82

[43] D.B. Holt *"The conductive mode"* in *SEM Microcharacterisation of Semiconductors*, edited by D. B. Holt and D. C. Joy, (Academic Press, London, 1989)

[44] P.A. Tove and W. Seibt (1967) *Plasma effects in semiconductor detectors*, Nuclear Instruments and Methods **51** pp.261-269

[45] H.J. Leamy (1982) *Charge collection scanning electron microscopy*, Journal of Applied Physics **53** (6) pp.R51

[46] M.M. Al-Jassim, F.S. Hasoon, K.M. Jones, B.M. Keyes, R.J. Matson and H.R. Moutinho (1993) *The morphology, microstructure and luminescent properties of CdS/CdTe Thin Film Solar Cells*, Proceedings of 23rd IEEE Photovoltaic Specialists Conference, Louisville. pp.459-465

[47] M.M. Al-Jassim, R.G. Dhere, K.M. Jones, F.S. Hasoon and P. Sheldon (1998) *The morphology, microstructure and luminescent properties of CdS/CdTe films*, Proceedings of 2nd World Conference on Photovoltaic Solar Energy Conversion, Vienna, pp.1063-1066

[48] J.A.C. Broekaert *"Atomic Emission Spectroscopy"* in *Glow Discharge Spectroscopies*, edited by R. K. Marcus, (Plenum Press, New York, 1993)

[49] I.M. Dharmadasa, M. Ives, J.S. Brooks, G.H. France and S.J. Brown (1995) *Application of glow discharge optical emission spectroscopy to study semiconductors and semiconductor devices*, Semiconductor Science and Technology **10** (3) pp.369-372

Chapter 4: Sample preparation

4.1 INTRODUCTION

The different deposition and processing techniques used for fabricating cadmium telluride solar cells can produce devices with significantly different characteristics. Results of studies carried out on a particular type of cell may not therefore be directly applicable to a device produced by another method. This chapter therefore examines in detail the fabrication steps for the cells examined in this work

4.2 FABRICATION

The solar cells used for this study were supplied by ANTEC GmbH, a commercial company based in Kelkheim, Germany. The cells were produced using research equipment prior to the completion of a full-scale industrial production line. Various differently fabricated and treated custom-made samples were provided to allow studies to be made of the effects of post-deposition treatments and the presence or absence of the CdS layer. Some of the post-deposition treatments were applied in Durham.

4.2.1 Deposition

All the cells studied were deposited on a substrate of soda-lime glass coated with a bilayer of ITO and SnO_2, supplied by Donnelley Applied Labs. The indium-doped tin oxide has a higher conductivity, required to reduce the sheet resistance of the front contact, whereas the purpose of the undoped tin oxide layer is to reduce the diffusion of indium atoms from the ITO layer into the rest of the cell. It also serves to reduce electrical losses due to any pinholes which may be present.

Both the CdS and CdTe layers were deposited using the close-spaced sublimation method (see section 2.4.1), with the substrate heated to a temperature of 500°C. The sulphide layer was 100nm thick, whilst the telluride was of 8-9μm in thickness depending on the sample. In addition, control cells were also made without a CdS layer, with the usual CdTe layer being deposited directly onto the TCO.

4.2.2 Post-deposition treatment

The importance of post-deposition processing on the performance of CdTe/CdS solar cells was described in Section 2.4.2. In order to examine the effects of this processing, two sets of samples were prepared:

Set 1 The samples used for the luminescence and EBIC measurements were supplied by the manufacturers unprocessed. From these, three differently treated devices were prepared.

1) As deposited; *i.e.* no further treatment was carried out.
2) Heat treated; the sample was annealed in air for 30 minutes at 400°C.
3) Chloride treated; a 60nm layer of $CdCl_2$ deposited on the CdTe surface by evaporation, followed by heat treatment as above. Residuals were then removed using boiling de-ionised water.

In addition, a further control sample was produced, in order to identify the effects of the sulphide layer in the cell:

4) CdS-free; a sample without the CdS layer, but chloride/heat treated as above.

Set 2 The samples used for the OBIC measurements were provided by ANTEC already processed. Each had been chloride treated and annealed as above, but using the following different thicknesses of $CdCl_2$:

1) 15nm
2) 30nm
3) 60nm
4) 120nm

4.2.3 Contacting

After treatment, back contacts were applied to the cells required for electrical measurements. The cells were firstly etched for around 5s in a 0.03% solution of bromine in methanol. This gave a tellurium rich p^+-type layer at the back surface of the cadmium telluride (see Equation 4.1). After rinsing with methanol, the samples were then immediately placed under vacuum, before the evaporation of a ~60nm layer of gold. The cells were not heated during the deposition of this layer. Electrical contacts were made to the TCO and the gold to provide connection to the measurement systems.

4.2.4 Device parameters

After completion of the cells, *I-V* characterisation was carried out for each one. This was to allow the later correlation of measured materials properties with the photovoltaic performance of the devices. The cells treated in Durham were measured using equipment described in Section 3.2.1, and the results are shown in Table 4-I.

Sample	J_{sc} (mAcm^{-2})	V_{oc} (V)	FF (%)	η (%)
Untreated	19.2	0.62	30.8	3.6
Heat-treated	15.3	0.58	42.8	3.7
$CdCl_2$-treated	27.8	0.72	60.7	12.2
CdS-free	23.4	0.22	46.5	2.4

Table 4-I Measured I-V parameters for the four cells used in the EBIC, CL and PL experiments. The J_{sc} values are subject to an error due to the use of a light source of uncalibrated intensity and spectrum, and this data should therefore be used for relative comparison only.

These cells show the untreated cell to have a relatively high conversion efficiency of 3.6%, with little improvement observed after annealing in air. This is due to the relatively high temperatures used during the initial deposition of the CdS and CdTe layers. The cadmium chloride deposition followed by annealing results in a considerable improvement in all *I-V* parameters. The similarly treated CdS-free control sample exhibits a significantly lower performance, with the open circuit voltage particularly affected.

The cells treated by ANTEC using varying thicknesses of $CdCl_2$ were characterised by the manufacturers. The results shown in Table 4-II were supplied with the devices, and show an improvement of all device parameters up to a chloride thickness of 60nm, with little change thereafter.

$CdCl_2$ layer (nm)	J_{SC} ($mAcm^{-2}$)	V_{OC} (V)	FF (%)	η (%)
15	17.2	0.720	57.3	7.1
30	19.0	0.775	65.4	9.6
60	19.3	0.794	66.1	10.1
120	19.7	0.793	64.3	10.1

Table 4-II Measured *I-V* parameters for the four cells used in the OBIC experiments. This data was measured by the manufacturer, and is not subject to the errors of Table 4-II.

4.3 PREPARATION OF THE CELLS FOR EXPERIMENTS

After completion of the fabrication steps, further sample preparation was required to carry out specific measurements. Figure 4.1 shows the three distinct cell geometries required.

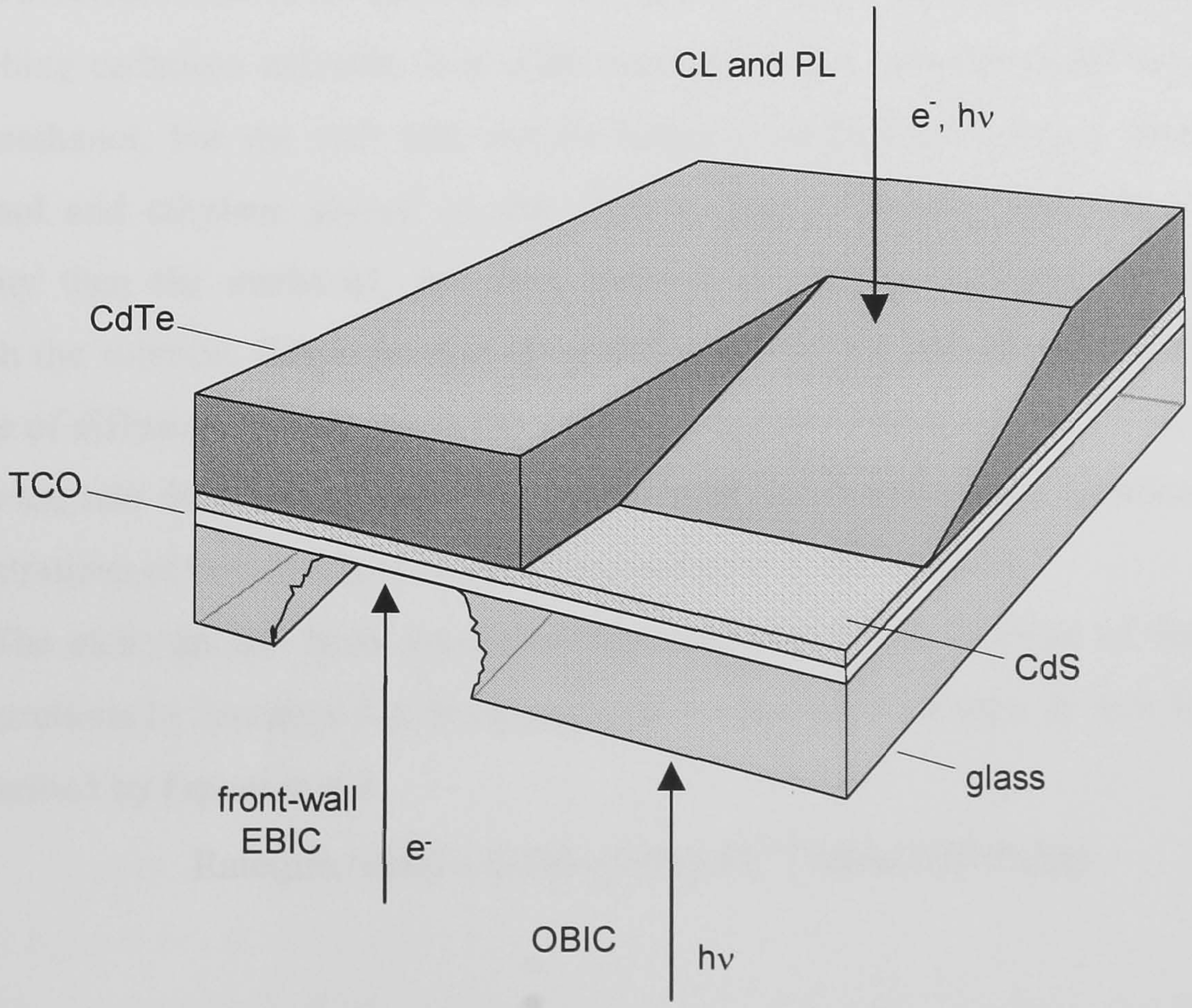

Figure 4.1 The sample geometries used for the various experiments in this work, showing the necessary cell preparation.

For the luminescence techniques (Chapter 8) to be carried out as a function of depth through the cell, a shallow bevelled plane through the cell was needed. OBIC measurements (see Chapter 5) could be carried out via the glass substrate, and these samples required no further preparation. The corresponding EBIC experiment (Chapters 6 and 7), however, necessitated the removal of this glass. Each of these preparative steps is outlined in the following sections.

4.3.1 Bevel etching

The luminescence techniques later described in Chapter 8 require electron and light beams to directly probe the material as a function of position through the solar cell. This was achieved by exposing an oblique plane through the sample, leaving an inclined, or bevelled, surface. This is shown in Figure 4.1. Such bevels have been fabricated elsewhere by the use of lapping techniques, but were made in this work by exposing parts of the sample to etching solutions for varying times, as described below.

The bromine/methanol etchant Bromine is widely used as an oxidising agent for etching cadmium telluride. It is often used in various concentrations in solution with methanol, but the etch rate can be better controlled by using a mixture of methanol and ethylene glycol† as the solvent. The ethylene glycol has a higher viscosity than the methanol, and thus controls the rate of diffusion of bromine through the solution. Since the rate of oxidation of Te^{2-} by Br^{0} is much faster than the rate of diffusion of bromine in the solution [1], this diffusion to the CdTe surface acts as the rate determining step. The overall etch rate is therefore a function of the concentrations of both the bromine and the methanol in the solution.

The etch rate has been experimentally determined as a function of these two concentrations by Jennings [2], using response surface methodology. It was found to be described by Equation 4.3.

$$\text{Rate}(\mu\text{m}/\text{min}) = 0.163 + 1.99\times10^{-4}[\%\text{MeOH}]^{2}[\%\text{Br}] \tag{4.3}$$

---

† Also known as 1,2-ethanediol, chemical structure $HO\text{-}CH_2\text{-}CH_2\text{-}OH$.

This rate was evaluated out for the (111)A face of a bulk CdTe crystal, and it was found that the etch rate for the polycrystalline samples used in this work was approximately an order of magnitude higher. Etchant concentrations used here were typically 0.5% bromine in a solvent mixture of methanol and ethylene glycol in equal volume.

Etching apparatus Figure 4.2 shows the apparatus used for the bevel etching procedure.

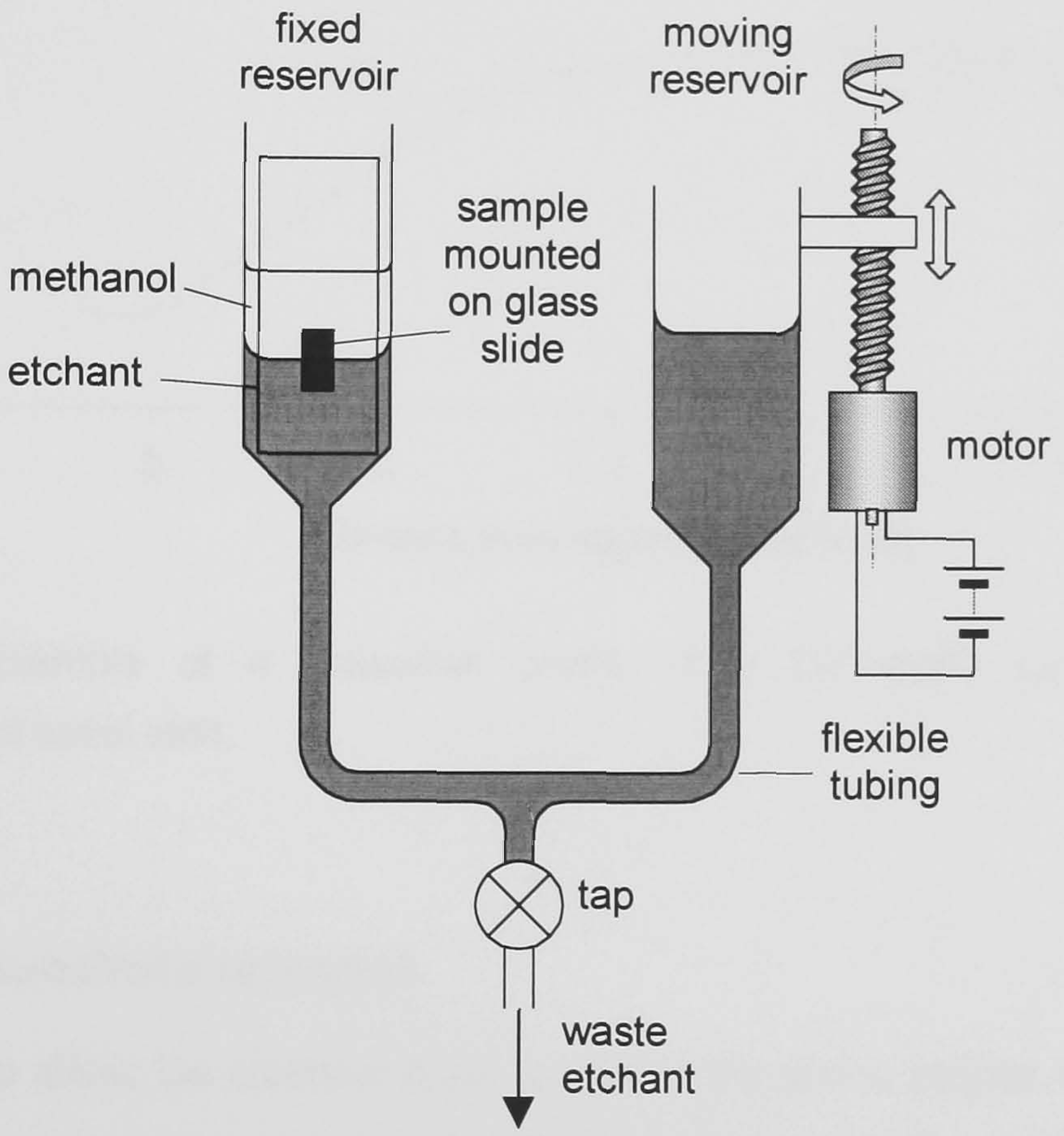

Figure 4.2 Apparatus used for bevel etching the solar cells using bromine/methanol-ethylene glycol.

The etchant was placed in a pair of connected reservoirs, one fixed and the other vertically movable. The position of the movable reservoir was controlled using an electric motor and a lead screw, as shown. A layer of methanol was floated on top of the etchant in the fixed reservoir, and the sample was placed in this side. Raising the movable reservoir caused the methanol/etchant interface to rise in turn, immersing an increasing proportion of the sample.

The composition of the etchant and speed of the reservoir were adjusted such that the entire thickness of the CdTe could be etched within a maximum of 20 minutes. After this time diffusion of bromine from the etchant to the methanol caused the interface to deteriorate, reducing control over the bevel shape.

The cross-sectional profiles of the resulting bevels were measured using a Tencor Instruments *Alpha-Step 200* step profiler. An example of such a profile is shown in Figure 4.3.

Figure 4.3 Example of a measured profile of a CdTe/CdS solar cell after a bromine/methanol bevel etch.

4.3.2 Substrate removal

In order to allow the electron beam access to the active region of the solar cell, some samples were prepared by removing the glass substrate. These devices are referred to as *front-wall* samples throughout this thesis; however, it should be noted that this term has been used in the literature with a different meaning. This alternative definition states that in a front-wall solar cell the light enters via the lower bandgap semiconductor (in this case CdTe), by comparison with a back-wall device where the light impinges upon the wide bandgap (CdS) side [3]. This nomenclature has been avoided in this work, and the front of the cell is assumed to be the side illuminated under normal device operation.

The glass removal was carried out after all of the necessary deposition, treatment and contacting had been completed. Figure 4.4 shows the steps involved in removing the substrate, which involved both mechanical and chemical processes.

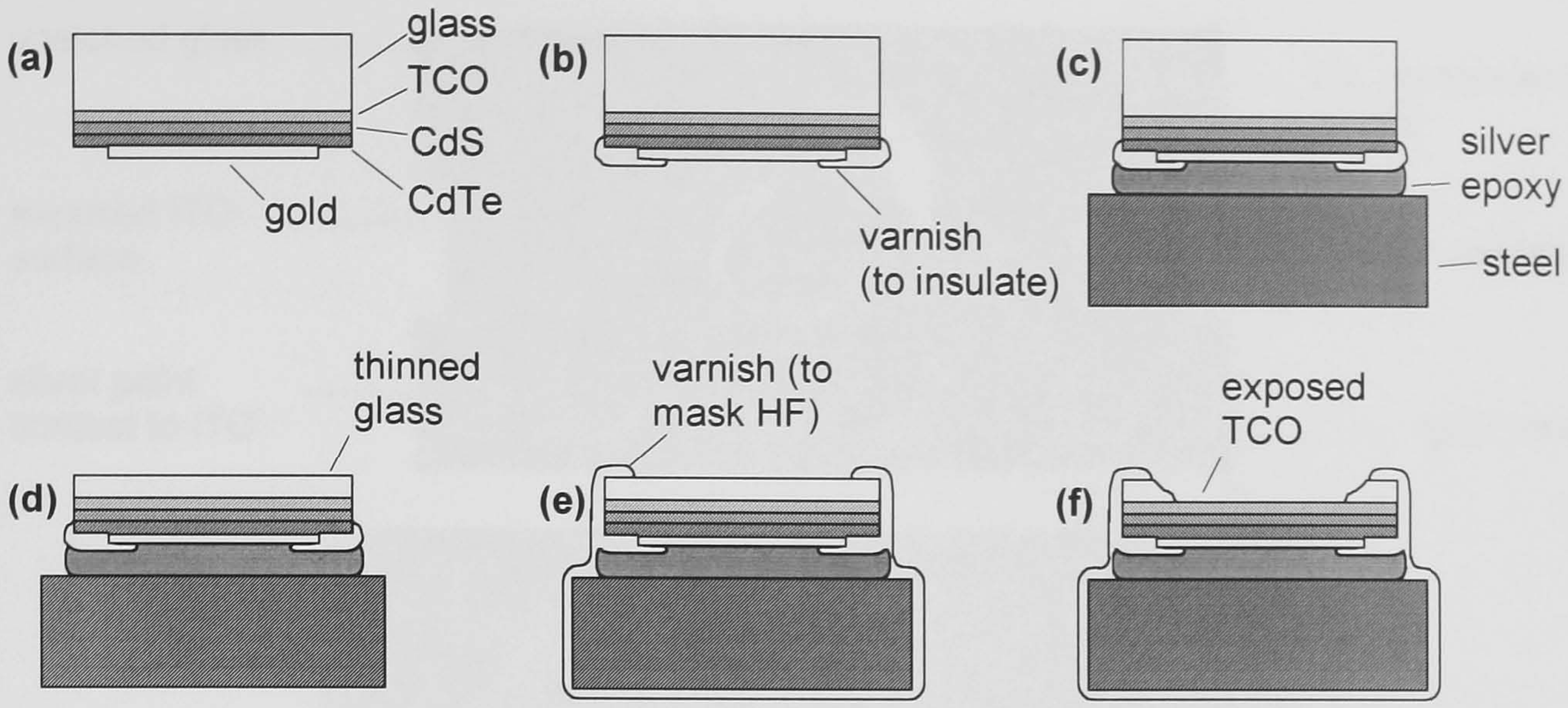

Figure 4.4 Preparation steps used to remove glass substrate for front wall EBIC measurements.

Mechanical polishing The sample was first polished mechanically to remove the major part of the glass thickness. This was achieved by first mounting the sample on a rigid steel disc, fixing the gold-contacted side to the steel using electrically-conductive silver-loaded epoxy resin (Figures 4.3a-c). Areas of exposed CdS and TCO were insulated from the disc using Lacomit varnish. A polishing machine with 17μm grit was then used to reduce the thickness of the glass substrate to the order of 100μm (Figure 4.4d).

Chemical etching All areas of the solar cell except the glass were then masked off (Figure 4.4e), and the sample was immersed in a 40% solution of hydrofluoric acid. The etching time used was between 15 and 30 minutes, depending on the thickness and mechanical integrity of the remaining glass. After etching, the HF left a clean and smooth surface (Figure 4.4f); this was assumed to be the former ITO/glass interface, with the ITO acting as an etch-stop layer.

In order to carry out EBIC, electrical contacts were made to the ITO surface and the steel block using silver paint. A photograph of the completed sample is shown in Figure 4.5.

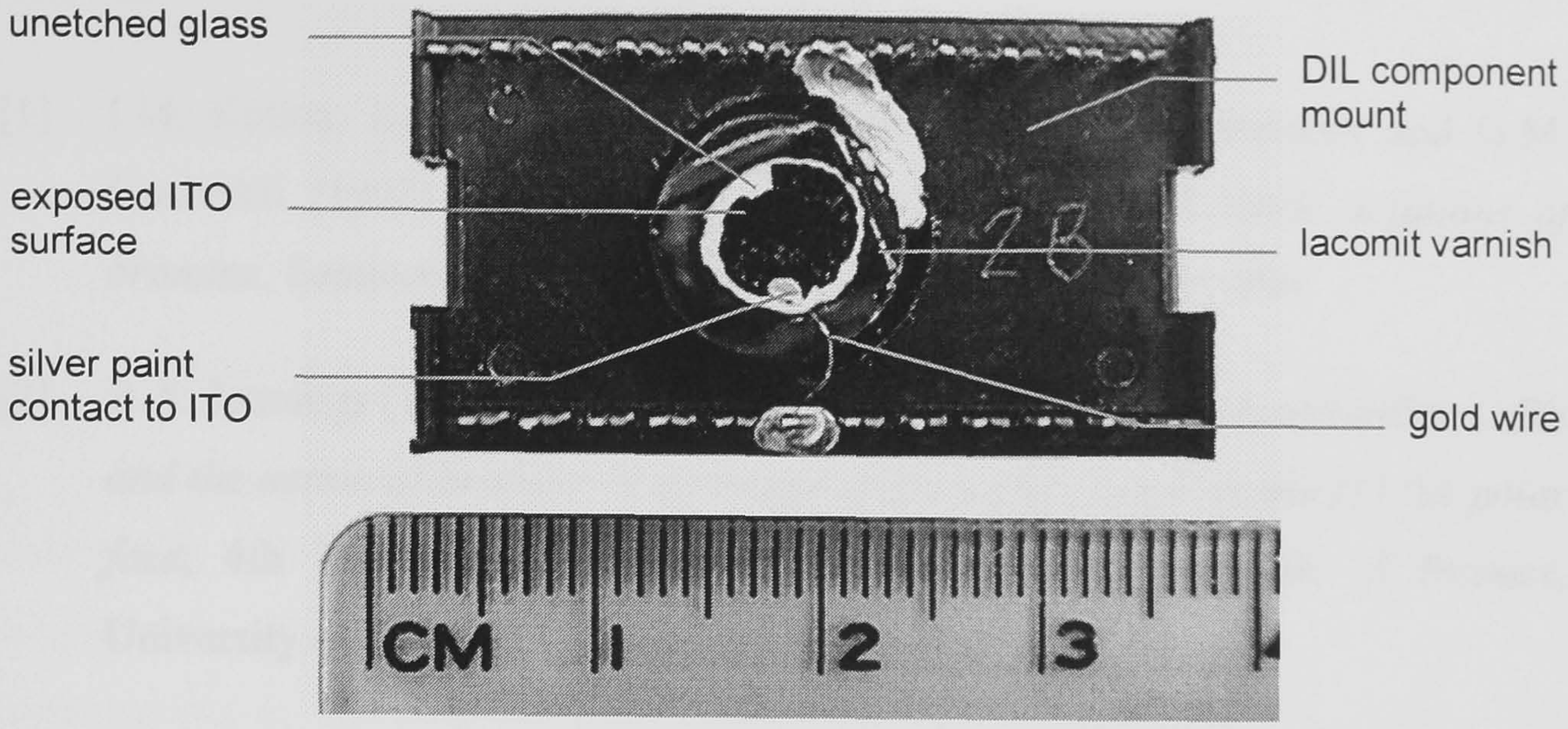

Figure 4.5 Photograph showing the plan view of a solar cell after removal of the glass substrate, contacted and mounted for SEM-EBIC analysis.

4.4 STORAGE

After preparation, the samples were stored in a moisture-free environment pending the measurements. This ensured that degradation did not occur due to environmental conditions. The one exception to this was the set of samples prepared for the OBIC experiments, which were exposed to room conditions for some weeks before the measurements were carried out. The resulting deterioration in the cell performances is described in Section 5.4.

4.5 SUMMARY

The various preparation methods outlined above were used to produce a variety of different devices, on which comparative studies could then be carried out. These include investigations into the effect of the $CdCl_2$/annealing treatment, and of the presence of the CdS layer. Various techniques have also been used to expose regions of the cell not usually accessible to beam experiments, allowing novel depth-dependent and front-wall studies to be carried out. These techniques are described in the following four chapters.

REFERENCES FOR CHAPTER 4

[1] I.M. Kotina, L.M. Tukhkonen, G.V. Patsekina, A.V. Shchukarev and G.M. Gusinskii (1998) *Study of CdTe etching process in alcoholic solutions of bromine*, Semiconductor Science and Technology **13** pp.890-894

[2] B.A. Jennings (1995) *Structural defects occurring in bulk polycrystalline CdTe and the action of bromine in methanol/ethyleneglycol etch on the (111)A polar face*, 4th Year Undergraduate Research Project, Department of Physics, University of Durham

[3] L.L. Kazmerski *"Introduction to Photovoltaics: Physics, Materials, and Technology"* in *Solar Materials Science*, edited by L. E. Murr, (Academic Press Inc., New York, 1980)

Chapter 5: Optical beam-induced current measurements

5.1 INTRODUCTION

In order to determine the effect of polycrystallinity on the performance of the solar cells, it is desirable to directly examine the electrical properties of the grain boundaries in the CdTe. This cannot be achieved using the conventional solar cell characterisation methods (such as *I-V* analysis and spectral response), and microscopic beam techniques more often associated with the analysis of defects in semiconductors must be used. The OBIC method, described in detail in Section 3.3, is capable of resolving features on the same scale as grains; whether the resolution of the technique is sufficient to also examine the grain boundaries depends on the dimensions of the light probe, and hence on the optics used. This chapter describes the results of applying this technique to CdTe/CdS devices.

5.2 EXPERIMENTAL DETAILS

5.2.1 Samples examined

The cells studied in this experiment were those treated with layers of $CdCl_2$ of varying thickness (15, 30, 60 and 120nm) followed by annealing in air. Details of the deposition and processing of these devices are given in Section 4.2, and the measured *I-V* parameters are shown in Table 4-II. After contacting, no further preparation of the samples was required, as the OBIC measurements are carried out with the device intact.

5.2.2 Scanning optical microscope

The scanning optical microscope (SOM) used for this work was constructed at Oxford University by Holland [1], and was designed specifically for use in the photocurrent mode. Figure 5.1 shows a schematic diagram of the optical arrangement used.

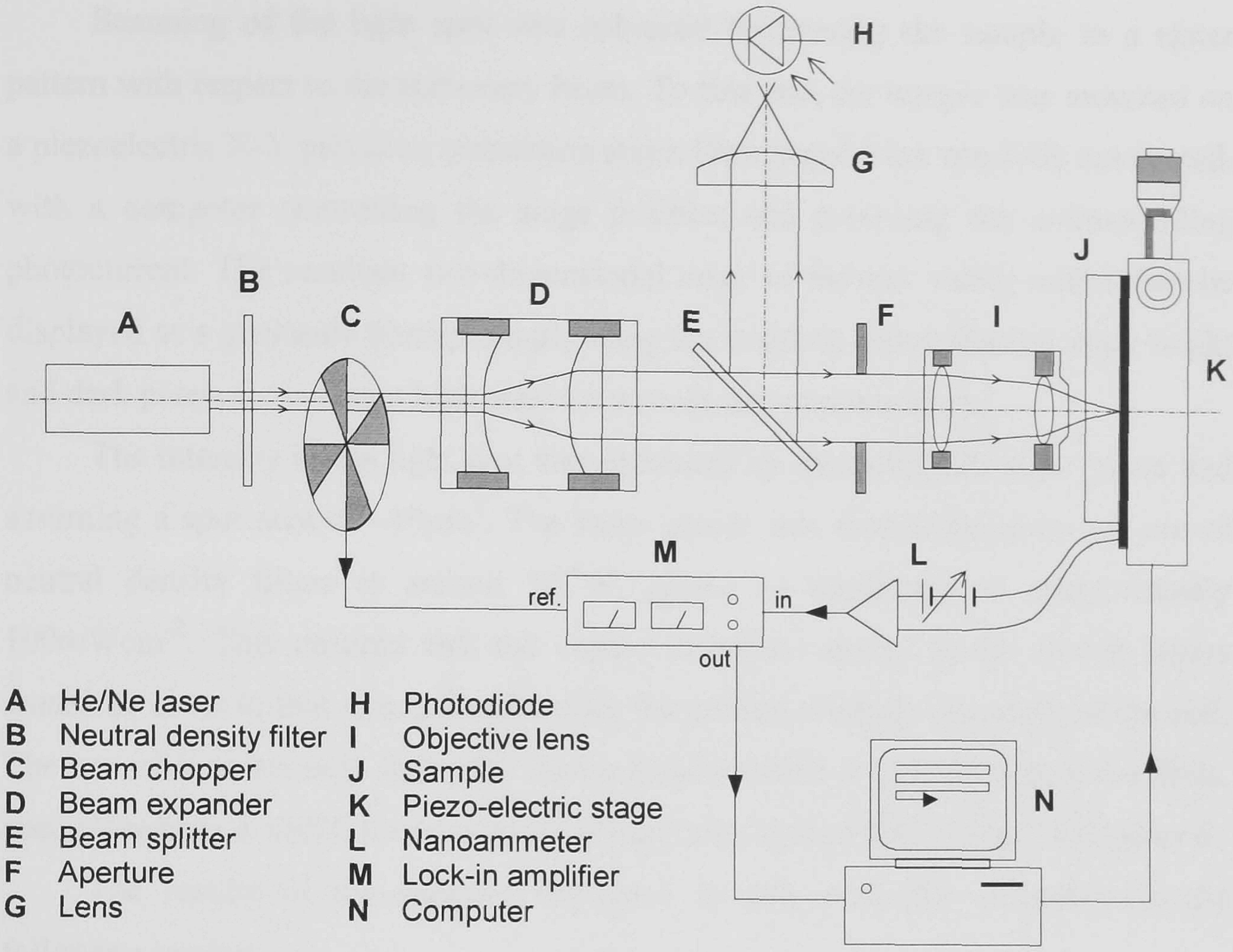

Figure 5.1 Schematic arrangement of optical components which comprise the scanning optical microscope.

A low power He/Ne laser (λ=632.8nm) was used as the light source and was chopped to allow lock-in signal detection to be used. The narrow beam was then expanded to fill the objective lens, in order to reduce divergence and minimise the spot size. A long focal length microscope objective was used to focus the beam through the glass substrate of the sample onto the active layers. By considering the numerical aperture of the objective, and the spatial resolution of the OBIC images, the diameter of the light spot was estimated to be ~3µm. The induced current from the cell was amplified using a high sensitivity current to voltage converter, and the output of this was passed to the phase-sensitive detector. Measurements could be taken in both short-circuit mode and with the application of an external bias voltage.

The reflected light from the sample was monitored using a beam splitter and a germanium *p-i-n* photodiode. This was used to aid focusing and to monitor the optical power of the light falling on to the sample.

Scanning of the light spot was achieved by moving the sample in a raster pattern with respect to the stationary beam. To this end, the sample was mounted on a piezoelectric X-Y precision translation stage. Data acquisition was fully automated, with a computer controlling the stage position and recording the corresponding photocurrent. The resultant two-dimensional array of current values could then be displayed as a greyscale bitmap image, using the standard convention of using bright and dark pixels to represent high and low current values respectively.

The intensity of the light spot was estimated by measuring the light power and assuming a spot area of ~10μm^2. The beam power was then adjusted by the use of neutral density filters to around 10^{-8}W, giving an irradiance of approximately 100mWcm^{-2}. This ensured that the carrier injection density in the device layers would be close to that encountered during the normal working operation of the cell. The use of low intensity light also avoided the possibility of high injection effects, seen elsewhere in OBIC measurements [2] and also in the EBIC results of Chapter 6.

The results of the samples examined in this study are presented in the following section.

5.3 OBIC RESULTS

OBIC images were obtained for each of the four samples, under applied voltages of between 2V reverse bias and 0.5V forward bias. This effectively yielded spatially resolved illuminated *I-V* characteristics. For clarity, each of the OBIC images presented has been individually adjusted so that mid-grey corresponds to the mean current value of the image. To allow direct comparison of the OBIC contrast between differently treated cells and different bias settings, however, the full-scale contrast of each image is the same at 100nA. Thus black and white correspond to 50nA below and above the mean current respectively.

Figure 5.2 shows the OBIC results for the sample treated with a 15nm thick layer of $CdCl_2$.

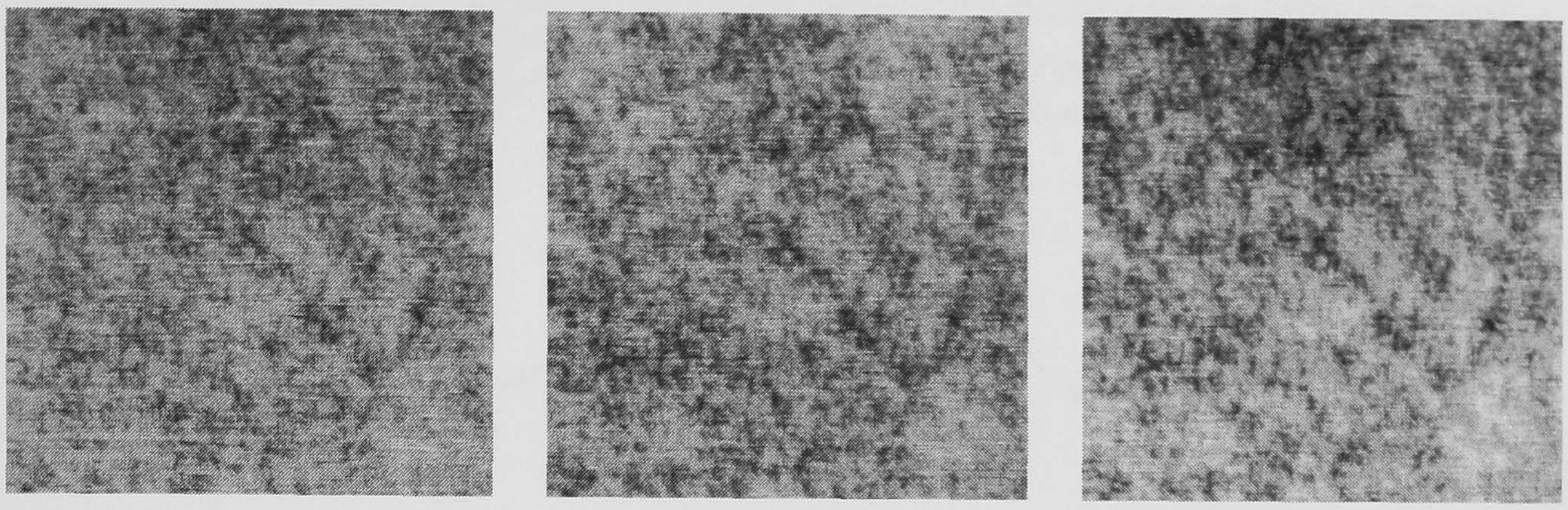

(a) 2V reverse bias **(b)** 1.5V reverse bias **(c)** 1V reverse bias

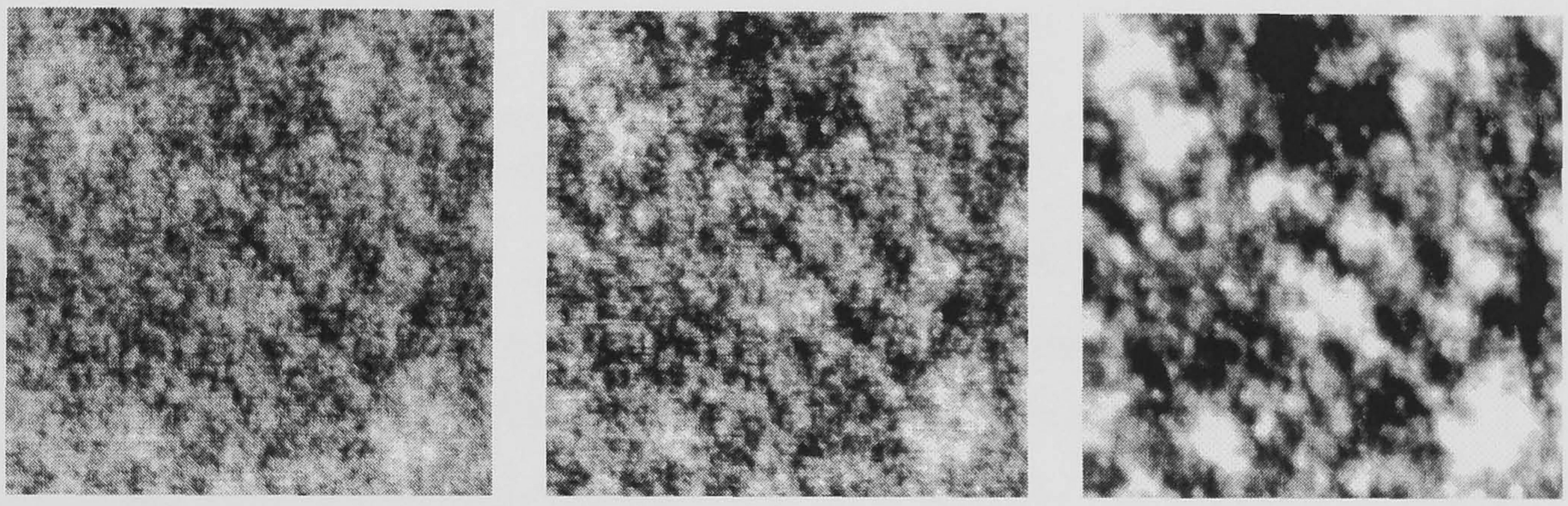

(d) 0.5V reverse bias **(e)** 0V bias **(f)** 0.5V forward bias

50μm

Figure 5.2 OBIC images at different bias voltages for a cell treated with a 15nm layer of $CdCl_2$. Full-scale black-white contrast corresponds to a variation in current of 100nA

These images show some OBIC contrast features on a scale of ~5-10μm, consistent with the size of CdTe grains observed in secondary electron micrographs of similar devices. Inhomogeneity is also seen on a larger scale (~50μm), indicating that grains are grouped into areas of good and poor collection. Application of a reverse bias can be seen to result in a marked decrease in OBIC contrast; this is despite an increase in the overall OBIC signal level, which may be seen in the corresponding linescans in Figure 5.3.

The variation with voltage of individual features from these linescans are plotted in Figure 5.4. This compares *I-V* curves for pixels corresponding to a peak in the linescans (denoted "good area" on the graph) and a trough ("poor area"), and also shows the mean for the whole linescan.

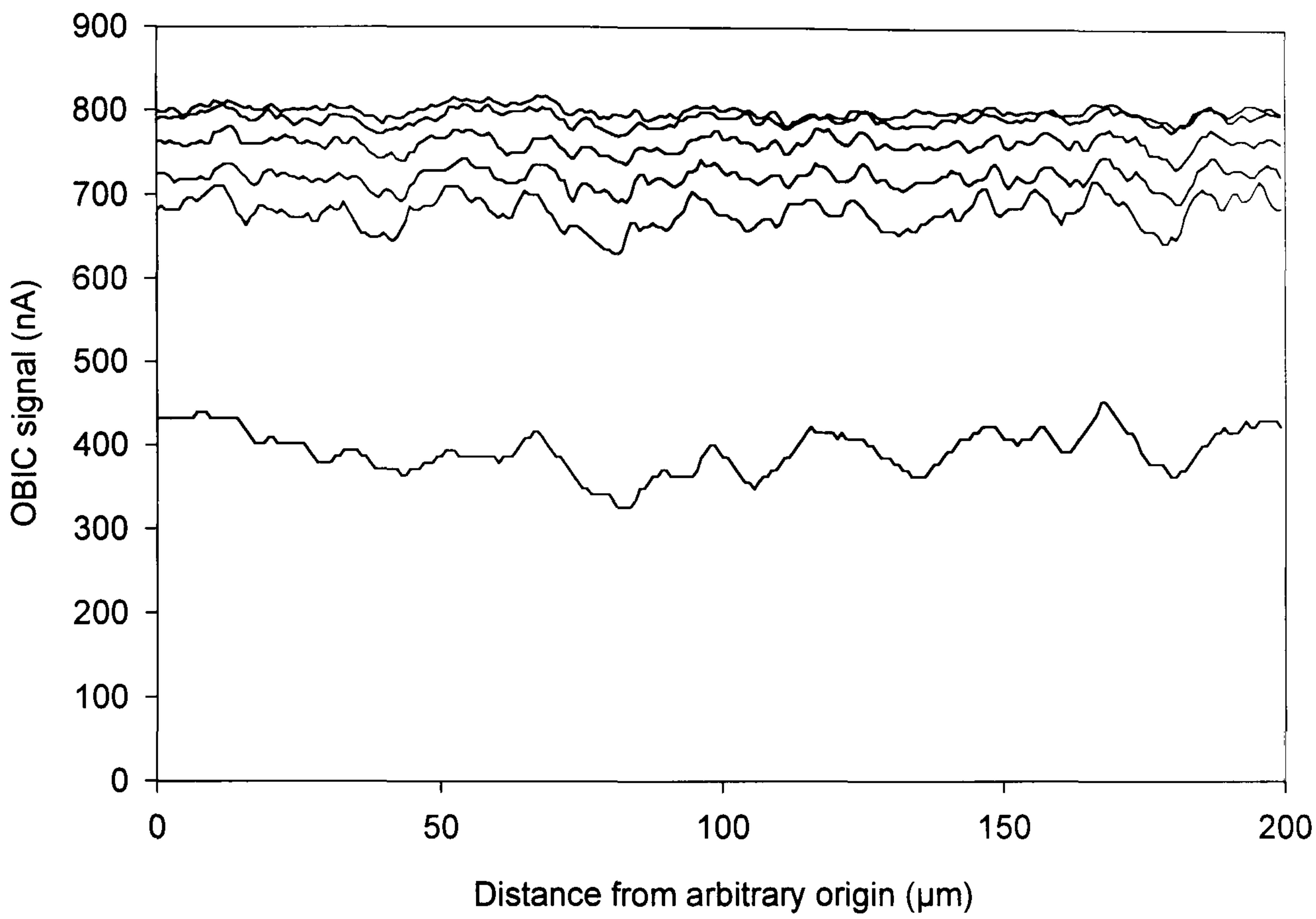

Figure 5.3 Linescans taken from each of the OBIC images in Figure 5.2 (15nm $CdCl_2$), with bias voltages of (from top to bottom) -2V, -1.5V, -1V, -0.5V, 0V and +0.5 V.

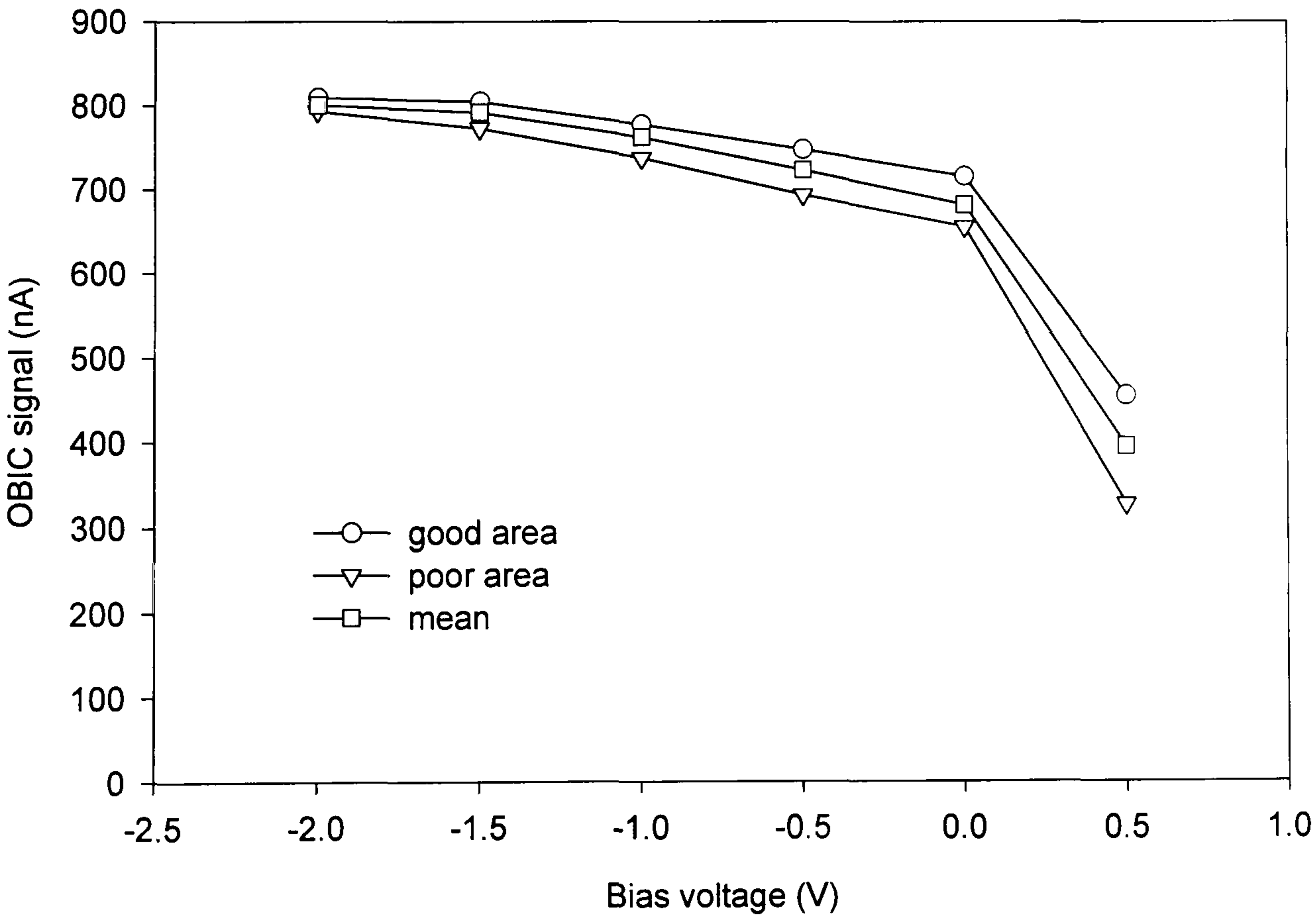

Figure 5.4 Comparison of OBIC values *versus* bias voltage for areas of good and poor collection for the cell treated with 15nm of $CdCl_2$. Also shown is the variation in mean OBIC.

Figure 5.5 shows the OBIC results for the sample treated with a 30nm thick layer of $CdCl_2$.

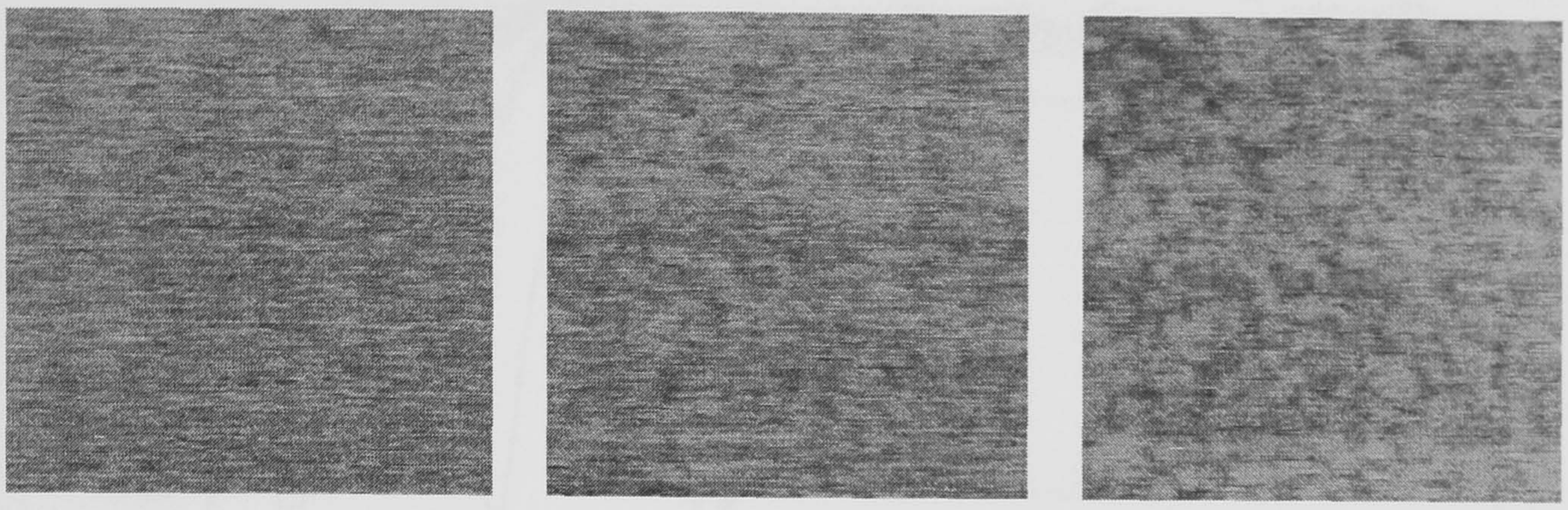

(a) 2V reverse bias **(b)** 1.5V reverse bias **(c)** 1V reverse bias

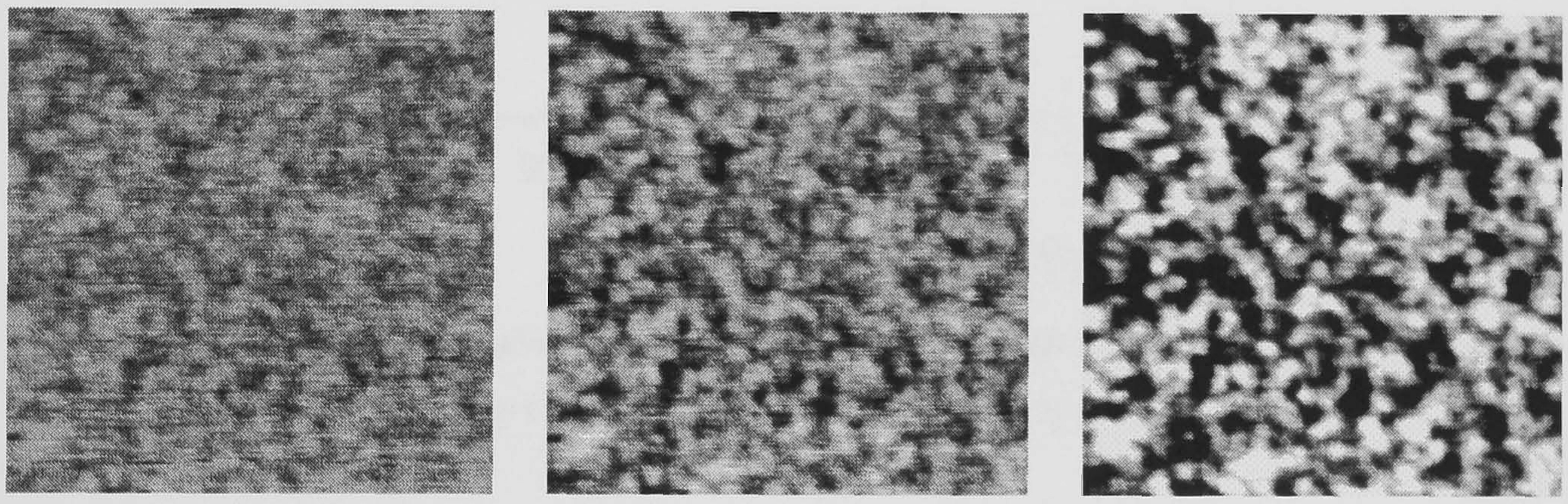

(d) 0.5V reverse bias **(e)** 0V bias **(f)** 0.5V forward bias

50μm

Figure 5.5 OBIC images at different bias voltages for a CdTe/CdS solar cell treated with a 30nm layer of $CdCl_2$.

At short circuit and forward bias (Figures 5.5e and f) these results show a granular variation similar in both magnitude and spatial scale to the 15nm treated cell. However, less large scale inhomogeneity is observed. At large reverse bias values (*e.g.* Figure 5.5a), the OBIC response shows greater uniformity than the previous sample. The overall OBIC signal can be seen to have increased with respect to the 15nm treated device, scaling approximately as expected from the I-V results of Table 4-II.

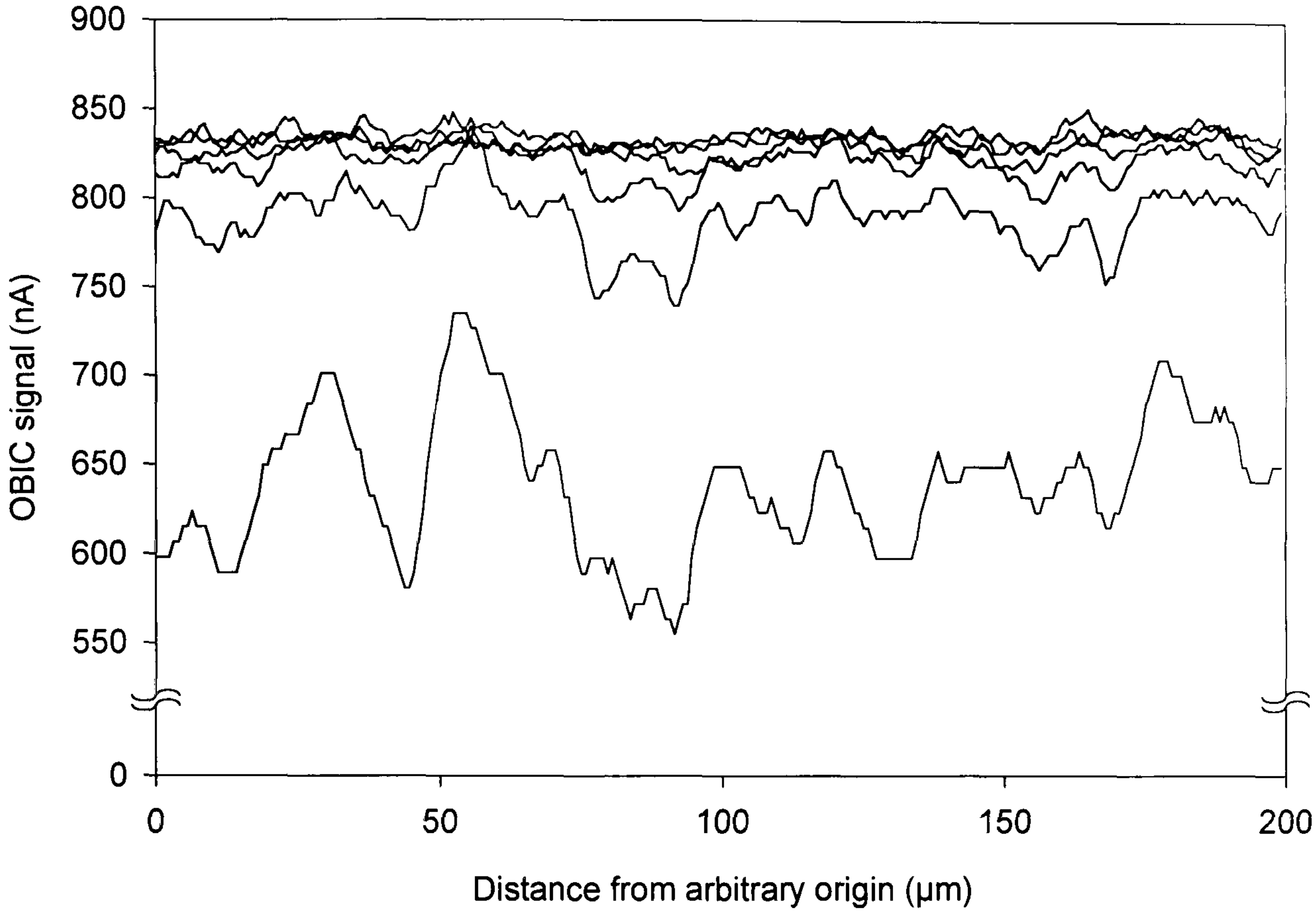

Figure 5.6 OBIC linescans taken from each of the OBIC images in Figure 5.5 (30nm $CdCl_2$), with bias voltages of (from top to bottom) -2V, -1.5V, -1V, -0.5V, 0V and +0.5 V.

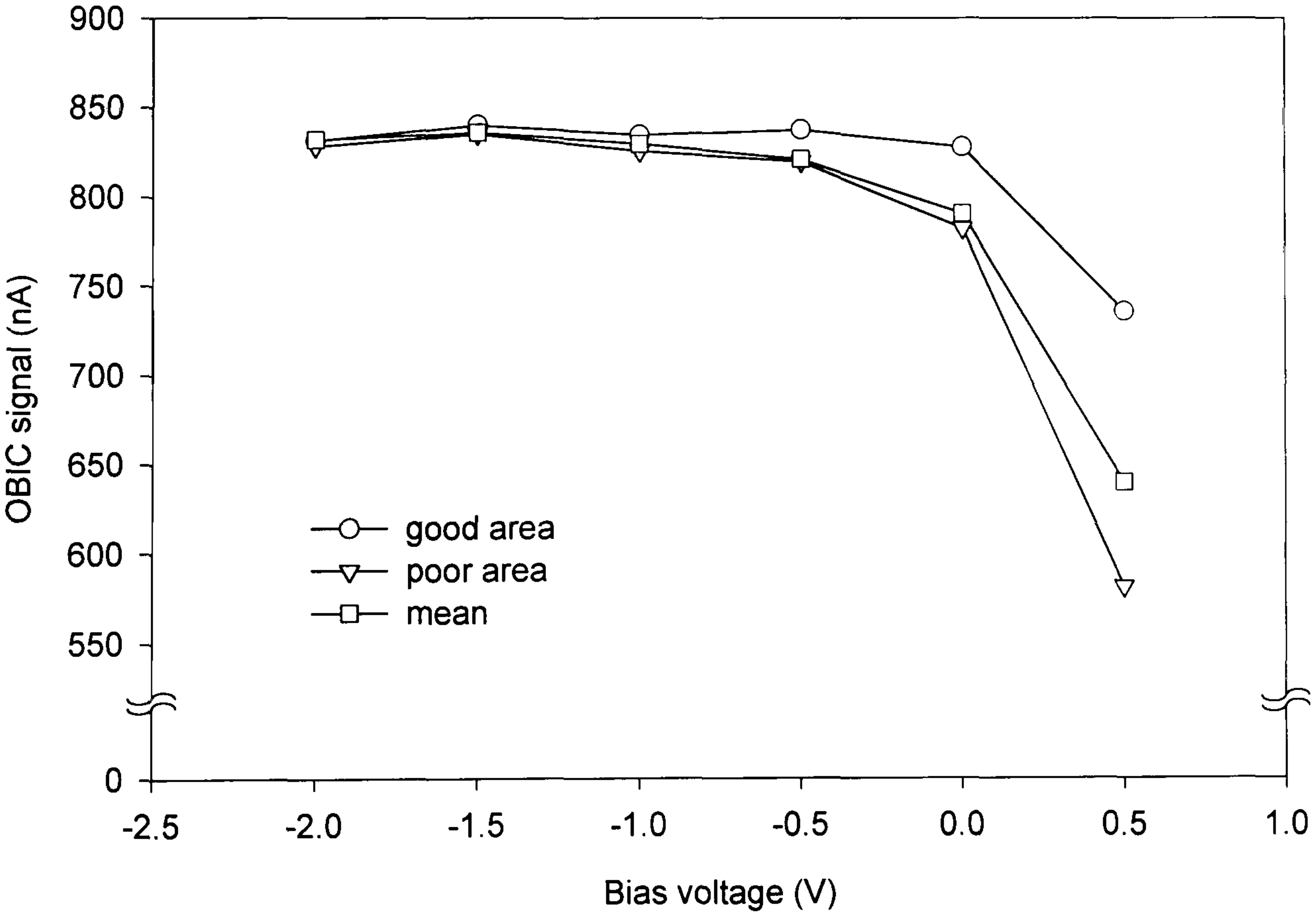

Figure 5.7 Comparison of OBIC values *versus* bias voltage for areas of good and poor collection for the cell treated with 30nm of $CdCl_2$. Also shown is the variation in mean OBIC.

Figures 5.8-5.10 show the OBIC results for the sample treated with a 60nm thick layer of $CdCl_2$.

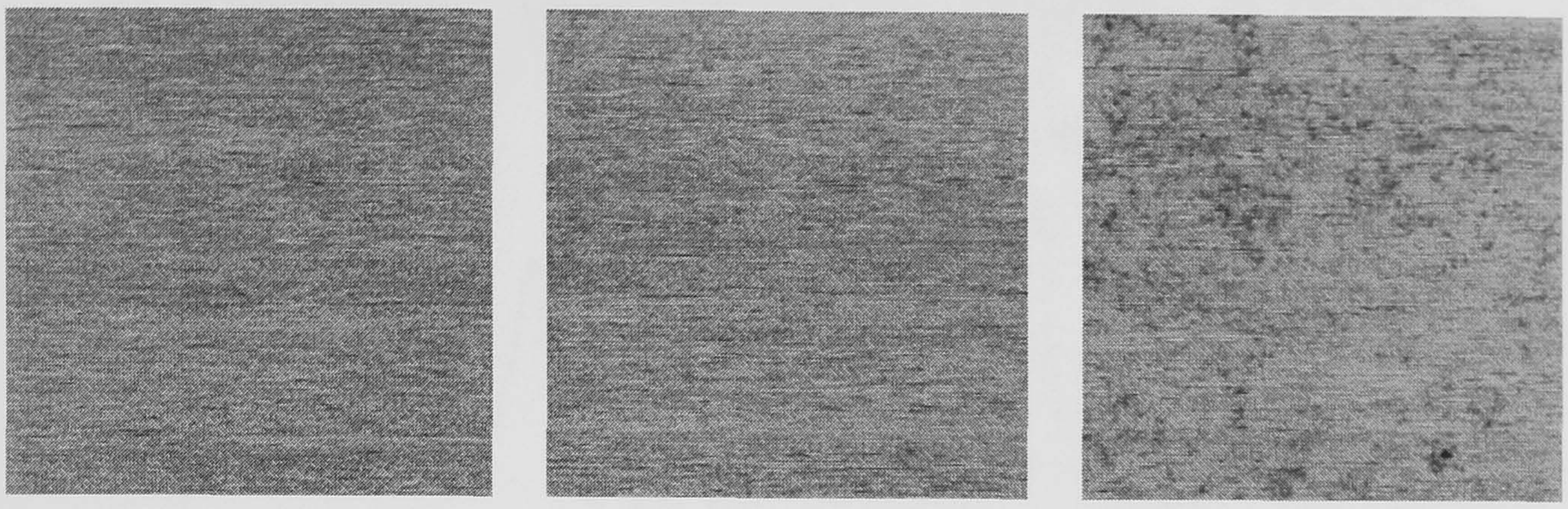

(a) 2V reverse bias **(b)** 1.5V reverse bias **(c)** 1V reverse bias

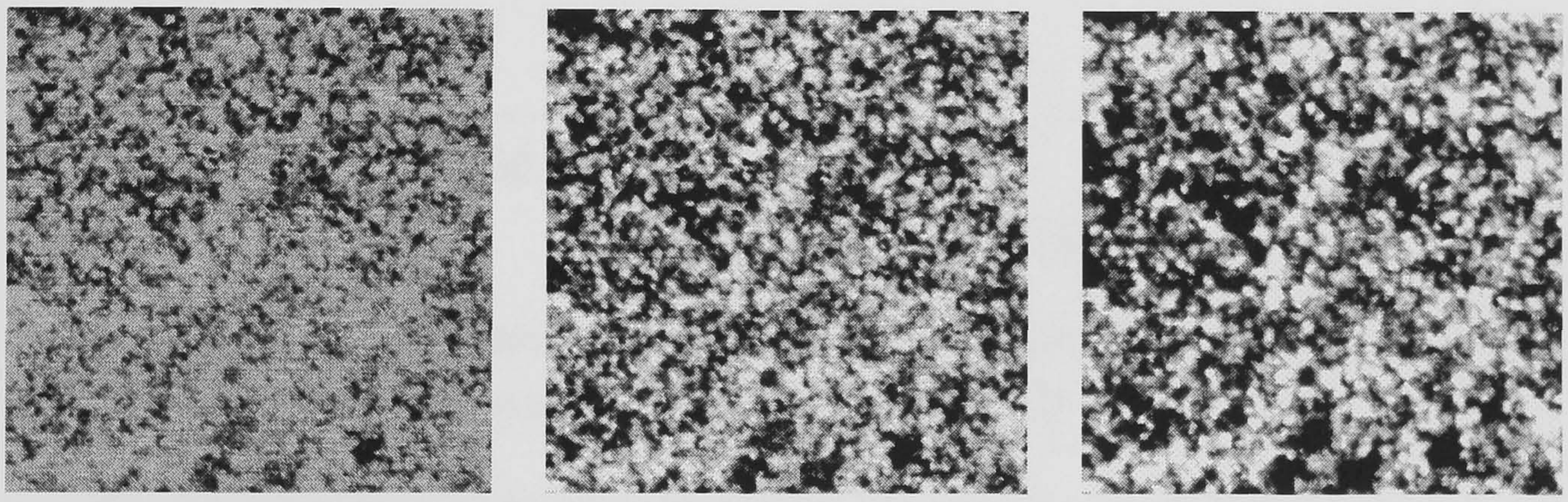

(d) 0.5V reverse bias **(e)** 0V bias **(f)** 0.5V forward bias

Figure 5.8 OBIC images at different bias voltages for a CdTe/CdS solar cell treated with a 60nm layer of $CdCl_2$.

These results show little change in the homogeneity of the device compared to the previous samples. The graph of the overall OBIC *versus* bias voltage shows an increase in signal level, again scaling approximately as predicted by the cell's *I-V* characteristics.

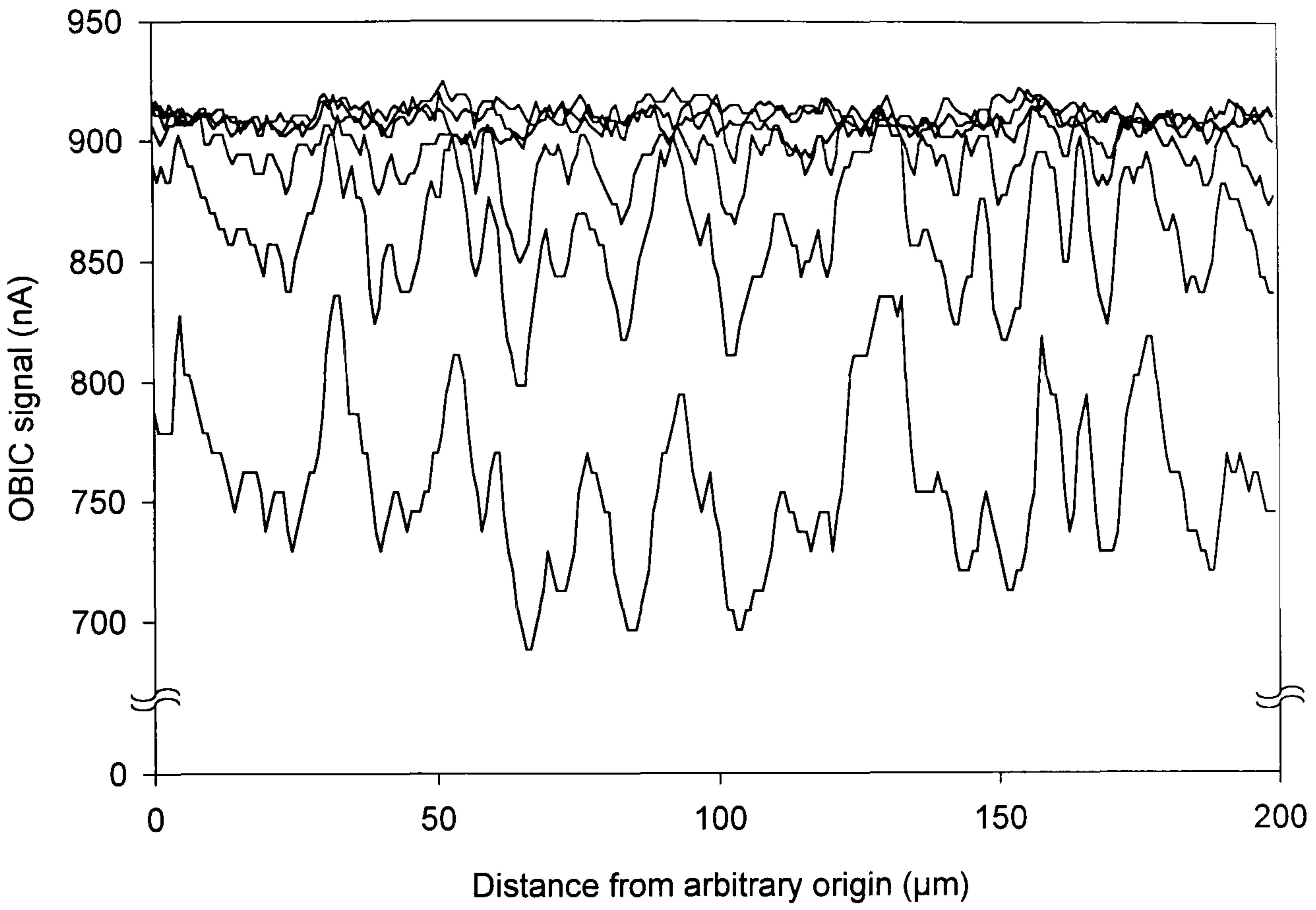

Figure 5.9 OBIC linescans taken from each of the OBIC images in Figure 5.8 (60nm $CdCl_2$), with bias voltages of (from top to bottom) -2V, -1.5V, -1V, -0.5V, 0V and +0.5 V.

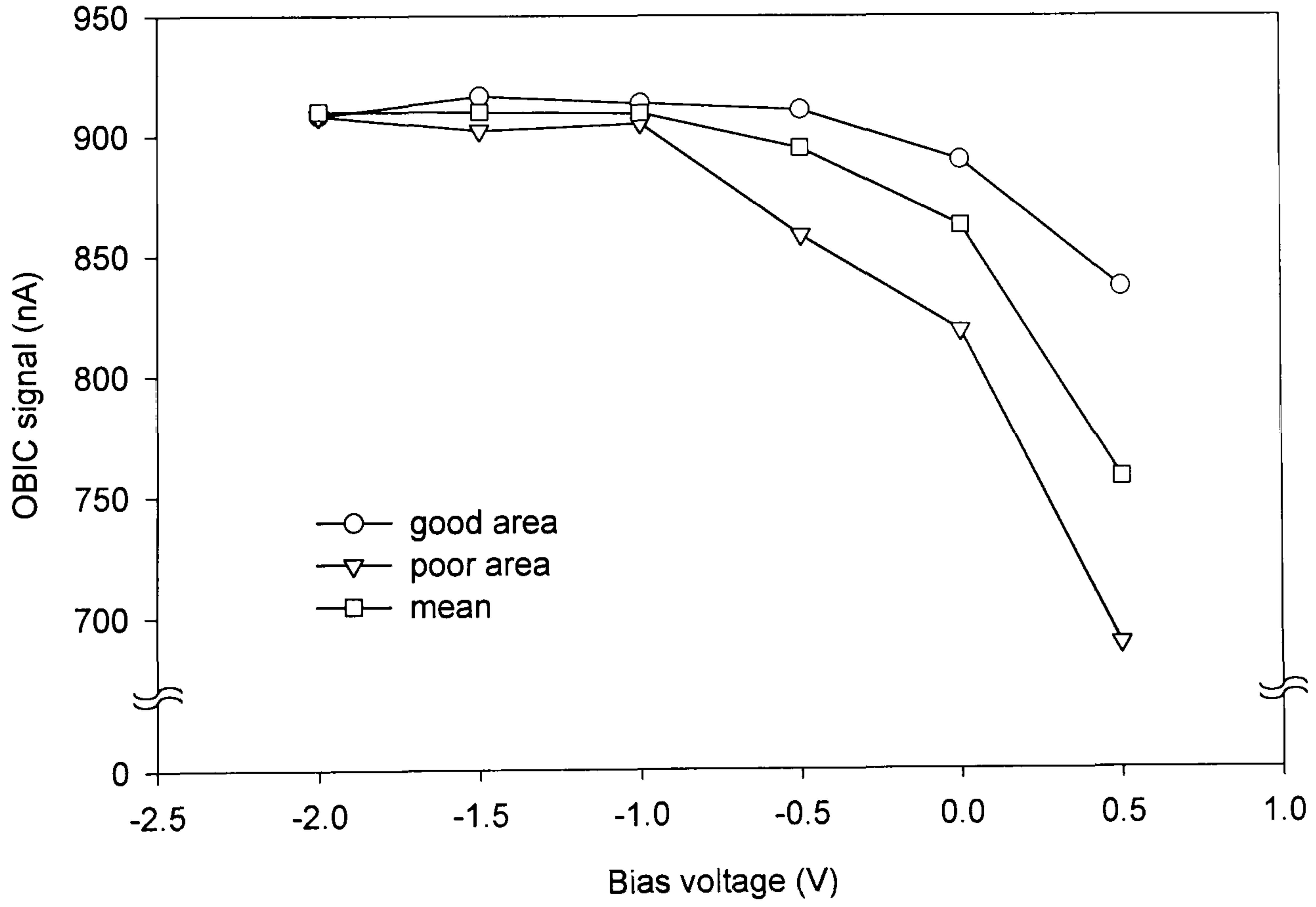

Figure 5.10 Comparison of OBIC values *versus* bias voltage for areas of good and poor collection for the cell treated with 60nm of $CdCl_2$. Also shown is the variation in mean OBIC.

Figure 5.11 shows OBIC images for the sample treated with a 120nm thick layer of $CdCl_2$.

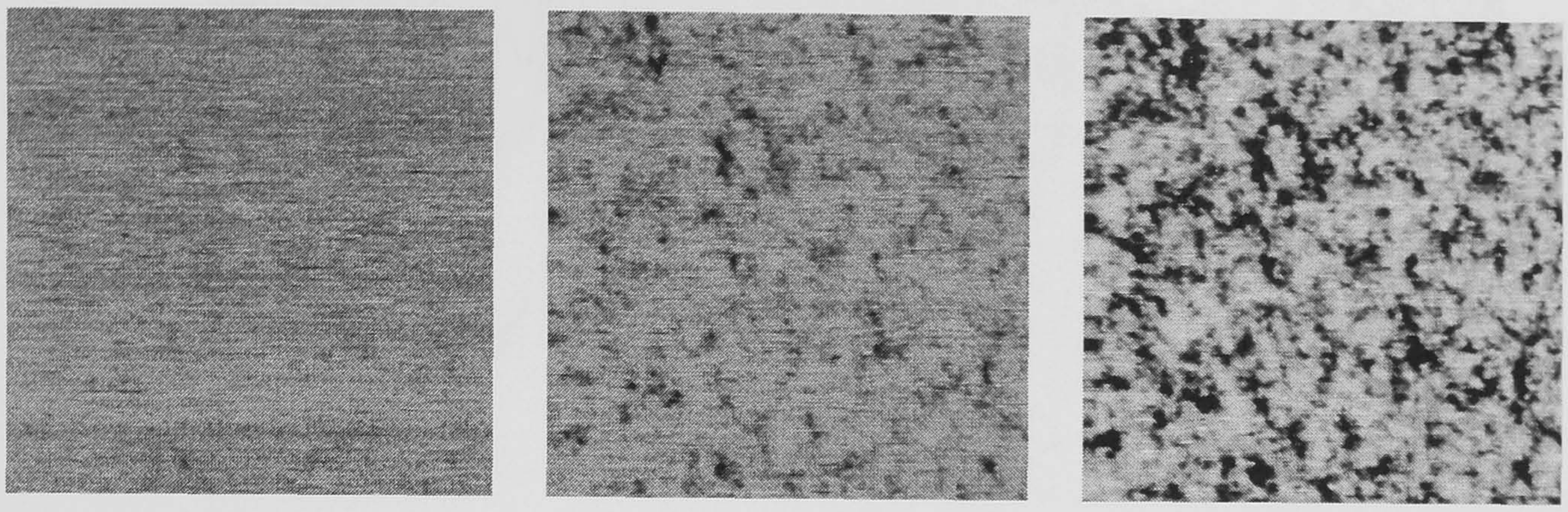

(a) 2V reverse bias **(b)** 1.5V reverse bias **(c)** 1V reverse bias

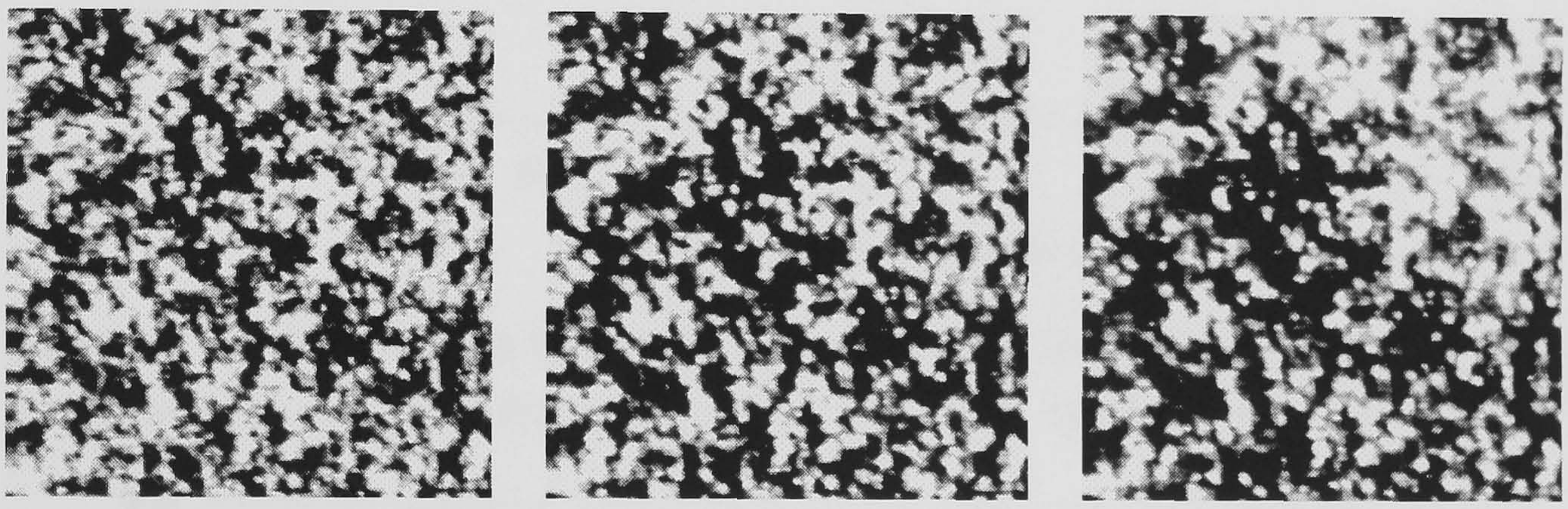

(d) 0.5V reverse bias **(e)** 0V bias **(f)** 0.5V forward bias

50μm

Figure 5.11 OBIC images at different bias voltages for a CdTe/CdS solar cell treated with a 120nm layer of $CdCl_2$.

These images display far greater contrast than expected for a cell of such a high photovoltaic conversion efficiency, at all voltages apart from high reverse bias (Figure 5.11a). The linescans and *I-V* plots in Figures 5.12 and 5.13 show that the overall signal level is also lower than expected. Furthermore, comparison of the *I-V* plots for good and poor grains shows a significant change in the shape of the curve.

Further analysis of the OBIC results is undertaken in the next section.

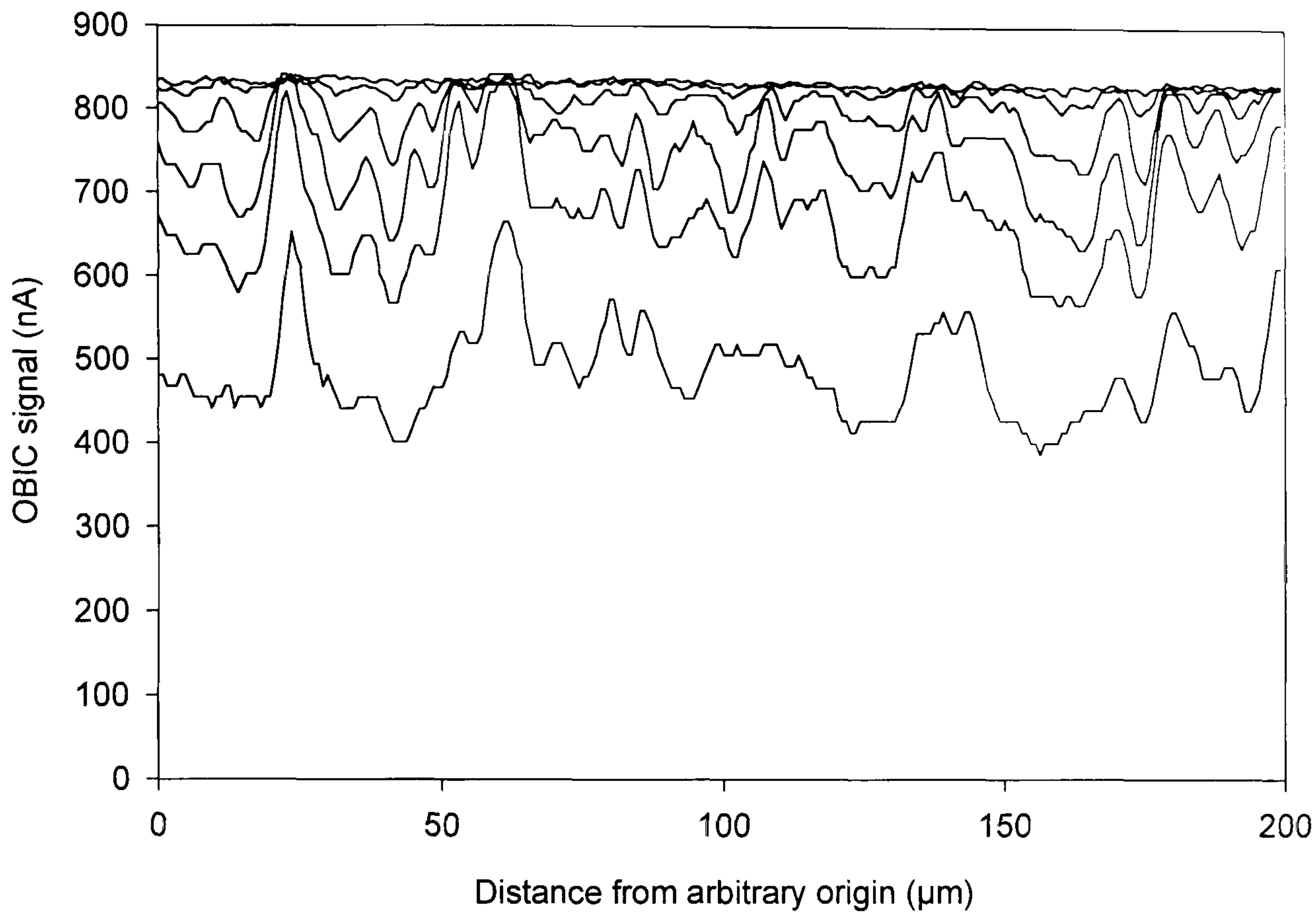

Figure 5.12 OBIC linescans taken from each of the OBIC images in Figure 5.11 (120nm $CdCl_2$), with bias voltages of (from top to bottom) -2V, -1.5V, -1V, -0.5V, 0V and +0.5 V.

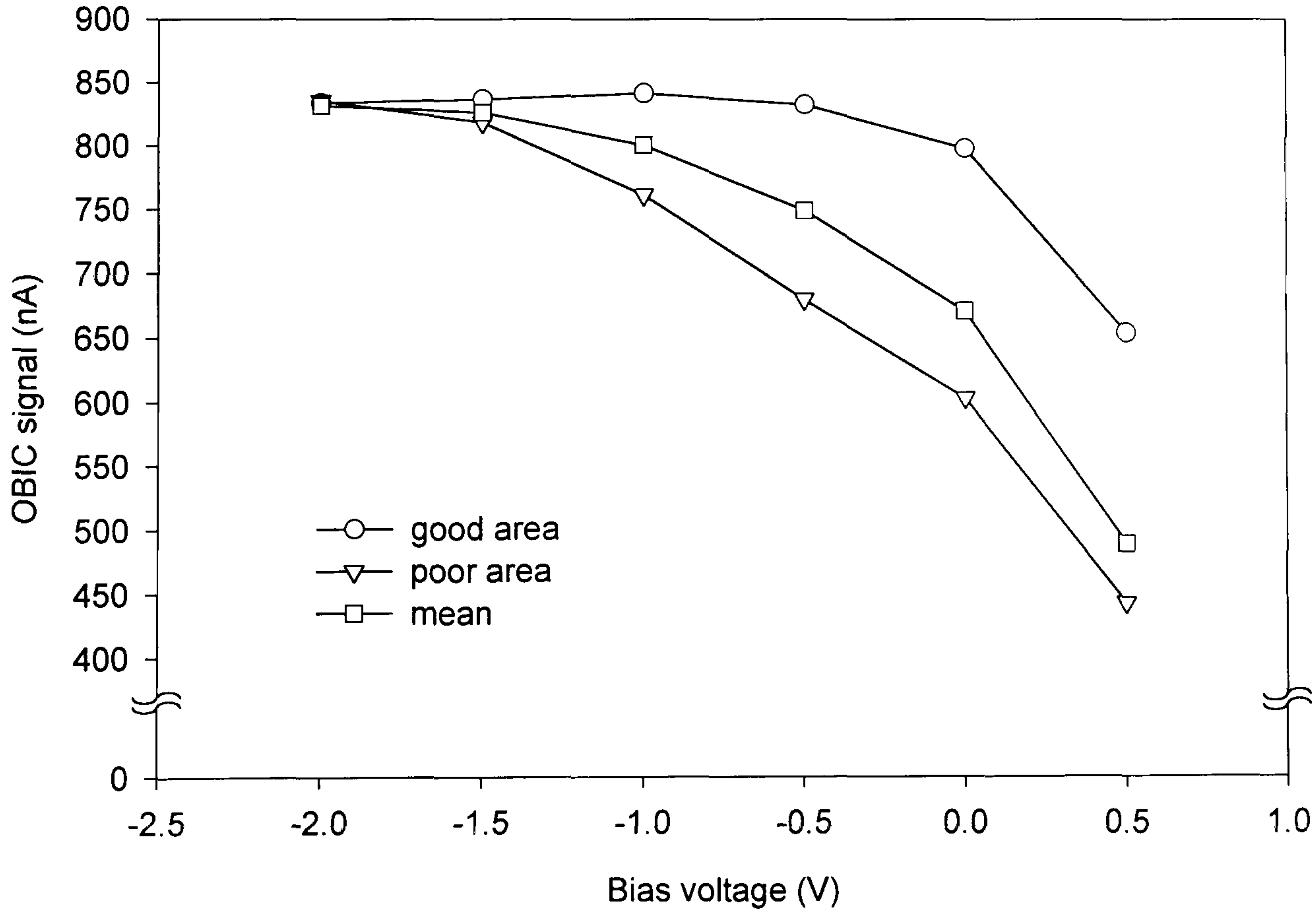

Figure 5.13 Comparison of OBIC values *versus* bias voltage for areas of good and poor collection for the cell treated with 120nm of $CdCl_2$. Also shown is the variation in mean OBIC.

5.4 DISCUSSION OF OBIC RESULTS

In order to see more clearly the effect on the OBIC data of the $CdCl_2$ layer thickness used, the distributions of pixel (OBIC current) values in the images have been analysed. The resultant histograms are shown in Figure 5.14. Each peak corresponds to an image at a different bias voltage, with the position and breadth of the peak representing the signal level and degree of contrast shown by the images.

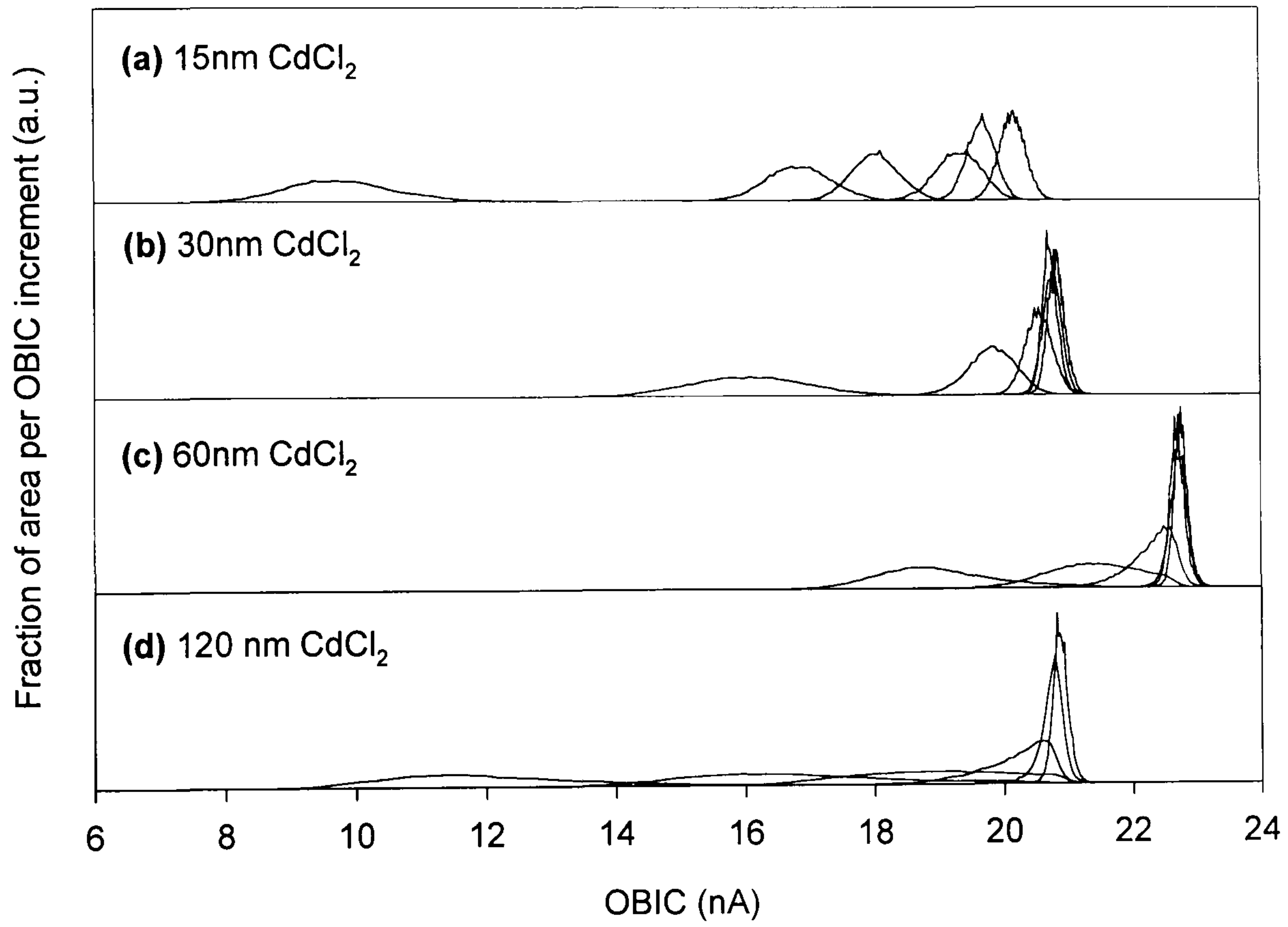

Figure 5.14 Histograms showing the distribution of OBIC values for each of the images presented in this section. For each of the four differently treated samples, results are shown for bias voltages of (from left to right): 0.5V forward bias; short-circuit; and 0.5 V, 1.0V, 1.5V and 2.0V reverse bias.

This figure clearly shows the effect of increasing reverse bias, which widens the depletion region and results in the collection of a higher fraction of generated carriers, and hence gives a larger photocurrent. This effect is further complicated by the presence of a dark current, due to carrier injection at the device junctions under an external bias. When the depletion region is wide enough to collect all excess carriers a limiting current is reached (ignoring the dark current, which is small at reverse bias). Such an effect is seen for the cells treated with 30nm or more of $CdCl_2$, but not in the 15nm sample. This indicates that for this cell the depletion region is very narrow, so that, even with the widening which results from the application of a reverse bias, it still does not collect from deep enough in the device to collect all carriers.

Figure 5.14 also shows how the amount of variation in OBIC, and hence the histogram width, decreases with increasing reverse bias. This can be explained by considering the different OBIC image pixels as an array of individual diodes [3]. Each of these components may be associated with different recombination rates, depletion widths and junction position. Under forward bias or at short-circuit, these position-dependent parameters each contribute to the OBIC image contrast. Increasing the reverse bias and widening the depletion region increases the current in a given pixel, as the electric field extends to prevent an increasing number of recombination events. Thus the number of pixels achieving complete collection increases, resulting in less variation between pixels. This may also explain the asymmetry seen in some of the histograms, which show a cut-off on the high current side of the distribution; see especially Figure 5.14c (0.5V r.b.) and Figure 5.14d (1.0V r.b.). However, the bias voltage would not affect the position of the collecting junction, and the remaining OBIC contrast seen at high reverse bias may be largely due to the varying depth of the buried homojunction.

The low and inhomogeneous OBIC response of the cell treated with a 120nm thick layer of cadmium chloride is not consistent with the results of the *I-V* measurements (see Table 4-II). Examination of the spatially resolved, illuminated *I-V* curves extracted from the OBIC data (Figure 5.10) shows that good and poor areas of the cell display different responses. The two curves coincide at high reverse bias, and appear to be of a similar shape but with the curve for a poor area being displaced ~0.6V to the left with respect to the curve for the good area. This suggests a voltage drop in this area of the device, leaving a lower voltage available to contribute to carrier collection.

A possible explanation for this effect is the degradation of the back contact. Singh *et al.* [4] have reported the effect of oxidation occurring between the CdTe and the back contact of the solar cell. The resultant layer of electrically insulating $CdTeO_3$ forms an electrical barrier, which inhibits current flow and results in a voltage drop. This occurs in unencapsulated devices (as used in this study) and is accelerated upon exposure to heat and humidity. Since the devices used in this work were vulnerable to the room environment for several months in between the *I-V* and OBIC measurements, this degradation is thought to be responsible for the anomalous results seen. This conclusion was confirmed by repeating the *I-V* measurements, which showed higher series resistances compared to the original measured characteristics.

5.5 CONCLUSIONS

Recording OBIC images as a function of voltage bias have been found to be an effective way of measuring the illuminated *I-V* response of CdTe/CdS solar cells with spatial resolution. Measurements have been carried out on cells treated with different amounts of $CdCl_2$ in order to determine the effects of this treatment. Analysis of this data has been carried out by treating OBIC image pixels as an array of individual solar cells with different parameters. Using this model, all the devices studied have been shown to have position-dependent depletion region widths and junction depths. One effect of the chloride treatment is to widen the depletion region, whilst not improving the homogeneity of the OBIC signal.

The results of this study have also demonstrated the vulnerability of unencapsulated cells to the oxidising effects of heat and moisture. This has a deleterious affect on the *I-V* response and hence photovoltaic performance of the device. In this study the degradation has limited the extent to which the results could be interpreted.

The spatial resolution of the OBIC system used was found to be insufficient to allow a direct analysis of the grain boundaries of the solar cells. For this reason, OBIC was abandoned in further studies in favour of the higher resolution EBIC technique. The results of this method are presented in the next chapter.

REFERENCES FOR CHAPTER 5

[1] A.J. Holland, *A scanning optical microscope study of semiconductors* (University of Oxford D.Phil. thesis, 1996)

[2] S.A. Galloway, P.R. Edwards and K. Durose (1999) *Characterisation of thin film CdS/CdTe solar cells using electron and optical beam induced current*, Solar Energy Materials and Solar Cells **57** pp.61-74

[3] P.R. Edwards, S.A. Galloway, P.R. Wilshaw and K. Durose (1997) *A study of the activation of CdTe/CdS thin film solar cells using OBIC*, Institute of Physics Conference Series **157** pp.583-586

[4] V.P. Singh, O.M. Erikson and J.H. Chao (1995) *Analysis of contact degradation at the CdTe-electrode interface in thin film CdTe-CdS solar cells*, Journal of Applied Physics **78** (7) pp.4538-4542

Chapter 6: Front-wall EBIC imaging

6.1 INTRODUCTION

This chapter concerns the use of planar front-wall EBIC measurements to probe spatial variations in the carrier collection in the solar cells. The basic principles of the EBIC technique are outlined in Section 3.5.5.

6.2 BACK-WALL AND CROSS-SECTION EBIC MEASUREMENTS

The presence of the glass substrate on the front wall of the CdTe/CdS solar cell poses a problem for carrying out planar EBIC in the solar irradiation geometry, as the electron beam cannot penetrate the glass to reach the active layers of the device. For this reason, previous attempts to use EBIC on these devices have used either the cross-section geometry, or planar EBIC via the back contact side of the cell. Although such experiments are not the main part of the present work, a consideration of their findings is necessary to fully understand the front-wall EBIC results.

6.2.1 Back-wall EBIC

Figure 6.1 shows a back-wall EBIC image of a $CdCl_2$-treated ANTEC solar cell at room temperature, in a result obtained by Galloway *et al.* [1]. Before the application of a back contact, the sample was thinned to ~4μm by polishing with diamond paste. This eliminated any spatial variation in EBIC signal due to surface topology, as described in Section 3.5.3, and also allowed the electron beam to probe a region closer to the collecting junction. The device was contacted by bromine/methanol etching and the evaporation of a thin (~20nm) layer of gold.

The image shows many well-defined bright areas, corresponding to regions of high carrier collection. These features are on a scale consistent with their being crystal grains, as observed in secondary electron images of unpolished devices. Also visible, but poorly defined, are dark grain boundaries. Figure 6.2 shows an EBIC image of a similar area of the solar cell taken at 200K. The dark grain boundary contrast is much more defined in this image compared with that taken at the higher temperature.

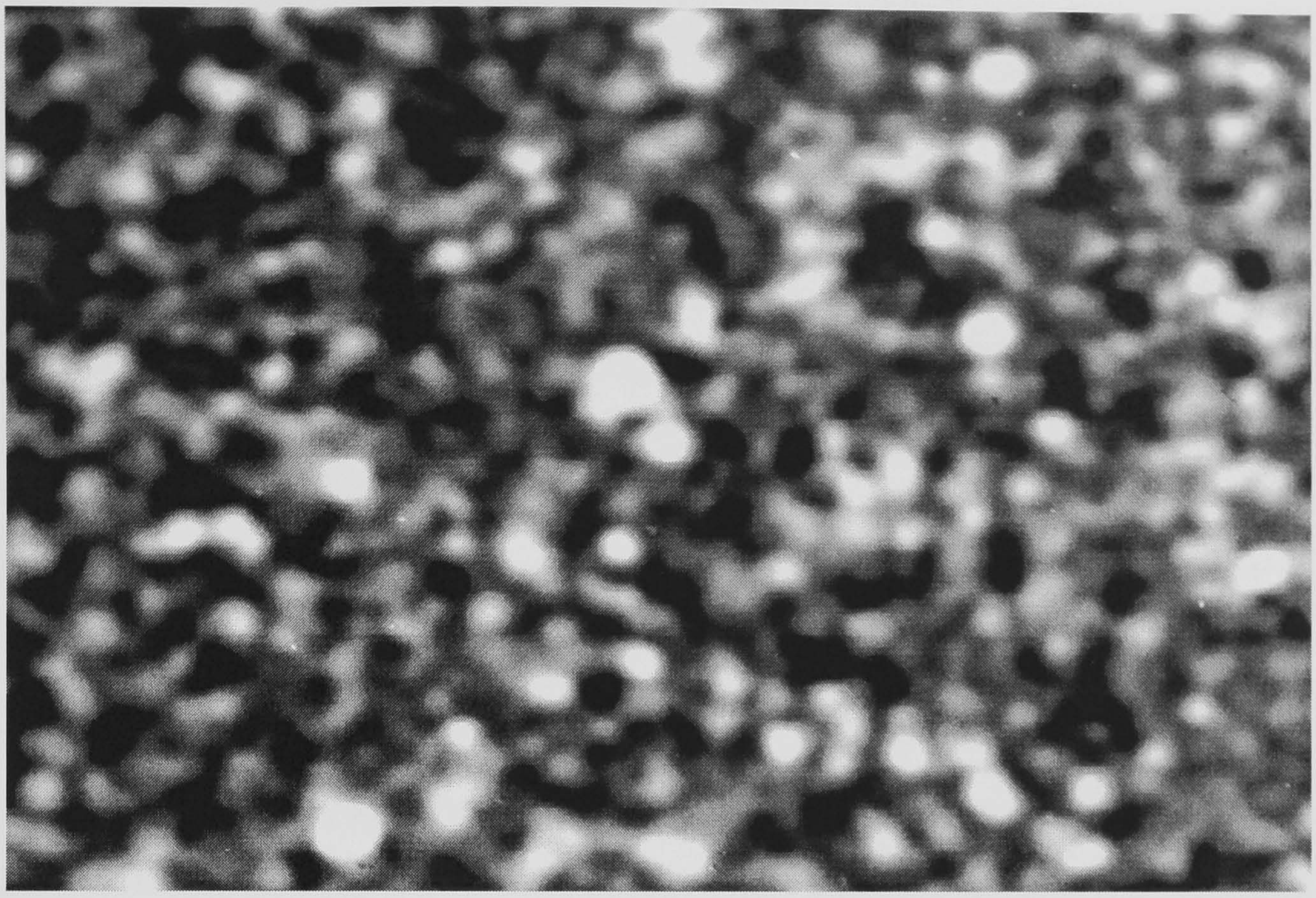

Figure 6.1 Back-wall EBIC image of a CdTe/CdS solar cell recorded at a temperature of 300K. A 25 kV electron beam was used, with a beam current of 0.5 nA.

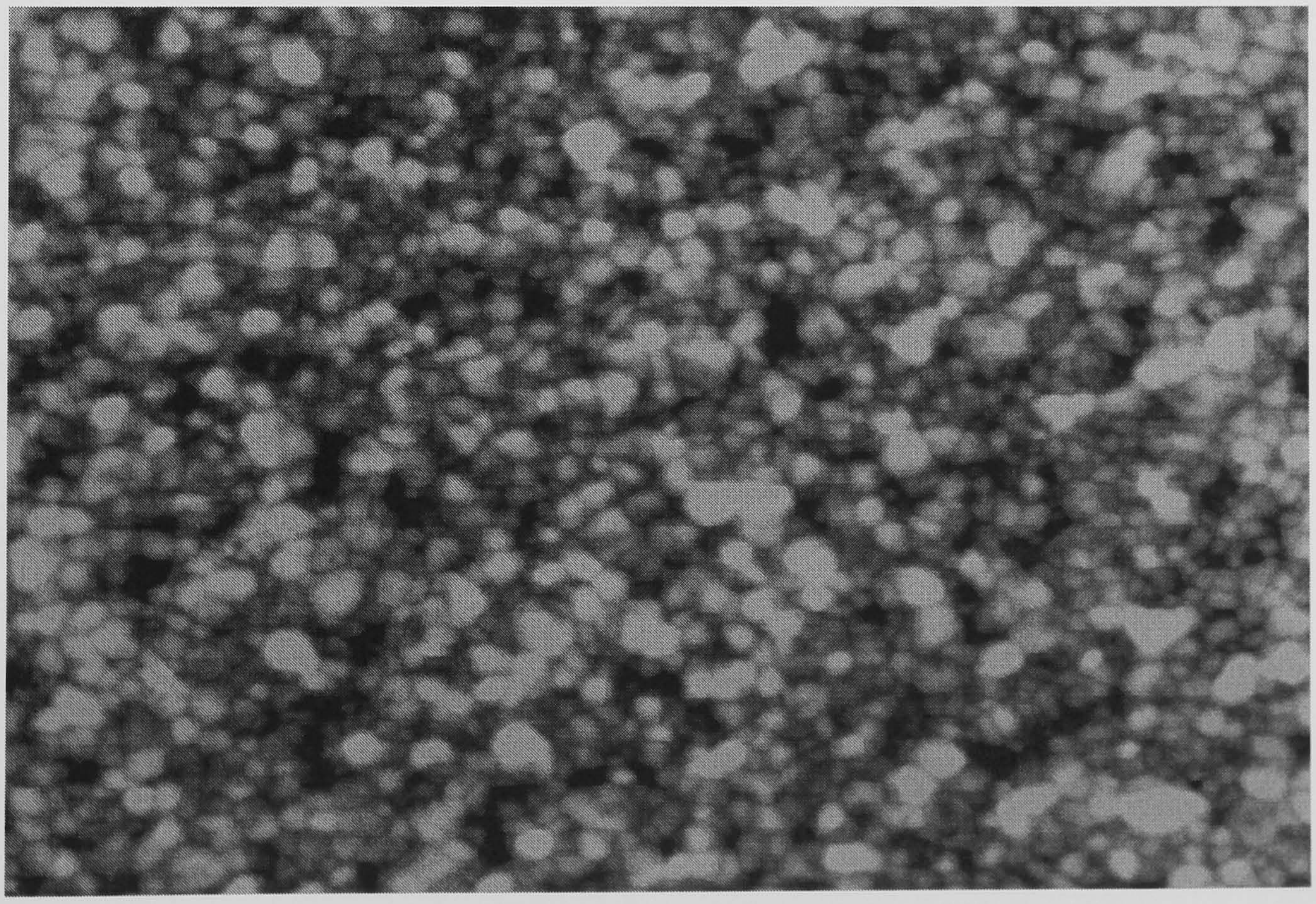

Figure 6.2 Back-wall EBIC image of the same area as Figure 6.1, recorded at 200K.

10µm

The presence of dark grain boundaries is often observed in EBIC, and is usually attributed to enhanced carrier recombination compared with the surrounding grains. However, such a simple interpretation does not explain the temperature dependence of the boundary contrast.

A major limitation of this method of EBIC is that the excess charge carriers are generated a long way from the collecting junction. Monte Carlo simulations indicate that even an electron beam with the relatively high energy of 25keV penetrates little more than 2µm into CdTe. The result of this is that the experiment probes an area of the device of little relevance to its normal working conditions.

6.2.2 Cross-section EBIC

Galloway *et al.* have also performed cross-section EBIC on these solar cells. This was achieved by cleaving the device and scanning the electron beam across the CdS/CdTe interface. This was carried out at different temperatures, and the results are shown in Figure 6.3.

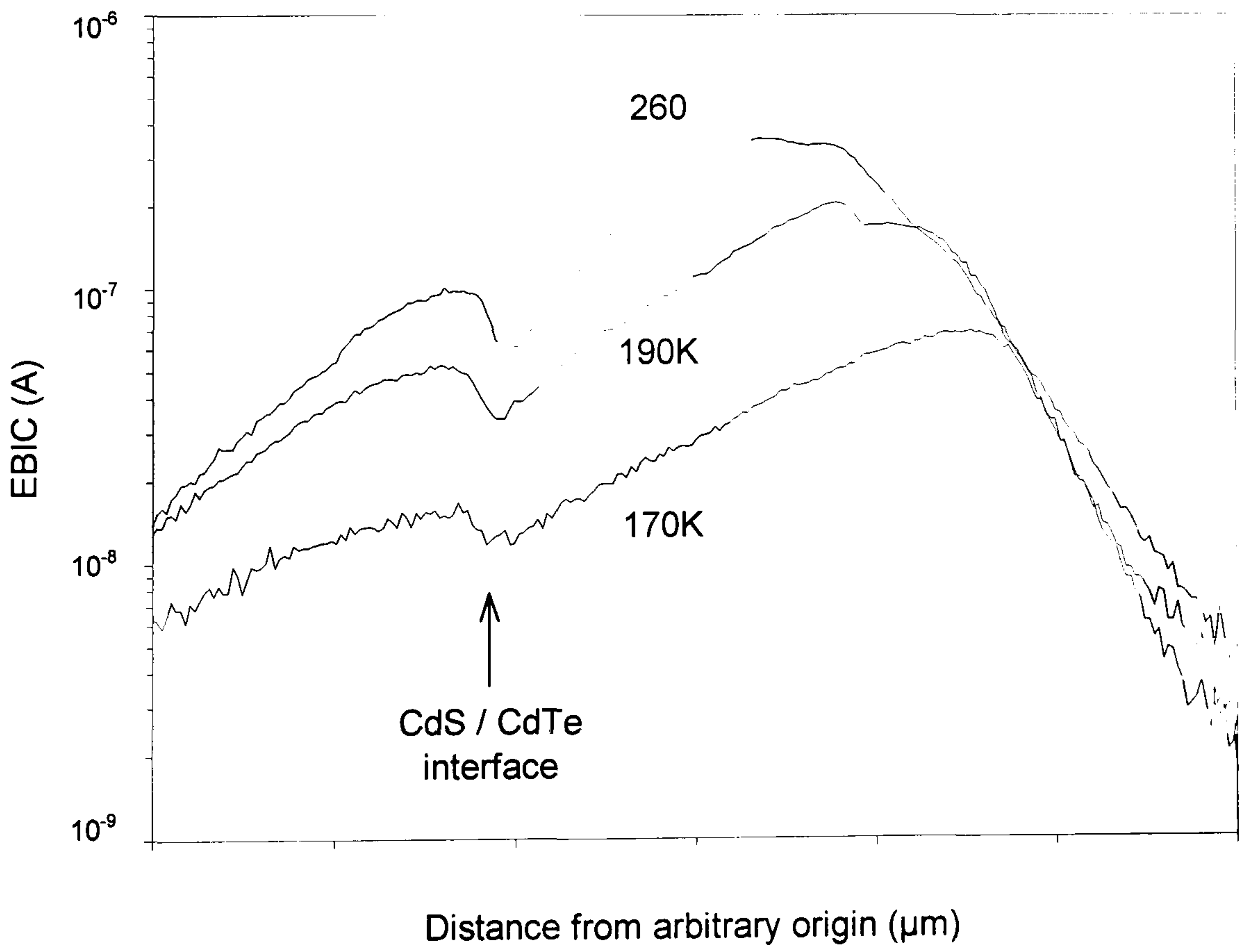

Figure 6.3 Cross-section EBIC linescans across the CdTe/CdS junction as a function of temperature.

These results show a decrease in EBIC signal at the CdS/CdTe junction, a result of recombination due to interface states. The EBIC maximum corresponds to the depletion region of the device, where carrier collection is most likely. An exponential decrease in current is observed in the neutral region of the CdTe, with a slope governed by the minority carrier diffusion length of the material.

The effect of reducing the temperature is to move the position of the collecting junction, allowing carriers to be collected from deeper within the device. This can be explained by carrier freeze-out, in which dopant atoms no longer have sufficient thermal energy to ionise, effectively reducing the semiconductor's doping concentration. This will in turn affect the width and symmetry of the depletion region.

A widely cited disadvantage of this technique is the difficulty with which the results can accurately be reproduced. Cleaving damage, variation in doping from grain to grain along the interface, and surface recombination can all contribute to a complex and unstable EBIC linescan [2-4]. However, the results shown in Figure 6.3 are self-consistent, in that they were recorded from the same, apparently damage-free, part of the cell.

6.3 FRONT-WALL EBIC IMAGING AND ITS BEAM CURRENT DEPENDENT EFFECTS

In order to avoid the drawbacks inherent in back-wall and cross-section EBIC, a method has been developed of carrying out the technique in the front-wall geometry. The major advantage of this is that it is more relevant to the working conditions of the device, in that the carriers are generated at approximately the same depth in the cell as they would under solar illumination.

6.3.1 Samples examined

Front-wall EBIC was carried out on four different samples: three consisting of the complete TCO/CdS/CdTe structure after different post-deposition treatments (as-deposited, heat-treated and heat/$CdCl_2$-treated); and the fourth a CdS-free control sample (also heat/$CdCl_2$-treated). These treatments are explained in fuller detail in Section 4.2.2. The substrates were removed, leaving the active layers intact, using the method described in Section 4.3.2.

6.3.2 Experimental details

All the EBIC measurements in this section were obtained using the same electron beam accelerating voltage. 11kV was chosen in order to give a depth-dose function as close as possible to that of AM1.5 sunlight; the details of this calculation are shown in section 7.3.4, in which a Monte Carlo simulation of the interaction of an electron beam with the cell are compared with the calculated AM1.5 depth-dose function. All measurements were taken at room temperature, using front-wall injection geometry with the set-up shown in Figure 6.4.

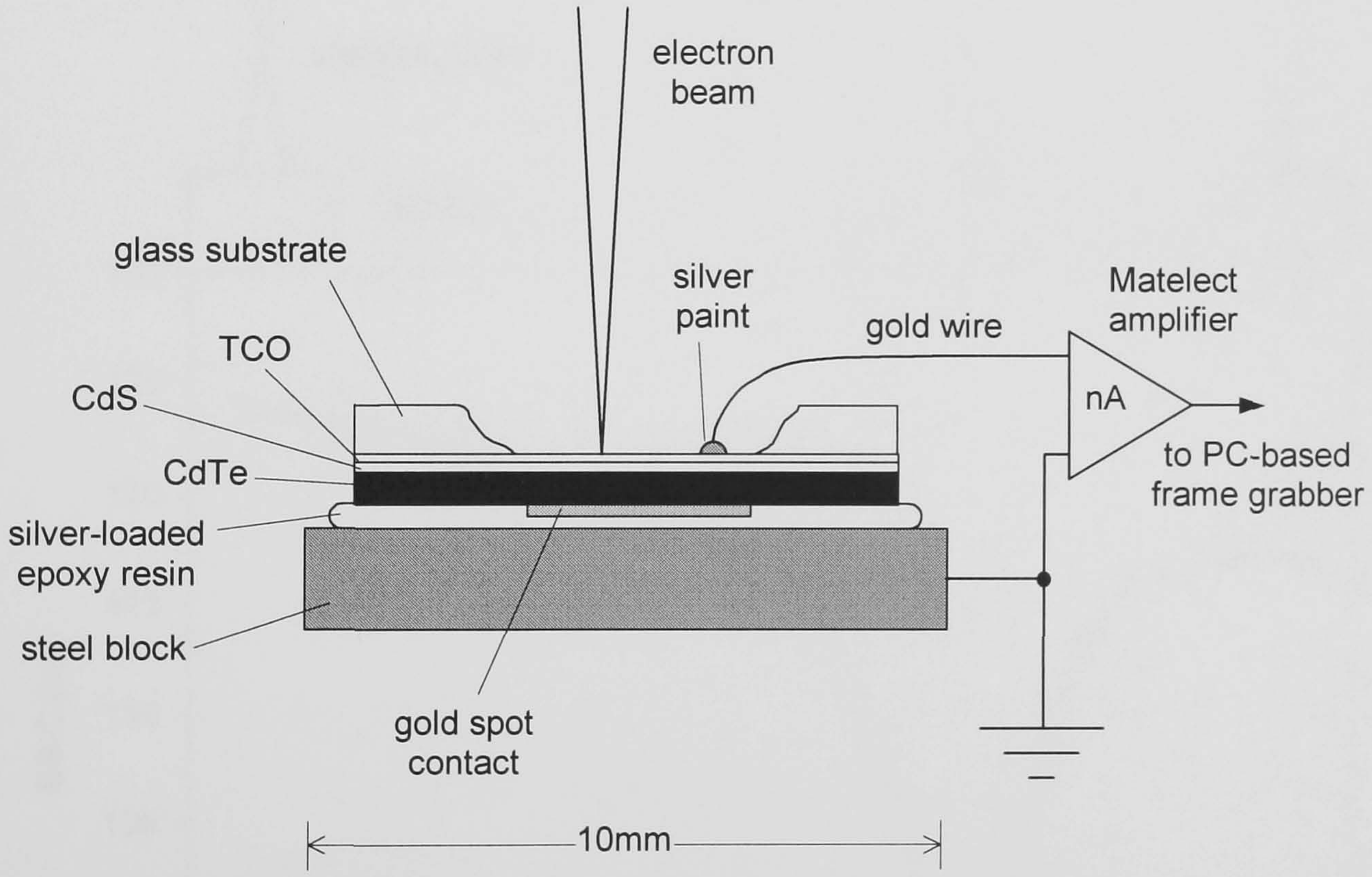

Figure 6.4 Experimental arrangement used for front-wall EBIC measurements.

Preliminary front-wall EBIC studies [1] carried out on CdTe/CdS solar cells indicated that sufficiently high injection densities can be created in the devices to cause the high-injection plasma effect described in Section 3.5.5. This effect occurs when the density of injected carriers is such that it outnumbers the equilibrium majority carriers in the region, and has a deleterious effect on the local EBIC signal.

In order to demonstrate clearly that the high injection regime can occur in CdTe/CdS solar cells under an electron beam, and that the effect leads to a significant drop in the measured current, EBIC has been measured as a function of electron beam focus. The position of the focal point of the beam was varied through a distance of around 15mm, from above the surface of the sample to beneath it. No other beam parameters were altered so that the carrier generation rate remained constant within a changing generation volume, hence changing the injection density. The results are shown in Figure 6.5.

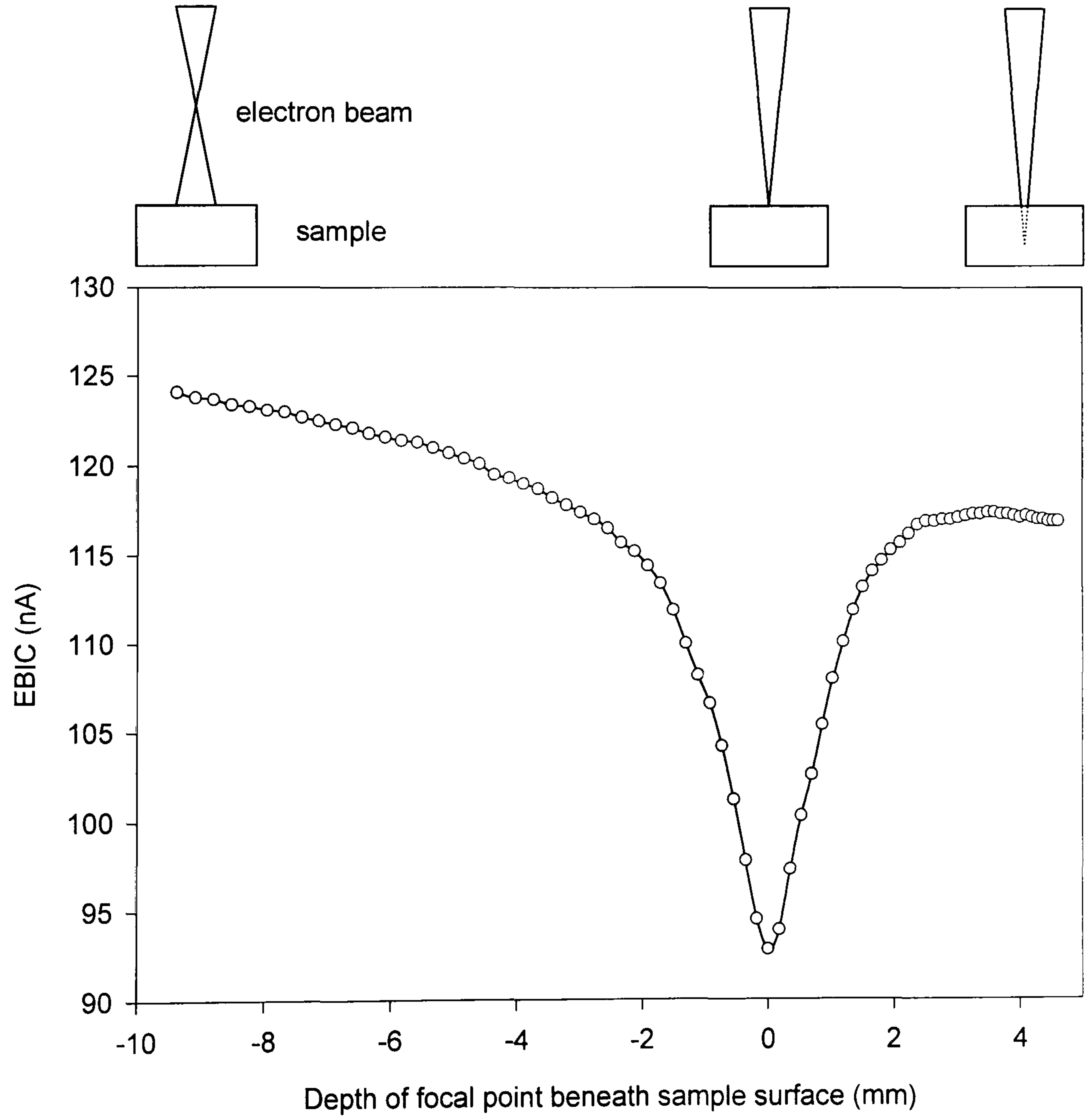

Figure 6.5 The plasma effect under high injection conditions in a CdTe/CdS solar cell, demonstrated by varying the focus position of the electron probe (and hence the carrier injection density). Shown at the top are schematic diagrams showing the corresponding positions of the electron beam focal point.

The results show a drop of ~20% in the EBIC value measured at the focal point (corresponding to the highest injection density) compared with that measured with a widely defocused beam. This demonstrates that the decline in EBIC efficiency is an effect of the changing injection density, supporting the findings in [1] that the injection density rather than the beam current itself is the critical parameter.

Since, for given beam conditions, the occurrence of high injection effects depends on whether or not the equilibrium majority carrier concentration is exceeded by the excess generated carrier density, the onset of these effects can in principle be used to estimated the equilibrium carrier levels in the device. The aim of this experiment was to exploit this concept to yield useful information about carrier distributions in the solar cell; for this reason all EBIC images were recorded as a function of electron beam current I_{beam} at a fixed accelerating voltage so as to vary the injection density.

6.4 FRONT-WALL EBIC RESULTS

For each of the four samples described in Section 6.3.1, EBIC images of the same area were recorded using 12 different beam currents, varying between 5pA and 20nA; Figures 6.6-6.9 show selected results from these series. Each of the images in the figures has been individually contrast enhanced by expanding the recorded contrast range to 100%. This ensured maximum visibility of the contrast at features related to grains in the material, but prevents immediate comparison of the overall EBIC levels or of the original relative contrast. However, this will be redressed in later analysis (Section 6.6.1).

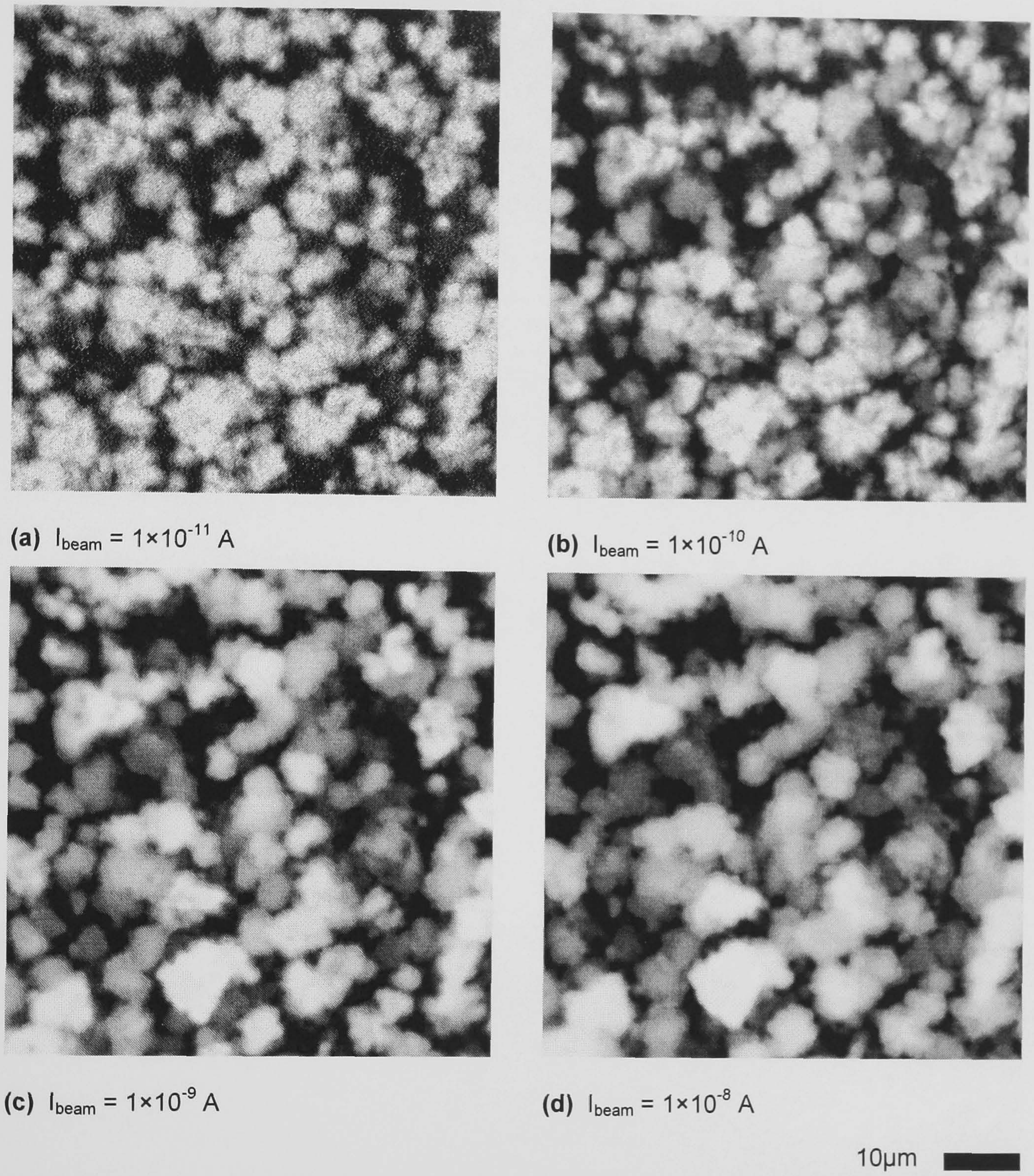
(a) $I_{beam} = 1\times10^{-11}$ A

(b) $I_{beam} = 1\times10^{-10}$ A

(c) $I_{beam} = 1\times10^{-9}$ A

(d) $I_{beam} = 1\times10^{-8}$ A

Figure 6.6 EBIC images of the same area of the as deposited cell, taken with different beam currents.

In Figure 6.6a, which shows the EBIC image of the as-deposited sample taken with a relatively low beam current, considerable inter-grain variation can be seen in the carrier collection. Dark grain boundary contrast and inter-grain regions may also be observed. Little effect is seen on increasing the beam current (b-d), except for some loss of spatial resolution resulting from the increased beam diameter associated with higher beam currents.

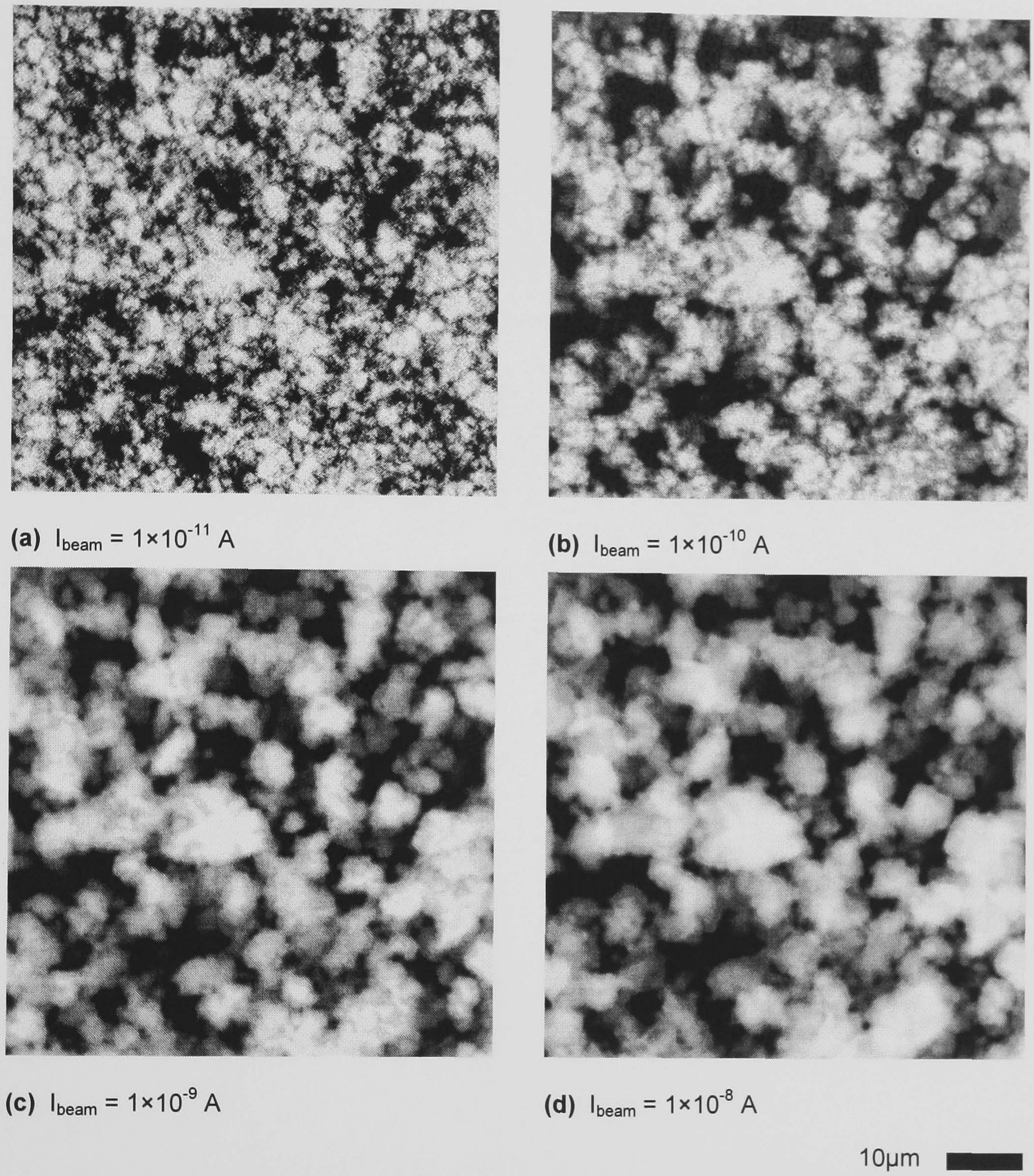

Figure 6.7 EBIC images of the same area of the heat-treated cell, taken with different beam currents

Figure 6.7 shows EBIC results from an area of the heat-treated sample, using the same beam current values as in Figure 6.6. The contrast is similar to that seen for the as-deposited sample, with comparable grain-to-grain variation and dark grain boundary contrast observed.

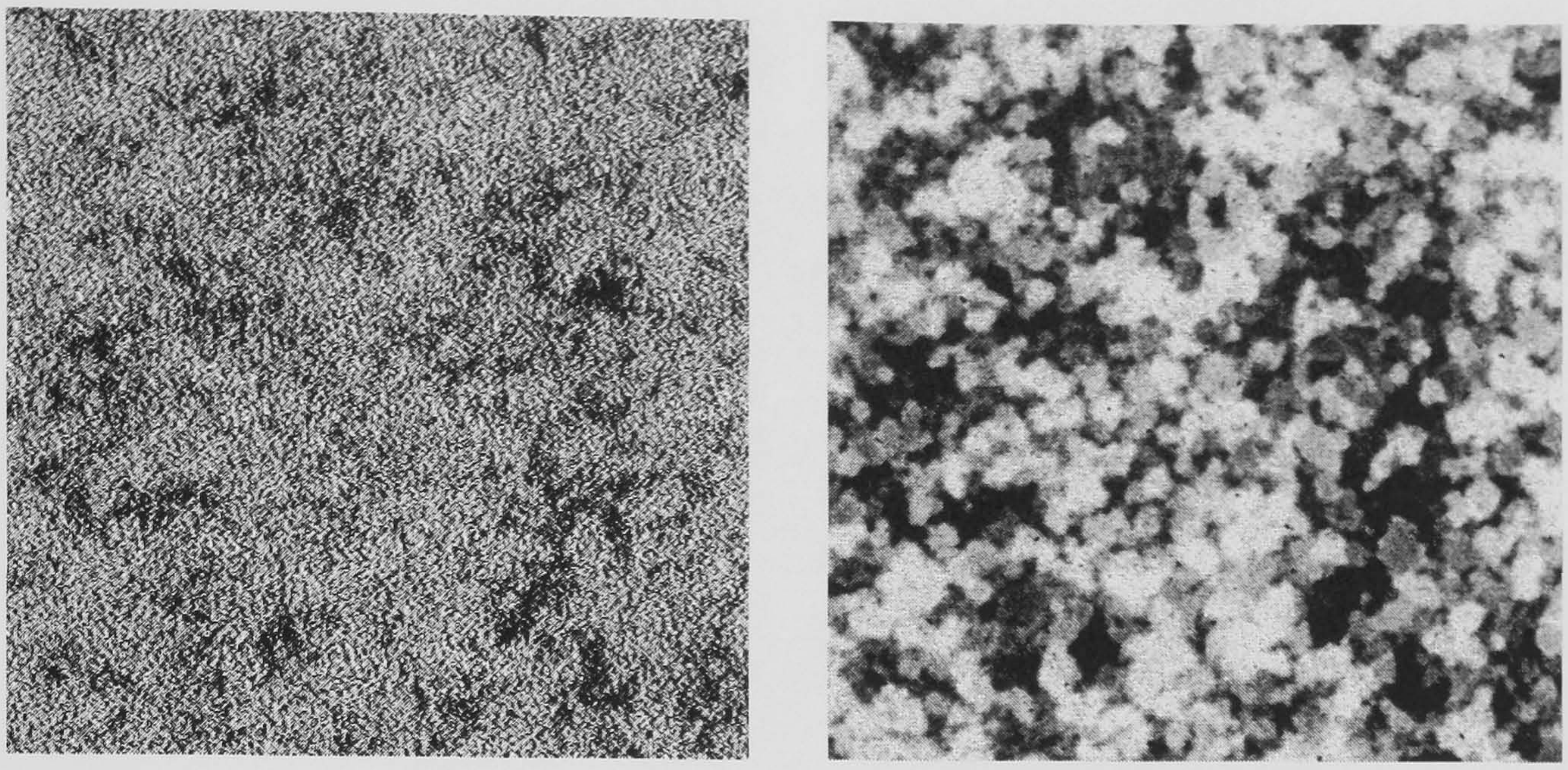

(a) $I_{beam} = 1\times10^{-11}$ A **(b)** $I_{beam} = 1\times10^{-10}$ A

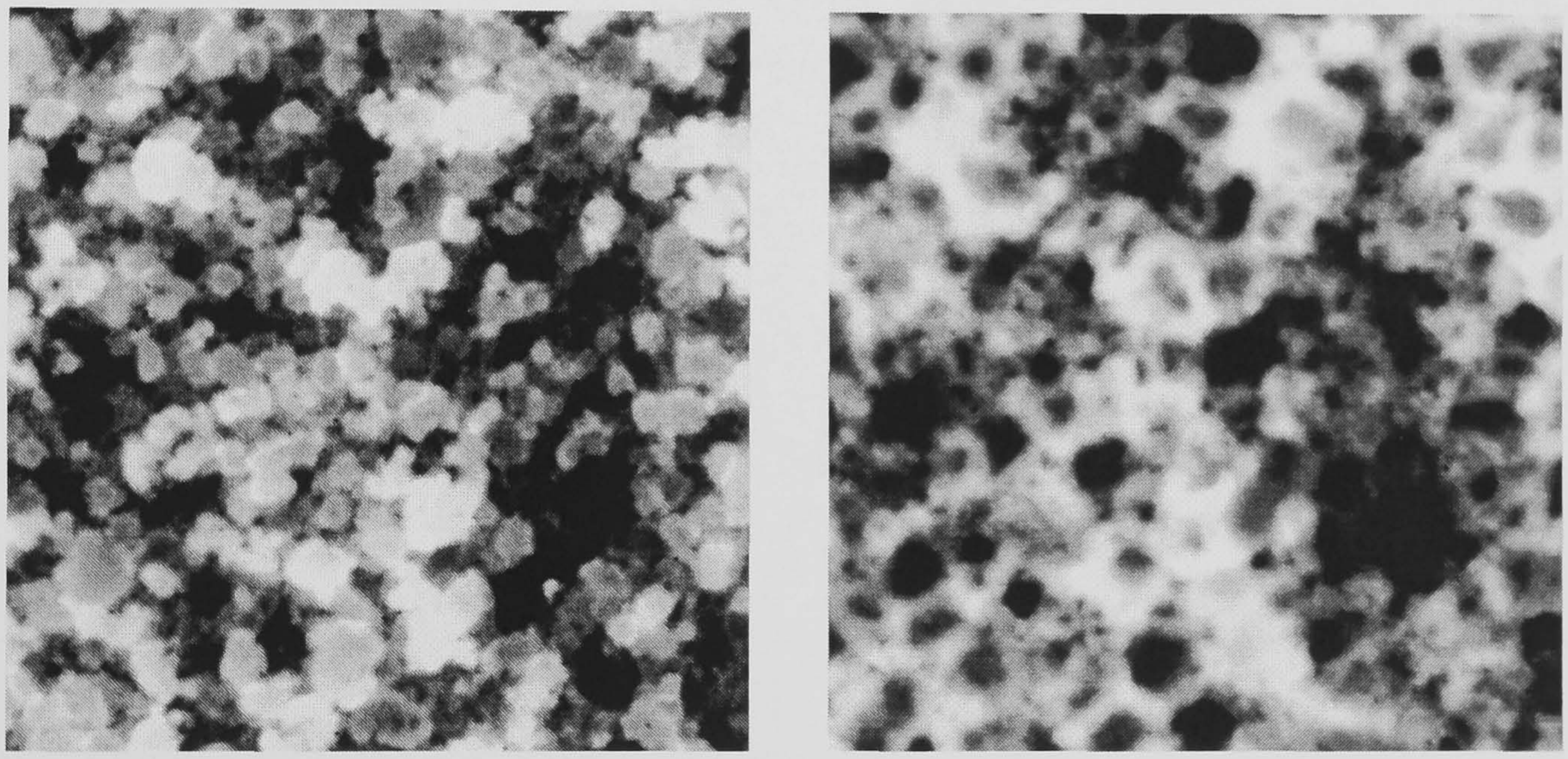

(c) $I_{beam} = 1\times10^{-9}$ A **(d)** $I_{beam} = 1\times10^{-8}$ A

Figure 6.8 EBIC images of the same area of the chloride treated cell, taken with different beam currents

Figure 6.8 shows EBIC images of the chloride-treated sample for the same four beam currents. A considerable difference can be seen in these images when compared to the results for the untreated and heat-treated cells. With a low beam current (Figure 6.8a), very little contrast is seen above the amplifier noise, although some dark contrast can still be seen, albeit to a lesser extent than in the other samples. Increasing the beam current by an order of magnitude (Figure 6.8b) results in more inter-grain contrast. At still higher beam currents (Figure 6.8c), some grain

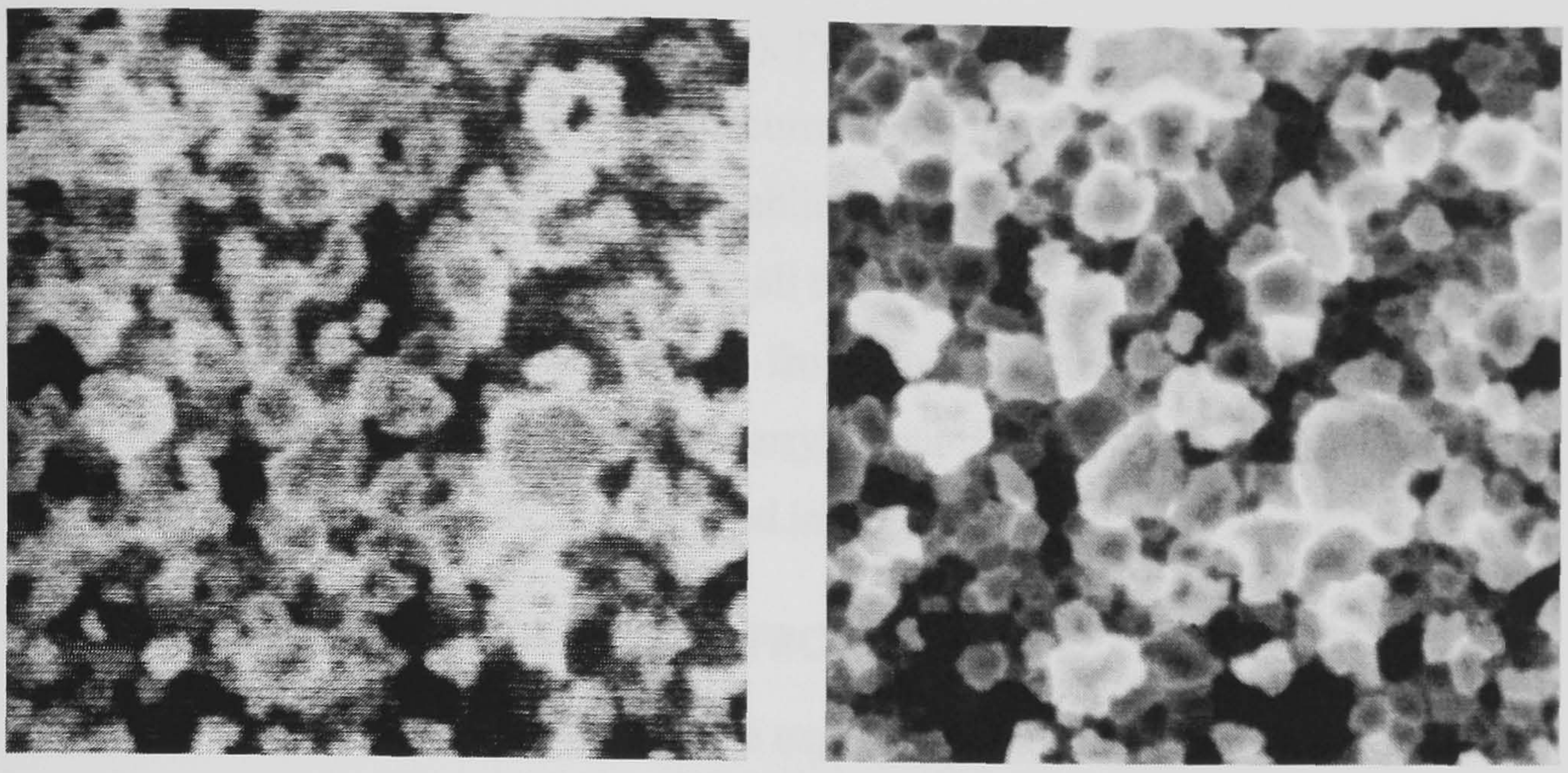

(a) $I_{beam} = 1\times10^{-11}$ A

(b) $I_{beam} = 1\times10^{-10}$ A

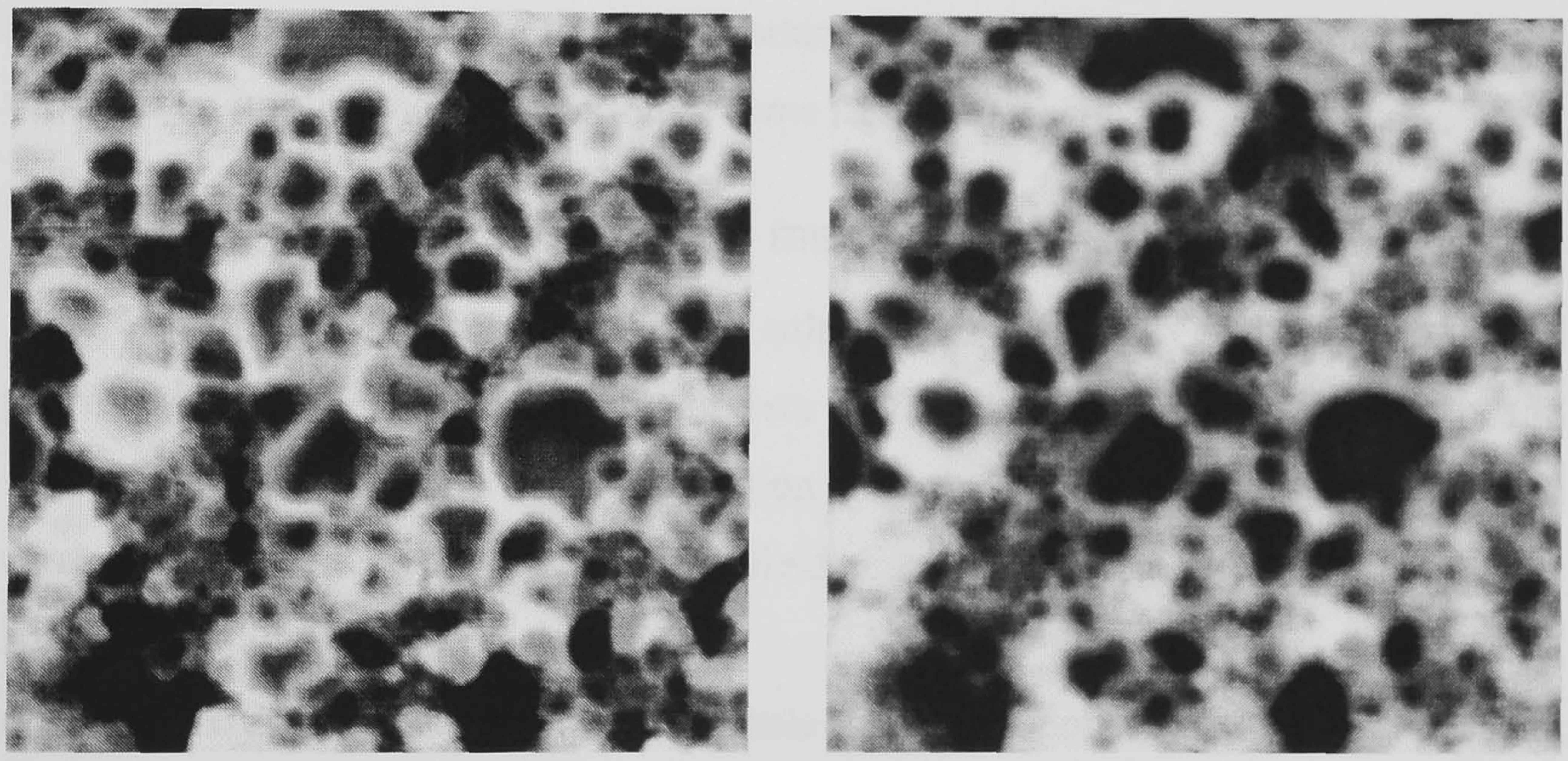

(c) $I_{beam} = 1\times10^{-9}$ A

(d) $I_{beam} = 1\times10^{-8}$ A

Figure 6.9 EBIC images of the same area of the CdS free cell, taken with different beam currents

boundaries begin to show bright contrast, an effect which is even more pronounced at the higher current (Figure 6.8d). This result indicates that, under some experimental conditions, collection from the grain boundary regions is more efficient that from the grain interiors.

Figure 6.9 shows the results taken from the CdS-free control sample. These images show a similar bright grain boundary effect to that seen in Figure 6.8. However, in this case the bright grain boundaries are highly pronounced, even at the lowest beam current setting (Figure 6.9a). Furthermore, some decrease in this bright contrast is observed at the highest beam current (Figure 6.9d).

In order to demonstrate the repeatability of the post-deposition treatments and their effect on the EBIC measurements, all the results presented in this section were repeated. Fresh samples were prepared from the untreated ANTEC material, and identical beam conditions were used in carrying out the EBIC measurements. Similar results were obtained, and these were used in alternative data analysis methods.

6.5 QUALITATIVE DISCUSSION OF FRONT-WALL EBIC CONTRAST EFFECTS

The results of Section 6.4 cannot be explained by a simple model in which dark contrast features are associated solely with enhanced recombination. Although this may be the cause of some of the EBIC features seen, the beam current dependence of the contrast implies the contribution of some further mechanism.

6.5.1 General EBIC contrast mechanisms

The EBIC signal measured in the solar cell is essentially a function of three processes: the generation of charge carriers by the interaction of the electron beam with the material; the rate of recombination of these carriers; and the probability of carriers being collected by the electric field. Each of these is likely to have some spatial variation through the device.

a) Generation The rate of electron-hole pair generation under an electron beam is a function of several properties of the sample. It depends firstly on the topography of the sample surface, due to variations in the rate of backscattered primary electrons, as discussed in Section 3.5.3. However, since no secondary electron contrast was observed for any of the samples investigated, it is assumed that there were no significant surface features on the scale involved. This is as expected if the substrate removal method reveals the smooth glass/TCO interface as the exposed surface.

The depth of penetration of a high energy electron through a solid also depends on properties of the material such as atomic number, mass number and ionisation potential, all of which have terms in the Bethe expression. In addition, the number of carriers excited by each beam electron depends on the bandgap energy of the material. All of these parameters may vary in a small degree as a result of doping and alloying of the CdS and CdTe. However, the effect of these variations on the generation rate is likely to be insignificant in comparison with other EBIC contrast mechanisms.

b) Recombination Carrier recombination results in dark EBIC contrast, and this effect is used as a standard technique for identifying extended crystal defects. Grain boundaries, with their associated energy states, are generally considered to lead to enhanced recombination, unless passivated. Point defects, such as vacancies and inclusions, may also contribute to the loss of excess carriers, as would interface states at the CdS/CdTe junction.

c) Collection The probability of carrier collection depends on the electric field and the associated bending of the conduction and valence bands. This results from both the depletion region of the CdS/CdTe and from local fields originating from charge trapped at grain boundaries. Local screening of the electric field is also possible as a result of plasma effects which occur at high injection, as described earlier.

6.5.2 Contrast seen in front-wall EBIC images

In this section, explanations of the various observed contrast features are proposed and discussed.

Grain boundary contrast The presence of dark grain boundaries in the as-deposited and heat-treated cells, observed over the full range of electron beam currents (Figures 6.6-6.7), suggests that the grain boundaries are acting as centres for recombination. This is in line with the conventional understanding of grain boundaries, where the presence of interface states produces a depletion region. Whether this simply produces band bending, Fermi level pinning or full inversion depends on the density of these states. The resultant electric field at the grain boundary attracts minority carriers, allowing recombination to occur via the grain boundary states. In addition, the potential barrier will limit the flow of majority carriers.

Band bending at grain boundaries may also lead to bright EBIC contrast, if the electric field is such that the minority carriers are repelled away from the boundary, and so aiding collection. This has, for example, been observed in polycrystalline

ZnSe bars examined in the REBIC geometry [5]. In this case though, enhanced REBIC at the grain boundaries was only observed upon application of an external bias. The mechanism of the bright grain boundary contrast observed in this work is the subject of further data analysis and discussion presented in Sections 6.6 and 6.7.

Inter-grain EBIC variation The wide variation in EBIC recorded for different grains, observed in all the samples (Figures 6.6-6.9), may be caused by recombination or collection effects. *i.e.*:

a) The recombination rate may be position-dependent, due to variations in the density of point or structural defects from grain to grain. Both impurity-related defects and threading dislocations, for example, could depend on the quality of the CdS grains upon which the CdTe grains nucleated, leading to a position dependence in the defect density.

b) Another contribution to inter-grain EBIC variation may be that of a position-dependent electrical junction depth which could influence collection. The position of the junction depends on the abruptness of the metallurgical interface and the doping concentrations on the two sides; variations in the concentration of impurities and the degree of CdS/CdTe interdiffusion may lead to non-uniformity in the position of the depletion region edge. Grains with a shallower junction will therefore collect more beam-generated carriers, yielding an increased induced current. This effect may also contribute to the bright boundary contrast observed (Figures 6.8-6.9), if the junction were closer to the front of the cell in the grain boundary regions. This is discussed further in Section 6.7.3. However, this mechanism alone would not explain satisfactorily the strong beam current dependence observed.

Low contrast images Low contrast was seen in the EBIC images of the chloride-treated cells at low beam currents (Figure 6.8a). At such beam currents the condition for high injection has not been reached, and injection is in the same regime as during solar irradiation. The lack of contrast seen indicates that some passivation of the grain boundaries has occurred. This is possibly caused by the filling of grain boundary states, resulting in trapped charge and causing band bending. For this to be effective the charge would have to be of the correct sign such that the resulting depletion region repels minority carriers from the grain boundary, reducing recombination. In addition, the grain boundary states that previously aided recombination are now filled and unavailable for electronic transitions. The observation of negligible grain boundary contrast under solar irradiation-like injection levels is a very important result for solar cells, as it indicates that the grain boundaries are not in themselves deleterious to device operation in chloride treated cells.

Of the various contrast effects discussed above, the beam current dependence of the grain boundary contrast is that least understood, and requires further analysis. The aims of sections 6.6 and 6.7 are firstly to analyse the general mechanism behind this effect; and secondly to present a model for the grain boundaries which will account for the observation of this effect in the CdTe/CdS solar cell.

6.6 ANALYSIS OF THE INJECTION LEVEL DEPENDENCE OF IMAGE CONTRAST

In this section the injection density dependence of the EBIC contrast is interpreted in terms of the threshold for high injection, *i.e.* the injection density required to exceed the equilibrium majority carrier concentration. This has been deduced from the data in three ways:

1. By estimating the overall EBIC contrast of the images determined from histograms of pixel values, and comparing these values for different values of I_{beam} (Section 6.6.1).
2. By measuring the contrast between specific bright and dark features on the image and noting how they change with I_{beam} (Section 6.6.2).
3. By examining how the EBIC signal varies with I_{beam} *for each pixel in turn*, and using this to find a beam current threshold for high injection for each point on the cell (Section 6.6.3).

6.6.1 Contrast analysis using pixel value distributions

The images in Figures 6.6-6.9 do not show the absolute level nor changes in the EBIC gain[†] that occurs with changing beam current. However, each pixel of the

---

[†] EBIC gain is the ratio of the EBIC signal to the beam current (see Section 3.5.5).

original images represents a quantitative measured EBIC value, with 1.6×10^5 such pixels per image. For a given image, the mean of these values will give an average EBIC value, which can then be studied as a function of the injection level. This information has been calculated from histograms of the pixels, and is shown for each of the four samples in Figure 6.10.

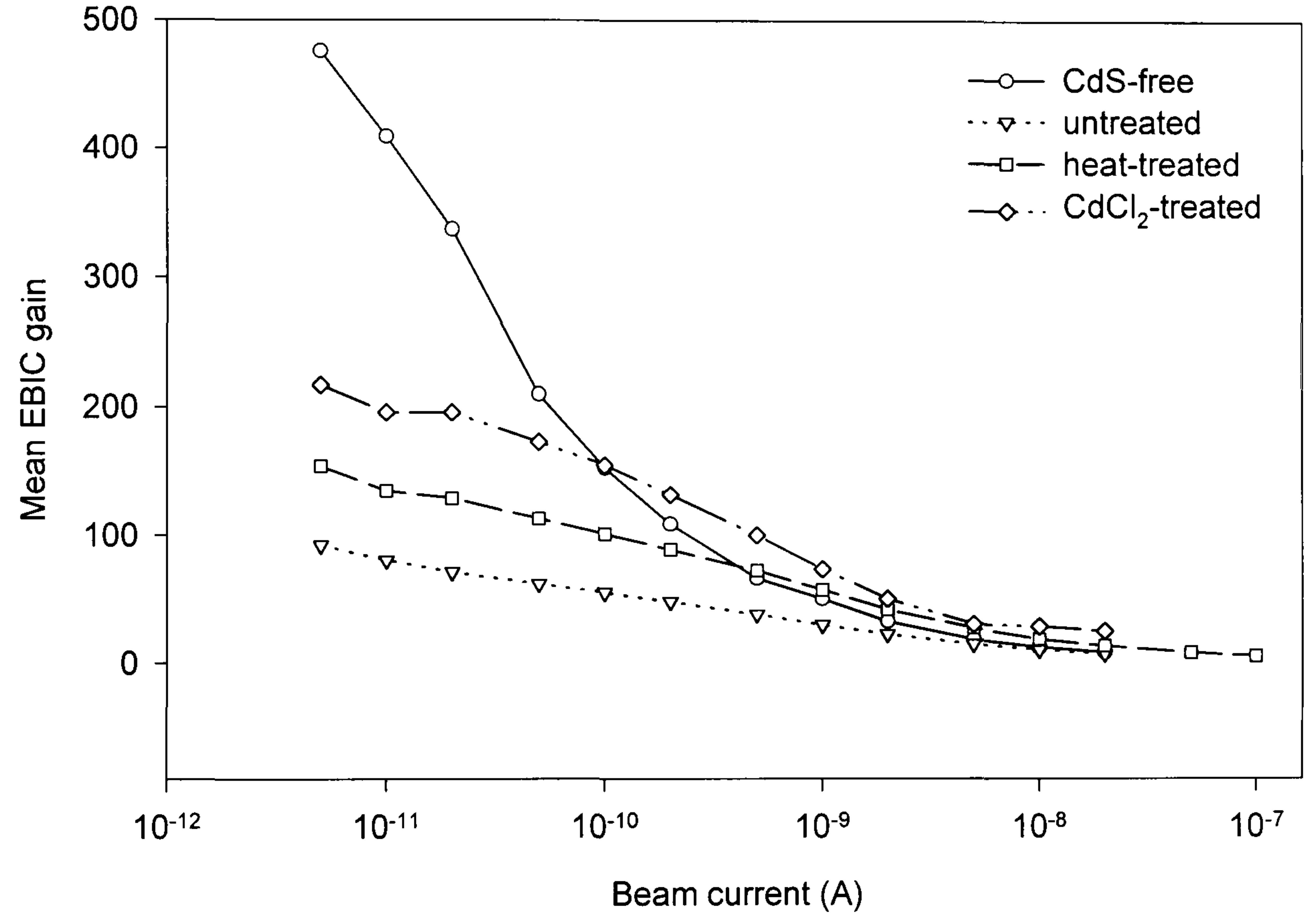

Figure 6.10 Variation of the mean EBIC gain with I_{beam}, as determined from histograms of image pixel values in Figures 6.6-6.9.

This shows that for all the cells the overall EBIC signal level decreases with increasing beam current, an effect attributed to the onset of high injection effects. At low values of I_{beam}, the CdS-free sample gives much larger EBIC signal than the full TCO/CdS/CdTe cells; this may be caused by the better collection of this device from the region in the cell close to the front-wall; this is seen later in Section 7.5. It should also be taken into consideration that the absolute EBIC values might not be directly comparable between cells. This is because the current may be subject to losses in the cell due to their fragile nature after the removal of the substrate. However, the variation of the EBIC signal level with treatment for the full cells is as expected.

A statistical measure of the amount of variation in EBIC across a sample can be obtained by determining the spread of the EBIC values. In this study, this has been carried out by calculating the standard deviation of the pixel histograms. These results appear in Figure 6.11.

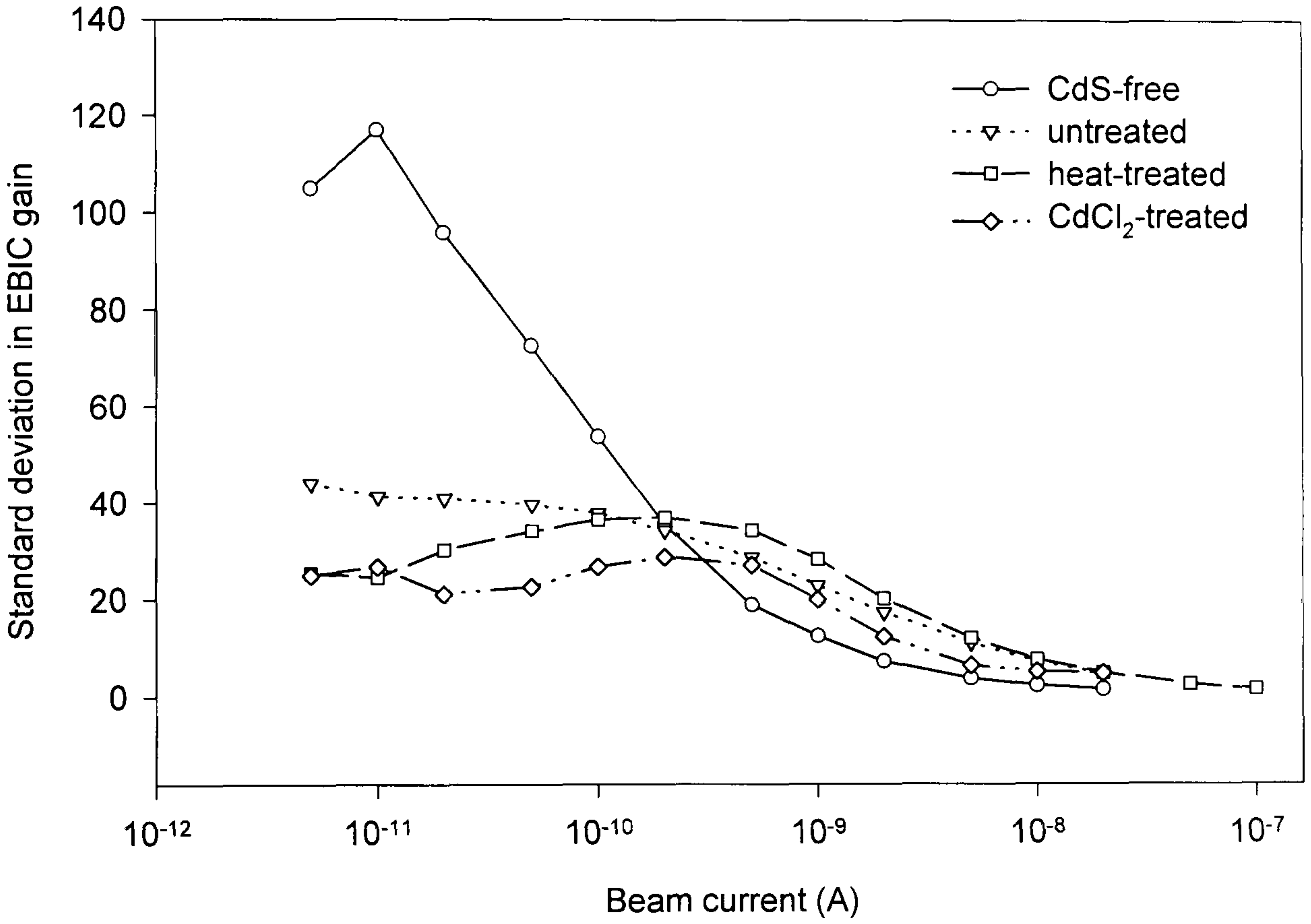

Figure 6.11 Standard deviation of the EBIC gain as a function of I_{beam}, as determined from histograms of image pixel values.

However, it is difficult to extract useful information from this data, as the overall EBIC signal level (as well as the standard deviation) varies with I_{beam}. To resolve this, a relative deviation has been estimated by dividing the standard deviation by the mean, *i.e.*:

$$\text{variation in EBIC} = \frac{\text{standard deviation in EBIC}}{\text{mean EBIC}} \qquad (6.4)$$

The resultant plots show much more clearly the effect of I_{beam} on the EBIC variation, as seen in Figure 6.12.

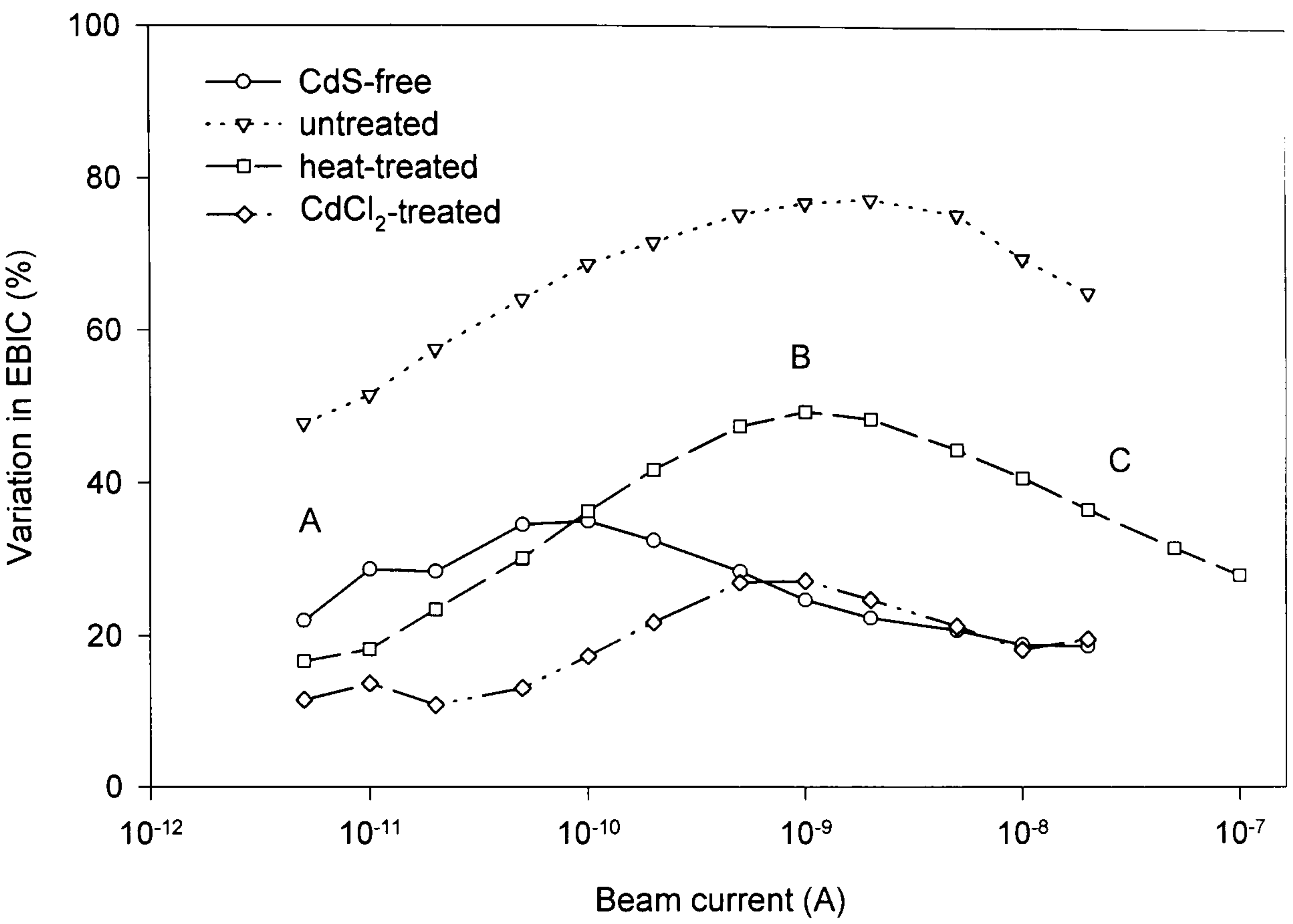

Figure 6.12 EBIC variation (as estimated from histograms of pixel values of EBIC images) as a function of the electron beam current. The three labels (A-C) denote different injection regimes referred to in the discussion in Section 6.7.

This data shows a similar pattern for each of the four samples investigated. EBIC variation is low at low beam currents (~10^{-11}A), rises by factor of ~2 with increasing I_{beam}, before decreasing again at higher currents (~10^{-8}-10^{-9}A). The position of the variation maximum differs between samples, with that of the CdS-free cell occurring at a beam current an order of magnitude below those of the three complete TCO/CdS/CdTe structures. Of the latter devices, the position of the variation maximum shifts to a lower beam current after heat treatment, and further still after the full chloride treatment.

The magnitude of the variation also changes between the differently treated samples, with the untreated, heat-treated and chloride-treated solar cells displaying successively less variation. In addition, the complete chloride-treated cell shows less variation than the corresponding CdS-free sample.

The advantage of this method of contrast analysis is that it is statistically based, and hence not susceptible to the same problems of signal noise encountered in the methods in the following sections. This is also, however, the major limitation of the technique, as it is a measure of average variation over the entire image area and may not accurately represent the contrast of the particular features of interest (*i.e.* grain features).

6.6.2 Analysis of contrast at individual grain boundaries

In order to test if the area-averaged results from Section 6.6.1 are valid for specific features, the contrast has been directly measured across several grain boundaries on the cell. This was achieved by sampling the current values at points on the EBIC images[†], using a square of 2×2 pixels. This was done either side of the grain boundary as well as on the boundary itself. The contrast was then calculated, applying the same convention used for measuring the EBIC contrast, C, at crystal defects:

$$C = \frac{I_p - I_D}{I_p} \qquad (6.5)$$

where I_D is the minimum EBIC current measured at the defect, and I_p is the current measured in a perfect crystal [6]. This is illustrated in Figure 6.13.

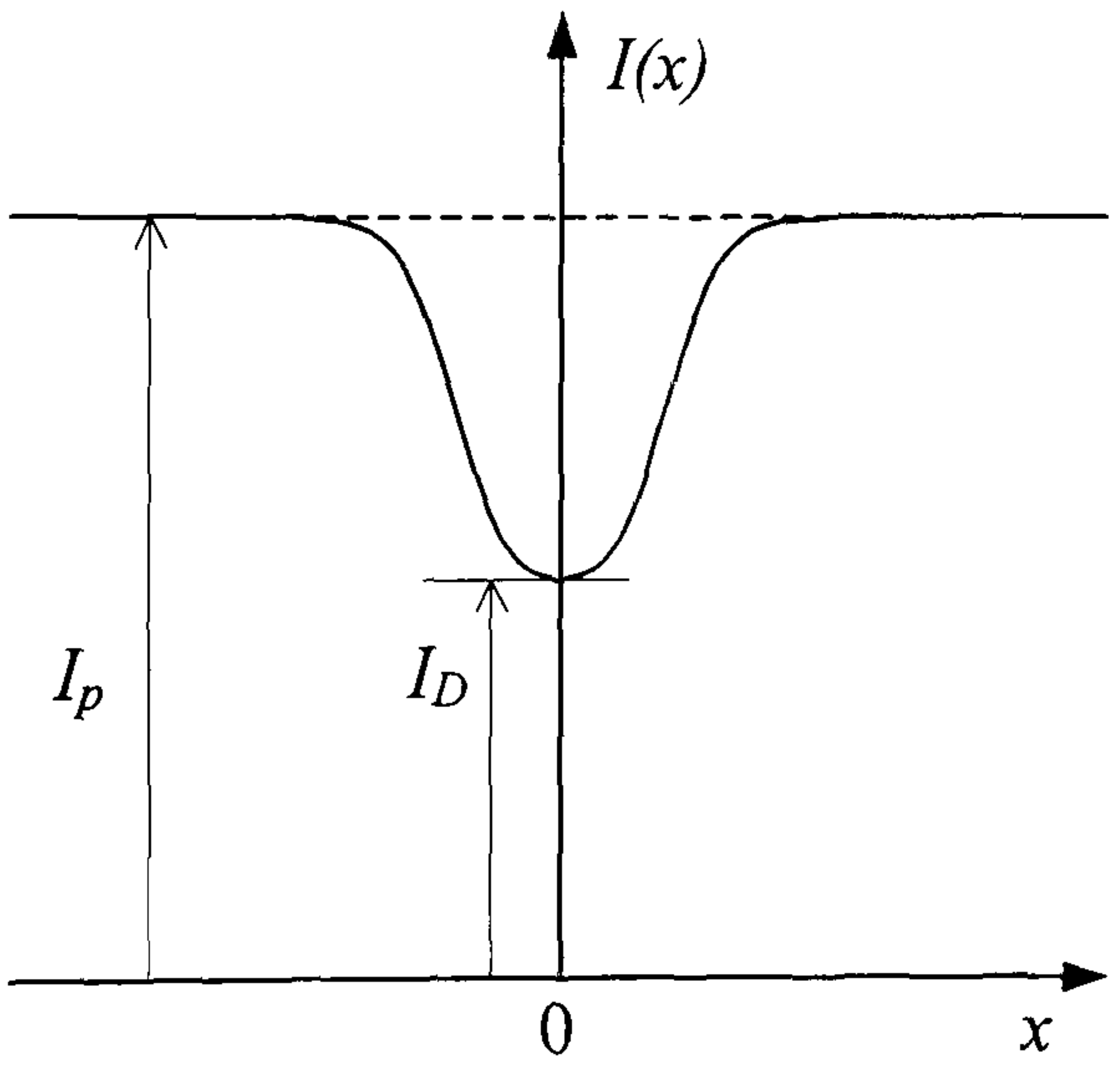

Figure 6.13 Conventional definition of EBIC contrast.

This convention yields positive contrast values for dark EBIC features, as would normally be the case for defects. The bright grain boundaries seen in some of the EBIC images therefore produce negative contrast values, as seen in the results for the cadmium chloride treated and CdS-free cells shown in Figures 6.14 and 6.15.

[†] Note that although this data was obtained from samples identical to those used earlier in this chapter, the EBIC images employed are not reproduced here. They may be seen in Edwards *et al.* [7].

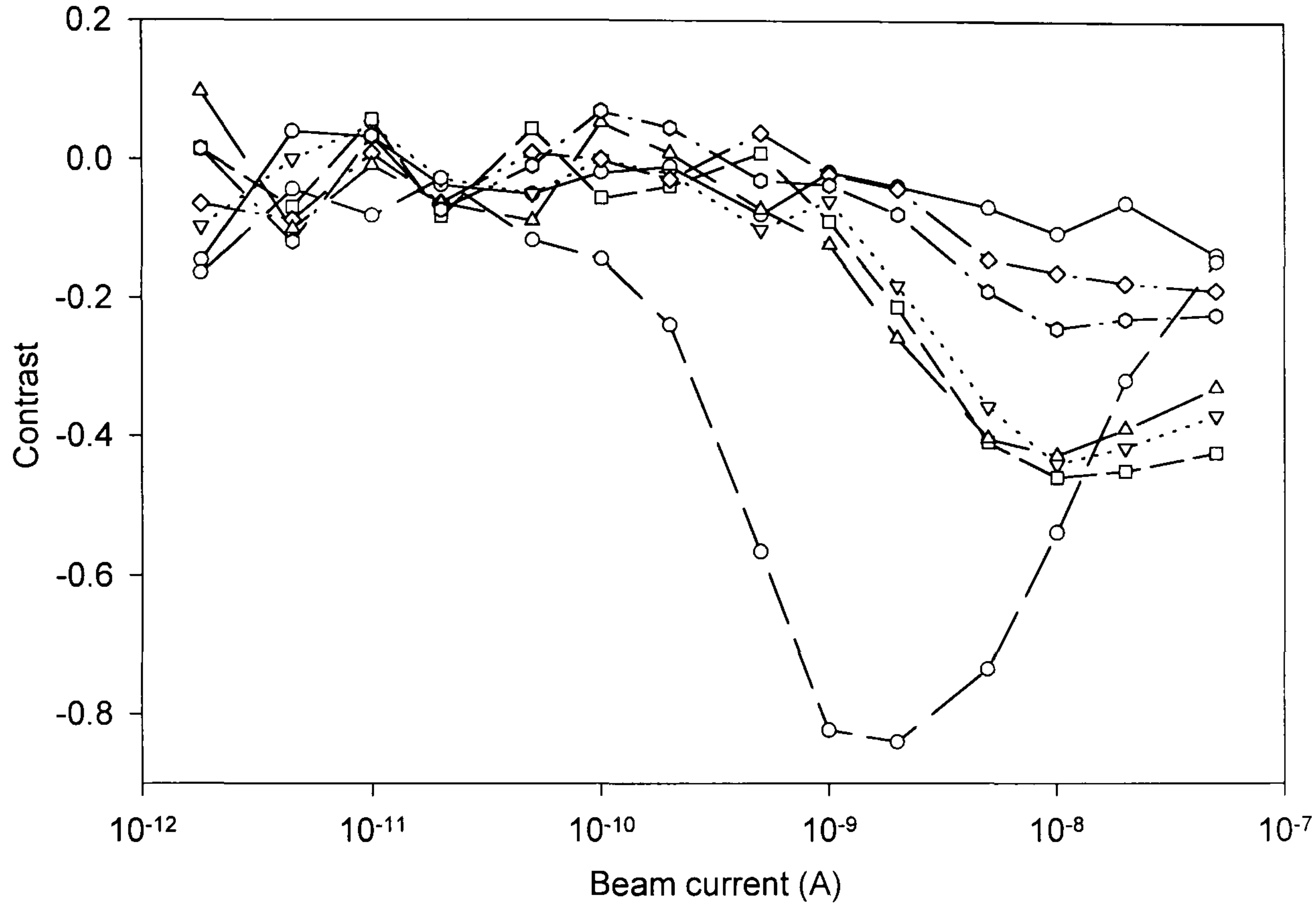

Figure 6.14 The EBIC contrast of various individual grain boundaries in the $CdCl_2$-treated cell as a function of I_{beam}.

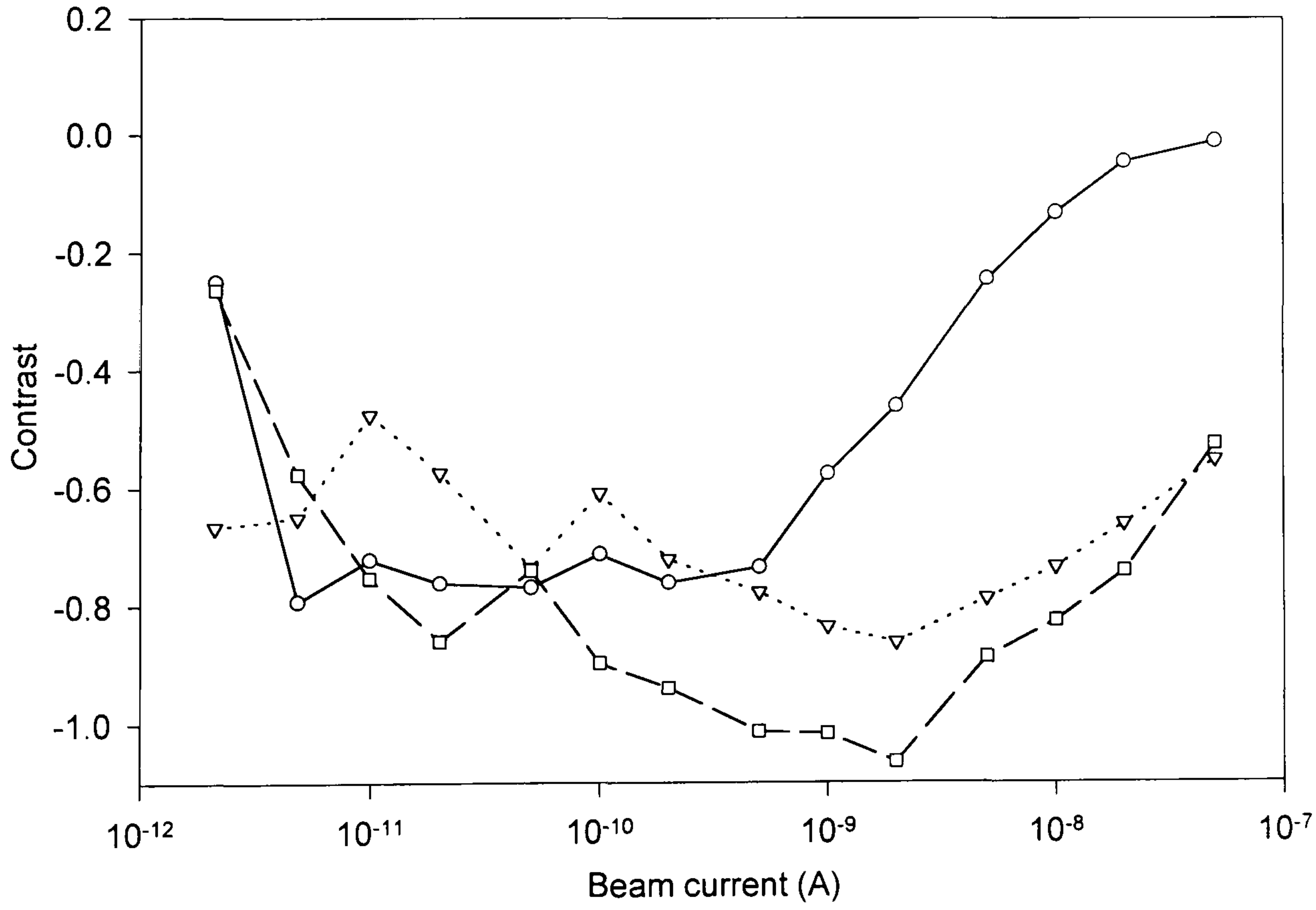

Figure 6.15 The EBIC contrast of various individual grain boundaries in the CdS-free cell as a function of I_{beam}.

Although more susceptible to noise than the results in Figure 6.12, the data for the individual grain boundaries shows similar characteristics to the statistical method of analysis. (The apparent inversion of the curves is a result of the lack of sensitivity to the sign of the contrast in the statistical method.) These results corroborate the observation that the contrast is low at low injection levels, increases with medium injection and then decreases again in the high injection regime. They also confirm that this effect occurs at lower beam currents for the sample without CdS (Figure 6.15) compared to the complete cell (Figure 6.14).

This method of analysis also shows that different features in the EBIC image vary with changing I_{beam} to a differing degree. This is seen, for example, in the fact that the plots in Figure 6.15 are not superimposed on one another. These variations were averaged together in the previous analysis method, giving the broadened peaks seen in Figure 6.13. An important advantage of this direct measurement method is that it enables a *particular type* of contrast and its beam current dependence to be analysed. Notably it has allowed the behaviour of the bright grain boundary contrast, observed only in $CdCl_2$-treated cells (both with and without CdS) to be measured directly.

6.6.3 Image analysis by injection threshold measurement

The final method of image analysis carried out on the EBIC data involved studying the beam current dependence of each pixel in turn. To illustrate the approach taken, quantitative linescans have been extracted from the EBIC images taken under the different beam currents. This linescan series is shown Figure 6.16, which shows data from the chloride-treated sample.

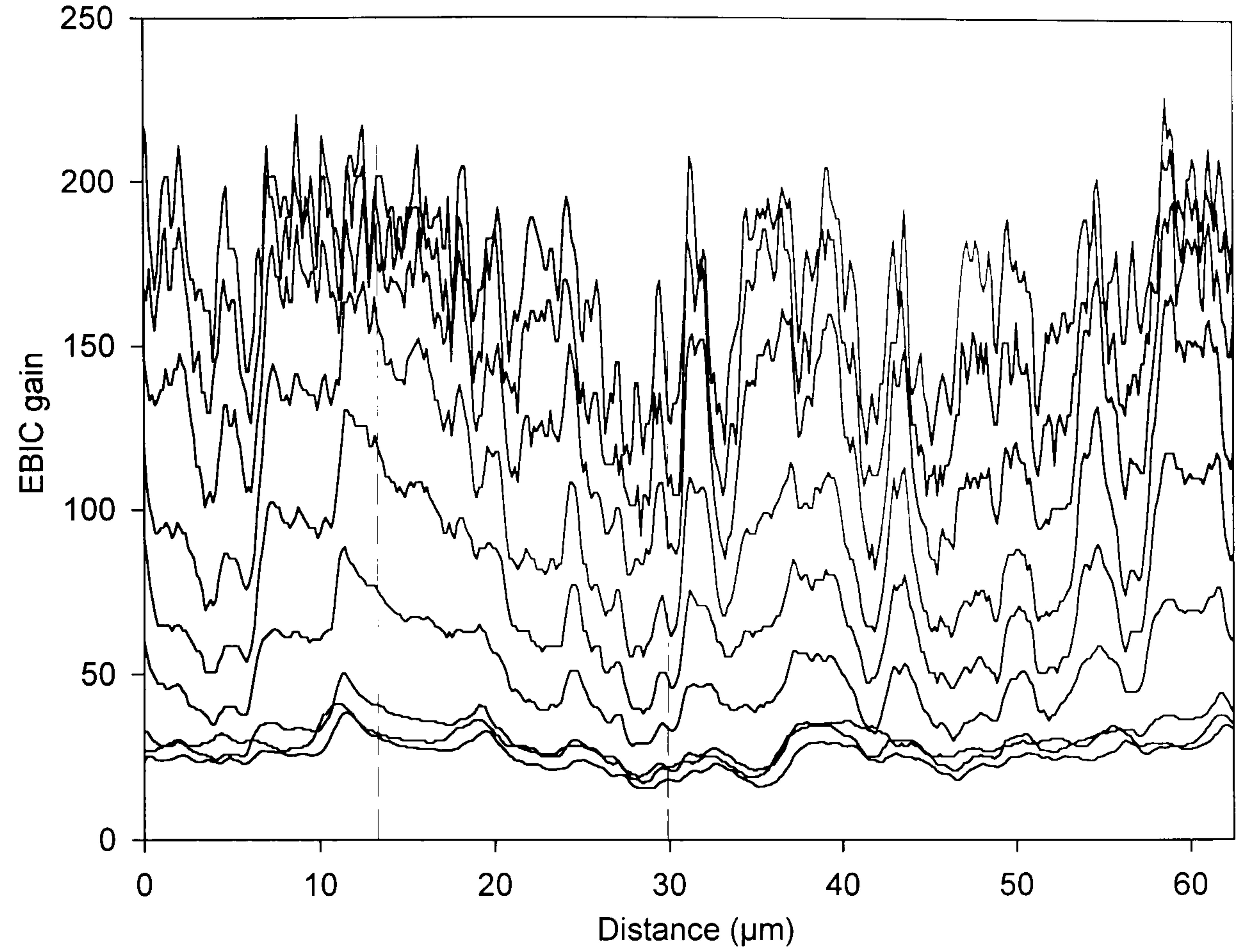

Figure 6.16 Linescans taken from EBIC images of the same position on the chloride-treated cell (Figure 6.8), as a function of I_{beam}. The lines correspond to values of I_{beam} of (from top to bottom): 50pA, 100pA, 200pA, 500pA, 1nA, 2nA, 5nA, 10nA and 20nA.

This data shows the decrease in EBIC gain over the entire region studied, due to the effect of high injection, as already seen in graph of the mean EBIC values in Figure 6.10. Moreover, the EBIC gain in different parts of the cell can be seen to vary with the beam current at different rates. In order to illustrate this more clearly, the EBIC gain *versus* beam current has been plotted in Figure 6.17 for two different points on the solar cell (indicated by vertical dashed lines in Figure 6.16).

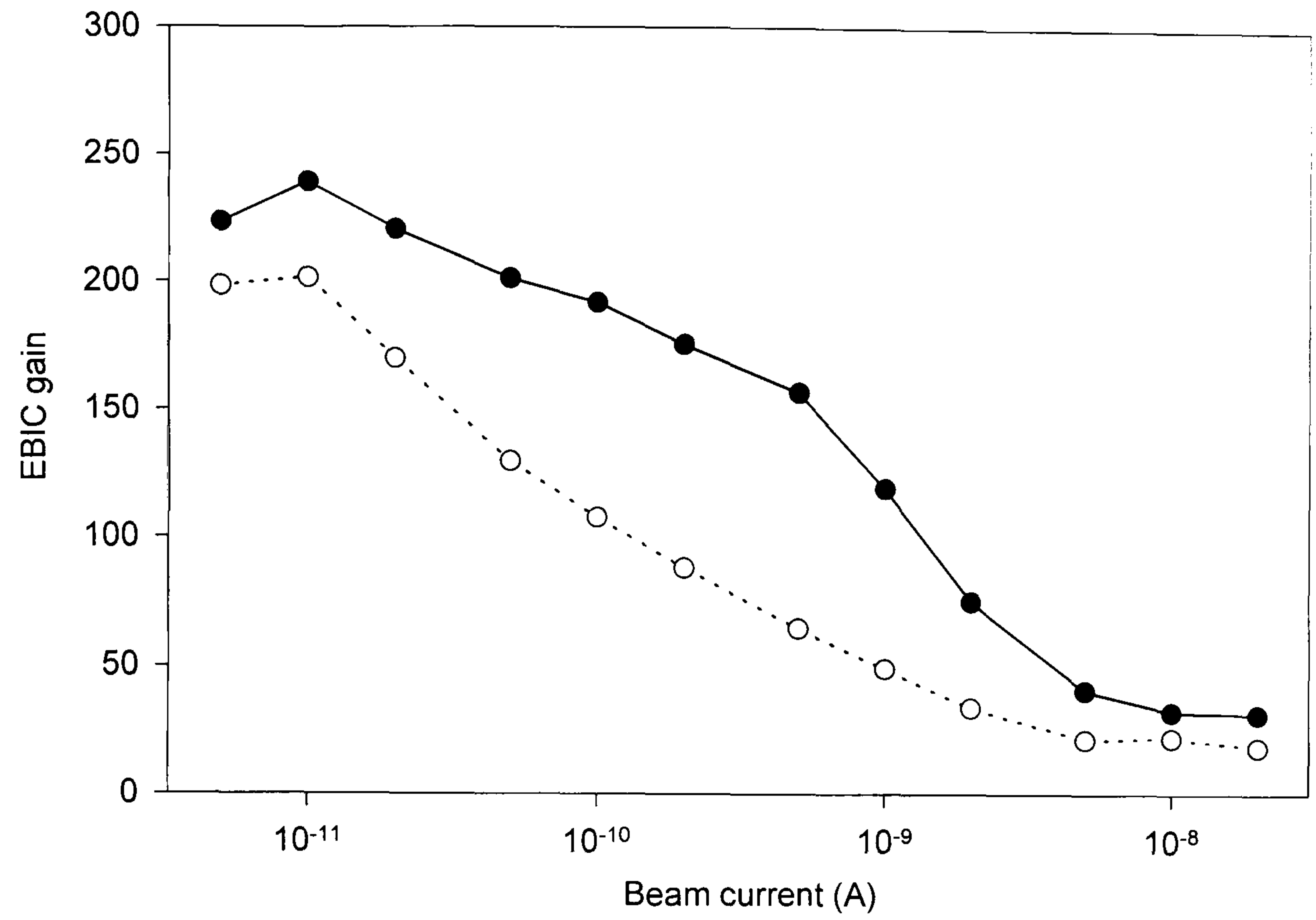

Figure 6.17 Variation of EBIC gain with beam current for two points on Figure 6.16, showing how the beam current needed to induce high injection varies at the two positions on the solar cell.

As has already been stated, the reduction in EBIC gain is effected when the probed area of semiconductor enters high injection conditions. By definition, these conditions occur when the number of injected carriers exceeds the equilibrium majority carrier concentration. In this work a "threshold" beam current has therefore been defined as the current at which the rate of decrease in EBIC is at its greatest; this value will, in principle, be related to the carrier concentration at that point on the device.

This threshold beam current has been evaluated for each point on the linescans in Figure 6.16. Computer software was written to estimate the point of inflection in the EBIC *versus* I_{beam} curve for each pixel. This worked by calculating the gradient of the line joining each adjacent point, giving a plot like that seen in Figure 6.18.

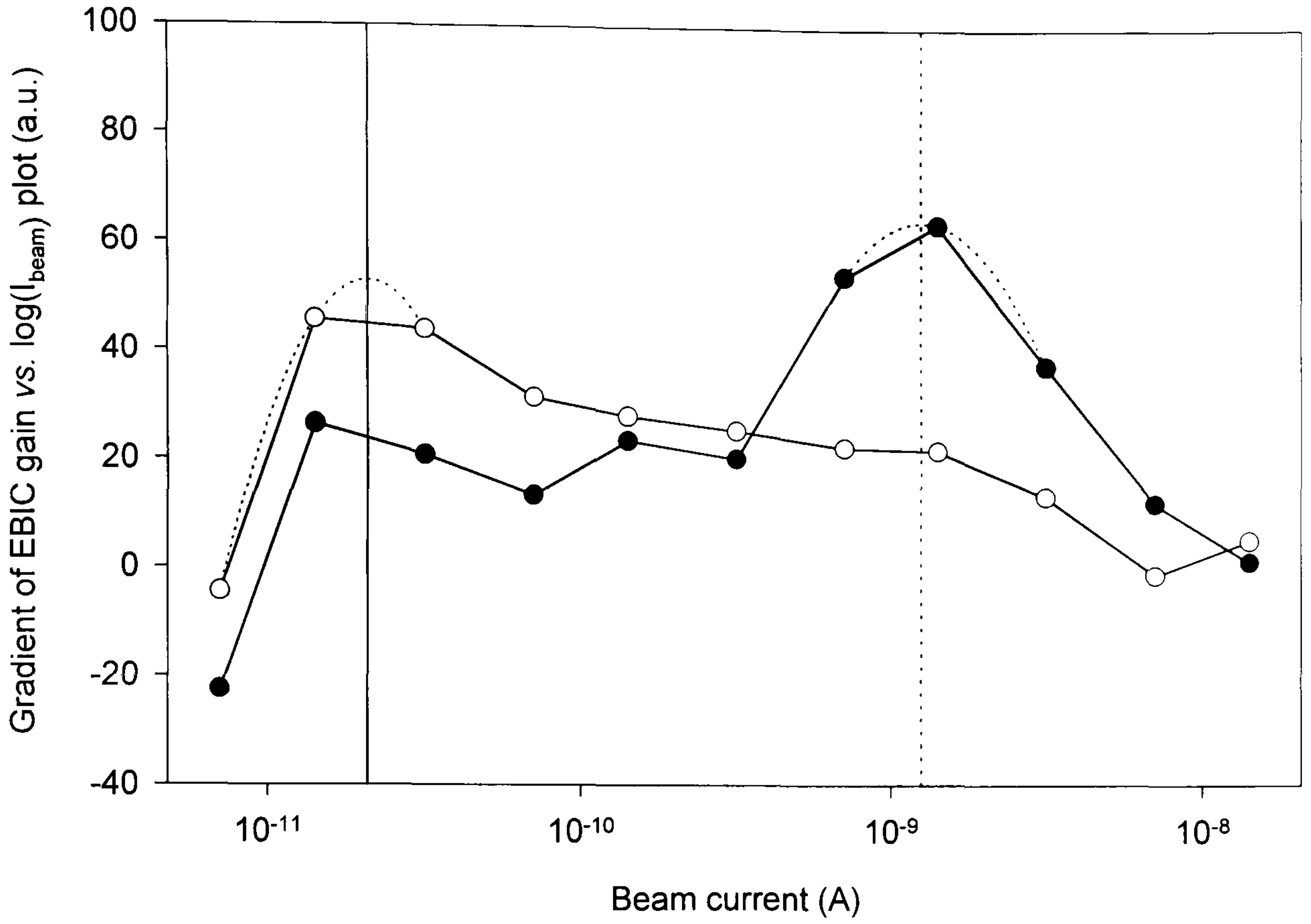

Figure 6.18 The result of the simple "differentiation" of the plots in Figure 6.17 with respect to I_{beam}. Parabolic fits to the peaks are shown, from which the points of inflection of the EBIC *vs.* I_{beam} plots were interpolated.

The point of inflection of the EBIC *versus* I_{beam} curve corresponds to the maximum in the differential plot. This point was estimated by fitting a parabola to the highest and two adjacent points, yielding a beam current threshold for high injection. The threshold values thus calculated were then reassembled to produce the linescan shown in Figure 6.19.

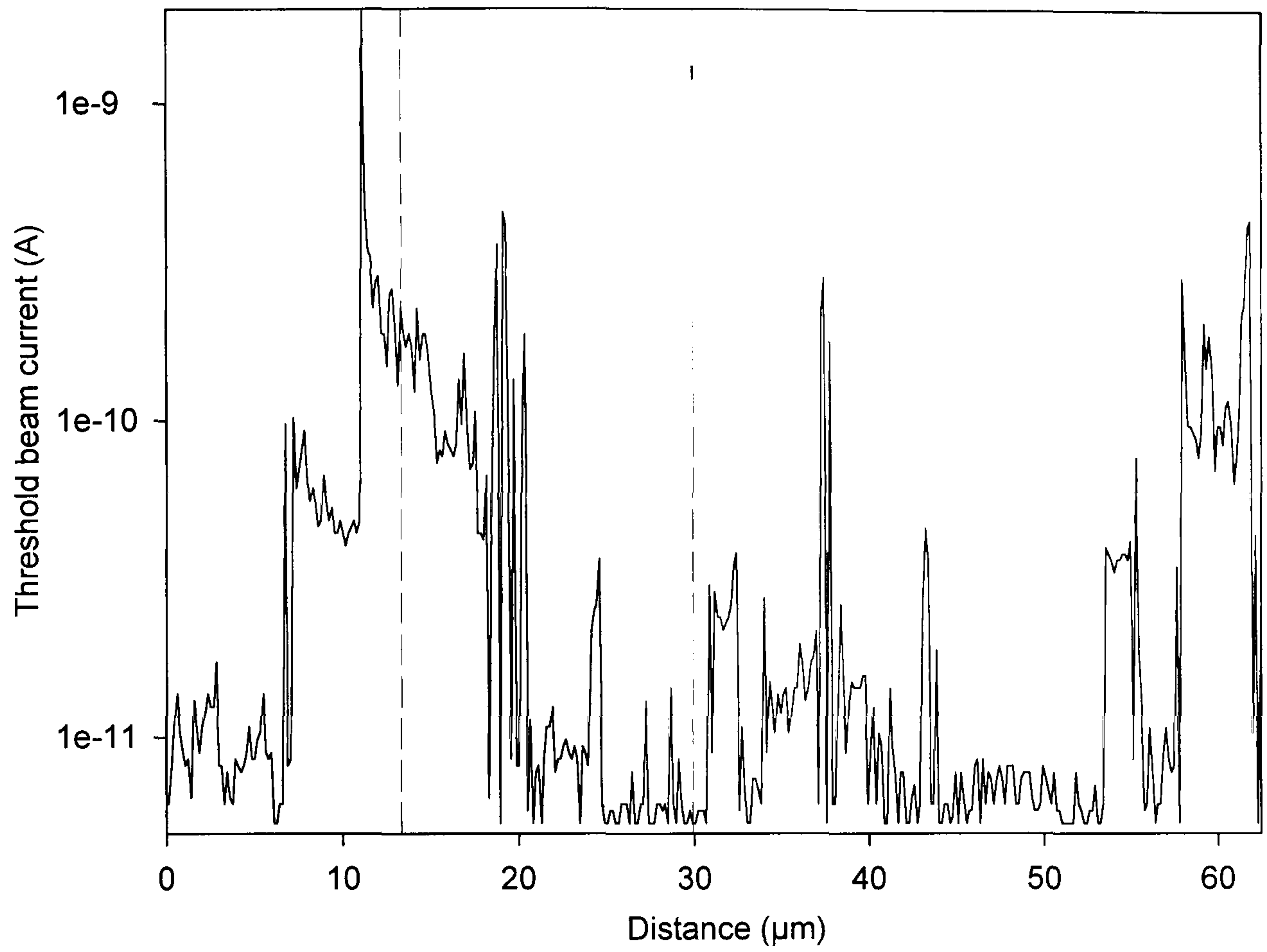

Figure 6.19 Linescan of calculated current threshold values assembled from data in Figure 6.16

According to the model, this data should now represent an uncalibrated carrier density linescan of the same region of the solar cell as the data in Figure 6.16. Despite its obvious susceptibility to the combined noise of the linescans from which it was assembled, nevertheless separate grains can clearly be identified.

The same principle used for the one-dimensional linescan has also been used to produce two-dimensional maps of the carrier concentration, using the data from the full EBIC images. The results of this are shown in Figure 6.20.

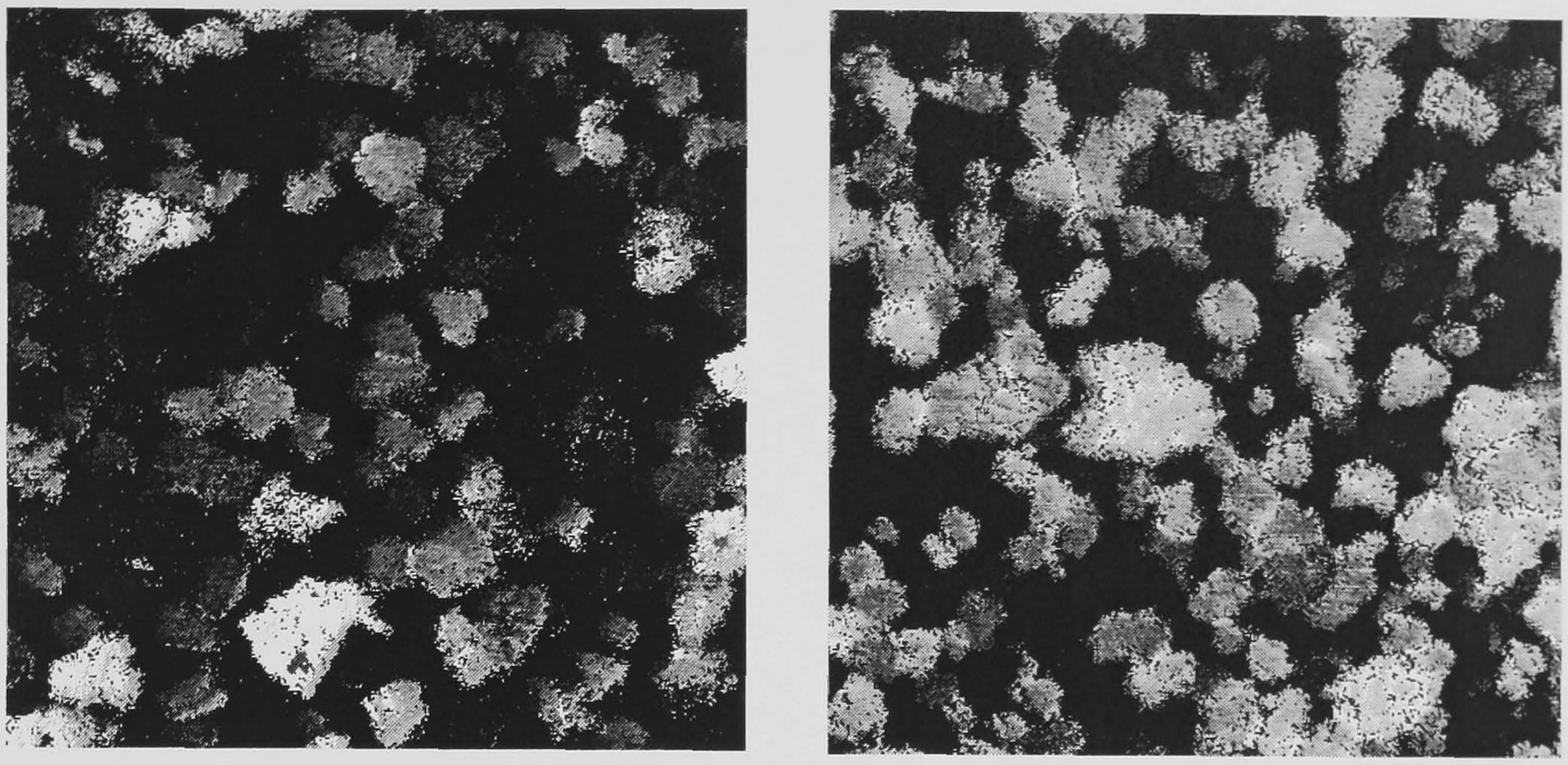

(a) As-deposited

(b) Heat-treated

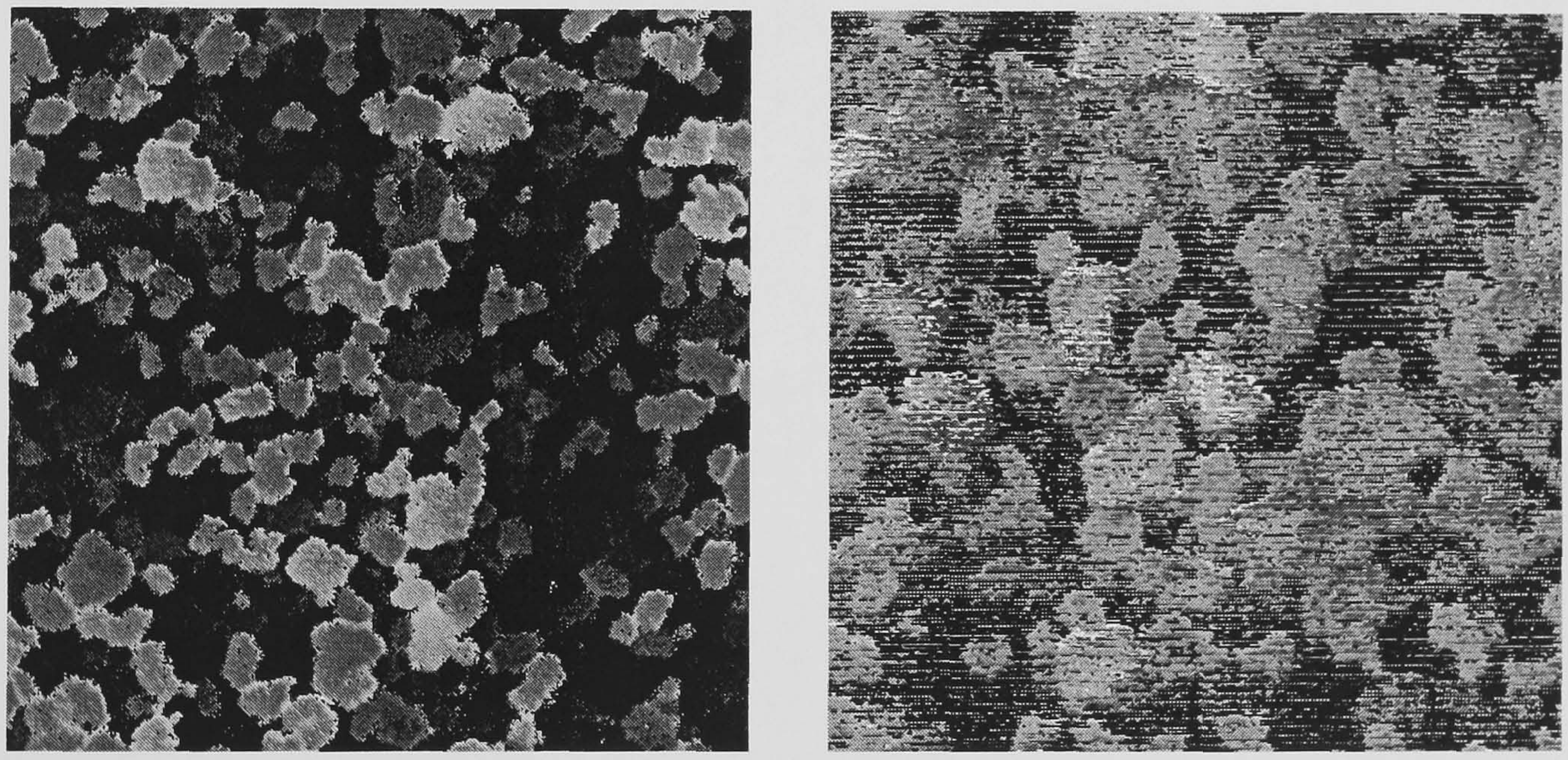

(c) Chloride-treated

(d) CdS-free

10μm

Figure 6.20 Current threshold map of the four cells, assembled from the data in Figures 6.2-6.5. These are essentially maps of the distribution of majority carriers in the device at equilibrium.(a) to (c) are shown with black-white corresponding to a beam current of 5pA-2nA , whilst for (d) the variation is only 5pA-50pA.

The as-deposited and heat-treated samples in Figures 6.20a-b show wide inter-granular variation in the concentration of majority carriers. Less variation is seen in the chloride-treated device (Figure 6.20c), but several of the grains do appear to have boundaries with higher carrier concentrations than the grain interior. This observation is significant to the model presented in the next section. The CdS-free sample (Figure 6.20d) shows much less variation; it should be noted that the full black-white scale used for this sample represents a smaller threshold range than for the other images.

6.7 DISCUSSION

6.7.1 Beam current dependence of EBIC contrast

High injection conditions are said to occur when the density of injected carriers in the probed region exceeds the equilibrium majority carrier concentration. These conditions are associated with the plasma effect which leads to marked reduction in the local EBIC signal. In this section, a mechanism is proposed in which this effect is responsible for the beam current dependence of the contrast observed in the front-wall EBIC images.

The explanation presented here has its basis in the assumption that different parts of the cell are associated with different carrier concentrations. Thus, for a given carrier injection density, some parts of the cell may be in high injection whilst other areas remain in low injection, giving areas of lower and higher EBIC collection respectively. This allows an explanation of the variation in EBIC contrast with increasing I_{beam}, seen in Figure 6.12. The labels A-C in this figure correspond to three distinct beam current regimes:

A) **Low I_{beam}** At low beam currents, the carrier injection density is sufficiently low for all areas of the cell to be in the low injection regime. Thus the only contrast seen in the EBIC images is that due to other mechanisms, *e.g.* carrier recombination.

B) **Medium I_{beam}** On increasing the beam current, some parts of the cell begin to enter high injection, and the EBIC values corresponding to these areas decrease. Other areas with higher equilibrium carrier concentrations are meanwhile still in low injection conditions. This leads to a greater variation in EBIC measured across the sample, yielding a higher value for the EBIC contrast.

C) High I_{beam} At still higher beam currents, even those areas with the higher majority carrier concentrations begin to enter high injection, and the entire device area is now in this regime. The EBIC signal level declines at all points, and this leads to a reduction in the EBIC contrast measured.

In the next section, this "high injection" model of contrast is used to discuss the particular case of bright grain boundary contrast in chloride treated cells.

6.7.2 A charge distribution model

If the above mechanism is proposed as the process behind the variation of EBIC contrast with I_{beam}, then its application to the case of bright grain boundary contrast in $CdCl_2$-treated cells points to a particular distribution of carriers within the solar cell. The contrast mechanism explains the behaviour well if it is assumed that in $CdCl_2$-treated cells the grain boundary regions are more *p*-type than the grain interiors.

Consider initially the results of the $CdCl_2$-treated complete cell. At low beam currents (Figure 6.8a), all areas of the cell are in low injection conditions. On increasing the beam current, the grain interiors enter high injection conditions, and the associated EBIC gain begins to decrease. The grain boundary regions, meanwhile, which are associated with a higher equilibrium carrier concentration, remain in low injection, leading to the appearance of bright grain boundary contrast (Figure 6.8b-c). On increasing the beam current still higher, the grain boundary regions themselves begin to enter the high injection regime as well, the EBIC signal level in all parts of the cell declines, and the bright contrast decreases (Figure 6.8d). If the threshold current map in Figure 6.20 is interpreted as being representative of carrier density, then it supports this conclusion, with higher concentrations of majority carriers (holes) around the grain perimeters.

Although all four of the samples studied show some variation in EBIC contrast with changing beam current, only the two $CdCl_2$-treated cells (with and without CdS) showed bright grain boundaries. It is therefore concluded that this bright grain boundary phenomenon is a result of the cadmium chloride treatment. The contrast effects seen in the as-deposited and heat-treated cells are likely to be due to a number of causes, such as recombination at defects, together with the high injection effects.

6.7.3 The origin of p^+-type boundary regions

The question of which acceptor or centre is responsible for the p^+ nature of the material near to the grain boundaries is part of the more general problem of how the so-called type conversion [8] from *n*-type to *p*-type is effected in the cell by the chloride treatment.

Although the presence of chlorine is now widely accepted as being necessary for this type conversion, it clearly does not act as a simple substitutional dopant. If this were the case, a chlorine atom on a tellurium site would produce *n*-type material. A centre often cited as being responsible is a complex formed between a chlorine atom on a tellurium site and a cadmium vacancy, *e.g.*

$$\left[\mathrm{V}_{\mathrm{Cd}}^{2+}\mathrm{Cl}_{\mathrm{Te}}^{-}\right]^{+}$$

This complex is known to act as an acceptor in crystalline CdTe:Cl [9,10], and is also thought to be the centre behind type conversion in CdTe/CdS thin-film solar cells [11]. Preferential diffusion along grain boundaries might be expected to lead to higher local impurity (and hence carrier) densities.

This concept of grain boundary regions being more *p*-type in nature is also consistent with a possible passivation mechanism. Figure 6.21 shows a likely band diagram for an unpassivated grain boundary. The presence of the boundary states causes band bending. This attracts minority carriers (in this case electrons), which combine more readily via the grain boundary states than they would for simple band-to-band recombination.

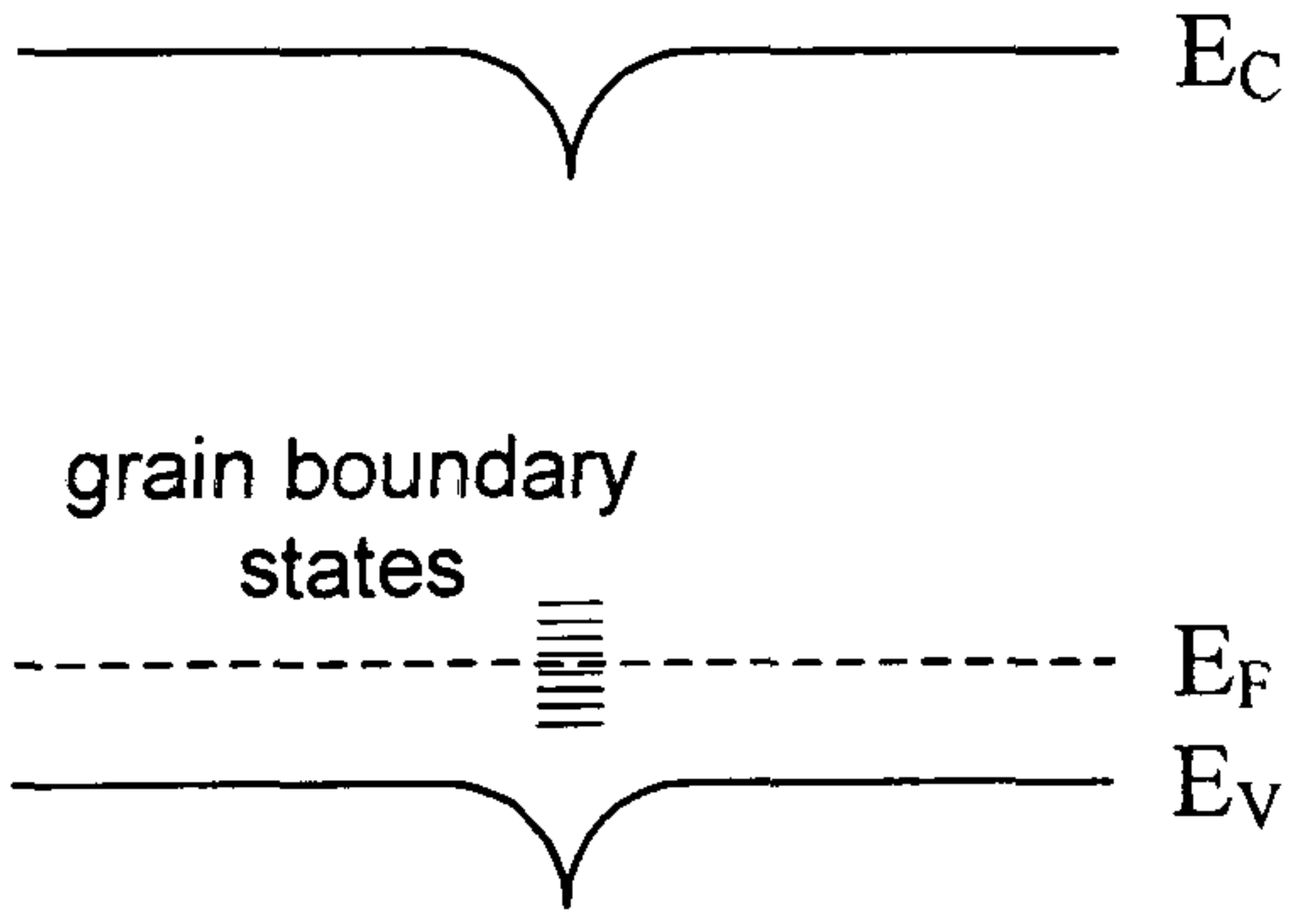

Figure 6.21 Possible band diagram for unpassivated grain boundary in *p*-type material.

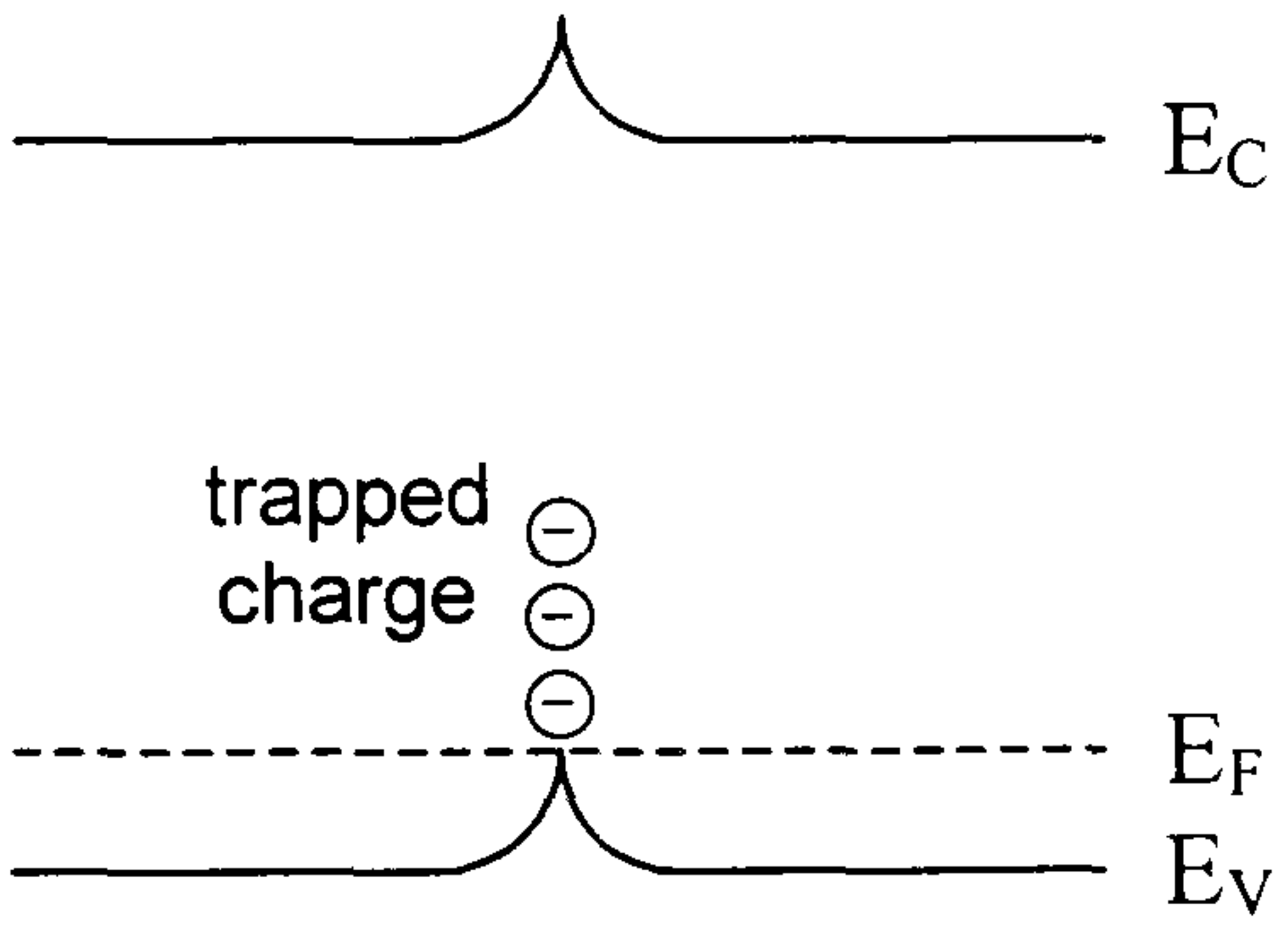

Figure 6.22 Possible band diagram for passivated grain boundary in *p*-type material.

If the grain boundaries states are now filled they are no longer available to aid recombination. In addition, the resultant trapped charge can influence the bending of the bands: a possible band diagram is shown in Figure 6.22. This would result in the repulsion of minority carriers (electrons), with the result being grain boundary passivation. This is not only in agreement with the low EBIC contrast seen for the $CdCl_2$-treated solar cell at low beam currents, but is also consistent with the grain boundary regions being effectively p^+ in nature.

Since the width of the depletion region in the CdTe depends on the hole concentration, spatial variations in the latter will lead to variations in the depth-dependent collection function across the cell. This can lead to contrast in front-wall EBIC images, as described in Section 6.5.2. However, the same effect may also be responsible for features seen in the back-wall images. Figure 6.23 illustrates this idea, with the width of the depletion region showing both inter-grain and grain boundary variations.

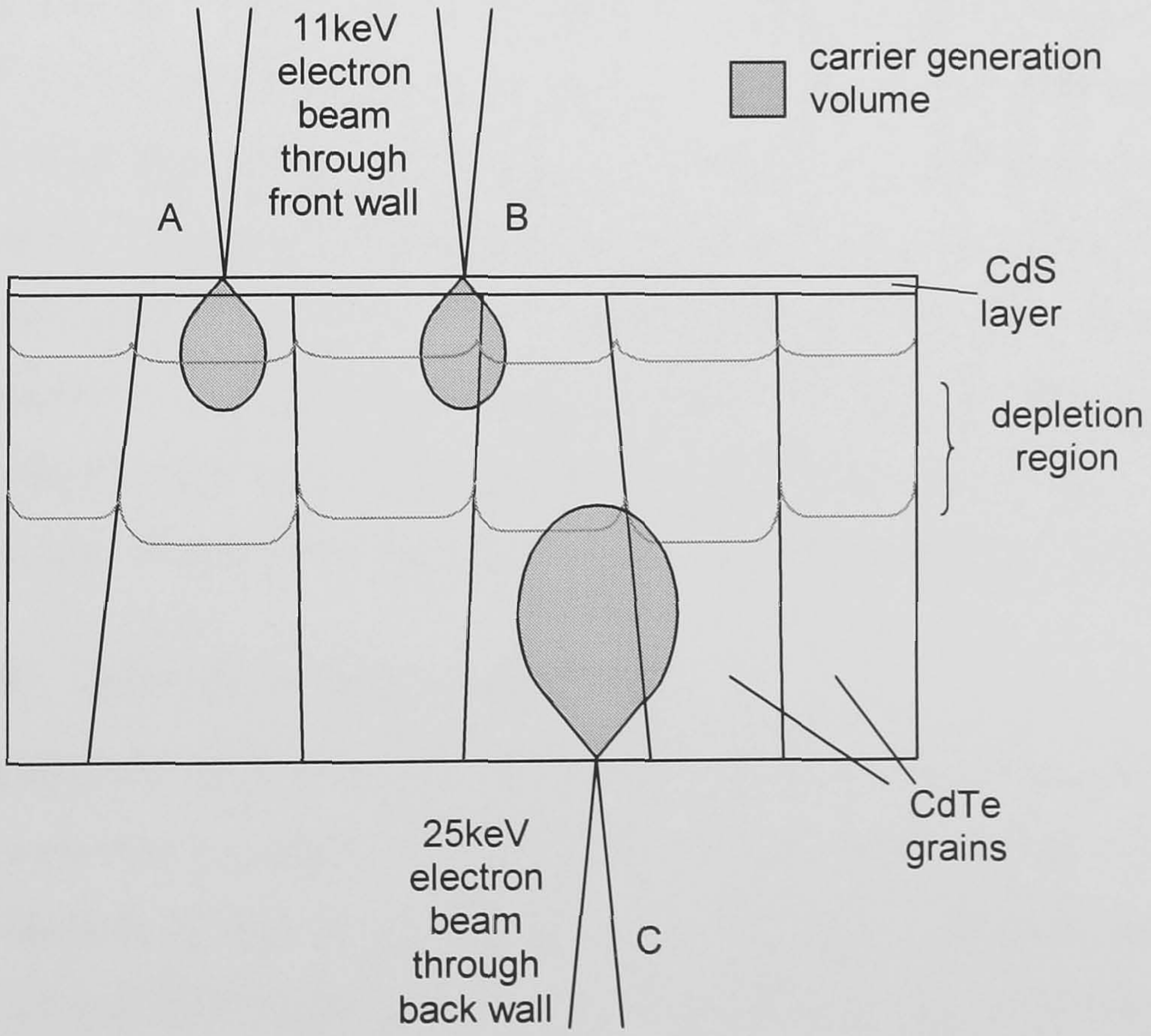

Figure 6.23 Diagram showing the effect of doping variations on the effective depth of the collecting junction.

The higher the concentration of acceptors in the *p* side of the device, the shallower the buried homojunction will be, and also narrower the region of space charge will be on this side of the junction. (The existence of such a buried homojunction will be demonstrated from the results of Section 7.5.) Thus the p^+ material near the grain boundaries will result in a narrower depletion region which is closer to the CdS than in the *p*-type grains. In the front-wall configuration, an electron beam in position A will, therefore, induce a lower current than that in position B, due to a greater number of carriers being generated within the depletion region. There will therefore be a difference between the EBIC signal strengths in different CdTe grains, as well as enhanced collection at the grain boundaries. The variation in the position of the depletion region will have a similar but reversed effect on the back-wall EBIC (beam position C), with dark grain boundaries evident. This is consistent with Galloway's results in Figure 6.1, further supporting the proposed carrier distribution.

Independent evidence of the grain boundary perimeters having higher conductivity is provided by Woods *et al.* [12], who carried out frequency-dependent resistivity and temperature-dependent current measurements on CSS grown CdTe/CdS devices. Their results showed an acceptor concentration of around $7\times10^{14}\text{cm}^{-3}$ in the bulk material, increasing to $\sim7\times10^{17}\text{cm}^{-3}$ in the vicinity of grain boundaries. The band model they proposed included a potential barrier to majority carriers, which although not observed in the present work is not inconsistent with the results presented here. The factor of 10^3 increase in the doping concentration near the grain boundaries is also significant, as this is approximately the same increase seen in the threshold beam current seen at grain boundaries in this work. This further supports the idea that this threshold is related to the equilibrium carrier density.

6.7.4 The role of sulphur diffusion

A comparison of the two chloride-treated cells, with and without the CdS layer, shows the influence of sulphur on the carrier concentrations in the device. Both the statistical analysis (Figure 6.12) and the direct boundary contrast measurements (Figures 6.15 and 6.16) show that the onset of high injection conditions begins to occur at beam currents orders of magnitude lower in the CdS-free device. Moreover, the beam current at which the contrast then starts to decrease again is also correspondingly lower. According to the postulated mechanism for injection density-dependent contrast, this indicates that the concentration of majority carriers is lower in the CdS-free cell than in the corresponding device with CdS, both in the grains and in the boundary regions. This conclusion is supported by the evidence of the beam current threshold maps in Figures 6.20(c-d), and demonstrates the important contribution made to the doping in the CdTe of electrically active species from the sulphide layer. Diffusion across the CdTe/CdS interface will be examined further in Section 8.2.

6.8 CONCLUSIONS

Front-wall EBIC investigations have been carried out on CdTe/CdS solar cells after different post-deposition treatments. The results of these measurements using low electron beam currents show that one effect of the $CdCl_2$ treatment is to passivate the grain boundaries in the polycrystalline CdTe layer.

The front-wall EBIC images have been seen to exhibit a strong dependence on the electron beam current used. The EBIC contrast has been analysed, both for individual grain boundaries and for entire images, with both showing maxima at the mid injection regime. This effect is attributed to high carrier injection effects coupled with spatial differences in the doping concentration, and analysis of each image pixel in turn has been used to produce speculative majority carrier concentration maps.

The use of this technique before and after the post-deposition treatment of these devices indicates that a further effect of the $CdCl_2$ treatment is to make the regions of the device near to grain boundaries more *p*-type. This contributes to the bright EBIC contrast seen at the grain boundaries under some beam conditions. The effect may be related to the grain boundary passivation mechanism, and in addition would lead to a position-dependent depletion region. This latter phenomenon is consistent with the grain boundaries being bright in front-wall EBIC images and dark in the back-wall configuration.

The presence of the CdS layer has been seen to increase significantly the overall concentration of holes in the CdTe. This observation confirms the importance to device performance of the diffusion of species across the CdTe/CdS interface.

REFERENCES FOR CHAPTER 6

[1] S.A. Galloway, P.R. Edwards and K. Durose (1999) *Characterisation of thin film CdS/CdTe solar cells using electron and optical beam induced current*, Solar Energy Materials and Solar Cells **57** pp.61-74

[2] S.A. Galloway and K. Durose (1995) *SEM/EBIC observations of CdTe/CdS thin film solar cells*, Institute of Physics Conference Series **146** pp.709-712

[3] R.H. Kenny, J.C. McClure and V.P. Singh (1988) *Electron beam induced currents in thin-film CdS-CdTe heterojunction cells*, Proceedings of 8th E.C. Photovoltaic Solar Energy Conference, Florence. Vol.II pp.1097-1101

[4] J. McClure, C. Chung and V. Singh (1990) *Grain-boundary effects in the EBIC response of thin-film solar cells*, Solid State Communications **75** (3) pp.171-173

[5] G.J. Russell, P. Waite, J. Woods and K.L. Lewis (1981) *Electrically active grain boundaries in polycrystalline zinc selenide*, Institute of Physics Conference Series **60** pp.371-376

[6] D.B. Holt *"The conductive mode"* in *SEM Microcharacterisation of Semiconductors*, edited by D. B. Holt and D. C. Joy, (Academic Press, London, 1989) p.298

[7] P.R. Edwards, D.P. Halliday and K. Durose (1997) *The influence of* $CdCl_2$ *treatment and interdiffusion on grain boundary passivation in CdTe/CdS solar cells*, Proceedings of 14th European Photovoltaic Solar Energy Conference, Barcelona, pp.2083-2086

[8] B.M. Basol (1992) *Processing high efficiency CdTe solar cells*, International Journal of Solar Energy **12** pp.25-35

[9] A. Rohatgi (1992) *A study of efficiency limiting defects in polycrystalline CdTe/CdS Solar Cells*, International Journal of Solar Energy **12** pp.37-49

[10] K. Zanio *"Cadmium Telluride"* in *Semiconductors and Semimetals*, Vol.13, edited by R. K. Willardson and A. C. Beer, (Academic Press, New York, 1978)

[11] S.A. Ringel, A.W. Smith, M.H. MacDougal and A. Rohatgi (1991) *The effects of $CdCl_2$ on the electronic properties of molecular-beam epitaxially grown CdTe/CdS heterojunction solar cells*, Journal of Applied Physics **70** (2) pp.881-889

[12] L.M. Woods, D.H. Levi, V. Kaydanov, G.Y. Robinson and R.K. Ahrenkiel (1998) *Electrical characterization of CdTe grain-boundary properties from as processed CdTe/CdS solar cells*, Proceedings of 2nd World Conference on Photovoltaic Solar Energy Conversion, Vienna, pp.1043-1046

Chapter 7: Variation of EBIC with beam voltage

7.1 INTRODUCTION

The position and nature of the collecting junction are technologically important issues in CdTe/CdS solar cells. A better understanding of the metallurgical and electrical properties of the interface region would in principle allow the deposition and processing of the devices to be engineered such that the regions of highest carrier generation and collection in the cell coincide. This would help to optimise the photovoltaic conversion efficiency of the junction.

Determining the depth-dependent collection function of such a complex polycrystalline structure is not trivial. Ideally, a point source of excess carriers would be injected at a known depth z, and the collection probability $F(z)$ simply determined from the resultant current induced. As this is not possible, more complex depth-dependent carrier generation methods must be used. Such a method is the widely used spectral response experiment, in which the induced current is measured as a function of the wavelength of light used to illuminate the sample. This method has the advantage that it can be carried out via the glass substrate. However, the extraction of depth-dependent collection data depends on an accurate knowledge of the optical absorption coefficients as a function of wavelength, for not only the CdS and CdTe layers, but also the alloyed interface region.

For this reason, an electron beam analogue of the spectral response method has been used in this study. Since the penetration of the electron beam through a sample is a function of the accelerating voltage, the current induced under beams of different energy can be used to probe the carrier collection through the device thickness. Spectral response results are also reported to allow comparison of the two techniques.

7.2 CARRIER COLLECTION THEORY

The current induced by injecting mobile carriers into a collecting junction can be calculated by integrating the generation and collection functions over the width of the device. This remains valid irrespective of the origin of the excess carriers injected. The present work is dependent on the fact that, although the generation function differs, the probability of collection for a carrier at a given depth in the solar cell is the same under an electron beam as it is under solar irradiation. This is true as long as low injection conditions prevail. In its most general form the current I induced in a solar cell by the injection of excess carriers may be expressed as:

$$I = \int_0^\infty g(z)F(z)\,dz \tag{7.1}$$

where *g(z)* is the rate of generation of carriers per unit depth at depth z (by whatever mechanism) and *F(z)* is the probability of carrier collection at that position.

Since carrier collection is effected by the built-in electric field in the depletion region of the device, it is from this part of the cell that the collection probability is expected to be highest. Little current is contributed by the CdS window layer of the device, due to its low minority carrier lifetime and high carrier concentration [4]. Collection from the quasi-neutral CdTe layer beyond the space-charge region will be determined by the minority carrier diffusion length in this part of the device.

7.3 ELECTRON BEAM GENERATION OF CARRIERS

In order to later deconvolute the results of EBIC *versus* beam voltage experiments, an accurate profile must be obtained of how many carriers are produced at a particular depth in the sample for given electron beam conditions. This section briefly outlines the theory behind this, and reviews the various empirical and numerical methods available for modelling carrier generation functions.

7.3.1 The interaction of an electron beam with matter

A high energy electron travelling through a solid material undergoes both inelastic and elastic scattering along its path. In a semiconductor, one of the inelastic scattering mechanisms is that of impact ionisation. This is the process whereby an electron colliding with an atom has sufficient kinetic energy to break the lattice bonds, creating an electron-hole pair [1]. The ionisation energy e_i required for this to happen is approximately three times the bandgap of the material. Using this fact, it is possible to calculate the total number of electron-hole pairs ΔN generated in a sample for given beam conditions:

$$\begin{aligned} \Delta N &= \begin{matrix}\text{number of beam electrons} \\ \text{absorbed per second}\end{matrix} \times \frac{\text{energy per beam electron}}{\text{energy required per e-h pair}} \\ &= (1-f)\frac{I_b}{q} \times \frac{E_b}{e_i} \end{aligned} \tag{7.2}$$

where f is the fraction of beam electrons that are backscattered from the sample.

However, Equation 7.2 only yields the total number of carriers generated in the sample. In order to interpret fully the EBIC *versus* beam voltage results, the *depth-dose function* is required. This is defined as the number of carrier pairs generated per unit volume as a function of depth through the sample.

7.3.2 Analytical expressions for depth-dose function

Grün [2] studied the luminescence of air under an electron beam, and found that while electrons of a higher energy penetrated further, the depth-dose curve retained a similar shape when normalised to the beam energy. He defined a characteristic length to describe the depth of penetration of the beam, which he fitted to an empirical expression. This is known as the Grün range, R_G, and is given in μm by the equation:

$$R_G = \left(\frac{3.98 \times 10^{-2}}{\rho}\right) E_b^{1.75} \tag{7.3}$$

where the beam energy E_b is expressed in keV† and the density of the material ρ is in gcm^{-3}. Everhart and Hoff [3] incorporated this parameter into a semi-empirical function for the shape of the depth-dose curve:

---

† Since the energy of an electron (in keV) is equal to the accelerating voltage (in kV) through which it has been accelerated, these two parameters and units are used interchangeably when referring to the primary (beam) electrons

$$h(\xi)=0.60+6.21\xi-12.4\xi^2+5.69\xi^3 \tag{7.4}$$

where $$\xi=\frac{z}{R_G}$$

This is the most widely used analytical expression for energy deposition as a function of depth. Scheer [4] has modified this expression to account for multiple layers in his work on chalcopyrite solar cells. Another commonly used expression is that by Wu and Wittry [5], who used a modified Gaussian for their studies on Si and GaAs Schottky barriers. However, the use of analytical expressions in all but the simplest of systems has now been largely superseded by the introduction of Monte Carlo simulations.

7.3.3 Monte Carlo simulation of carrier generation

The Monte Carlo method is a general statistical technique used to simulate the motion of a large number of particles in a medium. It involves the consideration of one particle at a time, a trajectory for which is calculated with the use of random numbers. The calculation is then repeated for a statistically large number of particles, in order to be representative of the process.

The generation of electron-hole pairs in the sample was modelled using Monte Carlo simulation software developed by Napchan and Holt [6]. This program uses as its basis known semi-empirical expressions to calculate possible trajectories of a beam electron through the sample as it undergoes elastic and inelastic scattering. Repeating this for several thousand electrons yields quantitative information about the rates of secondary electron emission, primary electron backscatter and energy deposition in the sample. The software allows samples to be defined as series of layers of different materials. An example of this is given in Figure 7.1, which shows a 20keV electron beam impinging onto the front-wall of a typical CdTe/CdS solar cell, comprising of 50nm ITO, 100nm CdS and thick layer of CdTe.

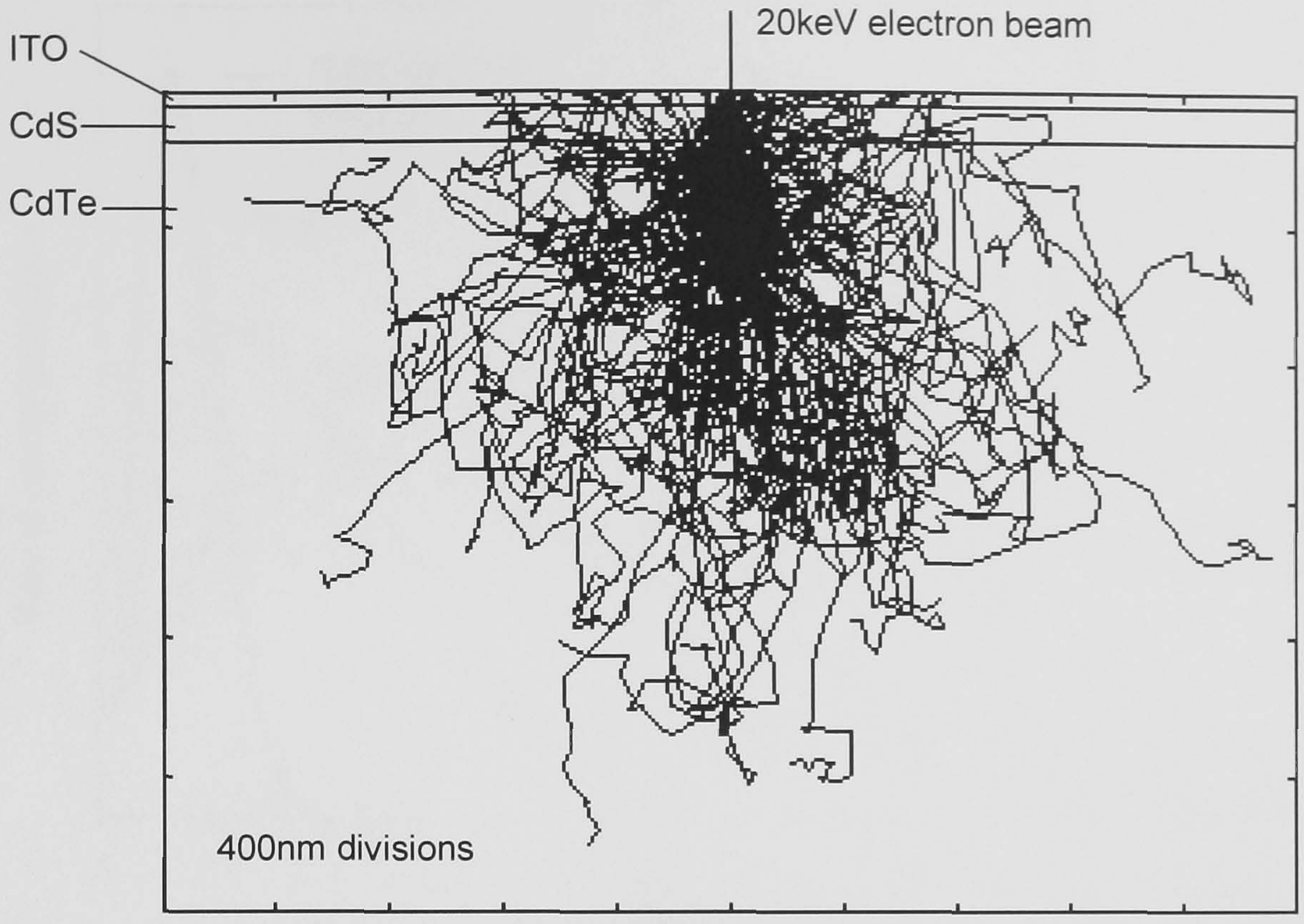

Figure 7.1 Electron trajectories simulated using Napchan's Monte Carlo software. This example shows the interaction of a 20keV electron beam with an ITO/CdS/CdTe solar cell structure via the front-wall.

This shows the 3-dimensional trajectories of 200 electrons projected onto a 2-dimensional plane. For fitting to the experimental data, simulations using 2×10^4 electrons were used to produce smoother depth-dose functions. A selection of such functions can be seen in Figure 7.2.

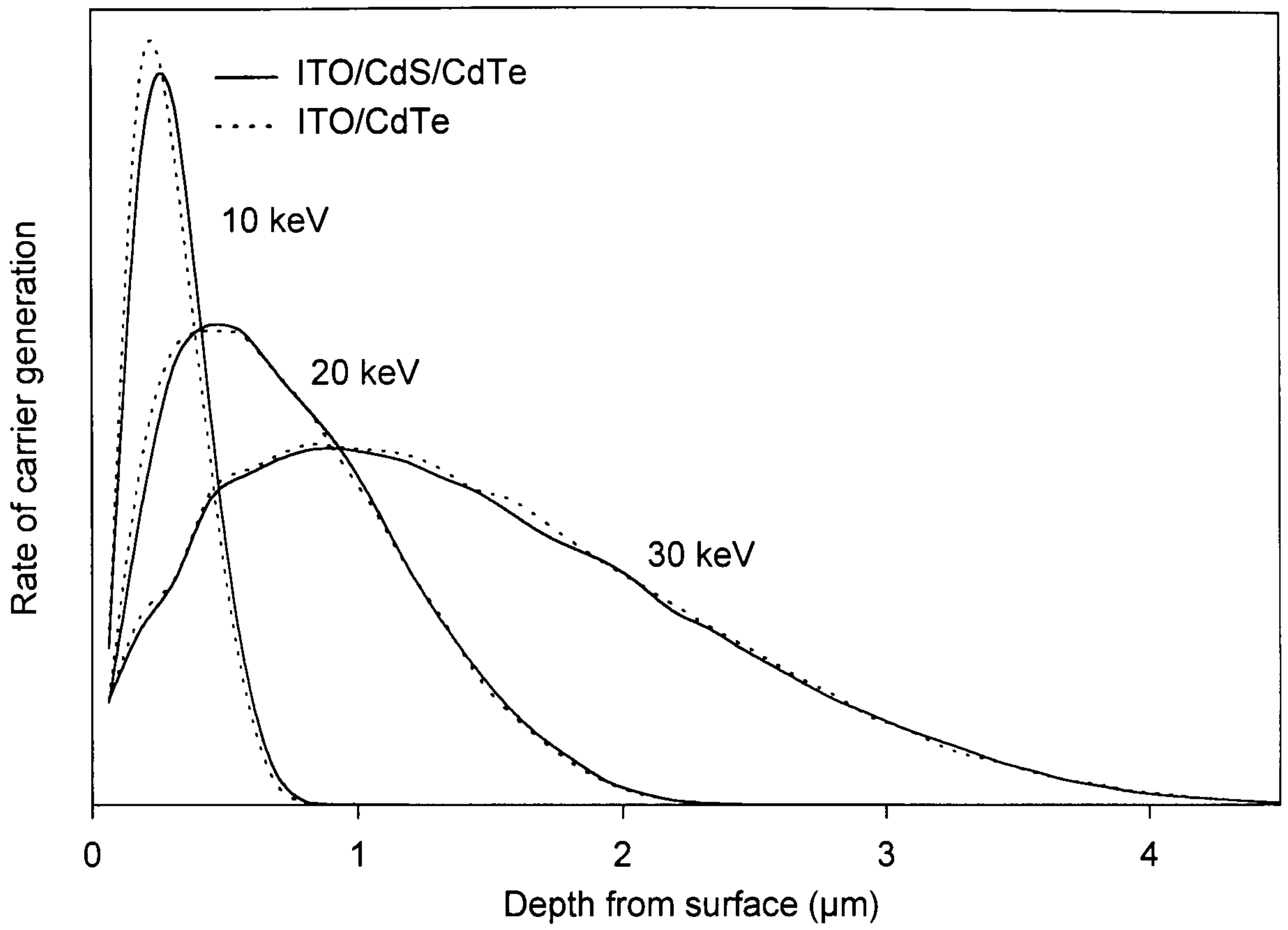

Figure 7.2 Depth-dependent generation functions for a front-wall ITO/CdS/CdTe solar cell and a CdS-free device under electron beams of three different accelerating voltages. These functions were simulated using Monte Carlo software, using 2×10^4 electron trajectories for each curve.

This software has previously been employed in the interpretation of voltage-dependent EBIC measurements by Grünbaum *et al.* [7], who used the technique to evaluate the minority carrier diffusion length in single-crystal III-V solar cells.

7.3.4 Comparison with photogeneration of carriers

Optical absorption in solar cells is dominated by single photon, intrinsic absorption, *i.e.* the excitation of electrons from the valence to the conduction band. Since the rate of photon absorption is proportional to the photon flux, this therefore has a depth dependence given by the simple exponential equation:

$$\Gamma(\lambda,z)=\Gamma_0(\lambda)e^{-\alpha(\lambda)z} \tag{7.5}$$

where z is the depth through the sample, $\Gamma_0(\lambda)$ is the incident photon flux at $z=0$ and $\alpha(\lambda)$ is the wavelength-dependent absorption coefficient of the material. From Equation. 7.5 it is possible to obtain the depth-dependent carrier generation function, $g(\lambda,z)$. The rate of electron-hole pair generation will be the same as the rate of photon absorption, which at depth z will be equal to the rate of change with depth of the number of photons absorbed *before* z, *i.e.*:

$$\begin{aligned} g(\lambda, z) &= \frac{d}{dz}\left[1 - \Gamma(\lambda, z)\right] \\ &= \alpha(\lambda)\Gamma_0(\lambda)e^{-\alpha(\lambda)z} \end{aligned} \tag{7.6}$$

For non-degenerate, direct bandgap semiconductors (including CdS and CdTe), the absorption coefficient α for photon energies near the bandgap varies in an approximately parabolic manner: [8]

$$\alpha(\lambda) = \alpha_0\left(\frac{hc}{\lambda} - E_g\right)^{0.5} \tag{7.7}$$

where α_0 is a constant and the photon energy hc/λ is above the optical bandgap E_g. At higher energies, where the absorption deviates from this rule, this work uses experimental values taken from the literature: [9,10] for CdTe and [11] for CdS. Using these absorption spectra with Equation 7.6 leads to the monochromatic carrier generation functions seen for a CdTe/CdS heterostructure seen in Figure 7.3.

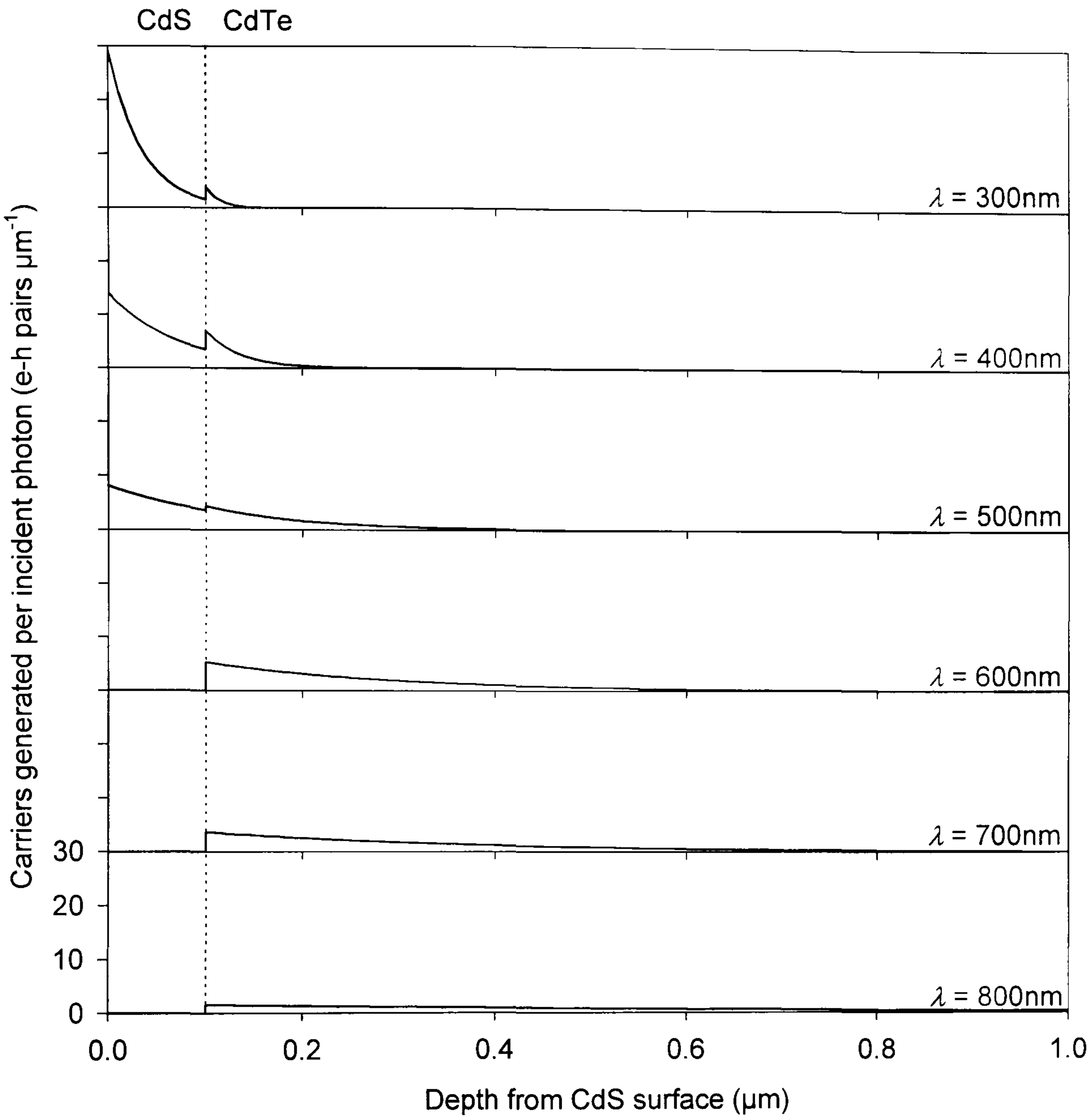

Figure 7.3 Carrier generation functions calculated for a CdTe/CdS heterostructure with different wavelengths of light.

The carrier generation rate for a device under solar irradiation $g_{AM1.5}(z)$ was calculated using the data in Figure 7.3 integrated over the solar spectrum:

$$g_{AM1.5}(z) = \int_{\text{all}\lambda} g(\lambda, z)\Gamma_{\text{AM1.5}}(\lambda)\,dz$$

where the photon flux $\Gamma_{AM1.5}(\lambda)$ under standard AM1.5 solar illumination is that quoted by Fahrenbruch and Bube [12]. The resultant carrier generation function is shown in Figure 7.4.

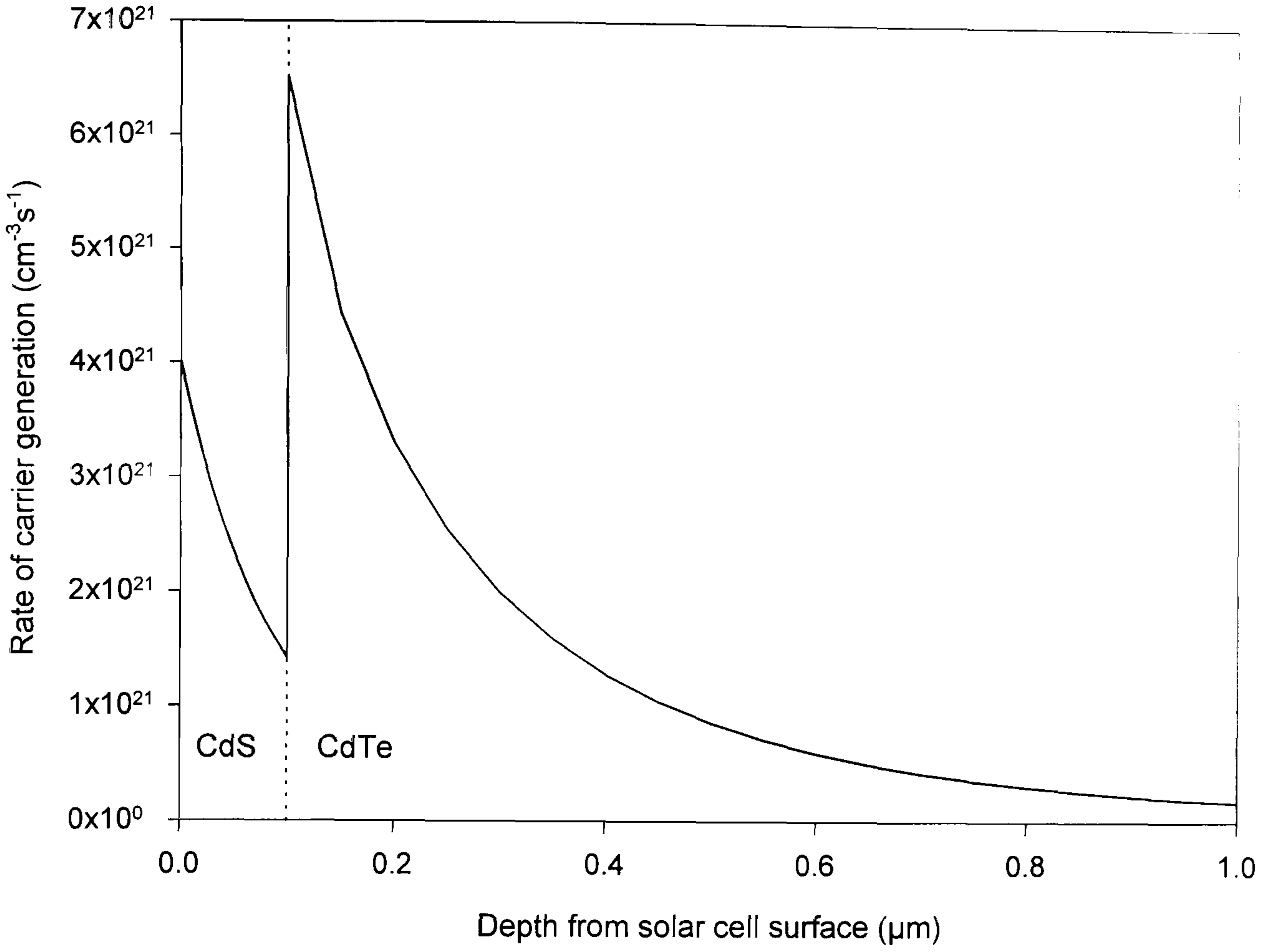

Figure 7.4 Calculated carrier generation function for CdTe/CdS heterojunction under standard AM1.5 solar irradiation.

Although the shape of the carrier generation function in the cell under sunlight differs considerably from that under an electron beam (Figure 7.2), the two were found to match most closely when an electron beam voltage of 11kV was used. It was for this reason that all the measurements in Chapter 6 used this accelerating voltage.

7.4 EXPERIMENTAL DETAILS: EBIC

The measurements were carried out on the same samples used for front-wall imaging in Chapter 6 and described in detail in Section 6.3.1. A similar experimental arrangement was also used (as shown in Figure 6.4), with the exception of the beam conditions employed.

Short circuit EBIC values were measured as a function of the electron beam accelerating voltage between 1kV and 35keV, for each of the four samples. The experiments were carried out with a widely defocused beam, to reduce the carrier injection density and hence eliminate the possibility of high-injection plasma effects occurring. The beam current was adjusted for each reading in order to give a constant beam power of 1μW. In order to obtain an EBIC value averaged over a relatively large area, a fast raster scan with dimensions of ~100μm was selected in preference to a stationary spot.

7.5 RESULTS: EBIC

Figure 7.5 shows the measured EBIC gain as a function of accelerating voltage. The general shape of these curves is broadly characteristic of a deep collecting junction. The following descriptions correspond to the regions on the graph labelled A-C.

A) At low electron energies (up to ~5keV), the electron beam does not penetrate deep enough into the sample for carriers to be collected by the device junction.

B) On increasing the accelerating voltage (~5-20kV), the carrier generation function begins to extend into the depletion region of the device, whence the carriers are collected with a high efficiency. This results in an increase in the induced current measured

C) At even greater beam voltages (~20-35kV), the depth-dose function begins to penetrate through the other side of the cell's depletion region. Depending on the minority carrier diffusion length of the absorber region, this can result in either a decrease in the measured signal (as seen for the untreated device) or a plateau (as for the $CdCl_2$-treated device).

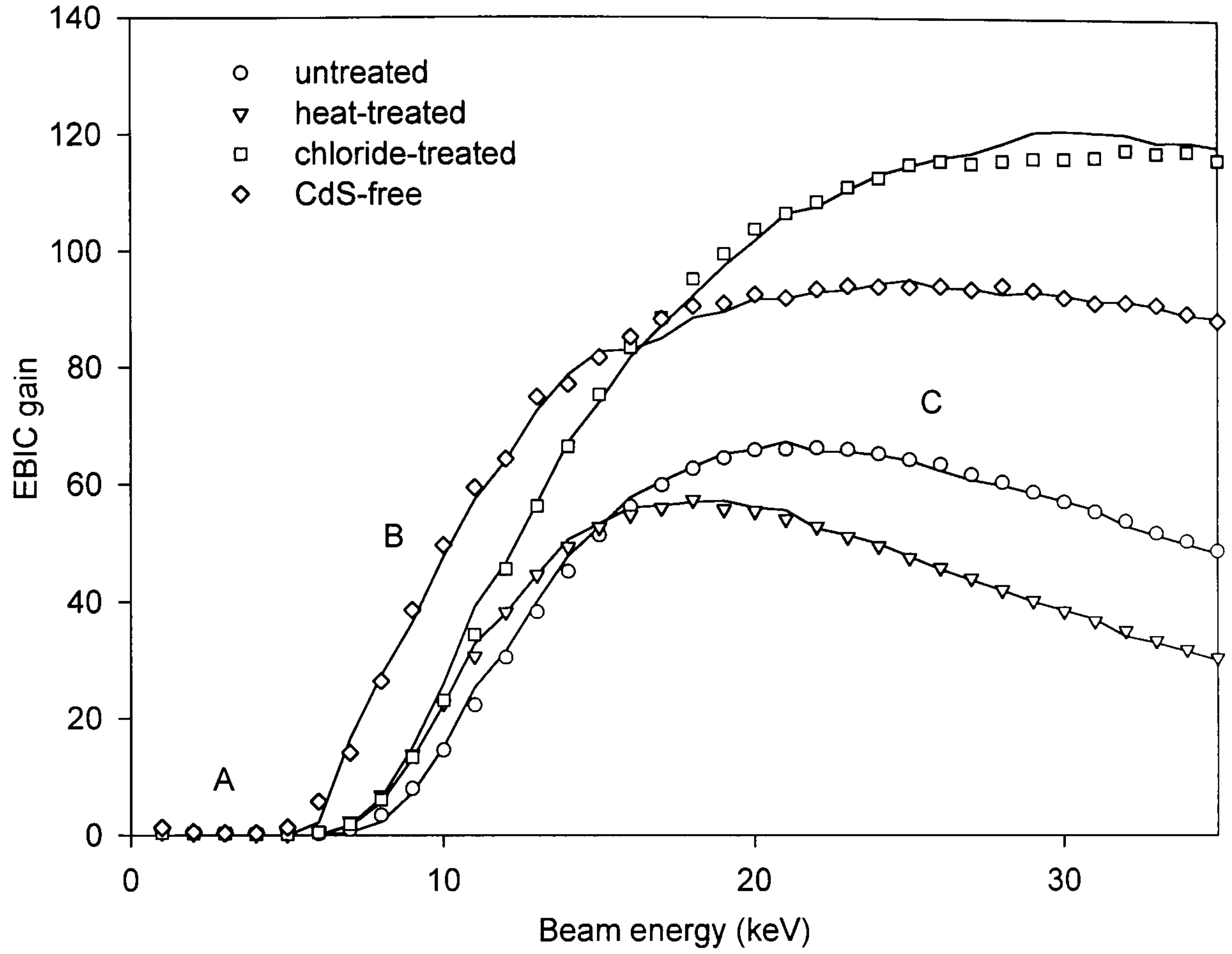

Figure 7.5 Results of beam voltage-dependent front-wall EBIC measurements (symbols). Also shown are fits to this data achieved using Monte Carlo simulated generation functions (lines).

Also shown in Figure 7.5 are the simulated curves fitted to this data. The simulated data points were obtained using Monte Carlo simulated depth generation functions (as shown in Figure 7.2) with a simple model for the depth-dependent carrier collection function. This model assumes the following collection efficiencies for the different layers:

ITO front contact	no collection
CdS window layer:	no collection
depletion region in CdTe:	complete collection
neutral region of CdTe:	collection efficiency decreases exponentially with distance from edge of depletion region, *i.e.*: $F(z) = \exp\left(-\frac{z}{L}\right)$

This latter function accounts for the diffusion of injected carriers to the depletion region, and in an idealised sample the exponential coefficient *L* would be equal to the minority carrier diffusion length in the CdTe. However, as the collection function outlined above is likely to be an oversimplified representation of a more complex system, *L* should not be considered to be an accurate measure of the diffusion length, but rather just a fitting parameter.

Fits to the data were obtained by adjusting the depth of edge of the depletion region from the sample surface, the depletion width and the exponential coefficient in the neutral CdTe. Also used was a scaling factor (<1), which allowed for further current losses in the device.

The parameters used for the fits in Figure 7.5 are listed in Table 7-I, and the corresponding depth-dependent collection functions are plotted in Figure 7.6.

Sample	Junction depth (μm)	Depletion width (μm)	Diffusion length (μm)	Scaling factor
Untreated	0.48	0.12	1.25	0.8
Heat-treated	0.44	0.11	0.66	0.8
$CdCl_2$-treated	0.44	1.56	4	0.9
CdS-free	0.2	0.8	5	0.67

Table 7-I Parameters describing the depth-dependent collection functions of the differently treated solar cells, used in fit to measured data shown in Figure 7.5.

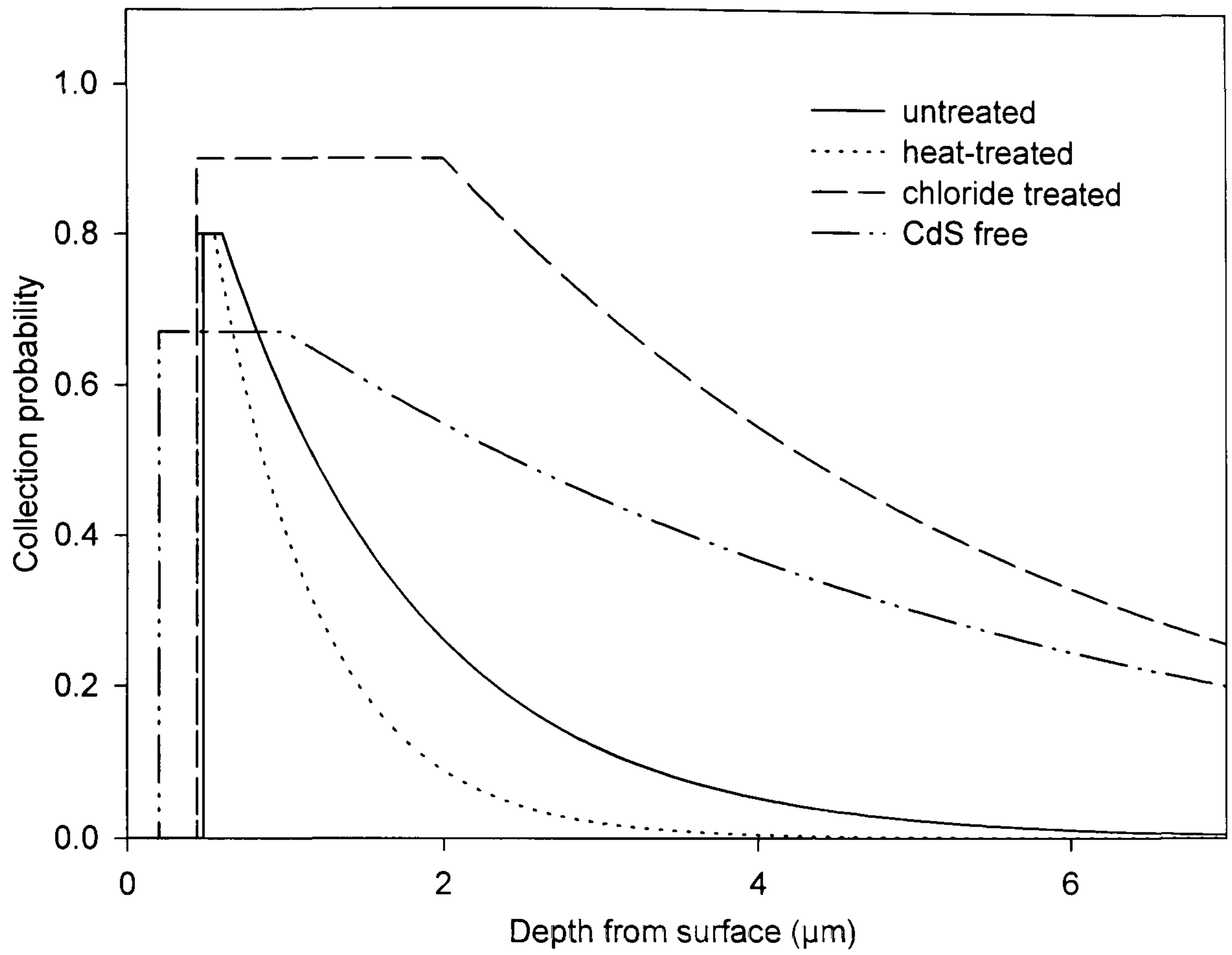

Figure 7.6 Modelled collection functions fitted to voltage-dependent EBIC measurements.

7.6 SPECTRAL RESPONSE

In order to allow comparison of these EBIC results with those from a more established technique, measurements were also taken of the spectral response of the cells. Given accurate optical absorption data, these measurements should yield similar depth-dependent information; this has been successfully demonstrated for thin-film chalcopyrite cells by Scheer *et al.* [13].

Spectral response measurements were made on the four differently treated samples prior to the removal of the glass substrates. The technique and apparatus used for this were described in Section 3.2.2. The results are shown in Figure 7.7.

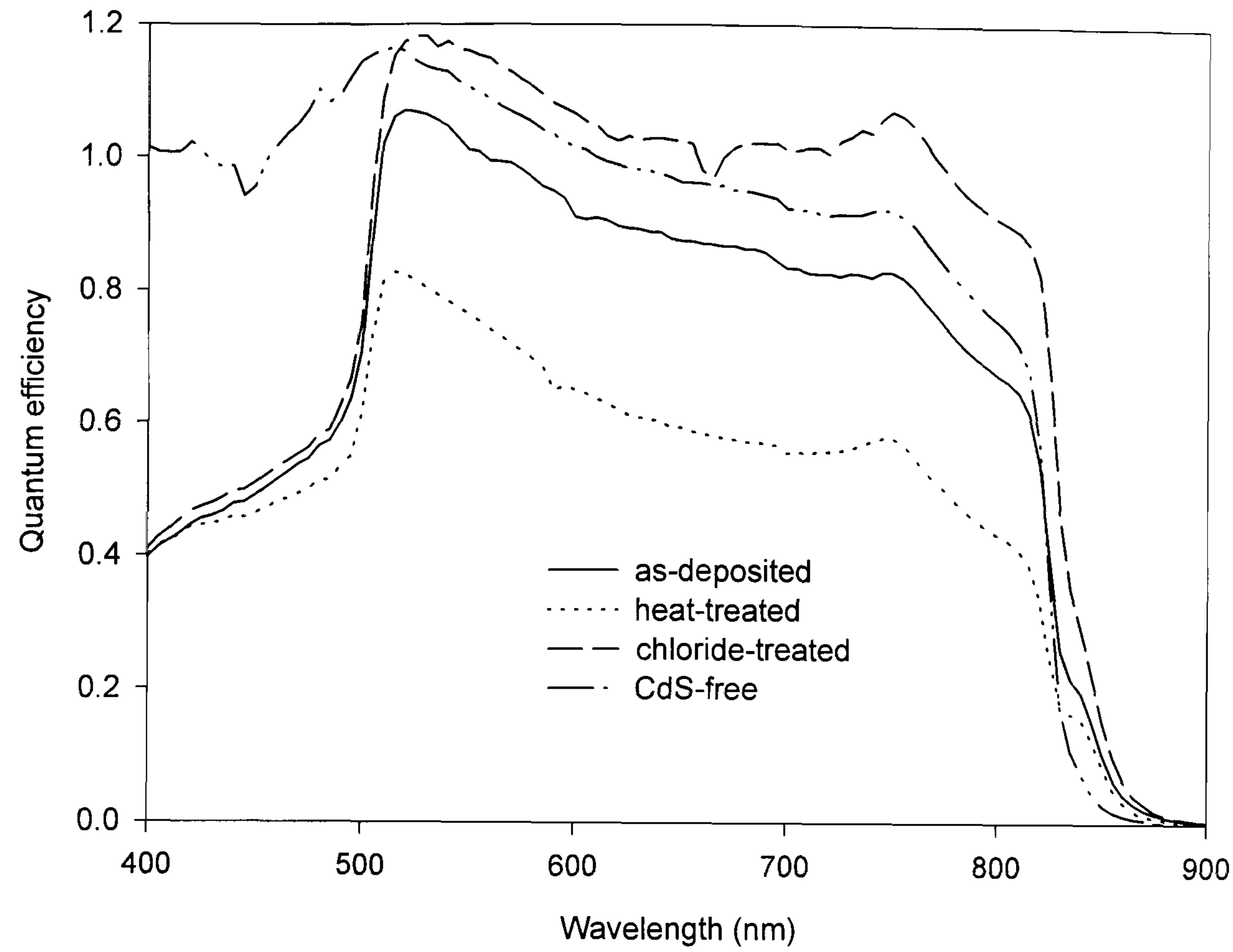

Figure 7.7 Measured spectral responses of the same four samples used for EBIC experiments.

The measurements carried out on the full ITO/CdS/CdTe structures exhibit the typical "top hat" shape characteristic of heterojunction solar cells (see for example [14]). At photon energies greater than the CdS bandgap (λ < 520nm), optical absorption in the window layer reduces the number of photons penetrating through to the depletion region. A similar cut-off is seen at 850nm, corresponding to the bandgap energy of CdTe. The response between these values is complex, and artefacts arising from the measuring system cannot be discounted.

The results show some values of quantum efficiency of greater than unity. This would apparently imply that some photons are generating more than one electron-hole pair in the sample. However, although this phenomenon has been observed in some Si and SiGe cells [15], it is unlikely to occur in these devices. This is because the incident photon would require an energy of at least twice the bandgap of the material, corresponding to a wavelength of less than ~430nm. The higher quantum efficiency seen at longer wavelengths is therefore attributed to a systematic error arising from a miscalibration of the measurement apparatus.

Comparison of the spectral responses of the as-deposited and heat-treated samples shows a marked decrease in the overall photocurrent following annealing. However, the results of these and the $CdCl_2$-treated sample coincide at short wavelengths, corresponding to the region of device closest to the front-wall and thought to be left relatively unaffected by processing. This suggests that the effect is genuine, and not due to experimental error. Furthermore, this decrease in current of ~20% is also consistent with the AM1.5 short-circuit current measurements shown in Table 4-I. The $CdCl_2$ treatment, however, has no such deleterious effect on the response.

The $CdCl_2$-treated CdS-free control shows a broadly similar response to the similarly treated complete cell, with the clear exception of the high-energy region of the spectrum. The absence of the window layer allows the quantum efficiency to remain near unity at these wavelengths. Some decrease in the photocurrent is seen in the CdS-free sample at longer wavelengths, corresponding to a lower collection efficiency deeper into the device.

7.7 DISCUSSION

7.7.1 The effect of processing on the EBIC and spectral response

In all three samples with a CdS layer, the junction (*i.e.* the edge of the high collection plateau) appears to be buried ~0.2-0.3μm within the CdTe. This is consistent with a buried homojunction arrangement, and is likely to arise from interdiffusion of electrically active species across the CdTe/CdS interface, so moving the position of the electrical junction. Since this is observed even for the untreated cell, it is thought to occur during the CSS deposition of the CdTe, and does not depend on the presence of the chloride. This can be seen to be a measurement within the limits of the technique by comparison with the CdS-free cell, which has a junction ~0.25μm shallower than the other devices. This can be explained partly by the absence of the 0.1μm thick CdS layer in that cell, but this thickness does not fully account for the difference. It is therefore concluded that the CdS/CdTe device has a more deeply buried junction than the ITO/CdTe structure.

A further effect of the simple heat treatment without the chloride is to reduce the collection deep in the device compared with the as-deposited cell. However, the opposite effect occurs following $CdCl_2$ treatment, which increases both the depletion region width and the minority carrier diffusion length in the CdTe. The latter of these effects occurs irrespective of the presence of the CdS layer.

Attempts to simulate spectral response data using collection functions and the optical generation functions shown in Figure 7.3 were made. Using the same values for the parameters (*i.e.* junction depth, depletion width *etc.*) as were used for fitting to the EBIC data resulted in simulated quantum efficiencies much lower than the experimental values at short wavelengths. Furthermore, no satisfactory fit to the experimental spectral response data could be achieved by varying these parameters. This leads to either one of two possible conclusions: that the simple collection function model fitted to the EBIC data is not accurate; or that the optical generation functions (and hence the absorption spectra) are not correct. This latter explanation is likely, as the absorption data used was not obtained from the cells used in this study. Therefore, effects such as alloying at the CdTe/CdS interface and impurities in the rest of the device, both of which can may produce significant variations in the optical absorption, are not taken into account. The difficulty of experimentally measuring such data, due to high absorption coefficients at energies above the bandgap, has meant that this has not been possible in the course of this work. Scheer *et al.* [13] have encountered similar (although less marked) discrepancies between EBIC and quantum efficiency data.

7.7.2 Limitations of the EBIC *versus* beam voltage technique

The interpretation of the results of the EBIC *versus* E_b experiment is open to some ambiguity. For example, recombination at the back contact may lead to significant errors in fitting to the data, especially when the diffusion length is on the same scale as the device thickness, as described by Scheer [4]. In addition, more than one combination of depletion width and effective diffusion length may produce a close fit to the measured data.

In principle, this technique could be developed further to yield spatially-resolved information. This would entail the recording of two-dimensional EBIC images instead of simply using the area-averaged signal. However, the interpretation of this data would be confounded by the plasma effects encountered in Chapter 6. Avoiding these effects would necessitate either a defocused beam (leading to a loss of spatial resolution) or a low beam current (resulting in a poor signal-to-noise ratio).

7.8 CONCLUSIONS

Measurement of the beam voltage dependence of EBIC has allowed the depth-dependent carrier collection functions of CdTe/CdS cells to be estimated. From the results of these experiments, three main conclusions can be drawn:

A) The collecting junction of the device is a buried homojunction located ~0.2-0.3μm into the CdTe. Comparison of the results from the variously treated cells indicates that this is the case in as-deposited cell layers, and the position is not significantly affected by post-deposition processing.

B) The apparent minority carrier diffusion length in the quasi-neutral CdTe layer increases as a result of cadmium chloride treatment. This allows more efficient carrier collection deeper into the cell, and occurs irrespective of the presence of the CdS layer.

C) The width of the depletion region increases. For this to occur, the presence of both CdS and $CdCl_2$ appears to be necessary. This observation is consistent with the evidence presented in Section 6.7.4 that diffusion of species from the sulphide layer contributes to the doping at the junction.

Despite the fact that quantitative collection function data could not be extracted from the spectral response measurements, their qualitative analysis is in agreement with the EBIC data. This is evident from the higher collection of longer wavelength light in the $CdCl_2$-treated sample compared with the as-deposited device (Figure 7.7), corresponding to higher collection deep within the CdTe layer.

Further investigations of depth-dependent materials properties are presented in the next chapter.

REFERENCES FOR CHAPTER 7

[1] D.B. Holt *"The conductive mode"* in *SEM Microcharacterisation of Semiconductors*, edited by D. B. Holt and D. C. Joy, (Academic Press, London, 1989)

[2] A.E. Grün (1957) Zeitschrift für Naturforschung **12a** pp.89-95

[3] T.E. Everhart and P.H. Hoff (1971) *Determination of kilovolt electron energy dissipation vs penetration distance in solid materials*, Journal of Applied Physics **42** pp.5837-5846

[4] R. Scheer (1995) *"Simulation of electron-beam-induced-current profiles for thin-film heterojunction analysis"*, Philosophical Magazine B **72** (1) pp.75-80

[5] C.J. Wu and D.B. Wittry (1978) *Investigation of minority-carrier diffusion lengths by electron bombardment of Schottky barriers*, Journal of Applied Physics **49** (5) pp.2827-2836

[6] E. Napchan and D.B. Holt (1987) *Application of Monte-Carlo simulations in the SEM study of heterojunctions*, Institute of Physics Conference Series **87** pp.733-738

[7] E. Grünbaum, E. Napchan, Z. Barkay, K.W.J. Barnham, J. Nelson, C.T. Foxon, J.S. Roberts and D.B. Holt (1995) *Evaluation of the minority carrier diffusion length by means of electron beam induced current and Monte Carlo simulation in AlGaAs and GaAs p-i-n solar cells*, Semiconductor Science and Technology **10** pp.627-633

[8] K. Seeger, *Semiconductor Physics*, (Springer-Verlag, Berlin, 1985)

[9] A.E. Rakhshani (1997) *Electrodeposited CdTe - optical properties*, Journal of Applied Physics **81** (12) pp.7988-7993

[10] T.H. Myers, S.W. Edwards and J.F. Schetzina (1981) *Optical properties of polycrystalline CdTe films*, Journal of Applied Physics **52** (6) pp.4231-4237

[11] S. Ninomiya and S. Adachi (1995) *Optical properties of wurtzite CdS*, Journal of Applied Physics **78** (2) pp.1183-1190

[12] A.L. Fahrenbruch and R.H. Bube, *Fundamentals of solar cells*, (Academic Press, New York, 1983)

[13] R. Scheer, M. Wilhelm, V. Nadenau, H.W. Schock and L. Stolt (1997) *Collection functions in chalcopyrite heterojunction solar cells: a comparison of* $Cu(In,Ga)(Se,S)_2$ *absorbers*, Proceedings of 14th European Photovoltaic Solar Energy Conference, Barcelona, pp.1299-1302

[14] K.W. Mitchell, *Evaluation of the CdS/CdTe heterojunction solar cell*, (Garland, New York, 1979)

[15] A. De Vos and B. Desoete (1998) *On the ideal performance of solar cells with larger-than-unity quantum efficiency*, Solar Energy Materials and Solar Cells **51** (3-4) pp.413-424

Chapter 8: Luminescence and elemental analysis

8.1 INTRODUCTION

This chapter documents the use of several techniques whereby radiative processes are induced in the solar cells to investigate their composition and structure. In particular, each of the methods has been used to probe intermixing at the CdTe/CdS junction. With the luminescence techniques (PL and CL), this has been carried out by measuring the change in bandgap with distance from the interface; the more direct elemental analysis technique, GDOES, relies on the emission of characteristic photon energies.

The luminescence methods also provide information about the presence of shallow donor and acceptor levels in the material. These techniques may therefore be used to provide information about the distribution of such impurities in the device, both as a function of depth (via PL on bevelled samples) and with spatial resolution in the layer plane (using CL imaging).

8.1.1 Formation of CdS_xTe_{1-x}

Intermixing of the CdS and CdTe layers during the deposition and processing of the solar cell is limited at equilibrium by the mutual solubility of the two compounds. The lowest temperature data points on the currently available pseudobinary phase diagram indicate that at 625°C a miscibility gap extends over most of the composition range of CdS_xTe_{1-x}: x=0.16 to 0.86 according to [1]. Consideration of the trends in the diagram further suggest that at lower temperatures (such as those used during CSS deposition), the miscibility gap will be wider still [2]. Despite this miscibility gap, however, metastable solid solutions of CdS and CdTe over the full composition range have been prepared by several workers in order to allow the properties of such alloys to be studied.

8.1.2 Bandgap bowing

The bandgap energy of the different CdS_xTe_{1-x} alloys does not vary linearly with x, but is known to exhibit a bowed shape. Such measurements are commonly fitted to a parabolic equation [3] of the form:

$$E_g(x) = E_{CdTe} + (E_{CdS} - E_{CdTe})x - bx(1\text{-}x) \tag{8.1}$$

where E_{CdTe} and E_{CdS} are the bandgap energies of the binary compounds and b is the so-called *bowing parameter*. Several workers report values of b of ~1.7eV [4-6].

Although it is probable that some diffusion of tellurium atoms into the CdS occurs, as well as sulphur into the CdTe, the thinness of the CdS layer prevents an accurate measurement of the extent to which this happens. For this reason, the present study is limited to analysing the diffusion of sulphur into the absorber layer. Figure 8.1 shows collected experimental data for the energy bandgap of these CdS_xTe_{1-x} alloys, for compositions where x<0.5.

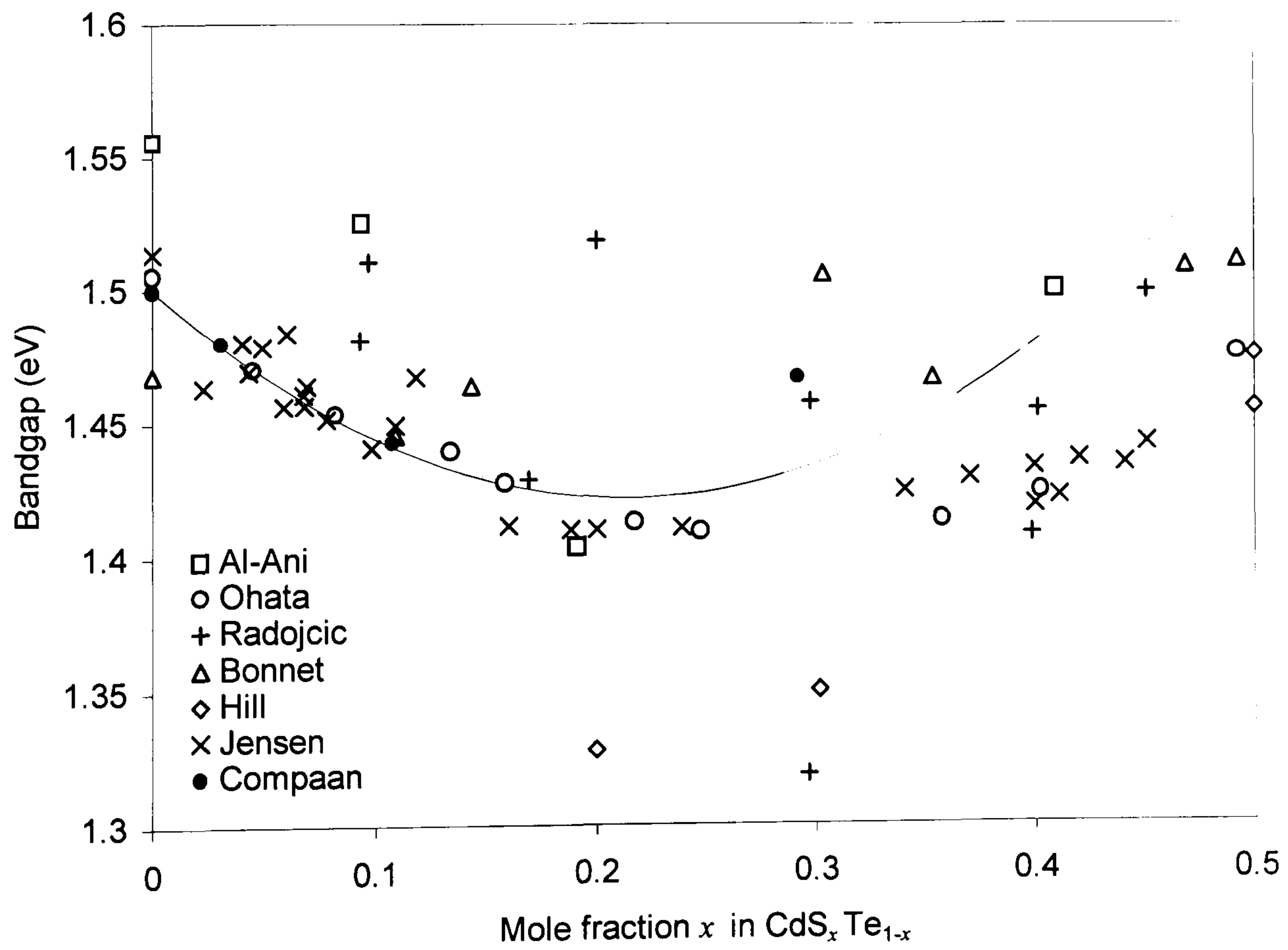

Figure 8.1 Room temperature bandgap as a function of alloy composition, calculated using Equation 8.1 (line). Also shown are the experimental data from Al-Ani [7], Ohata [4], Radojcic [8], Bonnet [9], Hill [10], Jensen [11] and Compaan [6].

Also shown in this graph is the curve calculated using b=1.7eV in Equation 8.1. Both this simulated line and the data points clearly shows the bowing effect, which within the limit of solubility ($x \lesssim 0.1$) results in a decreasing bandgap with increasing sulphur content. For low values of x, the slope of this curve is ~0.7eV/x, and the measurement of this shift in bandgap can in principle allow an estimation of the composition of a given alloy. The following two sections describe the application of luminescence measurements on solar cells to detect this bandgap shift.

8.2 PHOTOLUMINESCENCE SPECTROSCOPY

8.2.1 Introduction

In order to detect changes in the composition of the CdS_xTe_{1-x} alloy using the principle explained above, it is necessary to measure changes in the bandgap energy of the material. Photoluminescence offers this possibility, as excitonic emissions closely follow the bandgap of the semiconductor. This section describes the use of PL along a bevelled sample as a method of measuring the variation of bandgap with distance from the device junction, as well as the use of the technique to investigate the distribution of shallow levels in the CdTe.

8.2.2 Experimental details

The photoluminescence measurements in this work were carried out using the experimental arrangement shown schematically in Figure 8.2.

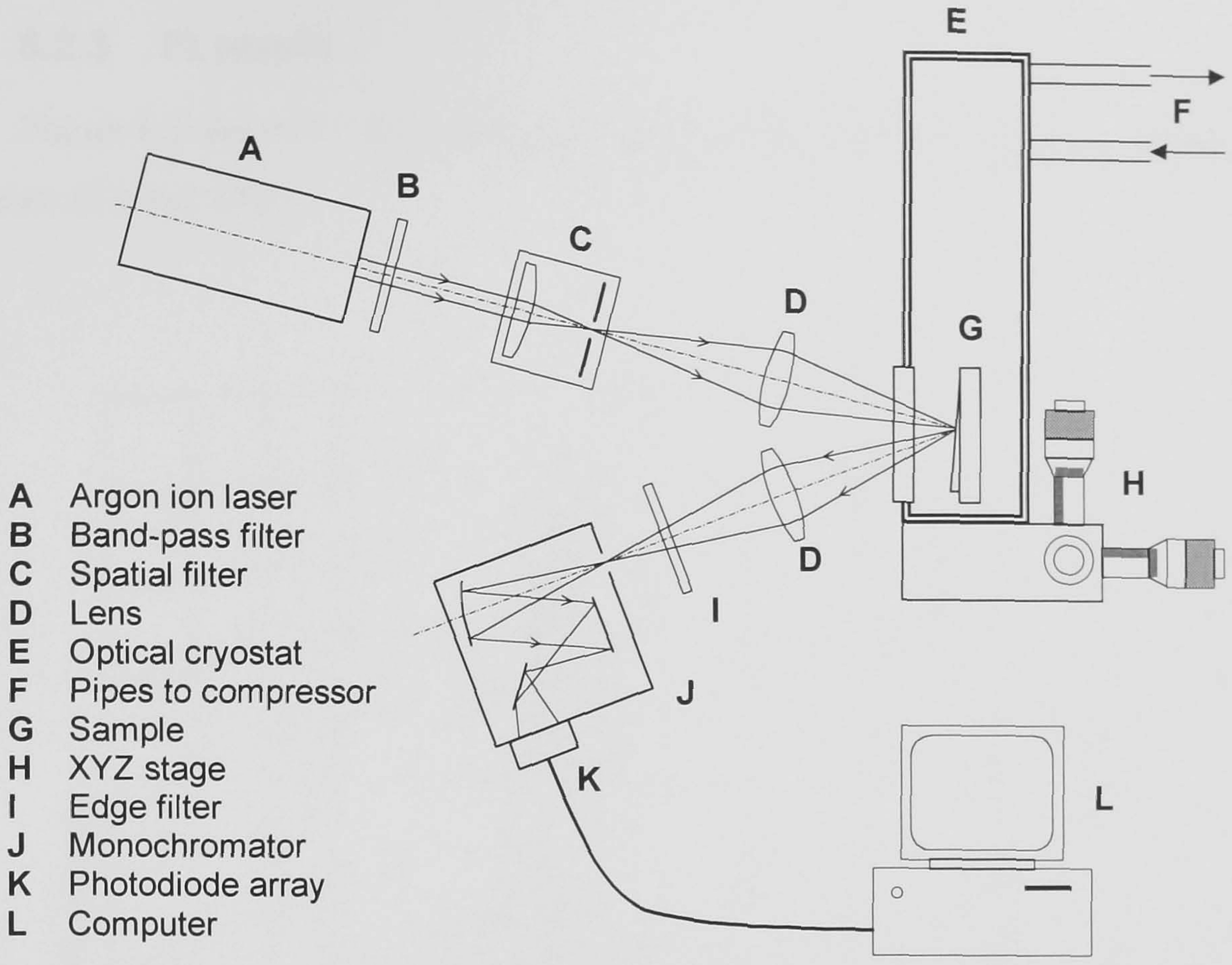

Figure 8.2 The experimental arrangement used for photoluminescence measurements.

The light source used was a continuous wave argon ion laser, from which the 488nm line was selected using a band-pass interference filter. This light was spatially filtered and focussed onto the sample with a spot size of the order of 100μm. The sample was mounted in an optical closed-cycle helium cryostat, resulting in a nominal temperature of 8.5K. The light emitted from the sample was focussed onto the entrance slits of a grating monochromator, and the spectrum recorded using a photodiode array interfaced to a computer. Reflected laser light was blocked from the detection system by the use of a colour glass edge filter. The cryostat was mounted on a manual XYZ stage to allow the position of the laser spot to be moved with respect to the sample.

Two samples were studied in this work: one a complete ITO/CdS/CdTe solar cell and other an ITO/CdTe control structure. Both devices were $CdCl_2$ treated and annealed as described in Section 4.2.2, and bevelled using the chemical process outlined in Section 4.3.1. Depth-dependent measurements were thus made by moving the light spot across the bevel.

8.2.3 PL results

Figure 8.3 shows the photoluminescence spectrum for the CdS-free sample as a function of bevel depth.

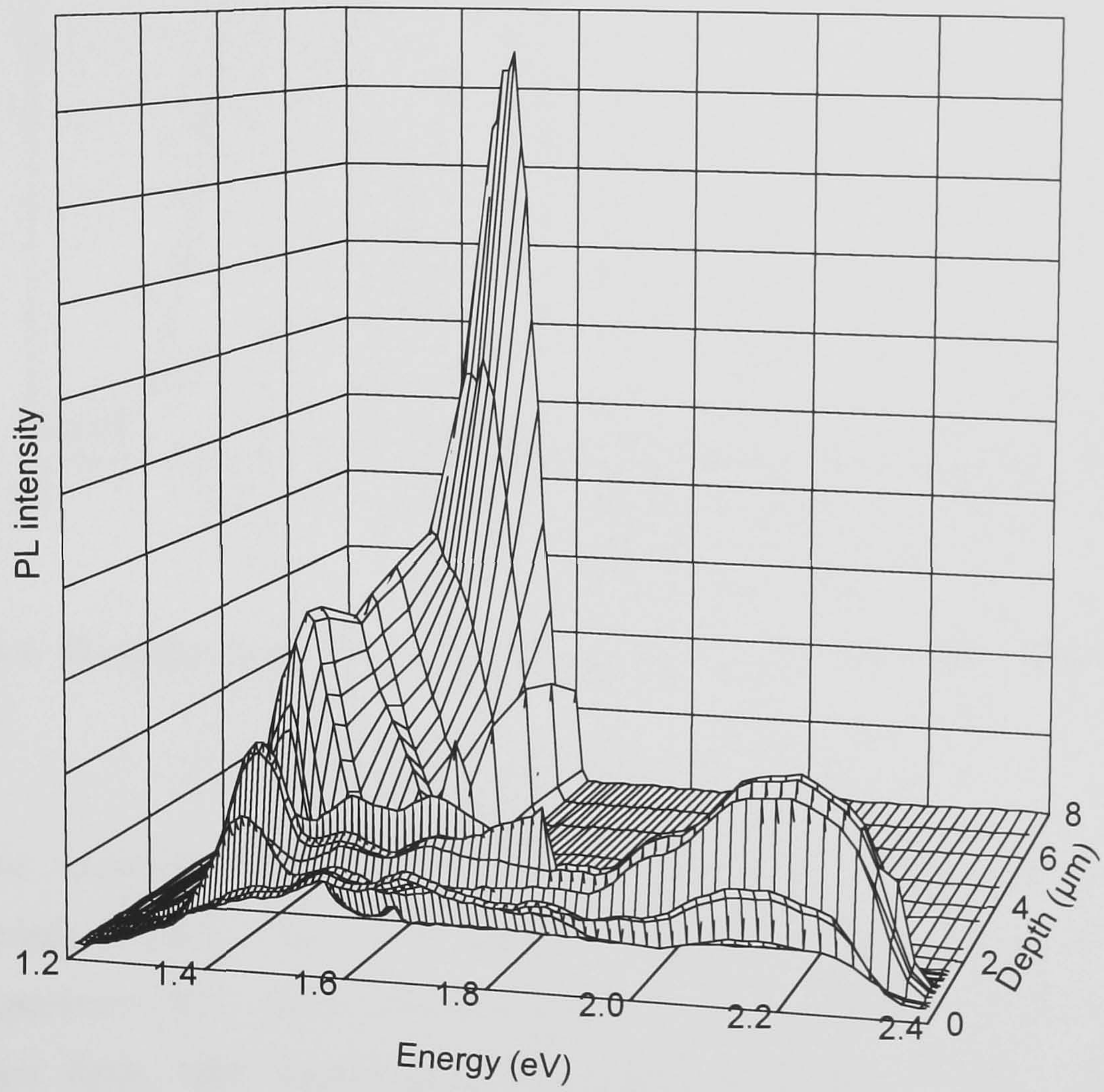

Figure 8.3 PL spectrum at 8.5K of a CdS-free cell as a function of bevel depth, in which 0µm corresponds to the ITO/CdTe interface and 8µm is the CdTe surface.

This data shows many luminescence bands with a complex depth dependence. For clarity, the spectra obtained from the unbevelled CdTe surface and from the ITO/CdTe interface region are reproduced in Figure 8.4.

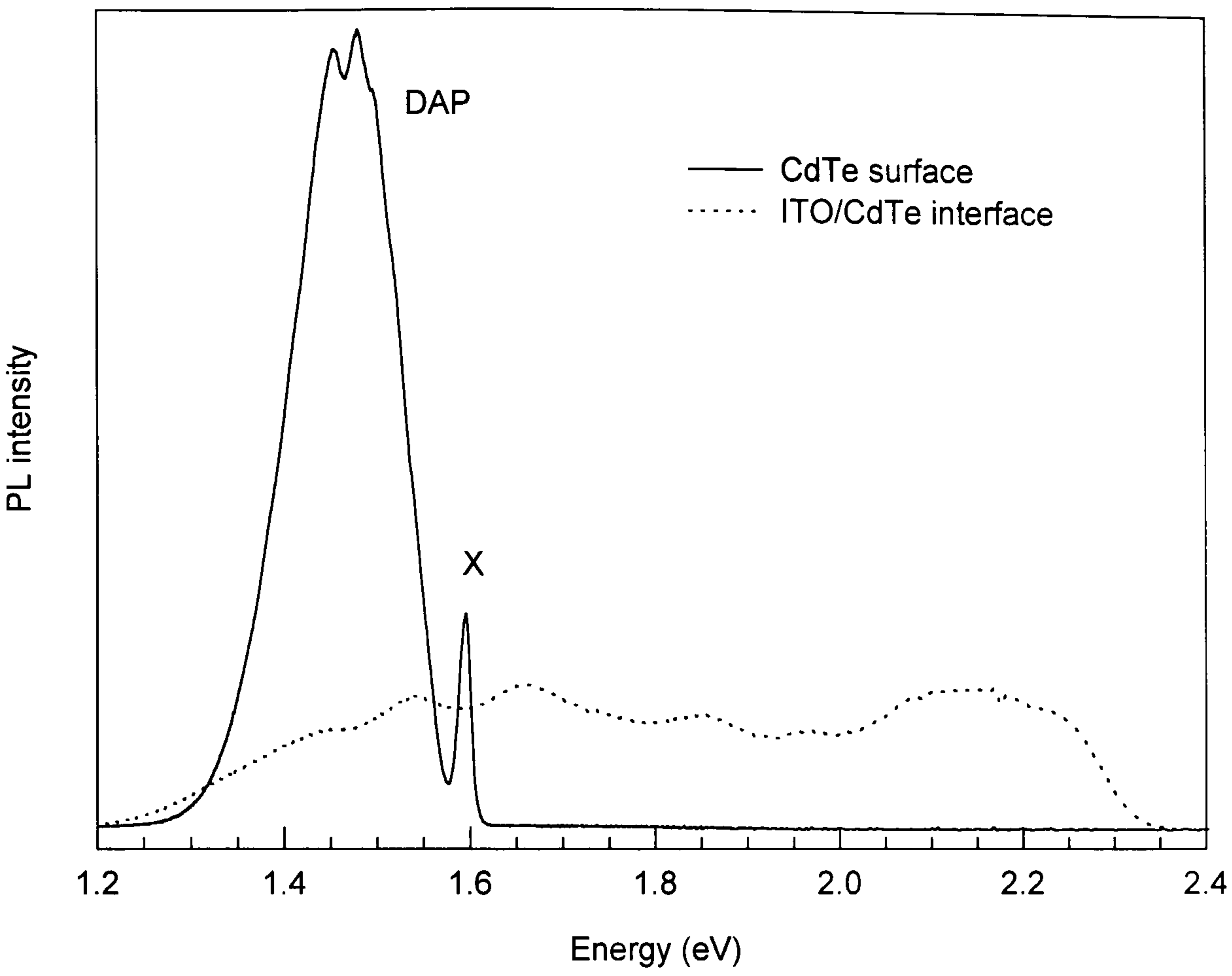

Figure 8.4 PL spectrum at 8.5K of CdS-free cell at the CdTe surface and the CdTe/TCO interface.

The spectrum from the unbevelled surface shows luminescence bands characteristic of CdTe. The 1.595eV peak is close to the bandgap energy of CdTe at this temperature [12], and is therefore likely to be attributed to bound excitonic transitions from near band-edge states. This is labelled X in Figure 8.4. Luminescence in the 1.4-1.5eV range is often observed in CdTe, and is the result of donor-acceptor pair transitions. This may include transitions involving the complex acceptor $(V_{Cd}Cl_{Te})^+$, for example, which is known to lie 120meV above the valence band [13,14]; transitions occurring between this centre and shallow donors will therefore result in ~1.4eV emission. The breadth of the DAP band is greater than that reported by others for similar materials [15-17], where this region of the luminescence is often separated into two distinct bands. However, no attempt is made in this work to separate the DAP band into the constituent transitions or their LO phonon replicas by curve fitting. The origin of these bands in single crystal CdTe is complex and is the subject of a great deal of literature.

The PL spectrum from the interface region of the cell shows a very broad luminescence band with no clearly discernible features. (Note that the intensity decrease at ~2.3eV corresponds to the cut-off wavelength of the colour glass filter used, and so this feature is an artefact of the measurement system.)

In order to measure any change in the bandgap of the material with depth through the sample, further spectra were taken of the excitonic region using a higher resolution diffraction grating. The laser spot position was moved across the bevel in 250μm steps, selected data is shown in Figure 8.5.

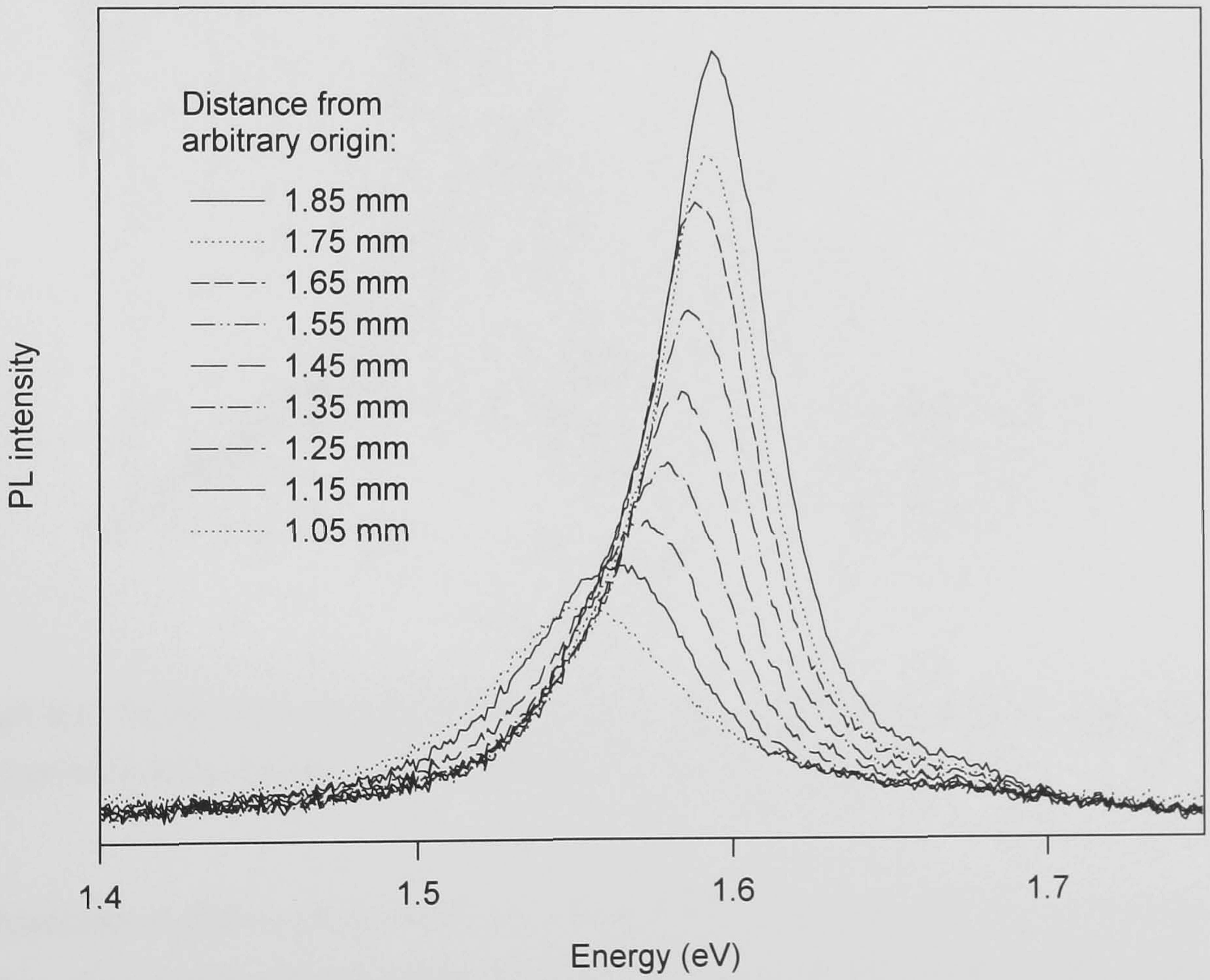

Figure 8.5 PL spectra at 8.5K for CdS-free sample, showing energy of CdTe exciton peak as a function of position on bevel.

Inspection of this graph shows the exciton peak to be dependent on the position on the bevel, with a shift towards lower energies closer to the ITO. This data will be discussed quantitatively and interpreted in the following section.

Figure 8.6 shows the position dependent PL data obtained for the full ITO/CdS/CdTe solar cell.

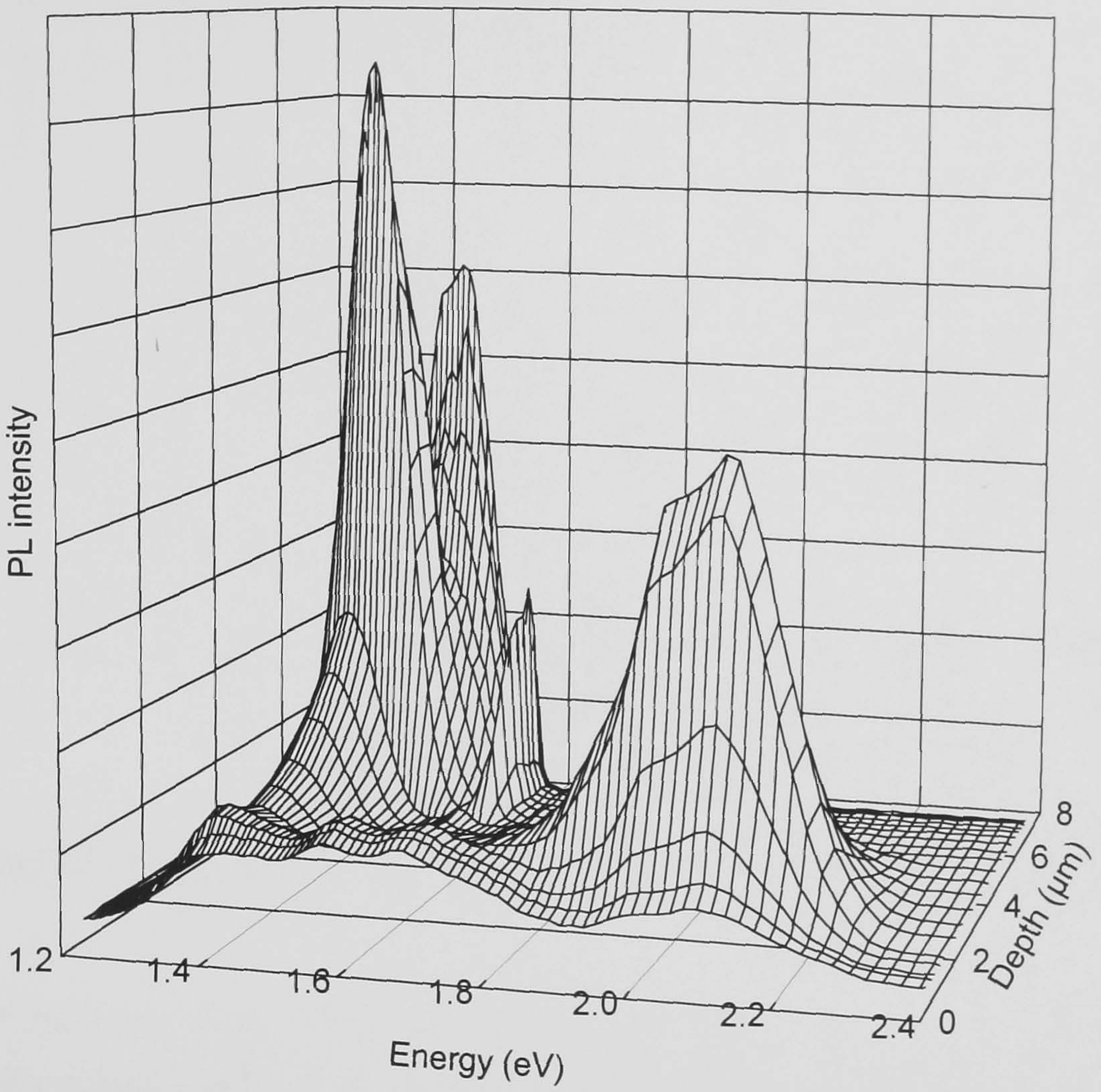

Figure 8.6 PL spectrum at 8.5K of a CdS/CdTe cell as a function of bevel depth, in which 0μm corresponds to the device junction and 8μm is the CdTe surface.

Comparison of these spectra with those of the CdS-free sample (Figure 8.3) shows a similar shape to the CdTe bands from the thicker part of the bevel, with both the donor-acceptor and exciton regions clearly visible. DAP luminescence from the CdS layer can also be seen at higher energies. The spectra from the CdS and CdTe parts of the bevel are shown in Figure 8.7.

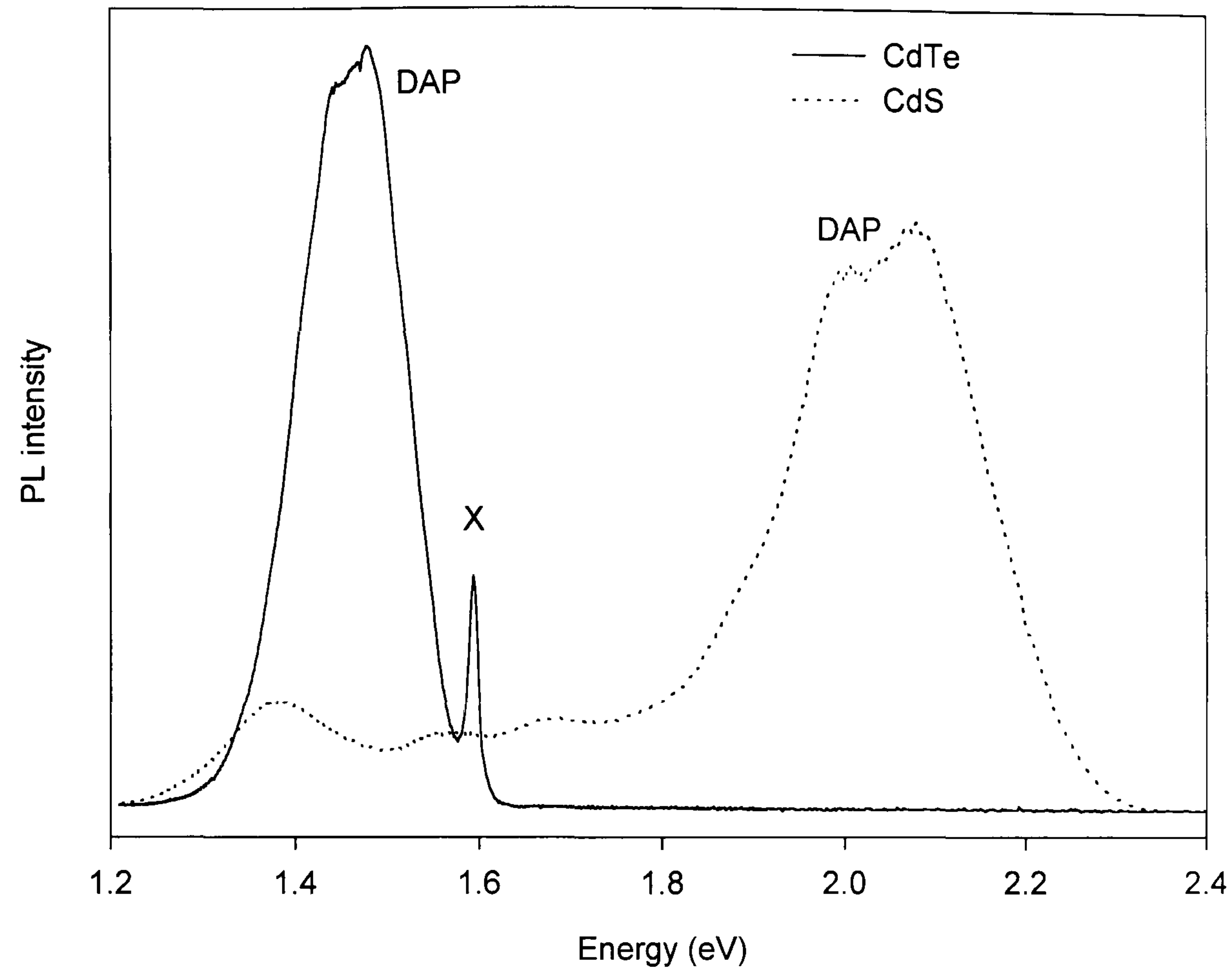

Figure 8.7 PL spectra at 8.5K from the CdTe and CdS regions of a CdTe/CdS cell.

The CdS excitonic peak (expected at around 2.58eV at this temperature [18]), was outside the range of this measurement since a filter was used to block the 2.54eV laser light. This may also be responsible for the decline in CdS DAP luminescence above 2.2eV.

Higher resolution scans of the CdTe excitonic region (shown in Figure 8.8) show a greater decrease in bandgap near the interface than observed for the CdS-free sample.

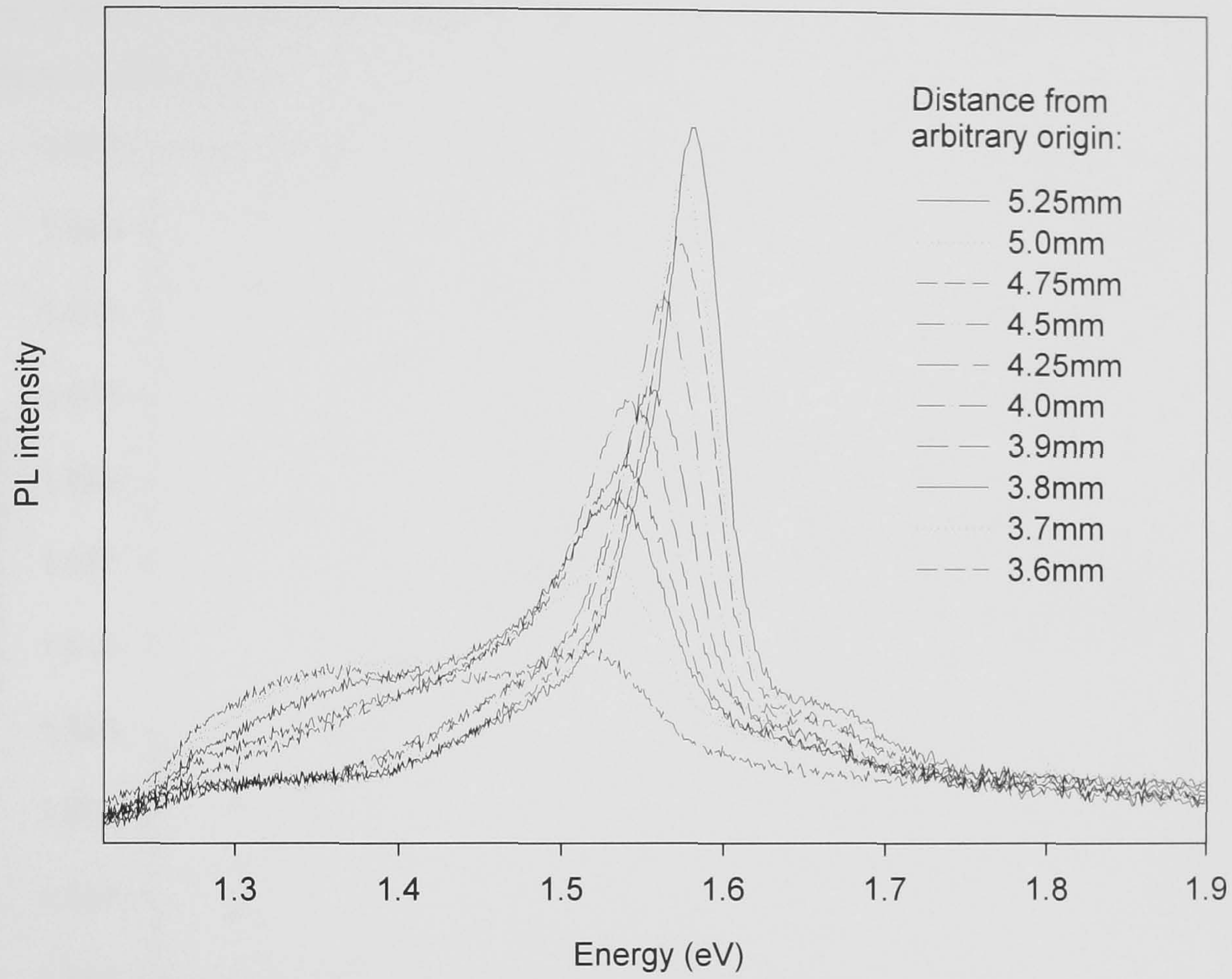

Figure 8.8 PL spectra at 8.5K showing energy of CdTe exciton peak as a function of position on bevel for a solar cell with a CdS layer.

A quantitative comparison of the bandgap shifts seen in the two samples is undertaken in the next section. Differences in the intensity of the DAP luminescence as a function of depth in the two samples are also discussed.

8.2.4 Discussion of PL results

Bandgap shift Figure 8.9 shows the variation of the observed CdTe excitonic peak energy with distance from the device interface for the two samples with and without a CdS layer.

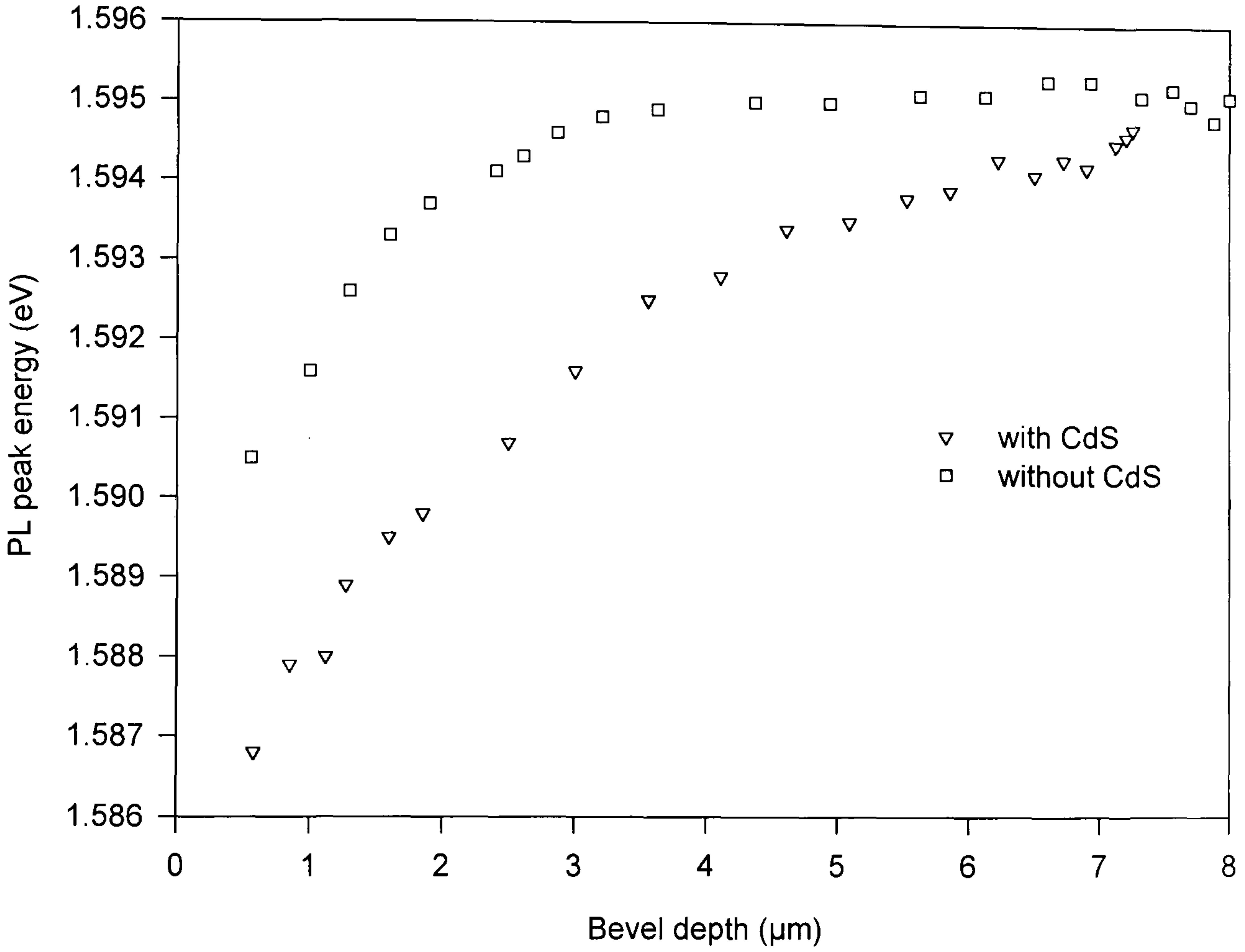

Figure 8.9 Energy of CdTe exciton peak as a function of bevel depth for cells with and without a CdS layer. (The ITO surface is at a bevel depth of ~0μm.)

The peak energies from this graph were taken from the spectra in Figures 8.5 and 8.8; the bevel depths were inferred by comparing the lateral position of the light spot on the sample with the bevel profiles (as seen in Figure 4.3).

Although the sample with the CdS layer does show some decrease in the bandgap energy with increasing proximity to the interface, some change was also observed in the CdS-free sample. This unexpected shift clearly shows that alloying with CdS in not the only factor to affect the CdTe exciton peak energy in this region of the device. Possible contributions could be the diffusion of species from the glass substrate or the TCO layer; or effects due to the electric field, which will be at a maximum in this region of the device. It can also be seen that this effect is only manifested within 3μm of the interface; by contrast, the sample with a CdS layer shows a measurable shift in exciton peak energy at up to twice this distance.

In order to interpret the exciton peak energy data in Figure 8.9 in terms of alloy composition it is necessary to assume that the energies are tied to the band gap energies. The E_g *versus* x data in Figure 8.1 could then be used to plot the composition of the cell with CdS as a function of depth directly as shown in Figure 8.10. This method shows the sulphur molar fraction x to be only ~1%, even within a micron of the interface.

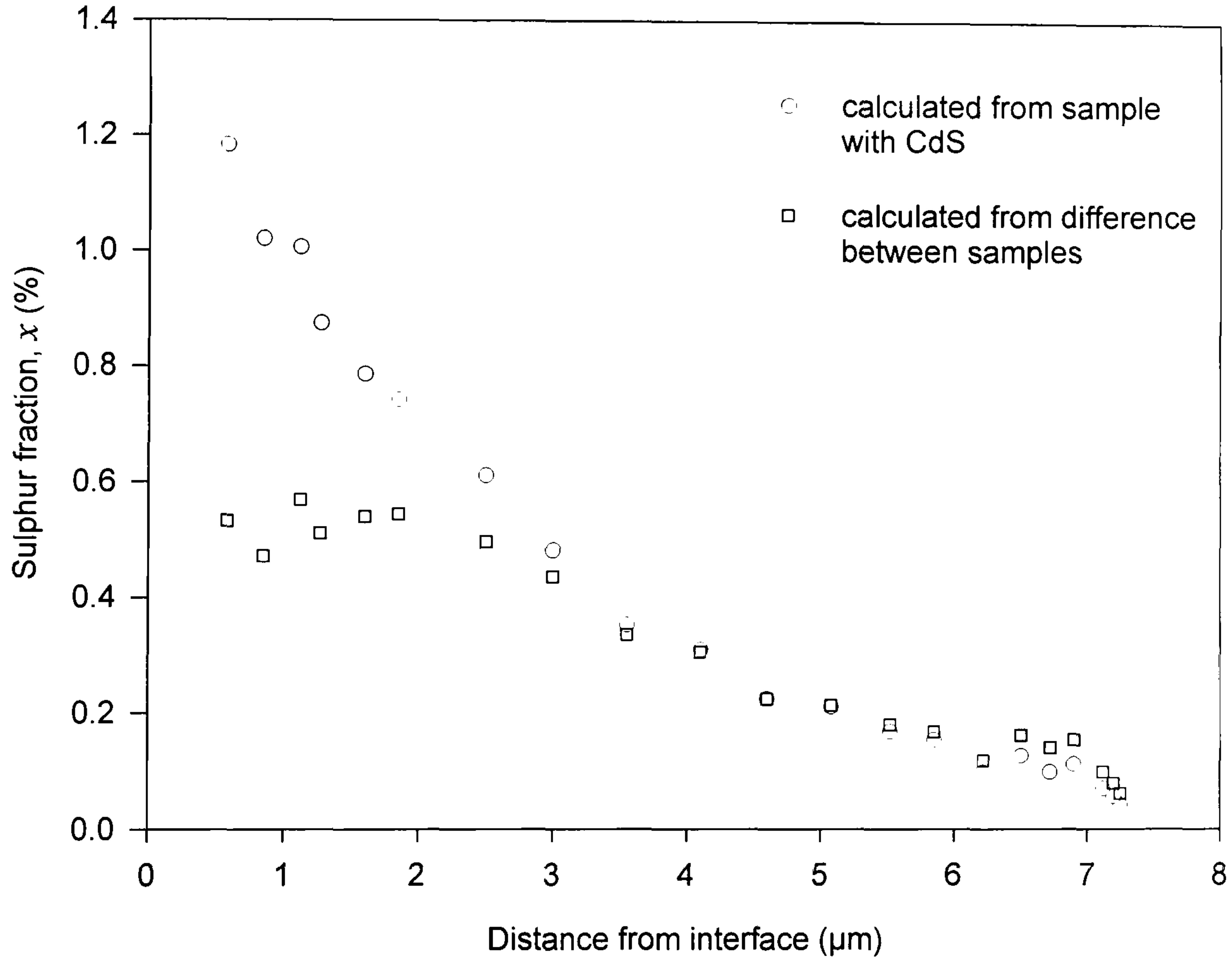

Figure 8.10 The estimated sulphur content of the cadmium telluride layer as a function of distance from the CdTe/CdS interface. The circles show the results of calculations based on the assumption that the observed exciton energy shift in Figure 8.9 is due solely to changes in alloy composition; the squares show data corrected by subtracting the energy shift observed in the CdS-free sample.

An alternative method would be to try to account for the factors which might shift the apparent bandgap by using the difference in energy of the CdS containing and CdS-free control sample peaks. The results of this are also presented in Figure 8.10, and show values of x of up to ~0.6%.

DAP intensity Depth dependent information about the distribution of optically active centres may also be inferred from the variation in the intensity of the PL with bevel position. Figure 8.11 shows the intensity of the 1.4-1.5eV DAP luminescence band in the CdS-free sample.

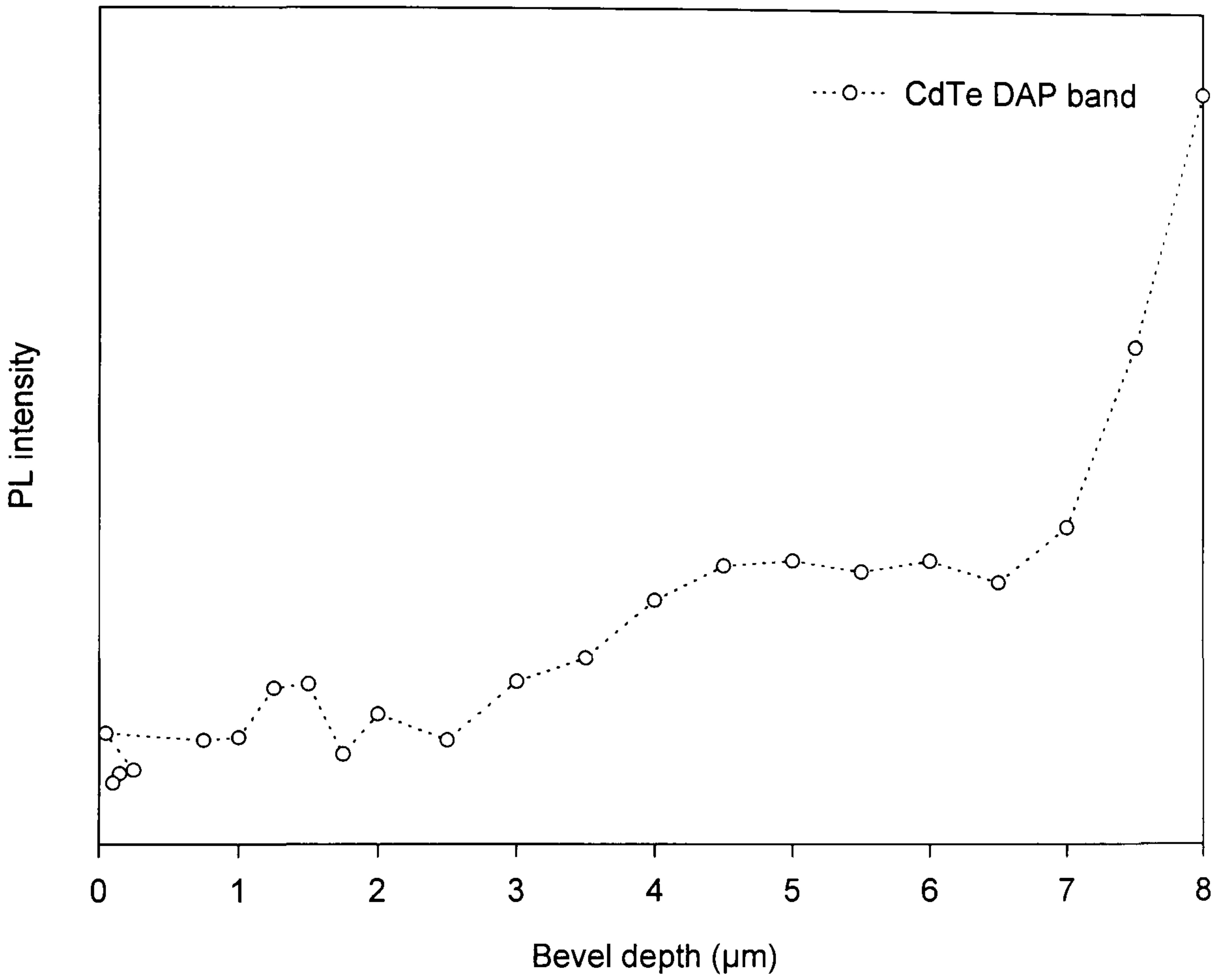

Figure 8.11 Intensity of the DAP luminescence band as a function of bevel depth for the CdS-free sample.

This shows the intensity of the emission to be low close to the interface; this is explained by the fact that the laser spot is now at the edge of the bevel, and not all the light may be incident on the CdTe. The intensity increases at around halfway through the CdTe layer to a plateau at 4-7μm from the interface. The intensity is then seen to increase significantly in the 1μm closest to the unbevelled CdTe surface.

These observed changes may be due to variations in either the concentration or type of centres involved in the radiative transitions. The increase in intensity at the back of the cell (*i.e.* the surface onto which the $CdCl_2$ was evaporated during post-deposition processing) suggests that the chloride treatment might be responsible. Possible centres involved therefore include shallow levels such as oxygen acceptors [19] and chlorine donors [13], and also deeper cadmium vacancy complexes.

However, since many different species and centres can be responsible for transitions in this energy band, and the materials used in the present work are chemically complex, it is not possible to be definitive in this case.

Figure 8.12 shows the variation of PL intensity with depth for the donor-acceptor related luminescence in the complete CdTe/CdS solar cell.

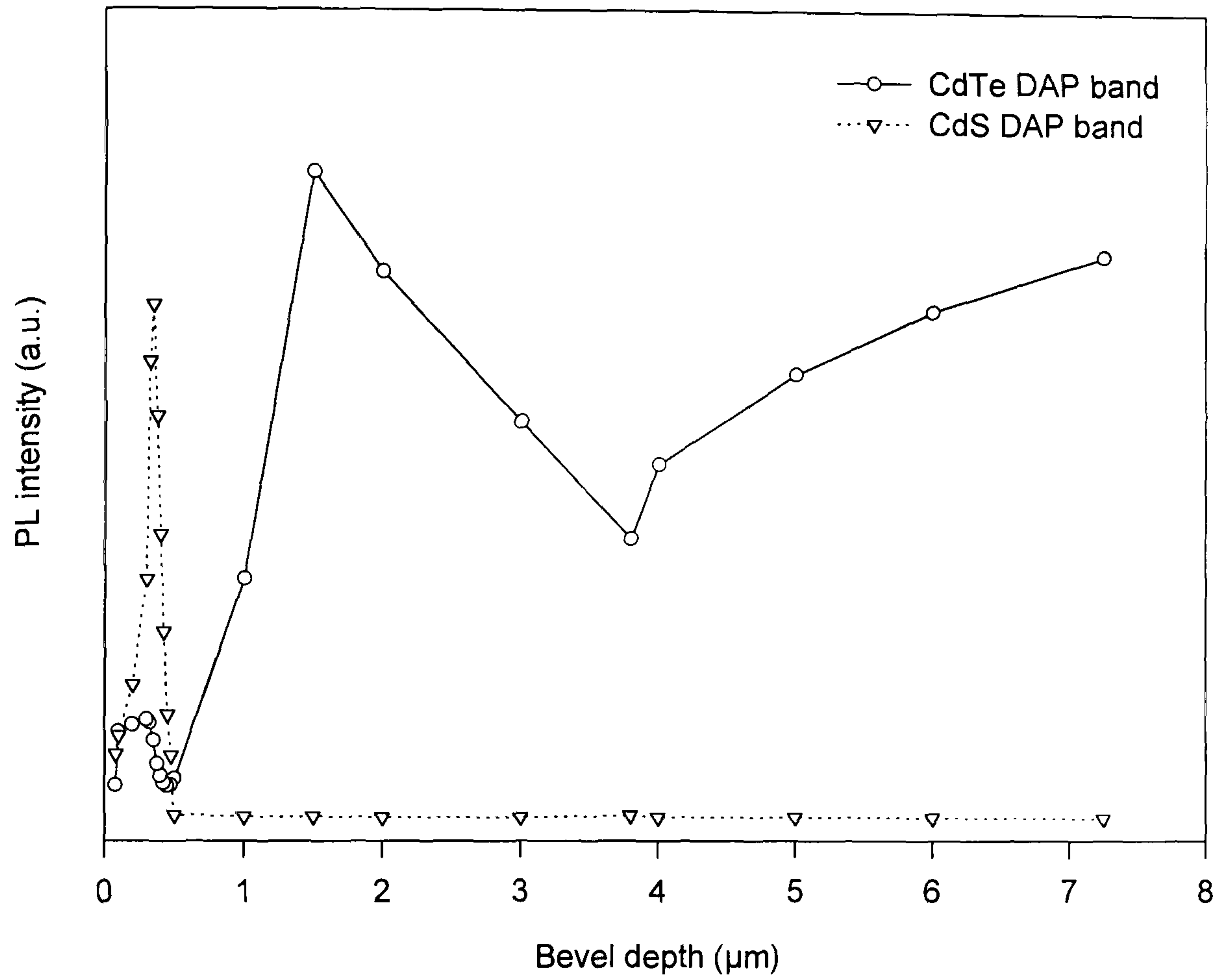

Figure 8.12 PL intensity as a function of bevel depth for solar cell with a CdS layer.

The thickness of the CdS layer was not sufficient to allow conclusions to be drawn about the distribution of luminescent centres through this layer. The 1.4-1.5eV band from the CdTe, however, shows a strong dependence on bevel thickness. The low intensity close to the interface is due to the bevel edge, as explained above. The sample shows a minimum in intensity at around the middle of the CdTe layer, increasing towards both the front and the back of the device. The abrupt change at the midpoint suggests the contribution of two separate mechanisms. This may be the result of the introduction of dopant centres from both the front of the cell (such as S, In, Sn, O, Na *etc.*) and the back (Cl, O, $V_{Cd}Cl_{Te}$ *etc.*), increasing the concentration of donors or acceptor (or both) available for radiative transitions. This is consistent with intermixing at the interface and with the diffusion of species from the back surface during the $CdCl_2$ treatment. However, it should be noted that there might also be other factors which influence the luminescence intensity. For example, there may be a depth dependence to the rate of non-radiative recombination, which would change the number of carriers available for the radiative transitions seen in PL. Notwithstanding that, it is the differences between this sample and the control which point to the mechanism as being impurity related.

8.3 CATHODOLUMINESCENCE

8.3.1 Introduction

CL measurements were carried out at Oxford Instruments using a JEOL JSM840A scanning electron microscope fitted with an Oxford Instruments MonoCL2 cathodoluminescence system and CF302 liquid helium cold stage. A schematic diagram of this system is shown in Figure 8.13.

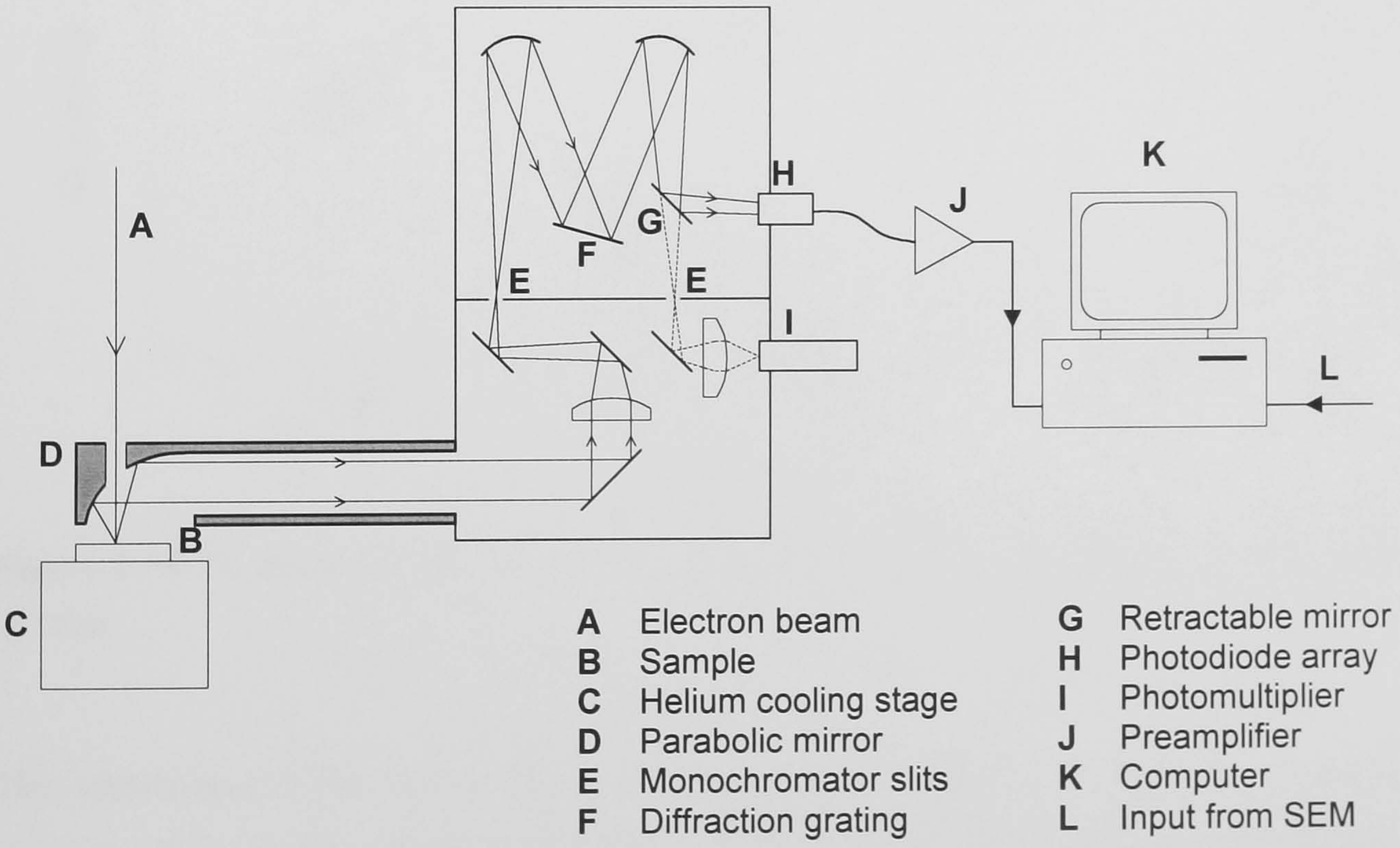

Figure 8.13 Experimental set-up used for the cathodoluminescence measurements in this study.

Light emitted from the sample is collected by a parabolic mirror and focussed directly onto the entrance slits of a grating monochromator. The CL spectrum is recorded either by scanning the monochromator grating and measuring the light level with a photomultiplier tube, or by means of a photodiode array. Both detection systems are controlled via a computer, which also uses triggering information from the SEM to allow recording of CL linescans and images.

A constant electron beam accelerating voltage of 12kV was used throughout this experiment. Due to the high efficiency collection optics of the system, the beam current could be kept lower than is often used for CL; values of 3 to 30nA were used, minimising the risk of beam damage to the samples.

8.3.2 CL results

Figure 8.14 shows the CL spectrum obtained from a thick region of a bevelled CdS/CdTe structure at a temperature of 117K.

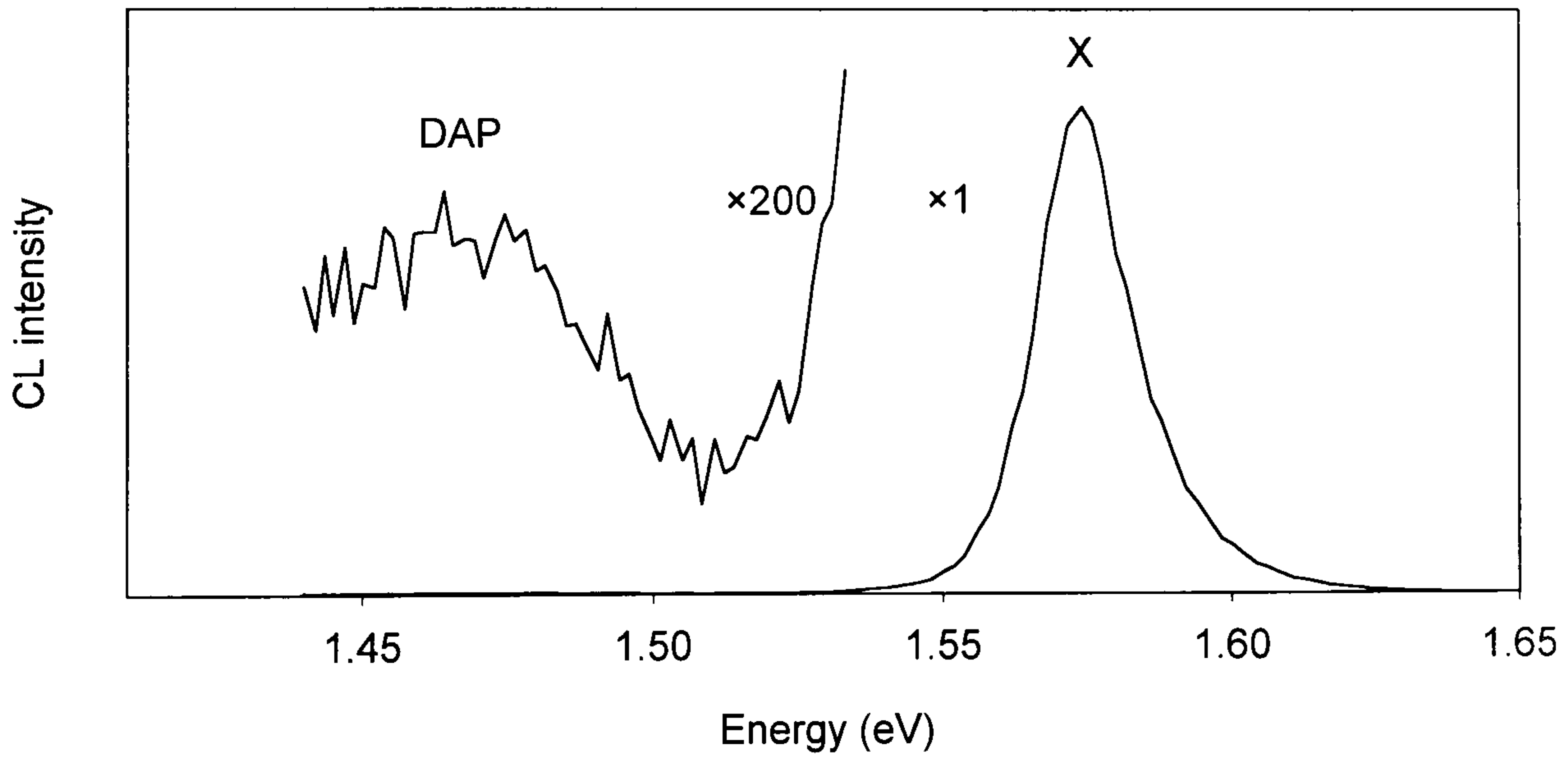

Figure 8.14 CL spectrum of a full CdS/CdTe structure, taken from a thick part of the bevel at 117K.

This shows an exciton related peak at ~1.57eV and a much less intense DAP band at around 1.45-1.50 eV. The breadth and skewed shape of the excitonic peak suggests that this is not due to a single transition, but that it has some substructure. It should be noted that this spectrum was obtained using a low resolution grating (150 lines/mm), with parallel data acquisition using a photodiode array. This resulted in a relatively low spectral resolution, but was sufficient to obtain monochromatic CL images. Such an image is shown in Figure 8.15, which was obtained with the monochromator centred on a photon energy of 1.59eV in order to collect only the exciton emission. This image shows the excitonic luminescence to be restricted to the grain interiors. The dark grain boundaries indicate luminescence quenching due to the prevalence of non-radiative recombination via grain boundary states. This observation is consistent with CL measurements carried out by others on grain boundaries in bulk CdTe [20,21].

A further image was taken from the same region of the cell using light centred on 1.44eV. This ensured only DAP luminescence contributed to the image, which is shown in Figure 8.16. In order to obtain enough light for this low intensity peak, the slit width was increased by a factor of 10 compared with that used for Figure 8.15. Comparison of this image with Figure 8.15 shows the DAP luminescence to originate mainly from the grain boundaries and the smaller grains, with the largest grains showing the least emission in this band. This suggests that the species involved in these transitions are present in a higher concentration near to the grain boundaries.

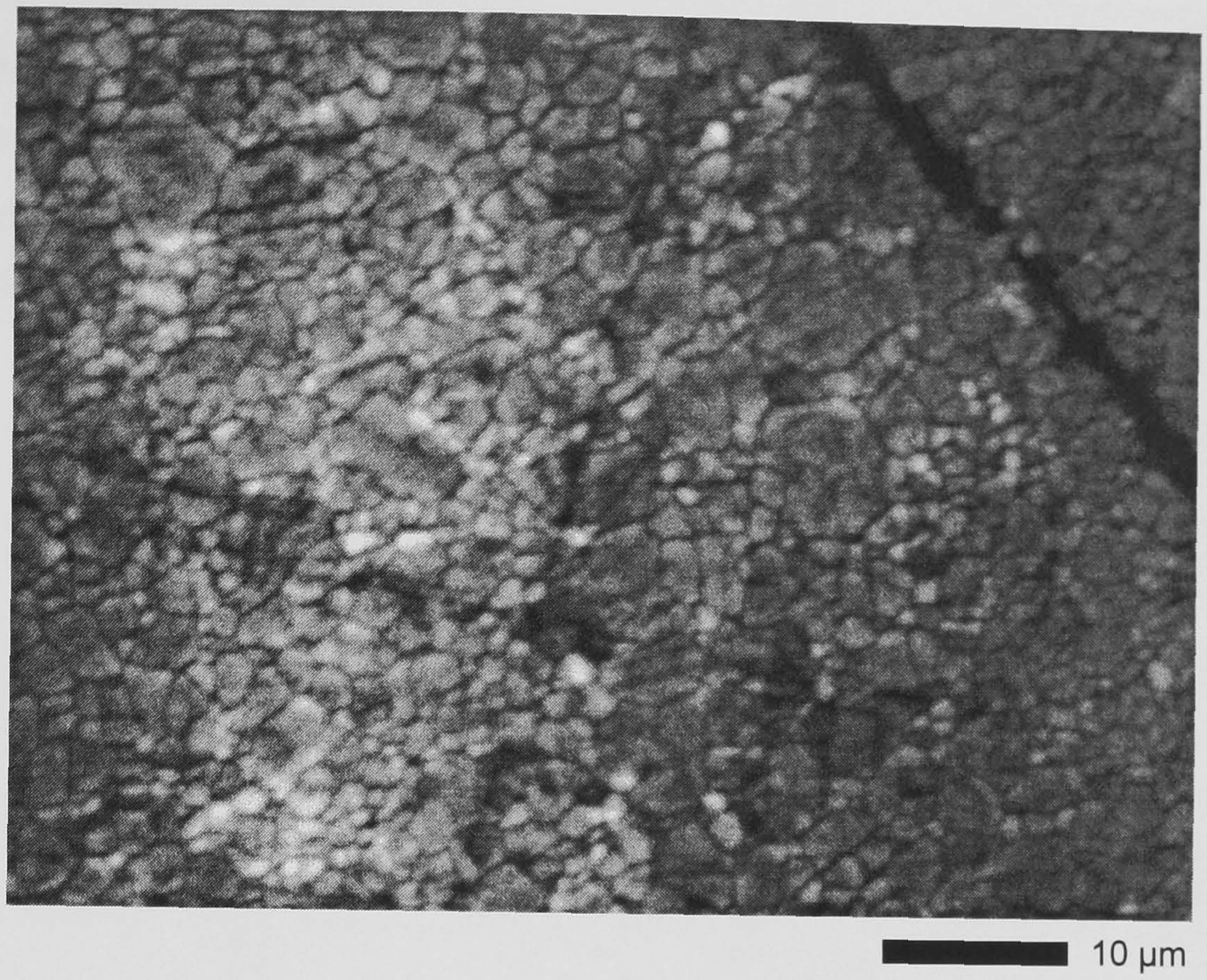

Figure 8.15 Monochromatic CL image taken at 117K from same position as the spectrum shown in Figure 8.14, centred on a photon energy of 1.59eV. Grain boundaries appear dark.

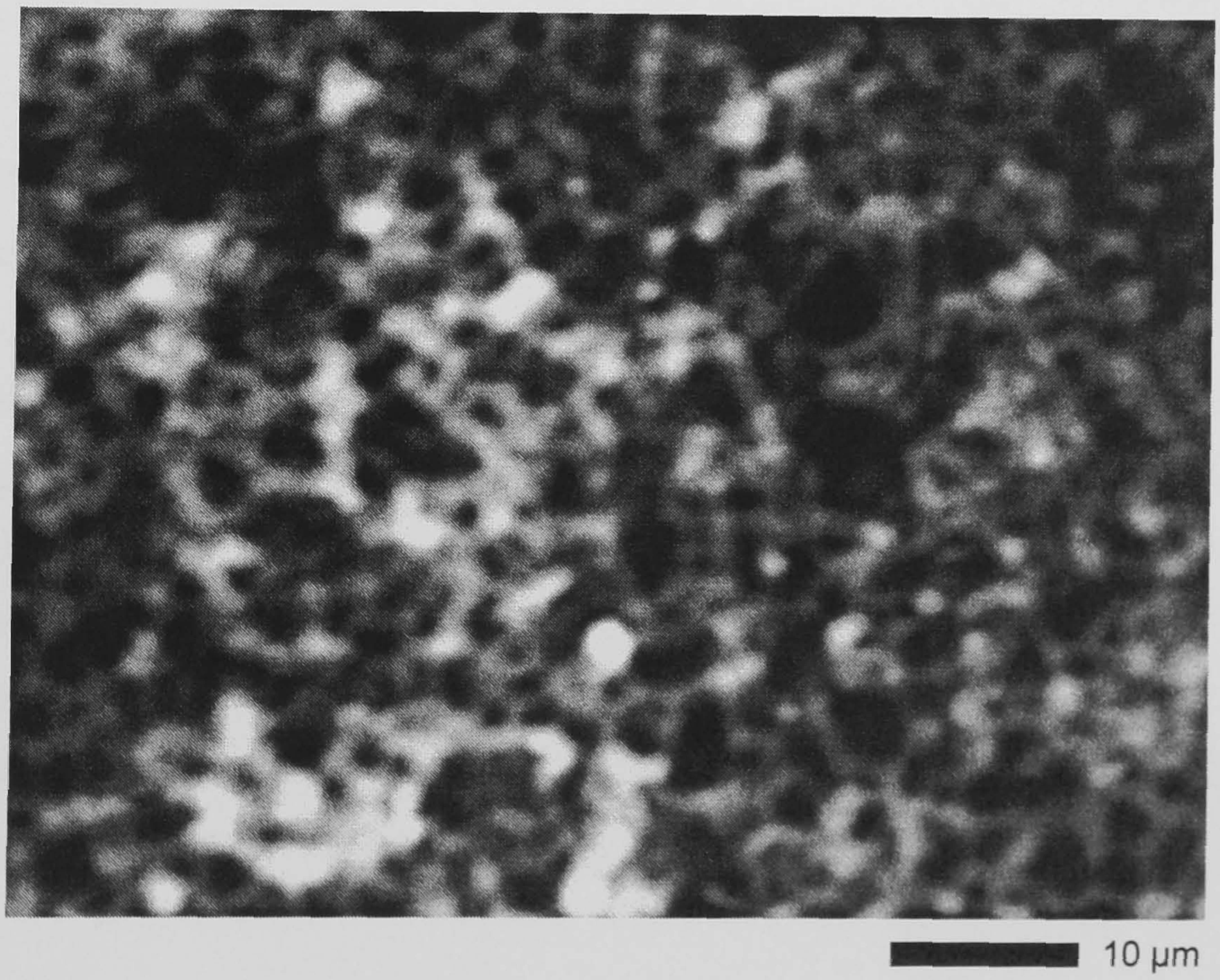

Figure 8.16 Monochromatic CL image at 117K of same area as Figure 8.15, centred on a photon energy of 1.44eV. Grain boundaries and small grains appear bright.

A further set of spectra and monochromatic images were taken from the same sample, but from a relatively thin part of the bevel. Figure 8.17 shows the CL spectrum. The luminescence is similar to that seen previously, but with an added exciton peak at 1.59eV. No peaks are evident in the region of the spectrum where previously the DAP emission was seen.

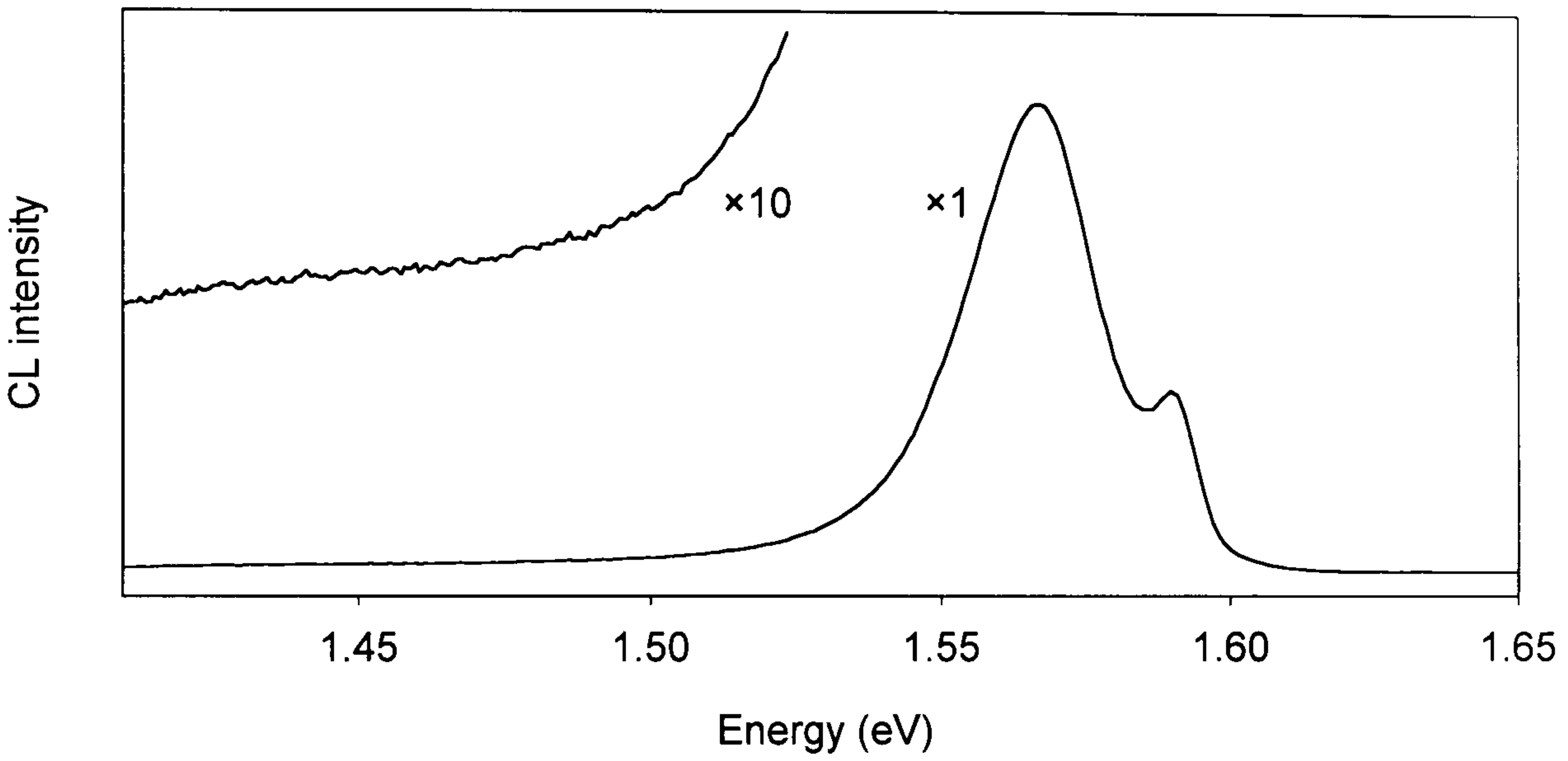

Figure 8.17 CL spectrum of a full CdS/CdTe structure, as for Figure 8.14, taken from a thinner part of the bevel at 5K.

The spatial origins of the two peaks in Figure 8.17 were investigated using monochromatic CL imaging. The results are seen in Figures 8.18 and 8.19, which were obtained with the monochromator centred on photon energies of 1.62 and 1.51eV respectively. The two images both show a reduced luminescence originating from grain boundary regions, as well as significant variation between grains. In addition, the luminescence intensities for the two different wavelengths do not vary consistently from grain to grain. To illustrate this, three individual grains have been highlighted on the images. The grain labelled A appears bright at both wavelengths; grain B is considerably brighter at the longer wavelength; whereas the luminescence from grain C appears to be limited to the higher energy peak.

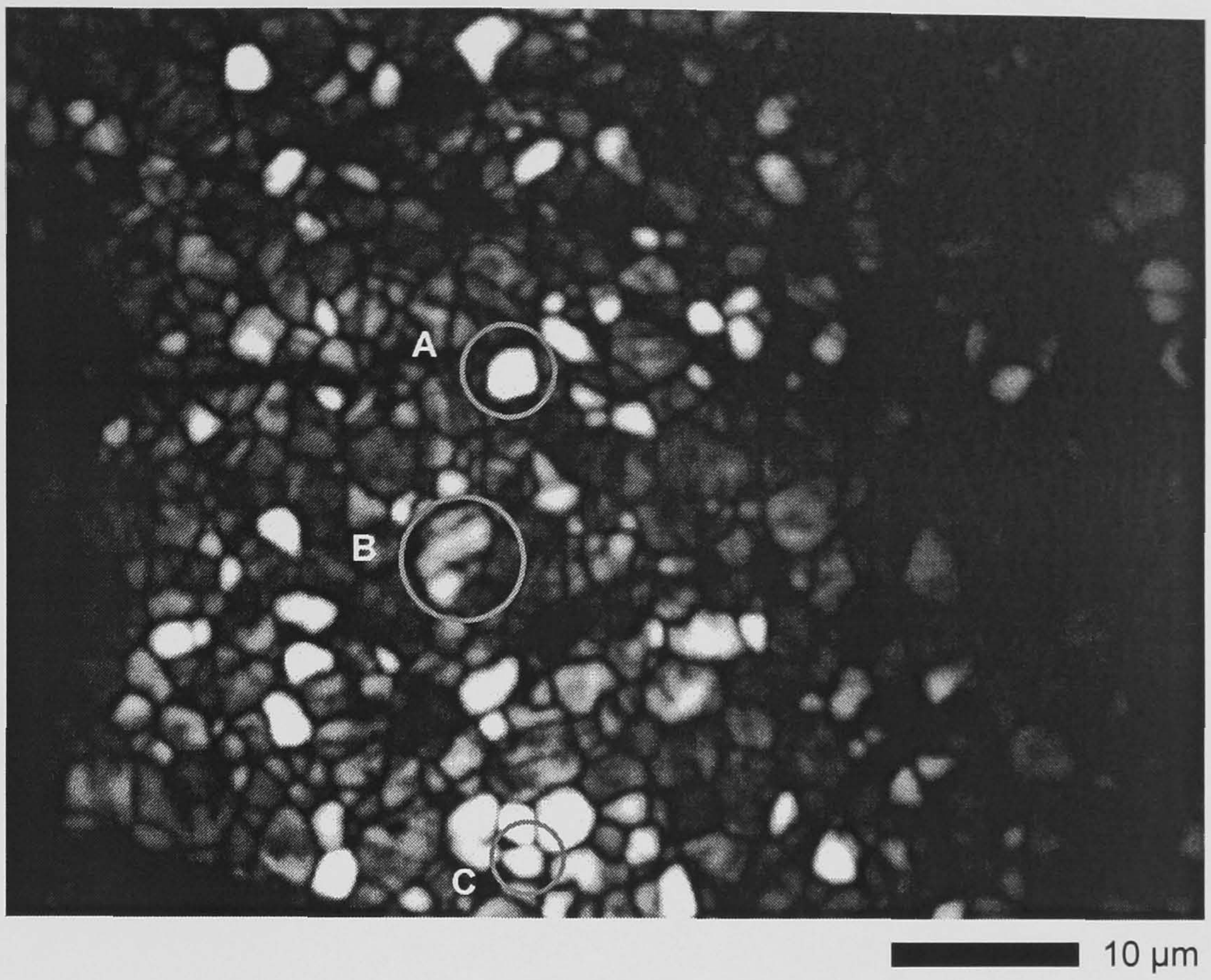

Figure 8.18 Monochromatic CL image taken from same position as the spectrum shown in Figure 8.17, centred on a photon energy of 1.62eV (T=5K).

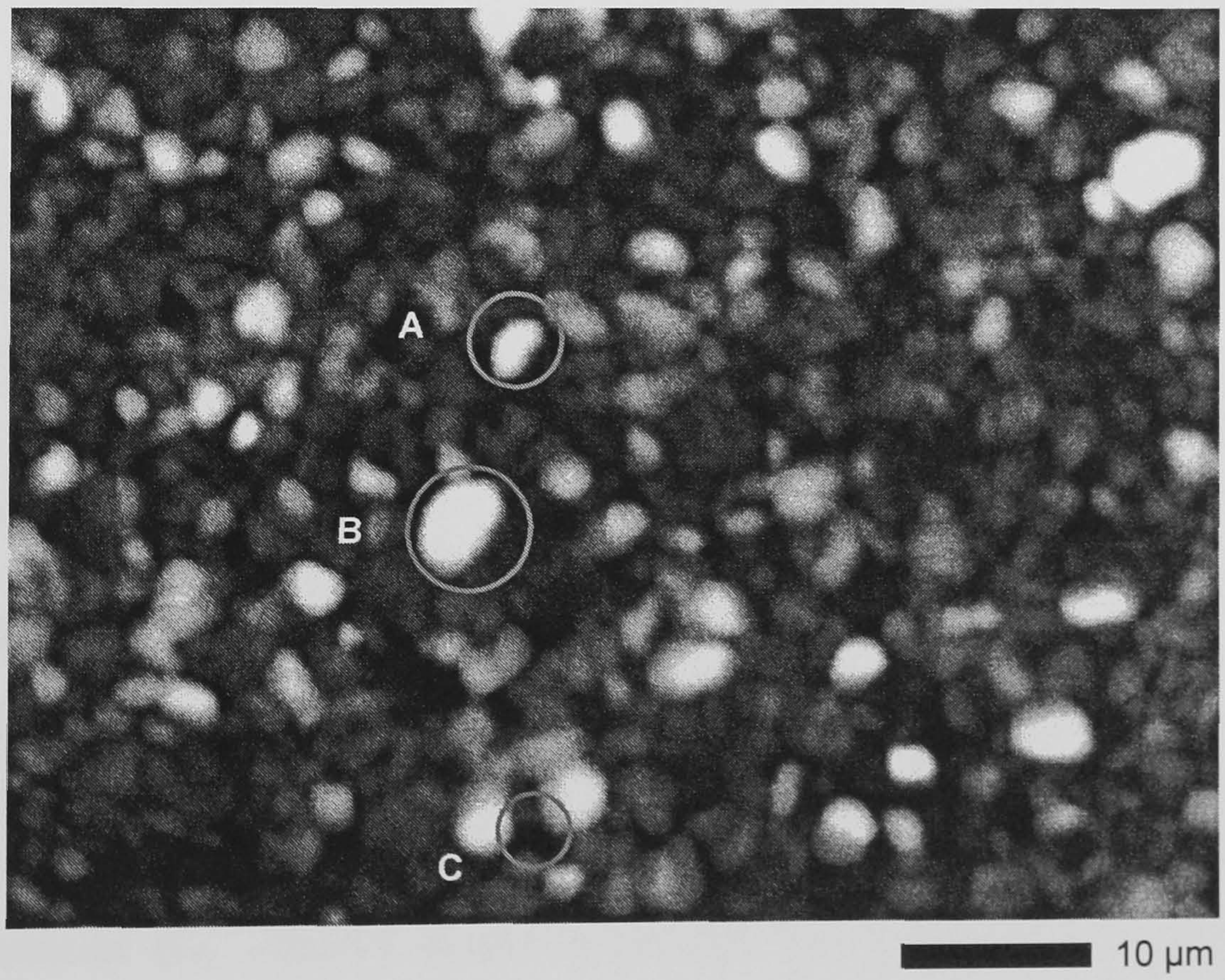

Figure 8.19 Monochromatic CL image of same area as Figure 8.18, centred on a photon energy of 1.51eV (T=5K).

In order to probe any variation in the bandgap of the CdTe as a function of depth, the exciton related region of the CL spectrum was recorded as a function of bevel position. This was carried out on another, identically prepared, sample to the results presented above. A nominal temperature of 5K was used for these measurements, the results of which are seen below in Figure 8.20.

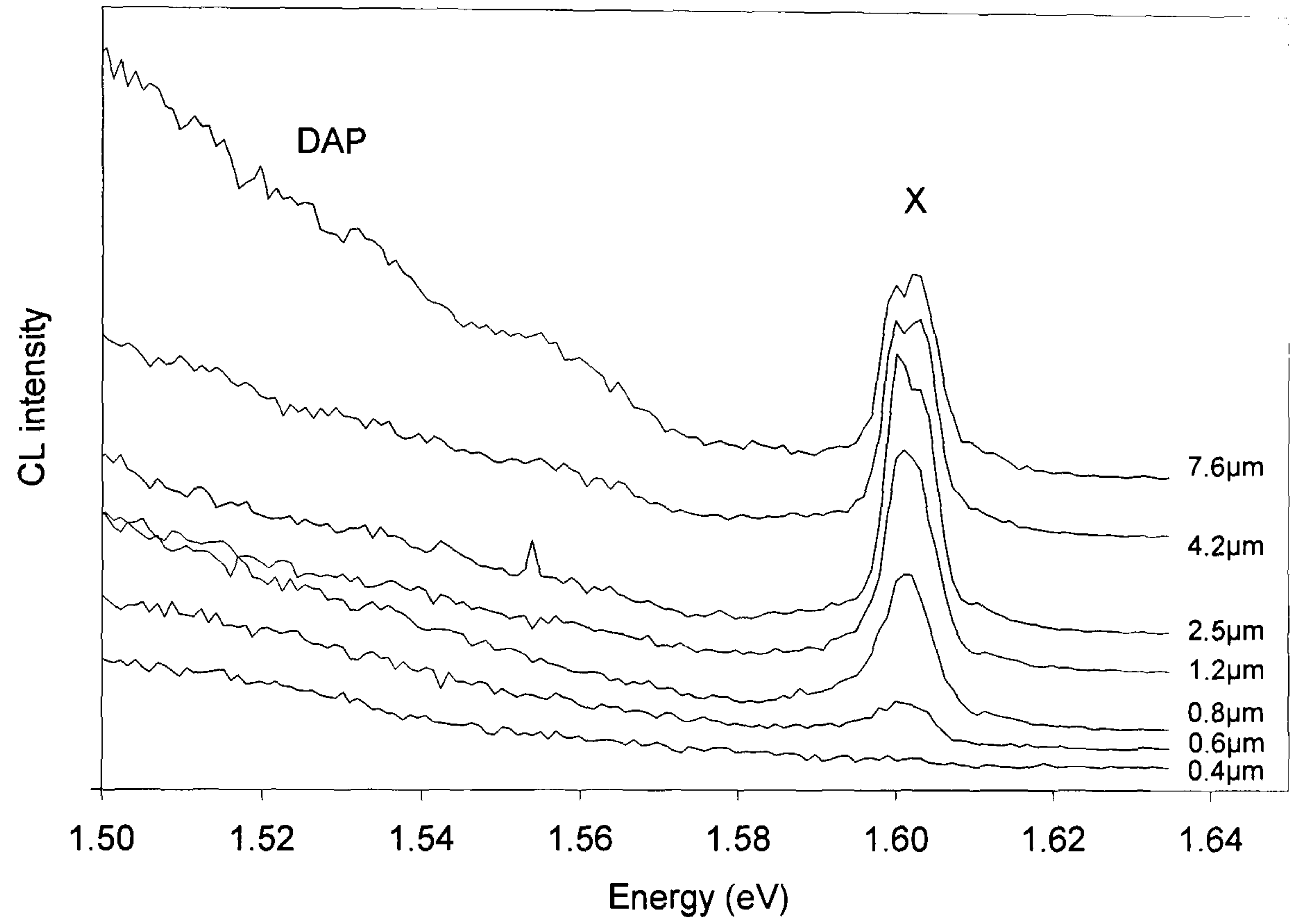

Figure 8.20 Excitonic region of the CL spectrum obtained for the CdTe/CdS solar cell, as a function of bevel thickness.

It can be seen that this spectrum shows no discernible energy shift with changing bevel thickness.

8.3.3 Discussion of CL results

The absence of any visible shift in the energy of the exciton peak with bevel position in Figure 8.20 above is in part due to the limited resolution of the grating used. However, a change in energy of the same order as that observed with the PL measurements (*i.e.* ~8meV) should in principle be observable in Figure 8.20. Another factor is the effect of the carrier generation depth. Unlike 488nm light, under which most carrier generation takes place within 0.2μm of the surface of the CdTe (see Figure 7.3), a 12keV electron beam results in a depth dose around 1μm deep.

This will result in the excitation of a greater depth and hence possible range of CdS_xTe_{1-x} compositions, and therefore a loss of spectral resolution.

8.4 GDOES ANALYSIS

8.4.1 Introduction

An alternative approach to measuring the extent of alloying at the CdTe/CdS interface has also been attempted. In contrast with the luminescence methods already reported in this chapter, GDOES is a technique which directly analyses the elemental composition as a function of depth through a sample. This technique, described more fully in Section 3.6, is more generally used to examine the surfaces of metals; however, its use with semiconducting samples has recently been proposed, and preliminary studies have demonstrated its feasibility [22].

8.4.2 Results

Measurements were carried out using a LECO GDS-750 QDP glow discharge spectrometer at Sheffield Hallam University. Differently treated samples were examined, which were mechanically polished to removed surface features before contacting with gold as described in Section 4.2.3. The results for the cadmium chloride treated CdS/CdTe device are presented in Figure 8.21, which shows eight of the 25 elements simultaneously monitored during the experiment. The time axis approximately represents the distance through the sample, with 0s corresponding to the gold back contact, and the glass substrate beginning at around 78s. The few points at either end of each trace are spurious, and are caused as the glow discharge is first initiated and then extinguished.

These results apparently show a large amount of sulphur deep within the CdTe layer. However, a consideration of the errors involved must be undertaken before this observation can be confirmed. An intense sulphur peak appears on the GDOES trace at 72s, corresponding to around 90% of the distance from the back contact to the glass substrate. This is far sooner than would be expected from a consideration of the relative thickness of the CdS and CdTe layers. Moreover, the In, Sn and O peaks, originating from the TCO layer, appear at almost exactly the same time. These observations are indicative of a serious limitation inherent in applying this technique to semiconductors, which will be further explained in the next section. Because of this, no further results are presented here.

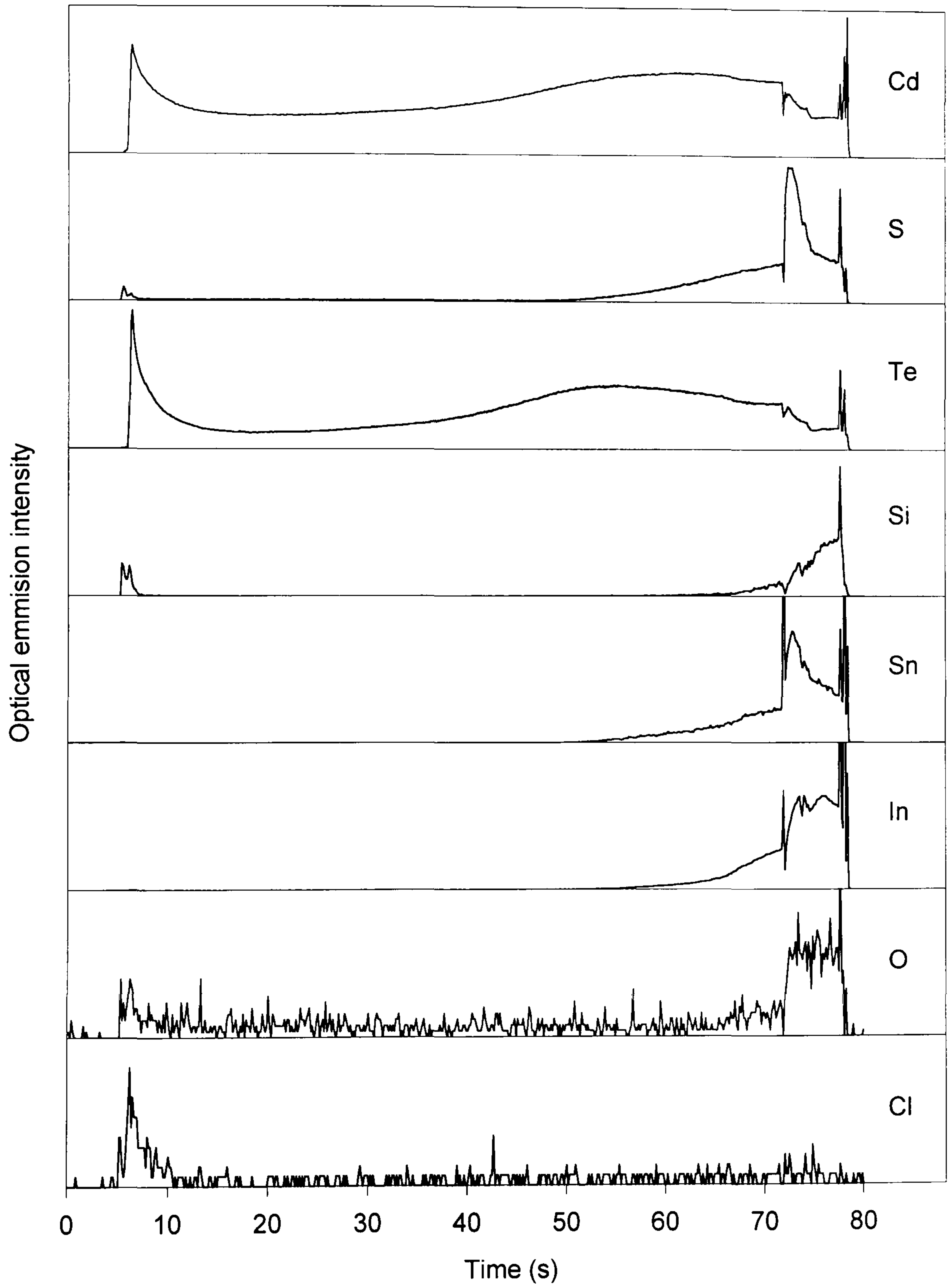

Figure 8.21 GDOES results for a $CdCl_2$-treated CdS/CdTe cell, showing eight selected elements from a total of 25 measured.

8.4.3 Discussion

The origin of the lack of spatial resolution seen in the results of Figure 8.21 can be determined by examination of the circular crater left by the GDOES experiment. Figure 8.22 shows the cross-section of the widest part of the crater, measured using a step profiler.

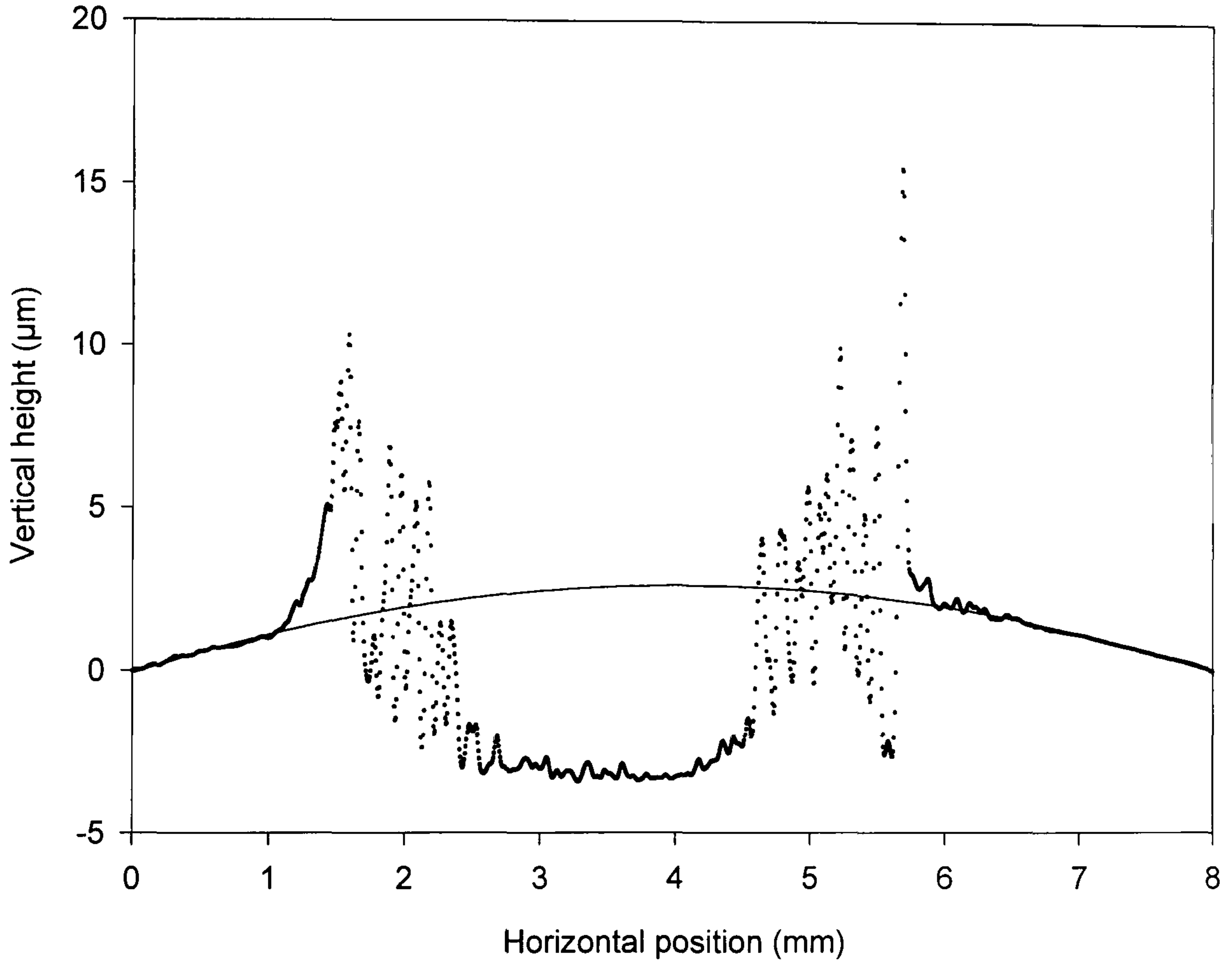

Figure 8.22 Measured profile of a crater left by the GDOES experiment on a solar cell. The solid line shows the approximate position of the original back surface of the solar cell, the apparent curvature of which is an artefact of the step profiler.

The apparent convexity of the solar cell surface seen here is an artefact of the profiler. Despite this aberration, however, the floor of the crater appears concave. From this it is clear that the rate of etching by the plasma in the Grimm glow discharge lamp did not occur at a constant rate across this sample. Variations in the depth of the crater of up to ~2μm can be seen, which would limit the depth resolution to a similar value. Thus it is concluded that little useful information concerning the variation of the solar cell composition with depth can be inferred from these results.

Changes in the etch rate with depth are also evident in the shapes of the elemental traces. For example, the cadmium signal, which would be expected to remain constant through the CdTe and CdS layers, shows significant variation. Corrections could be made to compensate for this, using the cadmium trace to normalise the other elements. However, this has not been considered profitable for these results, due to the non-uniform etch rates across the sample.

These variations in the etch rate, and the associated loss of depth resolution, have their origin in changes in resistivity through the sample. Since the sample itself acts as the cathode for the plasma source, its resistivity will affect the current and hence the temperature of the plasma. With metallic samples, with their high and homogeneous conductivity, a steady etch rate can achieved; careful choice of current will then lead to approximately rectangular crater cross sections and sub-micron resolution [23]. The resistivity of the solar cells, by contrast, will not only be considerably higher but will also vary from grain to grain, between grains and boundaries, and with depth. This will lead to continual fluctuations in the plasma current and hence the abrasion rate.

8.5 CONCLUSIONS

In this chapter, several experiments have been described which have attempted to determine the extent, type and role of impurities present in CdS/CdTe solar cells. Low temperature photoluminescence measurements on bevelled samples have indicated that post-deposition processing of the solar cells with $CdCl_2$ results in the introduction of active centres into the CdTe from both the back surface and CdS layer of the cell. These measurements also indicate that some alloying of the sulphide and telluride layers has occurred at the interface, although this observation is complicated by the presence of other factors which cause the bandgap to alter in this region. Cathodoluminescence was shown to lack the resolution necessary to see these intermixing effects, but has allowed the spatial origin of the luminescence to be determined. This has shown that the DAP luminescence is restricted to small grains and to the grain boundaries, which is consistent with grain boundary transport being the major mechanism for the introduction of impurities into the device during chloride processing.

REFERENCES FOR CHAPTER 8

[1] D.G. Moon and H.B. Im (1992) *Optical and electrical-properties of* $CdS_{1-x}Te_x$ *films*, Powder Metallurgy **35** (1) pp.53-56

[2] For a review of the current pseudobinary phase data available in the literature, see K. Durose, P.R. Edwards and D.P. Halliday (1999) *Materials aspects of CdTe/CdS solar cells*, Journal of Crystal Growth **197** pp.733-742

[3] D. Richardson and R. Hill (1972) *The origins of energy gap bowings in substitutional semiconductor alloys*, Journal of Physics C: Solid State Physics **5** pp.821-827

[4] K. Ohata, J. Saraie and T. Tanaka (1973) *Phase diagram of the CdS-CdTe pseudobinary system*, Japanese Journal of Applied Physics **12** (8) pp.1198-1204

[5] R. Pal, J. Dutta, S. Chauhuri and A. Pal (1993) CdS_xTe_{1-x} *films: preparation and properties*, Journal of Physics D: Applied Physics **26** pp.704-710

[6] A.D. Compaan, Z. Feng, G. Contreras-Puente, C. Narayanswamy and A. Fischer (1996) *Properties of pulsed laser deposited* CdS_xTe_{1-x} *films on glass*, Materials Research Society Symposium Proceedings **426**

[7] S.K.J. Al-Ani, M.N. Makadsi, Al-Shakarchi and C.A. Hogarth (1993) *Preparation, and structural, optical and electrical properties of the* $CdTe_{1-x}S_x$ *system*, Journal of Materials Science **28** pp.251-258

[8] R. Radojcic, A.E. Hill and J. Hampshire (1981) *Preparation and properties of mixed* CdS_xTe_{1-x} *thin films*, Solar Cells **4** pp.101-107

[9] D. Bonnet (1970) *Preparation and properties of polycrystalline* CdS_xTe_{1-x} *films*, Physica Status Solidi (a) **3** (4) pp.913-919

[10] R. Hill and D. Richardson (1973) *Energy gap variations and structural phase changes in CdS-Te alloy thin films*, Thin Solid Films **18** (1) pp.25-28

[11] D.G. Jensen, B.E. McCandless and R.W. Birkmire (1996) *Thin-film cadmium sulfide/cadmium telluride alloys*, Materials Research Society Symposium Proceedings **426** pp.325-330

[12] Landolt-Börnstein, *Numerical Data and Functional Relationships in Science and Technology, Group III Vol.17(b) §3.12*, (Springer-Verlag, 1982)

[13] B.K. Meyer, W. Stadler, D.M. Hofmann, P. Omling, D. Sinerius and K.W. Benz (1992) *On the nature of the deep 1.4eV emission bands in CdTe - a study with photoluminescence and ODMR spectroscopy*, Journal of Crystal Growth **117** pp.656-659

[14] A. Castaldini, A. Cavallini, B. Fraboni, P. Fernandez and J. Piqueras (1997) *Comparison of electrical and luminescence data for the A center in CdTe*, Applied Physics Letters **69** (23) pp.3510-3512

[15] D.P. Halliday, J.M. Eggleston and K. Durose (1998) *A photoluminescence study of polycrystalline thin-film CdTe/CdS solar cells*, Journal of Crystal Growth **186** pp.543-549

[16] D.P. Halliday, J.M. Eggleston and K. Durose (1998) *A study of the depth-dependence of photoluminescence from thin film CdS/CdTe solar cells using bevel etched samples*, Thin Solid Films **322** pp.314-318

[17] J.M. Eggleston, D.P. Halliday and K. Durose (1996) *Spectroscopic study on the effect of post-growth annealing of CdTe/CdS thin film photovoltaic devices*, Institute of Physics Conference Series **155** pp.441-444

[18] Landolt-Börnstein, *Numerical Data and Functional Relationships in Science and Technology, Group III Vol.17(b) §3.10*, (Springer-Verlag, 1982)

[19] K. Akimoto, H. Okuyama, M. Ikeda and Y. Mori (1992) *Isoelectronic oxygen in II-VI semiconductors*, Applied Physics Letters **60** (1) pp.91-93

[20] L.O. Bubulac, J. Bajaj, W.E. Tennant and P.R. Newman (1987) *Spectrally filtered cathodoluminescence of CdTe*, SPIE **794** pp.50-54

[21] L.O. Bubulac, J. Bajaj, W.E. Tennant, P.R. Newman and D.S. Lo (1988) *Spatial origin of various PL lines in CdTe at 77K*, Journal of Crystal Growth **86** pp.536-543

[22] I.M. Dharmadasa, M. Ives, J.S. Brooks, G.H. France and S.J. Brown (1995) *Application of glow discharge optical emission spectroscopy to study semiconductors and semiconductor devices*, Semiconductor Science and Technology **10** (3) pp.369-372

[23] H. Hocquaux *"Thin film analysis"* in *Glow Discharge Spectroscopies*, edited by R. K. Marcus, (Plenum Press, New York, 1993)

Chapter 9: Conclusions

9.1 CONCLUSIONS

This thesis has documented the use of beam-induced current measurements (OBIC and EBIC) and luminescence techniques (PL and CL) to examine the materials properties of cadmium telluride/cadmium sulphide thin film solar cells. In particular, the work has focussed on characterising the effect of the post-deposition treatment of the cells with cadmium chloride.

Optical beam-induced current measurements as a function of bias voltage have been used to probe spatial variations in the illuminated current-voltage characteristics (see Chapter 5). The results have shown that an effect of the $CdCl_2$/heat treatment is to widen the depletion region. Inhomogeneity in the photocurrent on the scale of grains was observed, both before and after treatment, and this has been attributed to microscopic variations in the depletion region position and width.

Since this optical technique provided insufficient spatial resolution to examine the grain boundaries, electron beam-induced current measurements were also carried out on the solar cells, as described in Chapter 6. A novel sample preparation technique was used to remove the glass substrate, whilst leaving the active layers of the device intact. This has allowed EBIC to be carried out in the solar illumination geometry for the first time on these devices. The EBIC images exhibited similar granular variation to that observed by OBIC, but were sufficiently spatially resolved to indicate that the grain boundaries were partially passivated by the $CdCl_2$ treatment.

By varying the electron beam current, it has been shown that the EBIC contrast of the chloride-treated cells is strongly dependent on the carrier injection density. This effect was particularly evident at high beam currents, at which bright grain boundary contrast was visible. In Section 6.7, a model was proposed to explain these effects in terms of high injection conditions. Under these conditions, the excess carriers injected form a plasma, shielding them from the collecting field and reducing the EBIC signal. In the model, the grain boundaries are associated with higher concentrations of carriers than the grain interiors. Since the onset of high injection conditions occurs when the equilibrium carrier concentration is exceeded by the density of excess carriers, the grains will therefore enter the high injection regime at lower carrier injection densities than the boundary regions. This would result in bright grain boundaries when the grains are in high injection and the boundary regions (with their high carrier concentration) are still in low injection. Various methods were used in Section 6.6 to analyse these effects, the most promising of which was found to be to define a beam current threshold at which high injection begins to occur. This analysis confirms the model of higher carrier concentrations near the boundaries.

This evidence supports the theory that the chloride treatment is involved in the type conversion of the CdTe from *n* to *p*-type, and that this diffuses along the grain boundaries. The species most likely to effect this type conversion is the cadmium vacancy complex:

$$\left[V_{Cd}^{2+}Cl_{Te}^{-}\right]^{+}$$

which is a known acceptor in chlorine-doped CdTe.

The observation of higher doping concentrations near to grain boundaries confirms observations made by Woods *et al.* [1]. Their work used dark temperature-dependent *I-V* measurements and frequency-dependent resistivity measurements to show that the grain perimeters were up to three orders of magnitude more highly doped than the grain interiors. This observation is consistent with the results presented here, since although the exact relationship between the high injection threshold and the equilibrium carrier concentration is not known, the grain boundary regions were found to enter high injection at beam currents around three orders of magnitude higher than at the grains. This can be seen in Figures 6.19 and 6.20. Woods *et al.* used their data to propose a band structure for the grain boundaries in which there is a potential barrier to the flow of both minority and majority carriers, which is also consistent with the results of this thesis.

The band bending at the boundaries has also been shown to be consistent with previous EBIC measurements made through the back wall of the solar cell. The higher doping concentration at the grain boundaries causes the junction depletion region to be narrower in these regions. This means that the edge of the depletion region at these points is further from the back contact, leading to dark grain boundary

EBIC contrast when the beam enters from the back of the cell (as seen in Figures 6.1 and 6.2).

A further observation from the EBIC results is that the presence of the CdS layer results in a higher overall doping concentration in the CdTe, but only following the $CdCl_2$ treatment. This confirms the fact that diffusion of sulphur from the CdS plays an important role in the post-deposition processing, although the exact mechanism is not known.

EBIC measurements have also been made as a function of the electron beam energy. These were presented in Chapter 7. Using Monte Carlo simulations to model the carrier generation function under different beam conditions, it has been possible to estimate the depth-dependent carrier collection function of the solar cell. This has shown that the collecting junction of all cells is 0.2-0.3μm into the CdTe, and that the device is therefore effectively a buried homojunction (see Figure 7.6). Post-deposition treatment appears to increase the electron diffusion length in the CdTe, enabling the device to collect deeper into the cell, and also results in an increase in the depletion width of the device. However, the latter effect appears to be dependent on the presence of the CdS layer.

In Chapter 8, low temperature photoluminescence measurements were also carried out on $CdCl_2$ treated CdTe cells, with both excitonic and donor-acceptor pair luminescence bands observed. A bevel profiling technique, not used elsewhere with PL, was used to examine changes in the PL spectrum as a function of depth through the device. The intensity of the DA luminescence was found to increase with proximity to the back surface for a CdS-free sample, suggesting the diffusion of an electrically active species from this surface (Figure 8.11). A similar increase in intensity near the back of the cell was seen for the complete CdS/CdTe device (Figure 8.12); however in this case there was also an increase in intensity towards the front of the device, with a minimum near the middle of the cell and a maximum ~1.5μm from the CdTe/CdS interface. This evidence confirms the EBIC evidence that the diffusion of species from the CdS layer influences electrically active centres in the device.

The energy of the exciton peak was measured as a function of depth, in order to detect any shifts in bandgap due to alloying of the CdS and CdTe. Although some decrease in the energy of the peak was observed in the full CdS/CdTe device, a similar effect (albeit to a lesser degree) was also observed for the CdS-free sample (Figure 8.9). The origin of this energy shift is not clear, although it may be due to a field-related phenomenon.

These PL studies were complemented by the use of cathodoluminescence imaging in Section 8.3, allowing the spatial origin of the different luminescence bands to be investigated. It was found that the exciton emission was excluded from the grain boundaries, and also varied in intensity from grain to grain. The DA luminescence, by contrast, was found to originate mainly from the grain boundaries and the smaller grains.

This evidence, when combined with that from the results described above, gives a clearer understanding of the effect of the $CdCl_2$ treatment. The variation in the intensity of the DA luminescence with depth suggests the diffusion of species into the CdTe from the back of the sample, introducing a shallow level. This luminescence has been shown using CL to be limited mainly to the regions near the grain boundaries, indicating diffusion along these boundaries. Moreover, the evidence of the front-wall EBIC measurements is that the chloride treatment results in an increase in the concentration of holes near the grain boundaries, implying the involvement of an acceptor level. Taken together, therefore, one major conclusion of this work is that the chloride/heat treatment introduces an acceptor level (possibly the cadmium vacancy complex suggested earlier), which diffuses through the grain boundaries effecting *n* to *p* type conversion.

9.2 SUGGESTIONS FOR FUTURE WORK

More work is required in order to develop further the beam current dependent EBIC technique described in Chapter 6. The dependence of the high injection threshold beam current on the equilibrium carrier concentration needs to be more rigorously proven. This could be achieved by the use of computer simulations of the interaction of the electron beam with the sample, coupled with the numerical modelling of the subsequent movement of the resultant excess carriers. This would allow an estimate to be made of the steady-state carrier injection density under given beam conditions, which could then be experimentally verified on samples with known doping concentrations. This would in turn allow the calibration of the current threshold maps (such as those seen in Figure 6.20) in terms of an absolute carrier density.

Further development of the EBIC *versus* beam voltage method may also be possible, as the technique could be extended to provide spatial information. Such work, however, would require a better understanding of the high injection effects mentioned above.

The novel cell geometries introduced by this work (namely the front-wall and bevel-etched configurations) will allow many more techniques to be used to characterise CdTe cells than were previously possible. Such possibilities include: the use of a scanning near-field optical microscope to carry out high resolution OBIC through the front of the cell; Rutherford backscattering spectroscopy of the CdS/CdTe region of the cell; and many different measurements as a continuous function of depth through the cell, including resistivity and grain size analysis.

REFERENCE FOR CHAPTER 9

[1] L.M. Woods, D.H. Levi, V. Kaydanov, G.Y. Robinson and R.K. Ahrenkiel (1998) *Electrical characterization of CdTe grain-boundary properties from as processed CdTe/CdS solar cells*, Proceedings of 2nd World Conference on Photovoltaic Solar Energy Conversion, Vienna, pp.1043-1046.

Appendix: List of publications and awards

PUBLICATIONS

P.R. Edwards, S.A. Galloway, P.R. Wilshaw and K. Durose (1997) *A study of the activation of CdTe/CdS thin film solar cells using OBIC*, Institute of Physics Conference Series **157** pp.583-586

S.A. Galloway, P.R. Edwards and K. Durose (1997) *EBIC and cathodoluminescence studies of grain boundary and interface phenomena in CdTe/CdS solar cells*, Institute of Physics Conference Series **157** pp.579-582

P.R. Edwards, D.P. Halliday and K. Durose (1997) *The influence of $CdCl_2$ treatment and interdiffusion on grain boundary passivation in CdTe/CdS solar cells*, Proceedings of 14th European Photovoltaic Solar Energy Conference, Barcelona, pp.2083-2086

P.R. Edwards, S.A. Galloway and K. Durose *"Carrier density microscopy of CdS/CdTe solar cells"* in *Growth and Processing of Electronic Materials*, edited by N. M. Alford, (IOM Communications, London, 1998) pp.50-57

P.R. Edwards, K. Durose, S.A. Galloway, D. Bonnet and H. Richter (1998) *Front-wall electron beam-induced current studies in thin-film CdS/CdTe solar cells*, Proceedings of 2nd World Conference on Photovoltaic Solar Energy Conversion, Vienna, pp.472-476

S.A. Galloway, P.R. Edwards and K. Durose (1998) *Characterisation of thin film CdS/CdTe solar cells using electron and optical beam induced current*, Solar Energy Materials and Solar Cells **57** pp.61-74

K. Durose, P.R. Edwards and D.P. Halliday (1998) *Materials aspects of CdTe/CdS solar cells*, Journal of Crystal Growth **197** pp.733-742

AWARDS

1996	North Holland Book Prize, for progress in first year of PhD.
1997	Quayle Postgraduate Bursary, to fund collaboration with the Materials Department at Oxford University.
1998	Poster presentation winner at the Institute of Materials "Congress '98" conference, Cirencester.
1999	Graham Russell Applied Physics Prize for outstanding achievement in final year of PhD.